

**High resolution and high efficiency biomolecular sensing using  
solid-state and hybrid bilayer MoS<sub>2</sub> nanopores**

by

Payel Sen

A thesis submitted in partial fulfillment of the requirements for the degree of

Doctor of Philosophy

in

Materials Engineering

Department of Chemical and Materials Engineering  
University of Alberta

© Payel Sen, 2021

## Abstract

Solid-state nanopores have emerged as stable label- and amplification- free biosensors for rapid detection of charged biomolecules. Analytes are electrophoretically pulled through nanopores and are detected using the characteristic blockade current due to the translocation. However, despite their stability and scalability, solid-state nanopores have few limitations which need to be overcome for achieving a versatile and efficient biosensor. One of the primary challenges of nanopore sensing is single molecule detection which requires both spatially and temporally resolved signals.

Monolayer molybdenum disulphide (a 2D material) due to its favourable surface charge, monolayer thickness, and stability in electrolytic medium have been used for single molecule sensing due to their superior spatial resolution. However, their ultra-thinness reduces analyte/nanopore surface charge interaction and makes translocation too fast to temporally resolve the signals, thereby reducing statistical confidence and efficiency of detection.

In this work, both simulation and experimental data demonstrate that bilayer MoS<sub>2</sub> nanopores (~ 1 nm thick) can detect single molecules (nucleotides in this study) with 5 times higher detection rate and 4% higher sensing efficiency by slowing down DNA translocation (i.e., improving temporal resolution) while maintaining a good spatial resolution.

Another limitation of solid-state nanopores is its charge versatility. Solid-state nanopores despite showing good sensitivity towards charged biomolecules, fail to show good neutral molecule detection sensitivity; the latter demanding increased signal-to-noise ratio and dwell times at the nanopore. A biological nanopore due to a chemically sensitive interface manifests minor charge

alterations with higher resolution, thus helping in neutral molecule sensing as well. However, biological pores alone are prone to thermo-mechanical instabilities and are unsuitable for manufacturing portable sensors.

Hybrid nanopores formed by incorporating biological pore in a solid-state nanopore can be suitable for both charged and uncharged molecule sensing. A hybrid of engineered outer membrane porin G (eOmpG) and bilayer MoS<sub>2</sub> nanopore was constructed. This hybrid nanopore demonstrated 1.9 times better signal-to-noise ratio and 8 times better dwell times for polynucleotide sensing as compared to solid-state BL MoS<sub>2</sub> nanopore, due to unique size controllability, gating properties and improved local-charge sensitivity of eOmpG. This hybrid nanopore was able to detect a change as low as 1 pM of delta-9-THC level, which is a neutral molecule, in saliva. The study on THC detection can also help in real-time monitoring of marijuana toxicity in users as well as predict consequences due to its toxicity. The eOmpG in hybrid nanopore also helped in obtaining THC orientation-specific information which can act as means to differentiate toxic and non-toxic elements of marijuana in future.

The study demonstrates that 2D material like MoS<sub>2</sub> is suitable for fabricating solid state nanopores which are repeatable and stable. Nanopores with different number of layers MoS<sub>2</sub> were studied and due to the inter layer interaction bilayer MoS<sub>2</sub> was found to be the optimum one for measurement of single nucleotides effectively and efficiently. Additionally, these BL MoS<sub>2</sub> were used to form hybrid nanopores using barrel protein OmpG which demonstrated reduction of the noise in the nanopore measurement. This hybrid nanopore was used for THC molecule detection which is normally not conducted using a nanopore. Hence, the work has opened the path for layered materials and their applications for nanopores.

## Preface

The research work presented in this thesis is carried out at University of Alberta, Edmonton, Alberta, Canada. All the nanopores were fabricated and characterized in the Fabrication and Characterization centre of nanoFAB (Class 1000 cleanroom and Characterization Area in ECERF and TEM facility at CME). The nanopore conductance and translocation measurements were carried out using Axon Instruments installed at ECERF W3-076 lab of University of Alberta. Dr. Manisha Gupta was involved in formulating the research idea for this research. The experimental protocols were developed, and analysis were carried out by me under the guidance and assistance of Dr. Manisha Gupta.

Chapter 3: This chapter explains the nanofabrication methods used for fabricating silicon nitride and molybdenum disulphide nanopores and also explains the model and physics used to conduct COMSOL Multiphysics simulations for Chapter 4 and Chapter 5. All fabrications and simulations were carried out by me under the guidance of Dr. Manisha Gupta. The authors of this manuscript will be Payel Sen and Manisha Gupta. The first draft of the manuscript was written by Payel Sen and is being edited by Manisha Gupta.

Chapter 4: This chapter explains the study conducted to test the repeatability of nanopore using silicon nitride as the nanopore material. The modelling, physics definition, comparison and analysis were performed by me under the supervision of Dr. Manisha Gupta. The authors of this manuscript will be Payel Sen and Manisha Gupta. The first draft of the manuscript was written by Payel Sen and is being edited by Manisha Gupta.

Chapter 5: This chapter presents a comparative COMSOL Multiphysics simulation-based study revealing the potential of bilayer MoS<sub>2</sub> nanopores in improving temporal resolution of DNA

sensing compared to monolayer MoS<sub>2</sub> and 3-6 layers MoS<sub>2</sub> nanopores and 50 nm thick silicon nitride nanopores. All simulations including modelling, physics definition and analysis were performed by me under the supervision of Dr. Manisha Gupta. The authors of this manuscript will be Payel Sen and Manisha Gupta. The first draft of the manuscript was written by Payel Sen and is being edited by Manisha Gupta.

Chapter 6: This chapter presents the study conducted to improve the efficiency of single nucleotide detection and DNA sequencing by using bilayer MoS<sub>2</sub> nanopores. All fabrications, membrane characterizations, nanopore conductance measurements, analyte translocations and data analysis were conducted by me under the supervision of Dr. Manisha Gupta. The first draft of the manuscript was written by Payel Sen and was edited by Manisha Gupta. This study has been published as “P. Sen and M. Gupta, Single nucleotide detection using bilayer MoS<sub>2</sub> nanopores with high efficiency, RSC Advances, vol. 11, pp. 6114–6123, 2021, doi: 10.1039/d0ra10222a”. RSC advances allows self-authored whole article and article material usage in thesis without copyright request requirement. The necessary acknowledgement for RSC advances has been added as a footnote to this chapter.

Chapter 7: This chapter presents the study conducted to design and develop a hybrid nanopore by combining solid-state bilayer MoS<sub>2</sub> nanopores and Outer Membrane Porin G (OmpG) for improving the sensitivity and signal to noise ratio of biomolecular sensing. Biological pore purification, modification and characterization involved in this study were carried out by Dr. Hiofan Hoi and used by me to construct hybrid nanopore and carry out further molecular sensing. I conducted all experiments involved in creating the hybrid nanopore construct, sensing polynucleotide molecules, and also performed subsequent data analysis under the guidance of Dr. Manisha Gupta. The first draft of the manuscript was written by Payel Sen and was edited by

Manisha Gupta. This manuscript for this study is under review in ACS Biomaterials with me, Dr. Hiofan Hoi and Dr. Manisha Gupta as co-authors.

Chapter 8: This chapter demonstrates Tetrahydrocannabinol sensing through hybrid bilayer MoS<sub>2</sub>/OmpG nanopore. Preparation of analyte solutions and sensing were performed by me under the guidance of Dr. Manisha Gupta. The authors of this manuscript will be Payel Sen and Manisha Gupta. The first draft of the manuscript was written by Payel Sen and is being edited by Manisha Gupta.

All results reported in this thesis along with their analysis, interpretations, and inferences are my original research work.

## **Acknowledgements**

I am sincerely grateful to my mentor and supervisor Dr. Manisha Gupta for constantly supporting and motivating me throughout my Doctoral research tenure. The success of this research majorly rests on the constant guidance, assistance, and dedication which she offered me in shaping my research and resolving research issues as and when required. But most of all, I am particularly grateful to her for giving me the freedom to be reasonably creative during this research, which made work fun, interesting and productive at the same time. This research would not have been possible without her enthusiasm, attention, and contribution. I also want to extend my gratitude to my co-supervisor Dr. Natalia Semagina for encouraging me, lending me a helping hand and being there as a generous and constant support, whenever required through my research program.

I would like to thank Uppiliappan Rengarajan, previous Masters' student of Dr. Manisha Gupta for guiding me through the initial silicon nitride nanopore cleaning, measurement, and fabrication procedures along with introducing me to preliminary COMSOL Multiphysics simulation methods. It really offered me a good foundation to develop on and sped up my initial research work. I am also extremely thankful to Dr. Hiofan Hoi for building biological nanopore construct, which was a crucial component of my research work. I am also thankful to her for being available to answer any queries related to the work and sharing relevant results and references with me. I would like to thank my wonderful lab-mates Jiaxin Fan, Darren Majak, Dipanjan Nandi, Seongdae Kang, Junsen Gao and Michael Faccini-Rakovich for their constant and enormous support and for maintaining a free and friendly work environment and helping me during and after work. I want to particularly acknowledge the contribution of my lab-mates and friends Jiaxin Fan for assisting me in preparing my buffer solution for THC analysis and Dipanjan Nandi for carrying out Raman

characterization of my membranes; two works which were very important for the progress of this research. I also want to thank all my lab-mates for being available for research-based discussions whenever required and sharing their valuable ideas with me.

I want to express my gratitude to nanoFAB staff members Dr. Aaron Hryciw, Stephanie Bozic, Scott Munro, Dr. Shihong Xu, Aditi Ganji and Peng Li for sharing their technical insights and training me on different fabrication and characterization tools, which were used throughout my work.

I would like to thank my friends and family for constantly boosting my morale. Last, I want to thank my husband, Kshitij Agarwal for his support and encouragement, without which I would not have been able to accomplish this research work.

This entire research had been possible due to the support provided by Faculty of Graduate Studies and Research (FEGSR) and Faculty of Engineering, University of Alberta; the Natural Sciences and Engineering Research Council of Canada and Alberta Innovates.

## **Table of contents**

<b>Abstract</b> .....	<b>II</b>
<b>Preface</b> .....	<b>IV</b>
<b>Acknowledgements</b> .....	<b>VII</b>
<b>1 Introduction</b> .....	<b>1</b>
1.1 Motivation.....	1
1.2 Outline.....	7
<b>2 Literature review</b> .....	<b>10</b>
2.1 General background of nanopore sensing.....	10
2.1.1 <i>Solid-state nanopore</i> .....	10
2.1.2 <i>Biological nanopores</i> .....	20
2.1.3 <i>Hybrid nanopore</i> .....	26
2.2 Relevant background literature.....	28
2.2.1 <i>Testing repeatability: standardizing cleaning procedures and narrowing down the range of nanopore diameter</i> .....	28
2.2.2 <i>Selecting membrane/nanopore material for spatially and temporally resolved sensing</i> .....	29
2.2.3 <i>Testing nanopore efficiency for sequencing single-stranded DNA</i> .....	30
2.2.4 <i>Designing a low-noise hybrid nanopore for more sensitive and temporally resolved sensing of both charged and uncharged analytes</i> .....	32
<b>3 Experimental and simulation methods</b> .....	<b>35</b>

3.1	Fabrication of nanopores.....	35
3.1.1	<i>Fabrication of silicon nitride nanopores</i> .....	35
3.1.2	<i>Fabrication of MoS<sub>2</sub> nanopores</i> .....	41
3.2	Ionic conductance-based characterization of nanopores.....	45
3.2.1	<i>Electrolyte preparation</i> .....	45
3.2.2	<i>Nanopore Cleaning</i> .....	45
3.2.3	<i>Custom-designed cell assembly and cleaning</i> .....	46
3.3	COMSOL Multiphysics simulation .....	48
3.3.1	<i>Geometry and parameters involved</i> .....	48
3.3.2	<i>Mathematical modelling</i> .....	50
<b>4</b>	<b>Predicting geometry and size repeatability of silicon nitride nanopores</b> .	<b>60</b>
4.1	Keywords .....	61
4.2	Abstract.....	61
4.3	Introduction.....	61
4.4	Methods.....	63
4.4.1	<i>Experimental section</i> .....	63
4.4.2	<i>Simulation section</i> .....	64
4.5	Results.....	68
4.6	Discussions .....	74
<b>5</b>	<b>Understanding molecular electrokinetic behaviour through monolayer and multilayer MoS<sub>2</sub> nanopores</b> .....	<b>76</b>
5.1	Keywords .....	77

5.2	Introduction.....	77
5.3	Methods.....	80
5.3.1	<i>Model definition</i> .....	81
5.3.2	<i>Geometry and mesh definition</i> .....	84
5.4	Results and Discussions.....	85
5.5	Discussions .....	92
<b>6</b>	<b>Single nucleotide detection using bilayer MoS<sub>2</sub> nanopores with high efficiency.....</b>	<b>95</b>
6.1	Keywords .....	96
6.2	Abstract.....	96
6.3	Introduction.....	97
6.4	Experimental .....	99
6.5	Results and Discussions.....	102
6.6	Discussions .....	112
6.7	Conclusion .....	115
<b>7</b>	<b>Low noise engineered OmpG and bilayer MoS<sub>2</sub> hybrid nanopore .....</b>	<b>133</b>
7.1	Keywords .....	135
7.2	Abstract.....	136
7.3	Introduction.....	136
7.4	Results and Discussions.....	140

7.5	Methods.....	155
7.5.1	<i>Protein engineering and characterization</i> .....	155
7.5.2	<i>Experiment protocol</i> .....	156
<b>8</b>	<b>Monitoring THC levels using highly sensitive engineered OmpG and bilayer MoS<sub>2</sub> hybrid nanopore .....</b>	<b>160</b>
8.1	Abstract.....	161
8.2	Introduction.....	162
8.3	Material and methods.....	165
8.4	Results and Discussions.....	167
<b>9</b>	<b>Summary of results .....</b>	<b>174</b>
	<b>Appendix A .....</b>	<b>207</b>
	<b>Appendix B .....</b>	<b>210</b>
	<b>Appendix C .....</b>	<b>212</b>
	<b>Appendix D .....</b>	<b>216</b>

## **List of figures**

<b>Figure 1.1.</b> Schematic of Coulter counter principle (adapted from MD Graham, 2013 [16]).	.....2
<b>Figure 1.2.</b> Cell set up and process of nanopore sequencing	.....3
<b>Figure 1.3.</b> Schematic showing (a) DNA sequencing through a solid-state nanopore, (b) DNA sequencing through a biological nanopore and (c) DNA sequencing through a hybrid nanopore formed by incorporating a biological nanopore in a solid-state nanopore.	.....4
<b>Figure 2.1.</b> Schematic of DNA sequencing through a solid-state silicon nitride nanopore.	.....14
<b>Figure 2.2.</b> Schematic of DNA sequencing through a solid-state graphene nanopore.	.....15
<b>Figure 2.3.</b> Schematic for nanopore-based DNA tunneling detector (adapted from Ivanov et al., 2011 [102]).	.....19
<b>Figure 2.4.</b> Schematics of Alpha hemolysin (dimensions from Ding et al. 2016 [144]), MspA (dimensions from Derrington et al. 2010 [145]), Aerolysin (dimensions from Iacovache et al. 2016 [146]) and OmpG (dimensions from Köster et al. 2015 [147]) nanopores as presented in literature.	.....22
<b>Figure 2.5.</b> (a) Alpha hemolysin with tethered DNA and (b) Alpha hemolysin insertion in silicon nitride nanopore to form a hybrid (adapted from Hall et al. 2010 [64]).	.....28
<b>Figure 3.1.</b> Schematic of a silicon- Si substrate with both sides coated by LPCVD (low pressure chemical vapor deposition) Silicon nitride- SiN <sub>x</sub> .	.....36
<b>Figure 3.2.</b> (a) L-edit layout of the photomask used for photolithography (b) Substrate with spin-coated photoresist and (c) Substrate with patterned photoresist (after UV exposure and development) exposing the part of the SiN <sub>x</sub> required to be removed.	.....37
<b>Figure 3.3.</b> (a) RIE etch of SiN <sub>x</sub> (not protected by photoresist), (b) A typical section of patterned and RIE etched SiN <sub>x</sub> on Si wafer, (c) KOH etch of uncovered silicon, (d) isometric bottom view, (e) isometric top view of free-standing SiN <sub>x</sub> formed after removal of silicon by KOH etch, and (f)	

optical image of free-standing SiN<sub>x</sub> membrane with inset showing the chip containing the membrane.....39

**Figure 3.4.** (a) Schematic for STEM drilling of nanopore drilling on free-standing SiN<sub>x</sub> membrane and (b) TEM image of a STEM fabricated SiN<sub>x</sub> nanopore.....40

**Figure 3.5.** (a) Schematic and (b) HiM image of a 200 nm hole fabricated by EBL and RIE on free-standing SiN<sub>x</sub> membrane. ....42

**Figure 3.6.** (a) Schematic of a free-standing MoS<sub>2</sub> membrane transferred by mechanical exfoliation to the 200 nm hole on SiN<sub>x</sub> after being aligned properly by using a dual-stage microscope and (b-d) TEM images of three typical bilayer MoS<sub>2</sub> membranes with the free-standing part clearly distinguished from the part supported by SiN<sub>x</sub>, as observed by the difference in contrast with the lighter part showing the free-standing portion of the membrane. It looks lighter due to its thinness allowing higher light transmission. ....43

**Figure 3.7.** (a) Schematic diagram of STEM drilling of MoS<sub>2</sub> nanopore and (b) HRTEM (High Resolution TEM) image of a STEM fabricated bilayer MoS<sub>2</sub> nanopore.....44

**Figure 3.8.** Schematic representation of custom-designed cell assembly for sensing [1. Amplifier, 2. Digitizer, 3. User interface, 4. Faraday cage, 5. Amplifier head, 6. Cell set up (a. Teflon cell containing KCl, b. Ag/AgCl electrodes, Gaskets to hold membrane, d. Membrane bearing nanopore)]. ....47

**Figure 3.9.** Geometry of COMSOL Multiphysics simulation model showing an hour-glass shaped pore with a cylindrical body; L = thickness of membrane/pore height = 50 nm, T = thickness of cylindrical part of pore = 10 nm,  $\alpha_1$  = half-angle of the top conical portion and  $\alpha_2$  = half-angle of the bottom conical portion of the pore.....50

**Figure 3.10.** (a) Boundaries in blue kept at no-slip condition, (b) Inlet and (c) Outlet boundaries kept at zero pressure conditions.....52

**Figure 3.11.** (a) Boundary representing electrode where a potential of 200 mV was applied, (b) Boundary representing the ground electrode, (c) Boundaries at zero charge, (d) Boundaries at a

surface charge of  $-0.031 \text{ C/m}^2$  for  $\text{MoS}_2$  membranes and  $-0.02 \text{ C/m}^2$  for  $\text{SiN}_x$  membranes and (e) DNA boundaries at a surface charge of  $-0.015 \text{ C/m}^2$ .....53

**Figure 3.12.** Boundaries conditions kept at 300 mM KCl (electrolyte) concentration.....54

**Figure 3.13.** (a) Schematic showing the major phenomena occurring in and around the nanopore under an applied electric potential involving electroosmotic fluid flow; viscous drag (VD), Electrostatic and resultant Electrophoretic forces acting on the translocating particle immersed in an electrolyte. The red and green circles indicate negatively and positively charged ions and the red and green boundaries represent negative and positive surface charge which gives rise to Electrical Double layer (EDL) due to counter-charge concentration around both the membranes and the particle and (b) Primary forces acting on the particle dispersed in an electrically biased compartment containing an electrolytic fluid .....57

**Figure 4.1.** Geometry of COMSOL Multiphysics simulation model showing an hour-glass shaped pore with a cylindrical body;  $L$  = thickness of membrane/pore height = 50 nm,  $T$  = thickness of cylindrical part of pore = 10 nm,  $\alpha_1$  = half-angle of the top conical portion and  $\alpha_2$  = half-angle of the bottom conical portion of the pore.....65

**Figure 4.2.** TEM fabricated solid-state nanopores on free-standing 50 nm thick  $5 \times 5$  mm silicon nitride on silicon windows: Pore diameters of (a) 2.5 nm, (b) 4.2 nm, (c) 5.6 nm and (d) 8.0 nm. The yellow circle in each image just shows the nanopore locations and is not used for size calculation. ....68

**Figure 4.3.** Ionic current for -200 mV to 200 mV voltage sweep for (a) a blocked pore and (b) a clean pore, (c) Normalized ionic current showing lower noise fluctuation amplitude for clean pore and (d) noise power spectra for the blocked and clean pore showing reduced low frequency noise for the clean pore, which may be caused by solvent residues or nanobubbles created during measurements.....70

**Figure 4.4.** Experimental (first reported measurement) and simulated IV plots for (a) 2.5 nm, (b) 4.2 nm, (c) 5.6 nm and (d) 8.0 nm showing a good fit for the experimental to simulated conductance and ionic response.....71

**Figure 4.5.** Measured ionic conductance after repeated pore cleaning and measurements through nanopores having (a) 2.5 nm, (b) 4.2 nm, (c) 5.6 nm and (d) 8.0 nm diameters. The bar plots show experimentally measured ionic conductance variation for each pore across 20 repeated measurements, each bar being mapped according to the color bar presented on the right of each plot showing the variation of characteristic nanopore diameter as estimated and extracted from simulation study. The color-bars show the nanopore diameter variation corresponding to the color gradation represented in the bar plots. ....73

**Figure 5.1.** 2D axis-symmetric models used for simulations representing (a) 1-layer, (b) 2-layers, (c) 3-layers, (d) 4-layers, (e) 5-layers, (f) 6-layers MoS<sub>2</sub>, and (g) 50 nm SiN<sub>x</sub> nanopores each having a characteristic diameter of 3 nm with each having an inset figure showing the membrane area zoomed in. ....83

**Figure 5.2.** 2D simulation geometry used for simulating electro-kinetics of DNA translocation through 1-4 layers MoS<sub>2</sub> nanopores, having 3 nm diameter.....84

**Figure 5.3.** (a) Simple schematic representation of the force balance used for simulating DNA translocation electro-kinetics through nanopores, (b) Simulated ionic conductance of 1-6 layers MoS<sub>2</sub> (thickness range: 0.65-4 nm), 50 nm thick SiN<sub>x</sub> and 76-layers MoS<sub>2</sub> (thickness: 49.4 nm), showing cross-over points, Cross-over 1 indicates the diameter beyond which ionic conductance for 2-layers thick MoS<sub>2</sub> nanopore is higher than 1-layer thick MoS<sub>2</sub>. Similarly, above cross-over point 2, the ionic conductance through 4-layers thick MoS<sub>2</sub> pore is found to be greater than that for 3-layers thick MoS<sub>2</sub>; inset showing the cross-over points clearly: data reported for -200 mV to 200 mV trans bias and 300 mM KCl (c) Simulated I-V profile for 1-4 layers thick MoS<sub>2</sub> (shortlisted from ionic conductance comparison) for 2.5 nm pore diameter (greater than cross-over point 1), showing highest non-linearly varying I-V response demonstrated by 2-layers thick MoS<sub>2</sub>: simulation conducted for -200 mV to 200 mV bias range and 300 mM KCl, (d) Representative nanopore circuit showing the active capacitance and resistances. ....86

**Figure 5.4.** (a) Velocity profiles of the translocating 10 nm long polyadenine molecule through 1-4 layers MoS<sub>2</sub> nanopores, with the highest possible nanopore area (i.e. for 4 layers) marked according the (b-c) which presents corresponding geometry showing the DNA position at its entry and exit to/from the nanopore. ....89

**Figure 5.5.** (a) DNA velocity vs translocation time plot showing 2-layers MoS<sub>2</sub> nanopore demonstrating least velocity and (b) Evaluated rate of change of velocity plot with respect to DNA position showing the effect of nanopore on the reduction of DNA velocity. ....91

**Figure 5.6.** (a) Ionic current, I vs normalized time trace for DNA translocation through 1-4 layers MoS<sub>2</sub> nanopores, and (b) Blockade current (evaluated as Ionic current, I – Baseline current, I<sub>0</sub>) vs normalized time plot showing blockade current magnitude varying as 3 layers < 4 layers < 1 layer < 2 layers and dwell time varying as 1 layers < 3 layers < 4 layer < 2 layers. ....91

**Figure 6.1.** a. HRTEM image of a typical exfoliated free-standing ML MoS<sub>2</sub> membrane on SiN<sub>x</sub> support with the inset diffraction pattern showing a single hexagon corresponding to monolayer and b. HRTEM image of AA' stacked BL MoS<sub>2</sub> membrane with the inset diffraction pattern showing two hexagonal domains twisted by 60° (image was filtered to remove noise). ....103

**Figure 6.2.** a. HRTEM image of 2.6 nm STEM fabricated ML MoS<sub>2</sub> nanopore, b. HRTEM image of a 2.7 nm STEM fabricated BL MoS<sub>2</sub> nanopore, c. IV plot for ML MoS<sub>2</sub> nanopore showing an ionic conductance 10.5 nS and d. IV plot for BL MoS<sub>2</sub> nanopore showing an ionic conductance 17.2 nS. The ionic conductance is determined from the average of the ratio of ionic current to bias value at each voltage. The error bars shown in IV plots correspond to the deviation obtained from 4 pore conductance measurements. ....104

**Figure 6.3.** Truncated typical single nucleotide peaks for a-b. dA, c-d. dT, e-f. dC and g-h. dG translocations through ML and BL MoS<sub>2</sub> nanopores respectively at 200 mV bias showing characteristic dwell time and blockade current values. i. Scatter plots of 3000 translocation events (unfiltered and 100-fold resampled) showing four different levels for each nucleotide for both ML and BL MoS<sub>2</sub> nanopores and distinctly higher dwell times for BL MoS<sub>2</sub> compared to ML MoS<sub>2</sub> nanopores and j. Plots showing mean and median dwell time values to be similar for each of the four nucleotides through ML and BL MoS<sub>2</sub> nanopores, suggesting a normal distribution. ....106

**Figure 6.4.** A typical truncated ssDNA translocation data (unfiltered and resampled) through a. ML MoS<sub>2</sub> nanopore and b. BL MoS<sub>2</sub> nanopore with single nucleotides being detected, Dwell time vs blockade current scatter plot for the single nucleotides detected from ssDNA translocation through c. ML MoS<sub>2</sub> nanopore and d. BL MoS<sub>2</sub> nanopore. and e-f. Percentage efficiency of

individual nucleotide detection per ssDNA strand and ssDNA sequencing efficiency for 3'-5' and 5'-3' orientations respectively showing that BL MoS<sub>2</sub> nanopore demonstrates better sequencing efficiency than ML MoS<sub>2</sub> nanopore for both sequencing orientations. ....110

**Figure 7.1.** (a) HRTEM image of a ~3.4 nm diameter solid-state pore on BL (~1.2 nm thick) MoS<sub>2</sub> membrane and (b) simple schematic of eOmpG integrated BL MoS<sub>2</sub> hybrid nanopore. ....141

**Figure 7.2.** (a-d) eOmpG spontaneous gating at a constant voltage of 200 mV, through BL MoS<sub>2</sub> at pH = 6.3, pH = 6.6, pH = 7.0 and pH = 7.4 respectively using 10 mM KCl, (e) scatter plot for eOmpG open times for five traces noted for 25 min each, showing improved hybrid nanopore stability at pH = 7 with an open probability of 99 % and (f) Ionic current vs voltage plot using 10 mM KCl before and after eOmpG insertion into the fabricated BL MoS<sub>2</sub> nanopore at neutral pH showing that the pore exhibits stable attachment at positive voltages and detaches at negative voltages. ....143

**Figure 7.3.** (a) Single dA30 molecule translocation traces through 3.4 nm diameter solid-state BL MoS<sub>2</sub> pore showing a steep drop of 1 nA at around 20 sec indicating single eOmpG insertion, insets showing schematics of solid-state and hybrid pore, (b) dA30 molecular sensing event through BL MoS<sub>2</sub> nanopore showing a molecular dwell time of about 6 ms, (c) dA30 molecular sensing event through hybrid eOmpG-BL MoS<sub>2</sub> nanopore showing a molecular dwell time of about 50 ms (6.5 times larger than the solid-state BL MoS<sub>2</sub> nanopore with 95% confidence), (d) Noise traces ( $I - I_{\text{mean}}$ ) of 2.5E6 samples that is 12.5 sec data at a sampling frequency of 20 kHz for solid-state (with 3.4 nm diameter) and hybrid (with 2.2 nm inner diameter) eOmpG-BL MoS<sub>2</sub> nanopores. A reduction in the noise level is observed after hybrid nanopore formation.  $I$  and  $I_{\text{mean}}$  are the ionic and the mean ionic current respectively., (e-f) Noise power spectral density (evaluated by pwelch method at cut-off frequency of 1 Hz) for 1.25E7 samples that is for ~1 min data of at a sampling frequency of 20 kHz (after the traces are high-pass filtered at 1 Hz for eliminating baseline fluctuations) for solid-state and hybrid nanopore. The dark blue and dark red traces showing moving average of the noise spectra for solid-state and hybrid nanopores respectively. The plots show reduction of low-frequency noise after hybridization, but the high frequency noise (>1 kHz) remains almost similar, although the trend and contributions differ. ....146

**Figure 7.4.** (a) Unimodal distribution of 1488 dA30 translocation events with respect to blockade current with blockades ranging between 600 to 850 pA having the highest density between 700-750 pA, (b) Bimodal distribution of dA30 events with respect to dwell times with molecular dwell times ranging between 2-7 ms having two closely placed peaks centered at 4.5 ms and 5.8 ms. ....150

**Figure 8.1.** a. Ionic current recorded in a saliva medium for 12 sec for a transmembrane voltage varied from -200 mV to 200 mV, showing a blank current of ~450 pA for a bias of 200 mV and b. Ionic current traces recorded at a bias of 200 mV through solid-state BL MoS<sub>2</sub> nanopore in presence of  $\Delta^9$ -THC showing that  $\Delta^9$ -THC translocation events obtained are not sufficiently resolved for reliable molecular sensing. ....168

**Figure 8.2.** Traces showing eOmpG insertion into solid-state BL MoS<sub>2</sub> and stepwise eOmpG opening with a fully open pore current of 415 pA. ....169

**Figure 8.3.** THC traces sensed through hybrid eOmpG-BL MoS<sub>2</sub> nanopore at different THC concentrations: a. 100 nM, b. 10 nM, c. 1 nM, d. 100 pM, e. 10 pM and f. 1 pM. ....170

**Figure 8.4.** Schematic diagram of a. Orientation 1 denoting THC translocation in its linear orientation which should produce characteristically smallest ionic blockade current and b. Orientation 2 denoting THC translocation in its transverse orientation which should produce characteristically highest ionic blockade current. ....171

**Figure 8.5.** 3D density plot of THC translocation events recorded for 600 ms, for concentrations of a. 100 nM, b. 10 nM, c. 1 nM, d. 100 pM, e. 10 pM and f. 1 pM showing highest density of peaks around 100-600  $\mu$ s dwell time and 10-40 pA blockade values. These signatures are obtained for 87% open eOmpG, which theoretically should have a characteristic opening of 1.9 nm which is just enough for letting in single THC molecules in linear orientation (Orientation 1). Therefore, we believe, these signatures correspond to single THC molecule translocation for Orientation 1. ....172

**Figure 8.6.** Concentration based response of a THC molecule sensing demonstrated by hybrid eOmpG-BL MoS<sub>2</sub> nanopore in a saliva medium. ....173

**Figure A- 1.** Electric field gradient contour plot (in V/m) obtained for (a) 1 layer, (b) 2 layers, (c) 3 layers and (d) 4 layers MoS<sub>2</sub> nanopores. ....207

**Figure A- 2.** K<sup>+</sup> and Cl<sup>-</sup> total (diffusive, convective, and electrical) flux contributions to the nanopore conductance for (a) 1 layer, (b) 2 layers, (c) 3 layers and (d) 4 layers MoS<sub>2</sub> nanopores. ....208

**Figure A- 3.** Potential gradient along the translocation axis for (a) 1 layer, (b) 2 layers, (c) 3 layers and (d) 4 layers MoS<sub>2</sub> nanopores. ....209

**Figure B- 1.** (a) MoS<sub>2</sub> nanopore fabrication steps and (b) Schematic representation of custom-designed cell assembly for sensing [1. Amplifier, 2. Digitizer, 3. User interface, 4. Faraday cage, 5. Amplifier head, 6. Cell set up (a. Teflon cell containing KCl, b. Ag/AgCl electrodes, Gaskets to hold membrane, d. Membrane bearing nanopore)].....123

**Figure B- 2.** (a) TEM line profile of ML MoS<sub>2</sub> with an inset raster plot of the same region showing the layer thickness of 0.71 nm, characteristic to a ML MoS<sub>2</sub>, (b) TEM line profile of BL MoS<sub>2</sub> with the inset showing its raster plot, showing the layer thickness of 1.42 nm, characteristic to a BL MoS<sub>2</sub>, TEM raster profiles of (c) ML MoS<sub>2</sub> and (d) (left) AB stacked BL MoS<sub>2</sub> and (right) AA' stacked BL MoS<sub>2</sub>. ....125

**Figure B- 3.** Recorded data for single nucleotide (for each of dA, dT, dC and dG) translocation for 5 sec and 1.5 secs through ML MoS<sub>2</sub> and BL MoS<sub>2</sub> nanopores respectively. ....126

**Figure B- 4.** Normalized histogram of the recorded dA, dT, dC and dG translocation events through (a) ML and (b) BL MoS<sub>2</sub> nanopores with respect to the blockades current produced for each type of analyte. ....127

**Figure B- 5.** 2D flat density plots showing distribution of polynucleotide traces with respect to both blockade current and dwell time with ML pores demonstrating highest density of peaks at 0.05-0.07 ms dwell time and BL pores showing highest density of peaks at 0.06-0.14 ms. ....129

**Figure B- 6.** Translocation traces for a mixture of the four nucleotides through (a) ML and (b) BL MoS<sub>2</sub> nanopores and (c) dwell time vs blockade current plot for the same. ....130

<b>Figure B- 7.</b> Color coded sequence for 60 ssDNA molecules (1800 nucleotides) detected through (a) ML and (b) BL MoS <sub>2</sub> nanopore: dA (red), dT (blue), dC (green), dG (violet) and undetected (yellow).....	130
<b>Figure B- 8.</b> Few instances of 3'-5' sequencing of ssDNA translocation through (a-b) ML and (c-d) BL MoS <sub>2</sub> nanopores.....	131
<b>Figure B- 9.</b> Few instances of 5'-3' sequencing of ssDNA translocation through (a-b) ML and (c-d) BL MoS <sub>2</sub> nanopores.....	131
<b>Figure B- 10.</b> Transient ssDNA bouncing events observed for (a) ML MoS <sub>2</sub> and (b) BL MoS <sub>2</sub> nanopore and single nucleotide non-translocation interactions observed for (c) ML MoS <sub>2</sub> and (d) BL MoS <sub>2</sub> nanopore. ....	132
<b>Figure B- 11.</b> Blockade current vs dwell time scatter plot for single nucleotide translocations through ML and BL MoS <sub>2</sub> nanopores for 100 mV, 150 mV and 200 mV transmembrane bias. ....	132
<b>Figure B- 12.</b> dA30 translocation traces through (a) ML and (b) BL MoS <sub>2</sub> nanopores, dT30 translocation traces through (c) ML and (d) BL MoS <sub>2</sub> nanopores and dC30 translocation traces through (e) ML and (f) BL MoS <sub>2</sub> nanopores. All traces recorded at 300 mM KCl and 200 mV trans bias. ....	210
<b>Figure B- 13.</b> (a-b) Scatter plot of dA30, dT30 and dC30 sensing events through two different nanopores for each of ML and BL MoS <sub>2</sub> , bar plots showing (c) mean blockade current and (d) dwell time obtained for polynucleotide (dA30, dT30 and dC30) sensing through ML and BL MoS <sub>2</sub> nanopores. ....	211
<b>Figure C- 1.</b> Four different STEM fabricated nanopores having ~3.4 nm diameter, showing the pore fabrication repeatability and controllability of BL MoS <sub>2</sub> nanopores.....	212
<b>Figure C- 2.</b> Ionic current vs voltage plot using 100 mM KCl before and after eOmpG insertion into the fabricated BL MoS <sub>2</sub> nanopore at neutral pH showing that the pore exhibits stable attachment at positive voltages and detaches at negative voltages.....	212

**Figure C- 3.** Sequence alignment of eOmpG and wOmpG. eOmpG equals wOmpG-Δ215-227/E163C/E229A/H231E. Modifications in eOmpG are highlighted in red. The beta-strand structures are highlighted with green background. ....214

**Figure C- 4.** SDS-PAGE gel of eOmpG. Lane 1: molecular weight ladder; 2: dissolved inclusion body before FPLC purification; 3: purified unfolded sample; 4: refolded eOmpG; 5: heat-denatured refolded protein. ....215

**Figure C- 5.** Schematic explaining the cis and trans sides of hybrid eOmpG-MoS<sub>2</sub> nanopore sensing set-up. ....215

## **List of Tables**

<b>Table 2.1.</b> Different biological nanopores and their sensing characteristics.....	24
<b>Table 2.2.</b> Advantages and limitations of different sequencing technologies, as presented by Leblanc et al., 2015 [171]. .....	31
<b>Table 3.1.</b> Geometry dimensions and parameter values used for simulation.....	49
<b>Table 4.1</b> Process flow followed in this work.....	67
<b>Table 4.2.</b> shows the conductance of the pores, extracted from the slope of experimental and simulated curves. The small deviation (error) can be due to difference in surface charge values. ....	72
<b>Table 4.3.</b> Variation of nanopore diameter after 20 repeated pore cleaning and ionic conductance measurements.....	74
<b>Table 5.1.</b> Simulation results for drawing an ionic conductance-based comparison between different type of nanopores (1-6 layers thick MoS <sub>2</sub> , 76-layers thick MoS <sub>2</sub> and 50 nm thick SiN <sub>x</sub> ) for 200 mV bias and 300 mM KCl. The ionic conductance for different nanopore types having 2.5 nm diameter are listed. The diameters at cross-over points 1 and 2 (extracted from <b>Figure 5.3.(b)</b> ) are also numerically mentioned below. ....	87
<b>Table 6.1.</b> Blockade current and dwell time for the single nucleotide translocation for both ML and BL MoS <sub>2</sub> nanopores along with the deviation. ....	107
<b>Table 7.1.</b> Comparison of SNR and RMS noise obtained for solid-state and hybrid nanopore with previous studies. Solid state, biological and hybrid nanopores from literature are shown here. ....	151
<b>Table A- 1.</b> Hydrodynamic, electrostatic, and total force acting on the translocating DNA. ....	208
<b>Table B- 1.</b> T-test results conducted on ~300 nucleotides (each for dA, dT, dG and dC) and polynucleotide molecules (dA30, dT30, dC30) translocated through ML and BL MoS <sub>2</sub> nanopores. ....	129

**Table C- 1:** T-test results for dwell time comparison for dA30 sensing through solid-state BL MoS<sub>2</sub> and hybrid BL MoS<sub>2</sub>-eOmpG nanopores.....214

# Chapter 1

## 1 Introduction

### 1.1 Motivation

Understanding the precise structure, composition and function of biomolecules (for e.g., ions, nucleic acids, alcohols, proteins, and sugars) is essential in developing diagnostic tools for accurate detection of health issues and symptoms to treat and prevent diseases (both genetic and non-genetic), allergies and toxic reactions. Biosensors have been developed for genome sequencing [1]–[3], protein sensing [4], [5], allergens and allergy detection [6]–[8], toxicology [9], [10] and immunology [11]. Some of the techniques used in the development of biosensors are piezoelectric, thermal, optical, amperometric, potentiometric, conductometric and impedimetric [12].

Nanopore sensing is an amplification-free impedimetric passive biosensing technique which has proved to be very promising for label-free detection of biomolecules. Nanopore is a nanometer sized pore fabricated on thin insulating or semiconducting membranes. High throughput and real-time sensing platform make nanopore sensing perfect for developing compact portable sensors for rapidly recognizing biomolecules in body fluids, essential for efficient health monitoring [13]. The sensing set up typically contains two electrolyte-filled containers separated by the nanopore [13], [14]. Molecules smaller than nanopore size are usually sensed following the Coulter counter principle [15], [16]. *Figure 1.1* presents a schematic of the Coulter counter principle [16]. This shows that small molecules are sensed by the ionic blockade caused during their translocation through the nanopore. The ionic blockade is primarily proportional to the size of the analyte molecule [17]–[19]. Large molecules (molecules larger than nanopore size) are usually measured

by noting current changes due to specific analyte charge interaction with the nanopore interface [17], [20]. Following these procedures, nanopores can be used to sense bacteria [21], [22], virus [23], [24], antibodies [25], [26], peptides [27], [28], DNA [13], [29], [30], RNA [31], [32] and other biomolecules having a size range of 2-1000 nm.

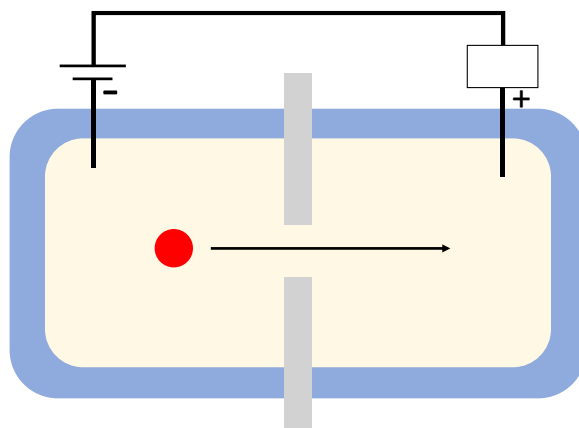


**Figure 1.1.** Schematic of Coulter counter principle (adapted from MD Graham, 2013 [16]).

One of the major applications of nanopore-based biosensors is in genetics i.e. for deoxyribonucleic acid (DNA) and ribonucleic acid (RNA) sequencing. DNA and RNA sequencing have multi-fold applications in medicine, forensics, archaeology, and species identification. In medicine, DNA sequencing help identify disease-causing genes or site-specific mutations for prediction and prevention of hereditary anomalies [33]–[36]. In forensics, DNA sequencing (a.k.a. DNA fingerprinting) help crime investigations through identification of paternal and maternal relations [37], [38]. In archaeology and species identification, it can help protect species by estimating risk of endangerment and extinction [39]–[41]. In this study, one of the things explored was the potential of nanopores as DNA sequencers and improving the sensitivity, resolution, and accuracy of single nucleotide sensing.

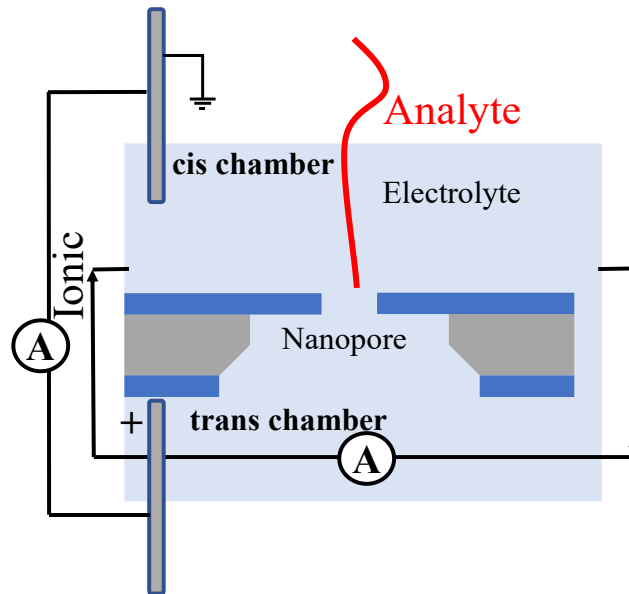


**Figure 1.2.** Cell set up and process of nanopore sequencing

DNA sequencing is the process by which the order and type of each nucleotide constituting a DNA strand is identified. DNA sequencing using a nanopore (nanopore sequencing) works by electrophoretically pulling DNA fragments through the nanopore and noting the current alterations as the DNA nucleotides pass through the nanopore. Each nucleotide passing through the pore produces a characteristic current change (usually drop) which are used as signatures to determine the sequence of the DNA. **Figure 1.2** depicts the process and set up for DNA sequencing through a nanopore.

DNA sequencing was first introduced through biological nanopores using transmembrane proteins or porins lodged in lipid membranes forming a constant sized porous structure. Biological nanopores produce good time-resolved signals for sensing due to slow molecular translocation across the nanopores [13]. This allows DNA to be immobilized at the nanopore long enough for maximizing surface charge interaction, for accurate sensing. However, biological nanopores are too delicate to be reused and transferred in varying environments, which raises the demand for

strong supports [13]. Solid-state nanopores are artificially fabricated nanometer-sized pores on semiconducting or insulating membranes, which have amazing stability, portability, and fabrication ease [13], [42]. But, nucleotide translocation through solid-state pores is too fast to properly resolve sensed signals. In order to overcome the limitations of both biological and solid-state pores, the pores can be combined to form a hybrid pore. The hybrid pore assembly can form a robust lightweight biosensor capable of producing signals with improved time resolution. **Figure 1.3** shows schematic of hybrid pore formation and DNA sequencing through them.

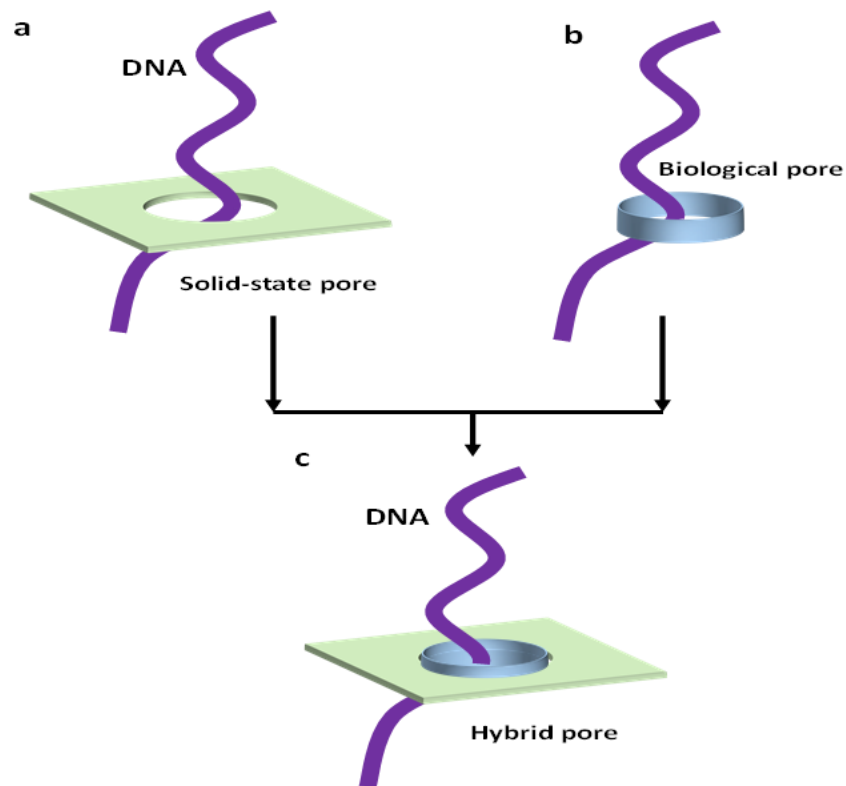


**Figure 1.3.** Schematic showing (a) DNA sequencing through a solid-state nanopore, (b) DNA sequencing through a biological nanopore and (c) DNA sequencing through a hybrid nanopore formed by incorporating a biological nanopore in a solid-state nanopore.

In addition to the time resolution, the signals should be spatially resolved too for correctly identifying each individual nucleotide. This requires the thickness of the membrane to be comparable with the length of the analyte molecule (nucleotide for DNA sequencing) such that at any time instant the nanopore holds and senses a single nucleotide only. For solid-state nanopore sequencing, several materials are used like Silicon nitride [43]–[45], silicon dioxide [46], [47], glass [48], [49], etc. By far, silicon nitride is the most extensively used nanopore material. This is mainly due to its ability to endure stress, strain and elevated temperatures which makes the sensors portable, and also due to its compatibility with standard fabrication procedures which allow the sensors to be produced in large scales. Silicon nitride is available in thickness in the range of 3 to 50 nm. However, for thickness below 10 nm, the membrane quality is found to deteriorate due to increased crystal defects. Therefore, usually membrane with thickness greater than 10 nm is used for nanopore sensing. However, such thickness is lot greater than single nucleotide dimension (~ 1 nm). Therefore, at any point of time the nanopore senses more than one nucleotide reducing the spatial resolution and sequencing accuracy. In order to improve the spatial resolution of sequencing, research had been carried out in selecting thinner but stable membrane materials.

This gave rise to 2D material nanopores made of 2D metal dichalcogenides (like MoS<sub>2</sub>, WS<sub>2</sub>, MoSe<sub>2</sub>), graphene, etc. [29], [50]–[55]. These materials have layers separated by van der Waals forces, thus allowing isolation of single-atom thick monolayers. Graphene (monolayer thickness: 0.35 nm) is found to provide good spatial resolution due to its thinness, but its hydrophobicity causes DNA to stick to the nanopore creating noisy disruptions to the sensed signals and can even compromise the sensor reusability. On the other hand, MoS<sub>2</sub>, a type of 2D metal dichalcogenide, prevents DNA sticking around the nanopore ensuring a smooth translocation with well-resolved signals. It is to be noted here that in addition to the spatial resolution, each identifiable event should

be resolved temporally too, to distinguish a nucleotide caused current change from ambient noise. So, the translocating DNA (like other analytes) should be sufficiently slowed to hold each nucleotide at the nanopore long enough for obtaining a good temporal resolution. However, in spite of a good spatial resolution, the ultra-thinness of the nanopore prevents optimal charge interaction around the nanopore thus reducing the temporal resolution required for confidently identifying each signal. It is found that different layers of MoS<sub>2</sub> experience different potential when a voltage is applied across them. Therefore, the resultant potential gradient is subject to change for different number of layers of MoS<sub>2</sub> used. Thus, the effect of number of layers of MoS<sub>2</sub> on spatial and temporal resolution of DNA sequencing and their role in improving the sequencing efficiency was tested.

DNA is a charged molecule which alters the surface charge at the nanopore/analyte interface differently compared to neutral proteins, drugs, and hormones. So, neutral molecule translocation is much faster than charged DNA translocation for the same nanopore assembly. Therefore, improved signal (temporal) resolution for neutral molecule sensing demands even more reduction of translocation speed. As explained earlier, hybrid nanopores with a biological pore interface improves temporal resolution thus detecting neutral small molecules which fail to produce recognizable signals with solid-state pores.

Therefore, to fulfill the vision of realizing a versatile sensor capable of sequencing DNA and sensing neutral molecules, the design was extended to a MoS<sub>2</sub> based hybrid nanopore sensor. To test the neutral-molecule sensing ability and further benefit medicine, another pressing issue prevailing in Canada and worldwide was addressed. According to Canadian Alcohol and Drug Use Monitoring Survey (CADUMS) 2012, 21.6% Canadians i.e. 8 million population in Canada suffer from drug addiction [56]. Cannabis or marijuana is one of the most popularly used psychoactive

herbal drug, which has medical benefits but is also used for recreational purposes. Since Cannabis legalization in Canada, a spike in Cannabis consumption has been witnessed. According to National Cannabis Survey (2019), cannabis consumption has increased from 14% in 2018 to 18% in 2019 [56]. This poses an increased risk of accident and psychotic behaviour due to continuous and overdosed consumption. Delta-9-tetrahydrocannabinol (THC) is the main psychoactive component in marijuana or cannabis [57]. It not only determines the degree of toxicity, but the concentration of THC also can be directly correlated with the time since last cannabis smoke or ingestion. In this work, hybrid nanopore was used in correlating THC detection rate with concentration for real-time monitoring and control of THC levels. It helps develop a method for separating frequent THC users from one-time users and identify the consequences of THC level thereof.

Therefore, the vision of this work was to design a portable nanopore sensor which can sense both charged and uncharged molecules over a large size range with good resolution and signal-to-noise ratio. The work explains stepwise determination of materials and parameters suitable to serve the above purpose.

## 1.2 Outline

**Chapter 2 (Literature review)** presents relevant literature to first explain different techniques and nanopore types used for sensing wide variety of analytes and then to introduce different challenges which needs to be addressed thereof.

**Chapter 3 (Experimental and simulation methods)** explains the detailed physics and model definitions behind the nanopore simulations conducted in this study. It also explains step-by-step nanofabrication procedures used for designing silicon nitride ( $\text{SiN}_x$ ) and molybdenum

disulphide ( $\text{MoS}_2$ ) nanopores, along with insights into the various tools and techniques used for each step.

**Chapter 4 (Predicting geometry and size repeatability of silicon nitride nanopores)** demonstrates the suitability of small ( $< 4$  nm) nanopores for achieving highly repeatable sensing, with repeatability improving with reduction in nanopore diameter. The chapter presents our study on testing repeatability of  $\text{SiN}_x$  nanopores by correlating nanopore geometry to experimental nanopore conductance using a COMSOL Multiphysics simulation-based model. The predicted nanopore geometry was utilized to determine the change in size suffered by different sized nanopores after multiple measurements.

**Chapter 5 (Understanding molecular electrokinetic behaviour through monolayer and multilayer  $\text{MoS}_2$  nanopores)** presents a simulation-based study to anticipate the suitability of 2 layers (bilayer)  $\text{MoS}_2$  (2D material) nanopores over 1 layer (monolayer)  $\text{MoS}_2$ , 3-6 layers  $\text{MoS}_2$  and 50 nm thick  $\text{SiN}_x$  nanopores for sensing polynucleotides with improved resolution, by slowing down translocation and improving ionic conductance.

**Chapter 6 (Single nucleotide sensing using bilayer  $\text{MoS}_2$  nanopores with high efficiency)** presents experimental evidence on the suitability of bilayer  $\text{MoS}_2$  nanopores (selected from simulation study explained in **Chapter 5**) over monolayer  $\text{MoS}_2$  nanopores (commonly used in literature) for high efficiency single nucleotide detection and DNA sequencing.

**Chapter 7 (Low noise engineered OmpG and bilayer  $\text{MoS}_2$  hybrid nanopore)** introduces the significance and utility of a hybrid nanopore (formed by inserting outer membrane

porin G in bilayer MoS<sub>2</sub> nanopore) in improving signal-to-noise ratio of polynucleotide detection. The porin used is engineered to obtain a stable and biocompatible sensor, with reduced pH-dependent spontaneous gating.

**Chapter 8 (Monitoring THC levels using highly sensitive engineered OmpG and bilayer MoS<sub>2</sub> hybrid nanopore)** demonstrates potential of the hybrid nanopore in detecting neutral molecules with good resolution. This chapter presents the sensitivity of the hybrid nanopore (introduced in **Chapter 7**) in monitoring THC levels in saliva (buffer) by correlating THC concentration with detection rate.

**Chapter 9 (Summary of results)** summarizes the primary outcomes of the entire work and introduces its future prospects.

# Chapter 2

## 2 Literature review

### 2.1 General background of nanopore sensing

Nanopores can be used for identifying small species (nanoparticles) and also for single molecule (both charged and neutral) sensing [13], [17], [58]. Few major applications involve sequencing DNA, RNA, and polypeptides for identifying site-specific modifications, new species, or effect of biochemicals and microbes on health and environment [20], [31], [32], [51], [59]. Different types of nanopores have been explored for this purpose: biological [13], [20], [21], solid-state [13], [51], [54] and hybrid [60]–[64].

#### 2.1.1 Solid-state nanopore

The ease of fabrication and application-suited chemical modification made solid-state nanopores the mostly used alternatives for building reusable and portable biosensors [13]. To understand more about the importance of solid-state nanopores in molecular detection, the measurement theory, and the role of physical and chemical properties of nanopores in sensing need to be clearly understood. Mainly two types of detection methods are prevalent for solid-state nanopores.

##### *2.1.1.1 Detection Method Based on Ionic Blockade Current*

Different types of analyte molecules (of different sizes and chemical composition) are sensed by nanopores including small molecules like ions [65], [66], nucleic acids [1], [26], [27], [36], [47], [67] and drugs [9], [13]; longer polymers like DNA [19], [20], [27], [29], [42], [47], [51], RNA [13], [31], [32] and polypeptides ; and also macromolecules like proteins [68]–[70]. As mentioned

earlier, the sensing mechanism of small molecules mainly follows the Coulter-counter principle [16]. The technique relies on electrophoretically pulling analyte molecules through a nanometer sized opening (nanopore) on a thin membrane which separates two chambers filled with a conductive electrolyte. When a bias is applied across the membrane/nanopore by two floating electrodes dipped in the electrolytic chambers, ionic flow is induced through the nanopore. In presence of small molecules (analytes), the ionic current magnitude is altered depending on the number of ions they block during their translocation through the nanopore and the nanopore/analyte interfacial surface charge interaction. The blockade current magnitude being characteristic to the size and charge of the analyte, can be used to detect them [17]. This blockade magnitude depends upon the fraction of the nanopore occupied by the analyte. Therefore, lesser the volume difference between nanopore and analyte, more prominent (resolved) is the acquired blockade signal. The nanopore sensing realm is entirely based on the control of surface properties of the nanopore and their interactions with the analyte. This interaction is highly dependent on the volume of the electrolyte occupied by the nanopore at any instant of time. The latter, in turn is dependent upon the dimensions and shape of the nanopore. The membrane thickness not only alters the interface interactions but also determines the time taken to drill a nanopore and hence affect the shape factor and size consistency of the nanopore. A detailed explanation of the various factors influencing ionic current detection is given below.

#### *2.1.1.1.1 Effect of surface chemistry and charges*

The ionic conductance depends on the pore wall/analyte interfacial charge interactions, dispersed electrolytic charges, magnitude of the potential gradient and degree of electric field concentration at the pore [71]. An optimum potential gradient is necessary to generate an electrophoretic drag enough to translocate analyte molecules without causing damage to the biomolecule. Moreover,

selection of a membrane material with a surface charge suitable to modulate the electrostatic force for smooth and slow molecular translocation is also essential.

#### *2.1.1.1.2 Effect of membrane thickness*

The membrane thickness is inversely proportional to its capacitance, which determines its ability to separate charges efficiently [20], [54], [72]–[74]. Moreover, the membrane thickness governs the pore height, which in turn dictates the sensing length. Hence, thinner the membranes, better is the spatial resolution and signal to noise ratio. A thinner membrane also offers an easier platform for nanopore drilling with size as small as a single molecule (~1-3 nm) [75], thus improving the detection accuracy. So, selection of a suitable membrane material and thickness is crucial for effective detection.

Normally, solid-state silicon nitride (3D material) solid state nanopores exhibit a low detection sensitivity due to reduced control on the surface charge alterations and interactions [13]. Owing to the intrinsic thickness of the membranes, multiple analyte molecules can reside at a particular sensing time in the nanopore. Hence, sensitivity to the single molecule level can hardly be anticipated. On the other hand, thin membranes can cause sensing length reduction along with signal amplitude amplification, two factors essential for single molecule level sensitivity [13], [20]. 2D materials with interlayer van der Waals force can separate monolayer thick membranes which can hold a single molecule at a time instant at the nanopore to be individually sensed with distinct current, resulting in an increased detection resolution [51], [52], [54]. The following section discusses significant progresses in nanopore sensing using different 3D and 2D membrane materials.

#### 2.1.1.1.2.1 3D or bulk material

The mechanism described before clearly states that the resolution of the sensed signals is greatly influenced by the cross-sectional area and height of nanopore (i.e. thickness of membrane) relative to the analyte. Therefore, selection of a suitable membrane material is crucial for nanopore sensing applications. Mostly dielectric materials are usually used as membranes like silicon nitride [43]–[45], silicon oxide [46], [47], aluminium oxide [76]–[78], titanium oxide [79] and hafnium oxide [67]. High chemical resistance and mechanical stability makes silicon nitride ( $\text{SiN}_x$ ) and silicon dioxide ( $\text{SiO}_2$ ) membranes the primary choice of nanopores [80]. The silicon-based membranes are usually high-temperature CVD (chemical vapor deposition) grown layers on silicon substrate ( $200\ \mu\text{m}$  -  $500\ \mu\text{m}$ ) which are available in varying thicknesses (usually 3-50 nm) [81]. The free-standing membranes are normally fabricated using a combination of photolithography, wet-etching and dry-etching techniques [82], [83]. Relatively small nanopores (1-10 nm) are fabricated on the free-standing part by using either an electron beam (transmission electron microscope - TEM) [43], [84], [85] or a focussed ion beam (helium ion microscope - HiM) [86], [87]. The shape and resolution of the beam determines the resultant geometry of the drilled nanopore. A salt buffer is used as the conductive liquid for screening the negative surface charge of the nanopores [71]. As opposed to  $\text{SiN}_x$  and  $\text{SiO}_2$  membranes, ALD (atomic layer deposition) grown materials like  $\text{Al}_2\text{O}_3$ , have positive surface charge which offer better signal-to-noise ratio compared to  $\text{SiN}_x$  [43], [88].  $\text{HfO}_2$  [67] and  $\text{TiO}_2$  [79] due to high dielectric constants reduces leakage current, thus offering improved electrical performance and reusability.

Silicon nitride ( $\text{SiN}_x$ ), the most commonly used semiconductor membrane material is compatible for fabricating a wide range of nanopore sizes improving the production scalability for multiplexed devices. **Figure 2.1** shows schematic of DNA sequencing through a solid-state  $\text{SiN}_x$  nanopore.

However, higher thickness of the membranes compared to molecular dimensions ( $\sim 1$  nm), makes highly resolved and sensitive detection difficult [89]. Fabrication of  $\text{SiN}_x$  membranes with as low as 3 nm thickness by polycrystalline silicon sacrificial layer method has been reported [90]. However, increased nitride thinning leads to increased probability of membrane damage and thickness non-uniformity [91]. This bottle-neck of detections calls for strong yet thinner membranes realized from 2D materials.

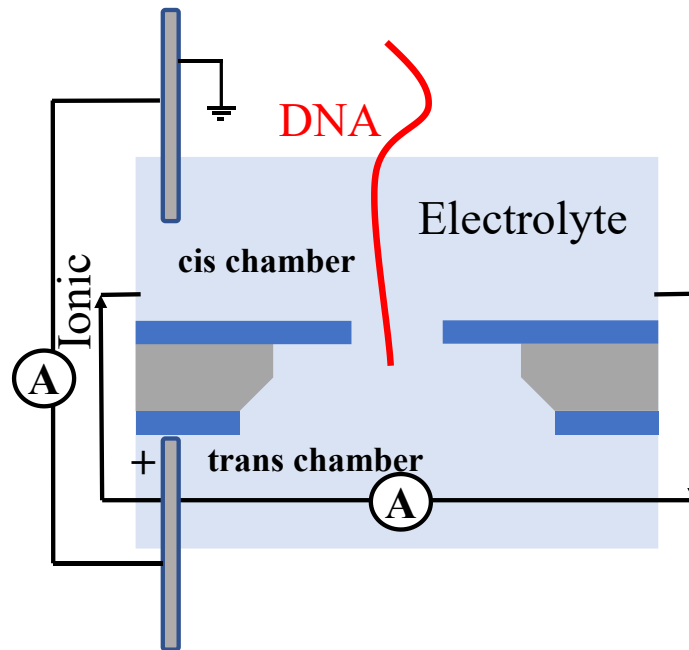


**Figure 2.1.** Schematic of DNA sequencing through a solid-state silicon nitride nanopore.

#### 2.1.1.1.2.2 2D material

2D materials are van der Waals bonded crystalline layered materials, which makes separation of monolayers possible [52]. A new era of solid-state electronics was marked by graphene isolation on insulating material in 2004 [92]. Graphene is a 2D material with densely packed single layer of hexagonal patterned  $\text{sp}^2$  hybridized carbon atoms [93]. It has continued to get attention in nanopore sequencing as a membrane material due to its atomically thin membrane fabrication feasibility to distinguish single molecules, and also for its mechanical strength. Sensing using graphene

transistors and biosensors have been demonstrated [94]. **Figure 2.2** shows schematic of DNA sequencing through a solid-state graphene nanopore.

However, the adhesion of proteins with graphene at the nanopore due to dangling bonds and the interference of conductive nature of graphene with ionic current pose challenges in smooth DNA translocation and detection [95]. Hexagonal Boron nitride (hBN) is another type of 2D membrane material which has proved to be good for nanopore sensing for its hydrophilicity [96]–[98]. Another group of material that is slowly gaining prominence in this field due to compatible surface charge interactions and structural stability. These are transition metal dichalcogenides or TMDs ( $\text{MX}_2$  type). These have a transition metal ( $\text{M} = \text{Mo}, \text{W}, \text{We}, \text{etc.}$ ) layer sandwiched between two chalcogen ( $\text{X} = \text{S}, \text{Se}, \text{T}, \text{etc.}$ ) layers [99]. They inherit all the basic 2D material properties but differ from graphene by the degree of hydrophobicity they induce at analyte/nanopore interface when suspended in an electrolyte.  $\text{MoS}_2$ , a type of TMD is found to be more sensitive than graphene in biosensing, the details of which will be discussed later.

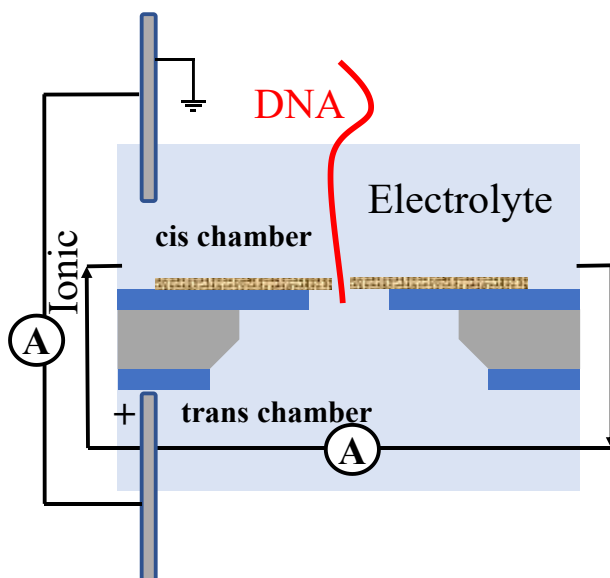


**Figure 2.2.** Schematic of DNA sequencing through a solid-state graphene nanopore.

#### *2.1.1.1.3 Effect of pore size and shape*

Controlled and reproducible fabrication of pores which are of comparable size and tunable to single molecular dimension is essential for a highly resolved and sensitive sensing. Nanopore volume relative to the analyte size determines the spatial resolution of the blockade current; the latter essentially being the fraction of the total nanopore volume occupied by the analyte at any time instant. Moreover, the pore size and shape determine the field concentration and velocity of analyte movement through the pore and hence the time resolution of the blockade current. Therefore, the drilling techniques (electron beam or ion beam drilling) are extremely crucial in obtaining a desired geometry of nanopore. The following section discusses the pros and cons of different techniques used for nanopore fabrication.

#### *2.1.1.1.4 Ion Beam drilling*

Focused Ion Beam (FIB) usually uses Gallium ions, a heavy ion which can make big pores in the range of 20 -100 nm [42]. It takes a short time to make uniform pores but due to its heavy mass it causes undesired redeposition on the drilled substrate hampering the size precisions. This also leads to doping with Ga ions which is not always desirable [100].

Helium Ion Microscopy (HiM) causes less redeposition since it is lighter and is usually used to make pores in the size range of 8-100 nm [87]. Moreover, a smaller pore requires faster drilling to avoid sputtered atom deposition on the drilled pore walls. Helium ion can uniformly thin membranes for easier and faster nanopore drilling [86], [87].

#### *2.1.1.1.5 Electron beam sputtering*

Pores with size greater than 20 nm have been patterned by Electron Beam Lithography (EBL) and dry etching [42]. Scanning Electron Microscopy (SEM) is usually used to drill pores followed by

pore shrinking by controllably depositing substrate atoms at the pores [42]. However, this technique could achieve pores greater than 10 nm only but with irregular shape. Transmission Electron Microscopy (TEM) offers a more powerful (high voltage) and focused beam which is mainly used to drill pores in 1-15 nm size range depending on membrane thickness. Hence, smaller nanopores required for sequencing are best fabricated by TEM [43], [52], [85], [90], [101].

All the techniques discussed above usually is applied for ionic blockade-based detection, which relies more on difference in size and surface charge of the molecules and less on the chemical structure. Therefore, often another approach is taken for more specific identification of molecules, which is based on tunneling current.

#### ***2.1.1.2 Detection Method using tunneling current***

Tunneling demands a slow translocation for readout of high bandwidth current with increased signal-to-noise ratio. The location and orientation of the analyte and the molecule-electrode distance as well as inter-electrode spacing governs the current fluctuations due to varied charge interactions [102]–[104]. This makes the tunneling measurement very challenging, hence attracting more research.

##### *2.1.1.2.1 Effect of surface chemistry and charges*

Tunneling current exploits the electronic structure of the molecules and hence can be detected individually as well as the adjacent molecule contribution can be identified, thus improving specificity. The influence of the energy of molecular states increases the sensitivity of detection by producing a more distinguished current for each molecule. Various materials like Au, Pt or C [102] are used as electrodes and graphene is used as the transmembrane due to its thinness to the atomic dimension.

#### 2.1.1.2.2 *Effect of membrane thickness and pore size*

To achieve tunneling thinner electrodes with smaller pores and lesser inter-electrode spacing are essential [105].

##### 2.1.1.2.2.1 3D or bulk material

Materials like  $\text{SiN}_x$  have good chemical, mechanical and thermal resistance favorable for maintaining fabrication stability and integrity, important for tunneling. However, for nanopore sequencing, the high thickness of silicon nitride makes drilling of sub-nm pores, required for tunneling extremely difficult.

##### 2.1.1.2.2.2 2D material

Materials like Graphene or TMDs are suitable for easy sub-nm pore fabrication due to their monoatomic thickness. Graphene is a conductive material with a zero band-gap which interfere with the pore/molecule interaction [106]. However, the semiconducting nature of  $\text{MoS}_2$  (with a band gap of 1.8 eV [107], [108]) makes it suitable for device fabrication.

Existence of van der Waals forces are not limited to interatomic layers of 2D materials but also between surface atoms of two materials free from any dangling bond, which makes formation of high quality 2D heterostructures over large areas possible. The increased probability of charge transfer between these heterostructures in turn opens new avenues for electronics research [55], [109]–[111].

Literature shows a p-n junction with an in-built interfacial electric field can be obtained by vertically stacked p-type tungsten diselenide ( $\text{WSe}_2$ ) and n-type molybdenum disulfide ( $\text{MoS}_2$ ), since the conduction band minima offset (720 meV) is largest for  $\text{MoS}_2/\text{WSe}_2$  heterojunction [112], [113]. However, charge transfer efficiency depends on the thickness of the depletion layer.

For 10-nm to 1  $\mu\text{m}$  thick junction, charge diffusion and drift dominates [112], [113]. However, charge transfer in atomically thin junction essentially occurs by quantum tunneling. Hence, monolayer TMD stacking can enable better electron-hole transfer at the interface with simultaneous preservation of the individual layer uniqueness. **Figure 2.3** shows schematic for nanopore-based DNA tunneling detector used for individual base detection as adapted from *Ivanov et al., 2011* [102].

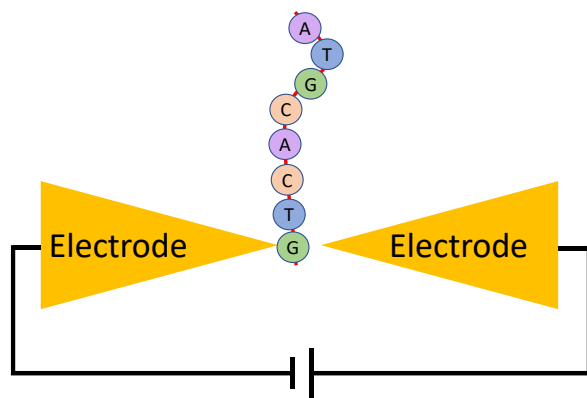


**Figure 2.3.** Schematic for nanopore-based DNA tunneling detector (adapted from Ivanov et al., 2011 [102]).

However, the biggest challenge still existing for 2D material tunneling device fabrication is the preservation of the surface properties and stability during deposition and after nanopore fabrication. Therefore, ionic current blockade approach is still considered relatively easier and standard. The above review also suggests that fabrication of small ( $\sim 2\text{-}3$  nm diameter) nanopores on ultrathin ( $\sim 1\text{-}2$  nm) membranes is necessary for single molecule detection resolution and TEM drilling is suitable for such fabrication. It is also found that  $\text{MoS}_2$  proves to be favourable for a smooth translocation and single molecule sensing and can be a good choice of solid-state membrane material.

However, inconsistency in the size and geometry of the nanopores posed an immediate concern with solid-state nanopores. Diverse challenges need to be addressed for effective detection, of which size-controlled drilling of nanopores and velocity modulation of translocating molecules are crucial for high-quality sensing [114]. DNA sequencing optimally occurs at 1-50 nt ms<sup>-1</sup> [115]. For solid-state nanopores, the speed is found to be as high as 3,000–50,000 nt ms<sup>-1</sup> due to lower pore size range (2-25 nm) and high applied bias voltage (100-800 mV) [51]. But, fast speed however limits the sensing resolution, which is the major bottleneck of solid-state DNA sequencing. Various methods have been employed to slow down translocation which include employing a viscosity gradient, pressure gradient, temperature gradient, voltage difference and ionic concentration gradient [51], [116]–[124]. However, a biological nanopore can sufficiently slow down analyte translocation too. For biological nanopore sensors, the speed is of the order of 2.5-70 nt s<sup>-1</sup> [51]. Below, details about the different biological nanopores used for sensing are discussed.

### **2.1.2 Biological nanopores**

The initial nanopore sequencing concept involved electrophoretically dragging a single-stranded DNA through a staphylococcal  $\alpha$ -hemolysin ( $\alpha$ -HL) protein pore in response to an externally imposed potential gradient, followed by recording the ionic current amplitude reduction specific to each base [125]. Biological nanopores usually use planar lipid or polymer membranes or liposomes as the substrate put in an electrochemical chamber [13]. Standard molecular biology techniques produce and purify channel protein with great homogeneity [126]. The biocompatibility and large-scale production ease make biological nanopores a great alternative for nanopore sensing. A number of protein pores with different properties have been used for sensing in pristine and modified forms.

Alpha haemolysin is a bacterial toxin which can create a heptameric nanopore. It has been the primary choice for DNA, RNA, and peptide sequencing for decades [127]. The toxin diffuses through the membrane/substrate creating a self-assembled mushroom-shaped nanopore [64]. The nanopore partition created in the membrane is 10 nm long with two regions: a top 5 nm long vestibule with a relatively larger volume which continuous to a smaller ~1.5 nm diameter beta-barrel shaped constriction at the membrane surface, thus giving a mushroom shaped structure to the resultant pore. The cylindrical ~1.5 nm diameter zone consists of seven subunits, the configuration of which changes with changes in the nanopore vicinity [128]–[131]. Such changes cause enlargement or narrowing of the pore, making the pore sensitive to a large range of analyte sizes [132]. Alpha haemolysin has been found to be stable for a wide range of temperature including sub-zero temperatures, which further attracted biosensing applications [133]. Over the years, the pore has been further bioengineered to alter surface chemistry and permeability to biomarkers and analytes, for more selective sensing [128]–[131].

The first study of DNA sequencing was conducted by *Kasianowicz et al.* in 1996 using Alpha hemolysin nanopore which provided a breakthrough for next-generation sequencing [125]. The 1.5 nm diameter constriction of Alpha hemolysin makes it suitable for pulling through and sensing single-stranded (ss) linear DNA molecule [125]. It suggested that the selected nanopore for DNA sequencing should have good spatial and temporal resolution for obtaining distinct and different signals for each individual constituting nucleotide. *Akeson et al.* experimentally demonstrated that different nucleotides can produce characteristically different signals by translocating polyadenine and polycytosine (purine and pyrimidine parts of DNA analogues) and polyuracil (RNA analogue) molecules [134]. The rate of DNA translocation however should be lowered under a specific bias to obtain the necessary conductance resolution, which requires chemical modification. Work has

been done by using enzymes to slow down the translocation events.  $\alpha$ -HL mutations are also adopted to improve DNA capture rate from solution [133], [135]. Exonuclease modification is sometimes employed to separate individual monophosphates from the DNA strand to attain single molecule sensing [136], [137]. The most commonly used technique is using labelled nucleotide with molecules which can be detected by fluorescence [79], [138]–[140]. Molecules can be detected by covalent/non-covalent interactions and adapter-mediated binding within the engineered pore, removing the requirement of molecular tags. However, the absence of adapter attachment led to no-detection periods and insufficient sensing resolution [17], [141], [142]. This drawback was removed by covalent adapter attachment giving real time, highly sensitive detection. An advanced nanopore detector with compatible exonuclease system was used to identify 5'-methylcytosine in presence of A, G, T, C for methylation pattern investigation [143].

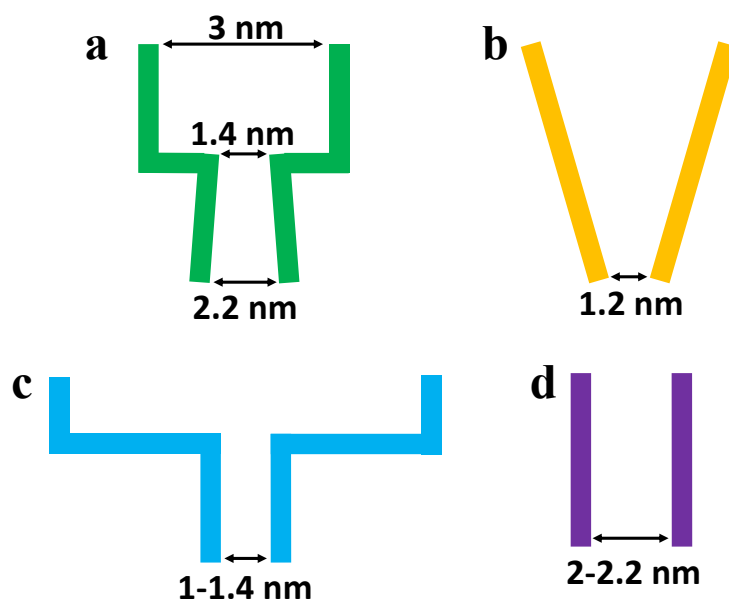


**Figure 2.4.** Schematics of Alpha hemolysin (dimensions from *Ding et al. 2016* [144]), MspA (dimensions from *Derrington et al. 2010* [145]), Aerolysin (dimensions from *Iacovache et al. 2016* [146]) and OmpG (dimensions from *Köster et al. 2015* [147]) nanopores as presented in literature.

The main limitation of alpha-hemolysin is its stem length which is longer than nucleotide dimension. This makes the sensing length longer than required to achieve sufficient spatial resolution. Mycobacterium smegmatis (MspA) are mycobacterium porins which have been suitable for DNA sequencing particularly for its topology [13], [145], [148]. Unlike alpha hemolysin, MspA are large goblet-shaped octameric pores with the smallest constriction having a diameter of 1.2 nm and length of 0.6 nm, which is ideal for DNA sensing without the use of additional structural adaptations [148]. However, they have a very thick hydrophobic outer membrane containing mycolic acid chains. Such hydrophobicity can lead to reduced sensor lifetime [149].

Aerolysin on the other hand, is hydrophilic thus providing favourable charge interactions. However, aerolysin pores are seldom used for DNA sequencing and more used for isolated small molecule sensing [150]. Another type of biological nanopore used mostly for small molecule sensing is Outer Membrane Porin G (OmpG). OmpG is a 32 kDa 14 stranded monomeric porin that has a uniform barrel-shaped structure allowing easy insertion in the solid-state pore. The symmetry also allows uniform surface charge interaction with the translocating or binding analyte [21], [151]–[153]. The most important advantage of OmpG pore is a phenomenon which is commonly referred to as gating; by which the permeability of the pore to analytes and ions can be regulated by simply changing the OmpG environment. OmpG has 7 extracellular loops, which respond differently in different pH, ionic or electric conditions [21], [151]–[153]. The discrete changes in protein dynamics induces more specific ionic current signals for analyte identification, without additional functionalization [21], [151]–[153]. The gating effect depends on a lot of factors including the proximity of the analyte with OmpG, charge interactions between OmpG and analyte, and conformation changes of the flexible groups. Such flexibility of the loops leads to high selectivity and sensitivity of OmpG pores unlike other rigid biological pores. At neutral pH, OmpG switches between open (permeable) and closed (non-permeable) states thus making fine tuning of the nanochannel possible. Additionally, OmpG allows easy adaptation of the loops by introducing mutations in the amino acid sequence. This provides better control on the signal

resolution required for single molecule sensing. Due to controlled gating technique, OmpG can also be suitable for sensing different types of molecules over a wide size range [151]–[153].

**Figure 2.4** shows schematics of Alpha hemolysin, MspA, Aerolysin and OmpG nanopores as presented in literature [144]–[147]. **Table 2.1** summarizes the biological nanopores and their sensing characteristics.

**Table 2.1.** Different biological nanopores and their sensing characteristics.

<i>Nanopore</i>	<b>Aperture size</b>	<b>Analytes</b>	<b>Advantages for DNA sensing</b>	<b>Limitation</b>
<i><math>\alpha</math>-Hemolysin</i>	Smallest constriction is 1.5 nm	Small molecules especially single-stranded DNA and RNA are usually sensed.	It can be engineered for specific molecular detection.	It is thermo-mechanically weak and has a stem length longer than nucleotide dimension, which compromises sensing resolution.
<i>MspA</i>	About 1 nm diameter	Mostly single-stranded DNA and RNA are sensed.	It is thermo-mechanically and chemically stable and can be engineered for specific molecular detection.	Its hydrophobicity compromises charge interaction in electrolytic medium.

<i>Aerolysin</i>	Diameter varies in the range of 1-1.7 nm diameter	Small molecules are sensed.	It is thermo-mechanically and chemically stable, can be engineered for specific molecular detection and is hydrophilic leading to improved nanopore/DNA charge interaction.	It is prone to size variation even due to minor modifications.
<i>OmpG</i>	Controllably tunable diameter	Both small and large molecules are sensed.	It can be engineered for specific molecular detection, is hydrophilic improving nanopore/DNA charge interaction and also has tunability size due to controlled gating.	It may suffer from spontaneous gating due to changes in nanopore environment.

Generally, two types of signals are obtained for molecular detection using biological nanopores.

### ***2.1.2.1 Cognate analyte detection***

Cognates analytes are detected from the current change obtained due to non-covalent binding of analytes with the nanopore or any target, creating a change in the structure, configuration, or orientation of the nanopore. This can cause either a minor current disruption or appreciable change depending on the strength of analyte interaction. Due to the specificity of these interactions, it can help investigate chemical reactions and targeted detections [13].

### ***2.1.2.2 Translocating analyte detection***

Translocating analytes are detected by Coulter-counter principle (as explained in **Section 2.1.1** solid-state nanopore). The charge alterations occurring at the nanopore during analyte translocation can produce current blockades characteristic to their size and surface charge. However, unlike solid-state pores, the charge interactions are stronger causing slow translocation of analytes through biological pores, thus producing more temporally-resolved signals [13].

Due to their biocompatibility and sensitivity, biological nanopores are being used since the dawn of nanopore sequencing. However, in spite of improved time resolution, biological nanopores are prone to disabilities due to sudden changes in environmental conditions and mechanical failure, making them unsuitable for building portable and reusable sensors. These limitations are however fulfilled by a solid-state nanopore. Such complementary behaviour of solid-state and biological nanopores gave rise to hybrid nanopores formed by combining the latter two.

### **2.1.3 Hybrid nanopore**

Both biological and solid-state nanopores have their own pros and cons [13]. Therefore, to harness advantages of both nanopores, a biological nanopore can be incorporated and planted inside a strong solid-state nanopore to form a hybrid nanopore. Solid-state nanopores offer greater

controllability over size and shape, longevity, and easier wafer-scale device integration [13]. The biological pores offer atomic precision suitable for more sensitive engineering, but the delicate lipid bilayers supporting the pore makes its integration difficult. The need for a specific environment makes long-term application for biological nanopores unfavorable [13]. Moreover, pores with precisely reproducible dimensions have remained a challenge. A hybrid nanopore with the incorporation of a biological nanopore in a solid-state one can offer the best of both systems [62]–[64], [154]. Hybrid nanopore formation has mostly focused on  $\alpha$ -haemolysin ( $\alpha$ HL) protein pores and artificial solid-state nanopores. DNA attached to the protein pore was electrophoretically threaded through the solid-state nanopore. DNA translocating through the protein / solid-state hybrid nanopore was then identified by the blockades obtained for each molecule [64]. **Figure 2.5** depicts formation of Alpha haemolysin and silicon nitride hybrid nanopore, as shown by *Hall et al., 2010* [64].

For single nucleotide detection, a DNA strand complimentary to the analyte DNA is tethered to the nanopore for obtaining nucleotide specific blockades due to specific complimentary DNA interactions. Similarly, for other analytes too, target molecules are used for inducing specific binding for identifying particular analytes [142], [155]. Sensing system with the hybrid also helps in creating wafer-scale device arrays improving molecular detection.

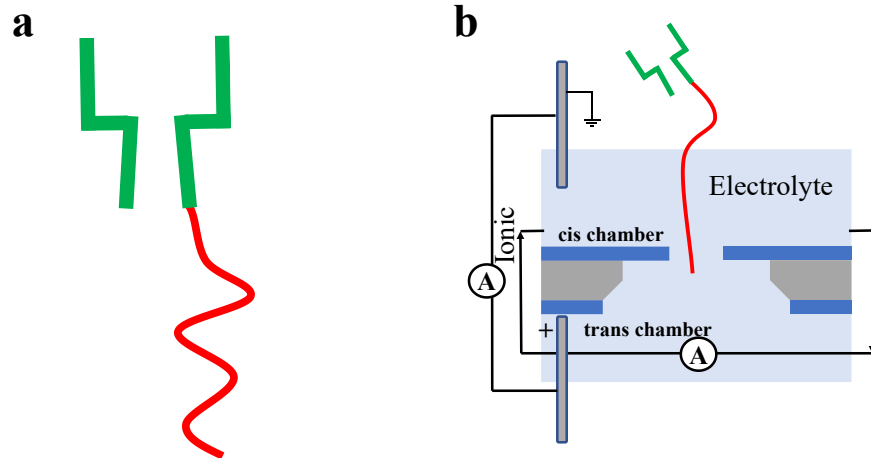


**Figure 2.5.** (a) Alpha hemolysin with tethered DNA and (b) Alpha hemolysin insertion in silicon nitride nanopore to form a hybrid (adapted from *Hall et al. 2010* [64]).

Therefore, hybrid nanopores can be ideal to lay the foundation of a versatile and highly sensitive nanopore sensor.

## 2.2 Relevant background literature

### 2.2.1 Testing repeatability: standardizing cleaning procedures and narrowing down the range of nanopore diameter

Silicon nitride has been by-far the most widely used stable and standardized nanopore material [88], [116], [156]–[160]. The primary aim for achieving a reliable sensor is ensuring that the signals it provides are repeatable. If the sensor provides varying signals for the same analyte, detection accuracy and confidence will be highly compromised making the efficiency of the sensor questionable. For that, first a clean signal should be obtained which requires minimization of noise which can cause unnecessary baseline fluctuations. *Beamish et al., 2013* has explained the requirements and procedure of nanopore cleaning to obtain a good signal [14]. Noise analysis can

help understand the importance of solution degassing, piranha cleaning and ensure a properly clean nanopore prior to any sensing, and thereby help in optimizing the cleaning parameters required for obtaining stable and repeatable signals. It can also help in interpreting the contributions of high-frequency particulate noise and nanobubble-induced low-frequency noise and their improvement after achieving a properly clean and wetted nanopore. Another factor influencing the repeatability of a nanopore sensor is its geometry which governs the magnitude of ionic conductance and blockade current for a particular analyte type. Various techniques have been used in literature for controlled fabrication of nanopore with better size and shape reproducibility [88], [116], [156]–[160]. Literature showed Transmission Electron Microscopy (TEM) to be suitable for controlled fabrication of small (2-5 nm) nanopores [85], [90], [161], [162]. Therefore, TEM was used for nanopore fabrication in this study. Owing to the thickness of the membranes, a uniform diameter (cylindrical pores) all along the membrane thickness is less probable particularly when fabricated by TEM. Hence, hour-glass or conical shaped nanopores are usually realized on SiN<sub>x</sub> nanopores. Therefore, in this study, a COMSOL Multiphysics based simulation model was first used to reconstruct the possible geometry of the experimented nanopores and then correlate the experimentally obtained ionic conductance of each pore with the nanopore geometry. After figuring out the geometry, multiple measurements were conducted on each pore and the change in ionic conductance was then related to the simulated diameters to figure out the change in size and therefore sensing repeatability (for different sized nanopores) due to multiple measurements. This study is presented in **Chapter 4**.

### **2.2.2 Selecting membrane/nanopore material for spatially and temporally resolved sensing**

Along with repeatability test, improving spatial and temporal resolution is also important for accurately identifying and denominating obtained signals. Single biomolecule detection has been

one of the major aims of nanopore technology. It can help in comprehending the physical and chemical properties for further technological advancements. However, for such detection single molecules should be rapidly and efficiently captured inside the nanopore for a length of time, sufficient enough to amplify charge interaction and resultant blockade signals. Therefore, the electro-kinetics of analyte translocation through different membrane/nanopore materials should be analysed for selecting a membrane suitable for obtaining improved signal resolution. One of the most common nanopore materials is silicon nitride-  $\text{SiN}_x$  (as mentioned in **Section 2.1.1**). However, due to its thickness,  $\text{SiN}_x$  produces low resolution signals, requiring further improvement for single molecule detection. Literature shows monolayer 2D material  $\text{MoS}_2$  to be more promising than thick  $\text{SiN}_x$  for highly resolved nanopore sensing and sequencing purposes [51], [52], [163]. So, in this study, COMSOL Multiphysics simulation study was first conducted to compare the sensing performance of nanopores on 50 nm  $\text{SiN}_x$  and monolayer  $\text{MoS}_2$  nanopores to create proof of concept. Literature review also showed monolayer and multilayer  $\text{MoS}_2$  behaves very differently under an applied electric field [164]. Additionally, slower peptide translocation was always obtained in previous simulation studies by using bilayer  $\text{MoS}_2$  nanopores instead of monolayer [165]. Therefore, in this study, the simulation model was further used to compare the sensing performance of 1-6 layers of  $\text{MoS}_2$  nanopores to understand the effect of number of  $\text{MoS}_2$  layers on the sensing characteristics (more specifically on the analyte translocation kinetics). This study is discussed in **Chapter 5**.

### **2.2.3 Testing nanopore efficiency for sequencing single-stranded DNA**

One of the major nanopore sensing applications is single nucleotide sensing, which can benefit accurate DNA sequencing and identification of single nucleotide polymorphisms (SNPs). This in turn can help prevent or cure various critical genetic diseases. Hence, genetic information readout

down to the molecular level is therefore essential to monitor minute changes in genetics or to anticipate the risk of hereditary diseases.

The first-generation sequencing was based on chain termination (*Sanger and Coulson, 1975 [166]*) and degradation (*Maxam and Gilbert, 1976-1977 [167]*) technology. The first successful human genome sequencing using this technology was achieved in 2001 [168]. The technology was improved which resulted in the second-generation sequencing based on target-oriented amplification-assisted replicative sequencing [169]. However, the amplification can introduce unnecessary errors in the read information [169]. The sensor therefore was built of advanced sensor array for parallel sensing to achieve good accuracy. However, that made the method too expensive for long readouts [169]. A good sequencing technique demands 1) good spatial and temporal resolution, 2) fast detection rates, 3) long read-length and 4) a low-cost sensing. The above two techniques lacked one or the other requirements. This led to third generation sequencing to eliminate the error-prone amplification steps to achieve fast, low cost, real-time long readouts with single-molecule resolution [169]. Nanopore sensors offer such a sequencing method. Oxford Nanopore- MinION is the leading commercialized portable low-cost sequencer [170]. **Table 2.2** lists the advantages and limitations of different sequencing technologies, as presented by *Leblanc et al., 2015 [171]*.

**Table 2.2.** Advantages and limitations of different sequencing technologies, as presented by Leblanc et al., 2015 [171].

Technology	Advantages	Limitations
First-generation sequencing	<ul style="list-style-type: none"> <li>• Long reads (~ 700 base pairs)</li> <li>• High accuracy</li> </ul>	<ul style="list-style-type: none"> <li>• Low throughput</li> </ul>

Second generation sequencing	<ul style="list-style-type: none"> <li>• High throughput</li> </ul>	<ul style="list-style-type: none"> <li>• Short reads (~100-500 base pairs)</li> <li>• Amplification biases generally occur</li> </ul>
Third generation sequencing	<ul style="list-style-type: none"> <li>• Long reads (average length can reach ~ 14 kilo base pairs)</li> <li>• High throughput</li> <li>• No amplification required</li> <li>• Can detect and distinguish bases</li> <li>• Has potential for miniature device fabrication</li> </ul>	<ul style="list-style-type: none"> <li>• High error rate</li> <li>• Biased towards long fragments</li> </ul>

Therefore, in this study, single isolated nucleotide triphosphates were sensed through monolayer (mostly used in literature [51], [52]) and bilayer MoS<sub>2</sub> nanopores (selected from **Chapter 6**) to form the library of current signatures for single nucleotides. Then DNA strands having a customized pseudo random sequence was sensed through the nanopores. The single nucleotide signal library previously created was then used to determine the sequence of the DNA. The efficiency of DNA sequencing evaluated for monolayer and bilayer MoS<sub>2</sub> nanopores was then used to infer the suitability bilayer MoS<sub>2</sub> nanopore for single nucleotide sensing and DNA sequencing. This study is explained in **Chapter 6**.

#### **2.2.4 Designing a low-noise hybrid nanopore for more sensitive and temporally resolved sensing of both charged and uncharged analytes**

Although solid-state MoS<sub>2</sub> nanopores are good alternatives for charged small molecule detection, they lack the necessary sensitivity and resolution required for neutral molecule sensing [50], [165].

A biological nanopore due to its chemically sensitive interface slows neutral molecule translocation and responds appreciably to minor localized charge changes, thus forming a suitable sensor. However, biological nanopore is too delicate to build a portable sensor. But, when encased in a solid-state nanopore support a durable and sensitive hybrid nanopore is formed, which can have the potential of sensing uncharged as well as charge analytes. Outer Membrane Porin G (OmpG) proves to be a good biological pore alternative for molecular sensing [151], [153], [172], the reasons of which are discussed in **Section 2.1.2**. The advantage of easy OmpG modification can be utilized to reduce noise and improve signal-to-noise ratio for molecular sensing. pH-dependent spontaneous OmpG gating can also be prevented by specific modifications to the outer OmpG loops. The hybrid platform thus created can therefore demonstrate low-noise sensing with high temporal resolution and signal-to-noise ratio. Therefore, in this study, polynucleotide translocation through OmpG hybridized bilayer MoS<sub>2</sub> nanopore was conducted to test the improvement in dwell time and signal-to-noise ratio. This work is discussed in **Chapter 7**.

Neutral molecule sensing ability of the hybrid nanopore is demonstrated in **Chapter 7**, THC (Tetrahydrocannabinol) was selected as analyte. The motivation behind selecting THC molecules are discussed in **Section 1.1**. THC is the component in Cannabis, which is primarily responsible for inducing psychotic behaviour particularly in high doses [57]. At low doses Cannabis is found to have good medical effects. Topical application has its anti-inflammatory and pain killing effect [173], [174]. It shows its localized effect in minutes and can last for hours. Sublingual cannabis sprays also have proved to be safe apart from a few side effects [175]. Oral cannabis intake and inhalation in low doses has been found to cause euphoric feelings, hallucinations, panic, sleepiness, etc. [176]. Although fatality due to cannabis overdose has not been reported, long-drawn usage can intensely harm memory, intellect or even majorly affect lungs and heart. Cannabis use during

pregnancy can even affect fetus health [177]–[179]. Therefore, it is extremely important to monitor THC levels (since it is the primary psychoactive component in Cannabis) in real time to control and prevent severe consequences. Cannabis can be orally ingested or smoked. Smoked THC manifests itself within a few minutes with its effect recognizable till 3 hours [180]. When administered orally, THC shows its effects after 30-90 minutes with its effect recognizable for as long as 12 hours [181]. Urine, blood, saliva and sweat are the fluid mediums mostly used for testing THC intake. However, in saliva THC has the highest lifetime of about 34 hours and is detectable in concentration as low as 0.5 ng/ml [182], which is 20-30 times lower than that of blood and urine [181], [182]. Therefore, THC sensing in saliva buffer was conducted for creating a platform capable of actively identifying more recent THC consumption. This study is presented in **Chapter 8**. Thus, research was carried out in building an MoS<sub>2</sub>-based nanopore sensor for highly efficient and resolved biomolecular detection.

# Chapter 3

## 3 Experimental and simulation methods

### 3.1 Fabrication of nanopores

This section explains the tools and techniques used for fabricating all SiN<sub>x</sub> and MoS<sub>2</sub> nanopores used throughout the study.

#### 3.1.1 Fabrication of silicon nitride nanopores

##### 3.1.1.1 *Silicon nitride substrate*

4-inch diameter prime silicon wafers (cut along <100> plane) with a thickness of 525±25 μm, coated with 50 nm thick low-stress LPCVD (low pressure chemical vapour deposition) silicon nitride (SiN<sub>x</sub>) on both sides were purchased from Rogue Valley Microdevices and used as the starting substrate for the SiN<sub>x</sub> membranes fabrication. First, the wafers were thoroughly cleaned by dipping the wafers in fresh piranha solution, which was prepared by mixing 96% H<sub>2</sub>SO<sub>4</sub> and 30% H<sub>2</sub>O<sub>2</sub> in 3:1 ratio. The high reactivity nascent oxygen in piranha solution helps in removing organic matter and cleaning the wafers. It also makes the surface more hydrophilic (by adding an -OH coating) making it favourable for sensing in an electrolytic environment. The wafers were then stripped off the acid by using DI water and then properly cleaned using a nitrogen gun. **Figure 3.1** shows schematic of the pristine substrate, scaled down to chip dimensions for better viewing.

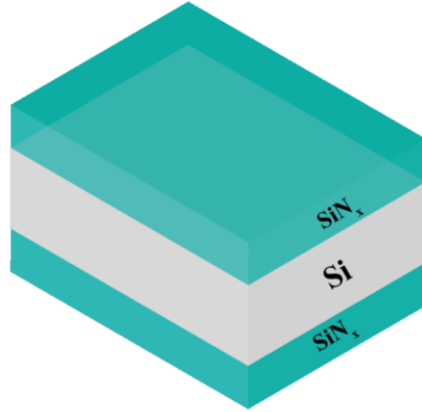


**Figure 3.1.** Schematic of a silicon- Si substrate with both sides coated by LPCVD (low pressure chemical vapor deposition) Silicon nitride- SiN<sub>x</sub>.

### ***3.1.1.2 Patterning of the nitride chips***

The wafers were taken for patterning the silicon nitride membranes by photolithography. A photomask for circular and square shaped chips were made with single and array of 20  $\mu\text{m}$  nitride openings were made using L-edit (layout given in **Figure 3.2.(a)**). Then AZ 5214E photoresist was spread at 500 rpm for 10 sec and spun coated at 4000 rpm for 30 sec on one side of the wafer. The photoresist was then soft-baked for 1 min at 90 °C. **Figure 3.2.(b)** shows the schematic of the substrate after spin-coating the photoresist. The wafers were photo-exposed for 2 sec using the mask (prepared by L-edit) 4 s at 64  $\text{mW.cm}^2$  power for patterning the membranes. AZ 5214E is a positive photoresist with an image reversal advantage, which results in a negative patterning. It is composed of naphthoquinone diazide, which is photoactive and when exposed becomes soluble in MF CD 319 developer and therefore can form the desired pattern. After exposure, it was hard baked at 120 °C for 2 min. This was done to crosslink novalak resin (also a component of AZ 5214E resist). Above 110 °C, the crosslinking agent and photo-exposed naphthoquinone diazide form a complex, which is absolutely insoluble in MF CD 319. So, after exposure and hard-bake

the exposed areas can be preserved while the unexposed areas (without any crosslinking) can be removed by developing. Finally, the resist is flood exposed for about 1 min to easily remove the unlinked resist. The resist was developed for ~40 sec in MF CD 319 developer to remove the unlined resist. **Figure 3.2.(c)** shows the patterned substrate after development.

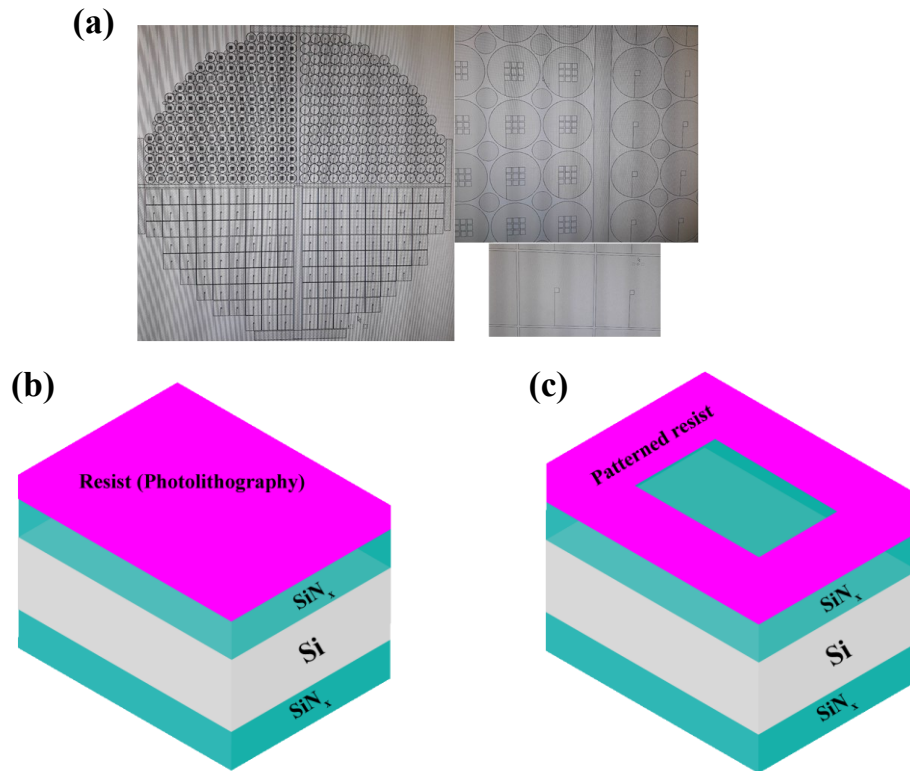


**Figure 3.2.** (a) L-edit layout of the photomask used for photolithography (b) Substrate with spin-coated photoresist and (c) Substrate with patterned photoresist (after UV exposure and development) exposing the part of the SiN<sub>x</sub> required to be removed.

### 3.1.1.3 Fabricating the free-standing membranes

The SiN<sub>x</sub> part, not protected by resist was etched by using dry etching (Reactive Ion Etch) using CF<sub>4</sub>/F plasma to expose the underlying silicon. The etch was carried out using Phantom III RIE from Trion Technology for 160 sec at a pressure of 150 mTorr, 45 sccm CF<sub>4</sub> and 5 sccm O<sub>2</sub>.

**Figure 3.3.(a)** and **Figure 3.3.(b)** show the schematic for RIE etch of the unprotected  $\text{SiN}_x$  and the image of a typical section of the patterned (by photolithography and RIE)  $\text{SiN}_x$  on Si wafer. The uncovered silicon (underneath the etched  $\text{SiN}_x$ ) was wet etched using a mixture of 32% KOH solution and IPA in 9:1 volumetric ratio for about 5 and a half hours, which is sufficient to remove almost 525  $\mu\text{m}$  of silicon (considering an etch rate of 1.6  $\mu\text{m}/\text{min}$ ) but leave few microns of silicon thickness to prevent the chips from separating from the wafer on its own. **Figure 3.3.(c)** shows the KOH etch of the silicon after removal of  $\text{SiN}_x$  by RIE. KOH solution results in an anisotropic etch of Silicon along  $\langle 111 \rangle$  plane at an angle of  $54.7^\circ$  (this factor was considered while making the L-edit photomask to leave out 50 nm  $\text{SiN}_x$  membrane with a  $20 \mu\text{m} \times 20 \mu\text{m}$  window size). The KOH bath was maintained at  $85^\circ\text{C}$  throughout the etching process to maintain reactivity. The wafer was taken out of the KOH bath and thoroughly cleaned. The chips were separated from the wafer slowly to avoid any damage to the free-standing  $\text{SiN}_x$  membranes. **Figure 3.3.(d)** and **Figure 3.3.(e)** show the isometric bottom and top views of the free-standing  $\text{SiN}_x$  thus fabricated after removal of Silicon by KOH etch. **Figure 3.3.(f)** shows the optical microscopic image of a typical free-standing solid-state  $\text{SiN}_x$  membrane thus fabricated, with the inset showing the chip containing the membrane (to be mounted into the measurement cell set-up for ionic current measurement).

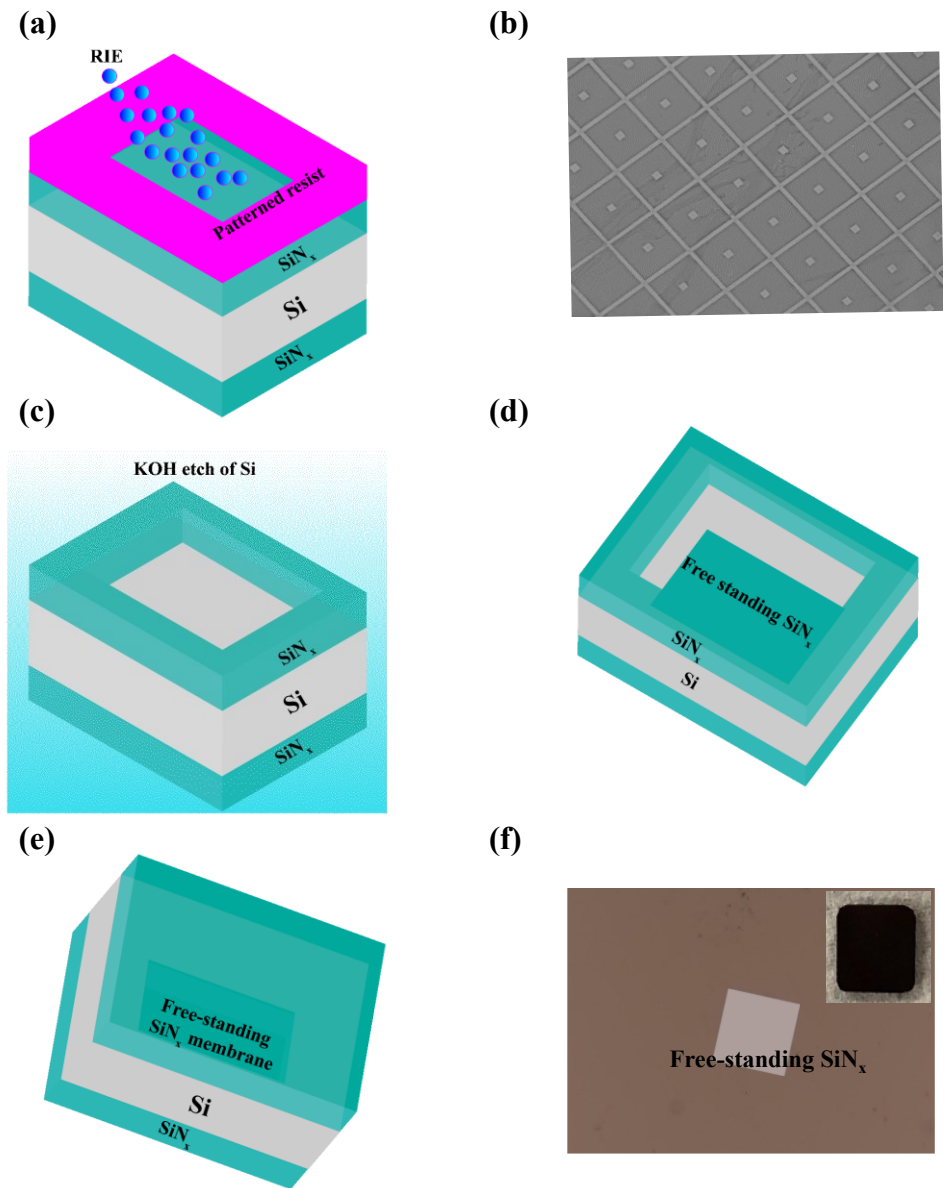


**Figure 3.3.** (a) RIE etch of  $\text{SiN}_x$  (not protected by photoresist), (b) A typical section of patterned and RIE etched  $\text{SiN}_x$  on Si wafer, (c) KOH etch of uncovered silicon, (d) isometric bottom view, (e) isometric top view of free-standing  $\text{SiN}_x$  formed after removal of silicon by KOH etch, and (f) optical image of free-standing  $\text{SiN}_x$  membrane with inset showing the chip containing the membrane.

### 3.1.1.4 Fabrication of silicon nitride nanopores

The 5×5 mm chips were used for nanopore fabrication. JEOL JEM-ARM200CF S/TEM Transmission Electron Microscope was used in the scanning mode using a 40 mrad corrected aberration probe at 200 keV with 0.1 nm resolution. The drilling was done for ~10 sec to obtain ~2-3 nm nanopores, for 30-40 sec to obtain 4-5 nm pores, for ~2 min to obtain 8-10 nm pores.

**Figure 3.4.(a)** shows schematic of STEM drilling for SiN<sub>x</sub> nanopore fabrication and **Figure 3.4.(b)** shows the TEM image of a 4.2 nm diameter STEM fabricated SiN<sub>x</sub> nanopore. The rate of boundary (size) expansion was found to be more rapid with increase in diameter. The nanopores, thus fabricated were used for molecular sensing.

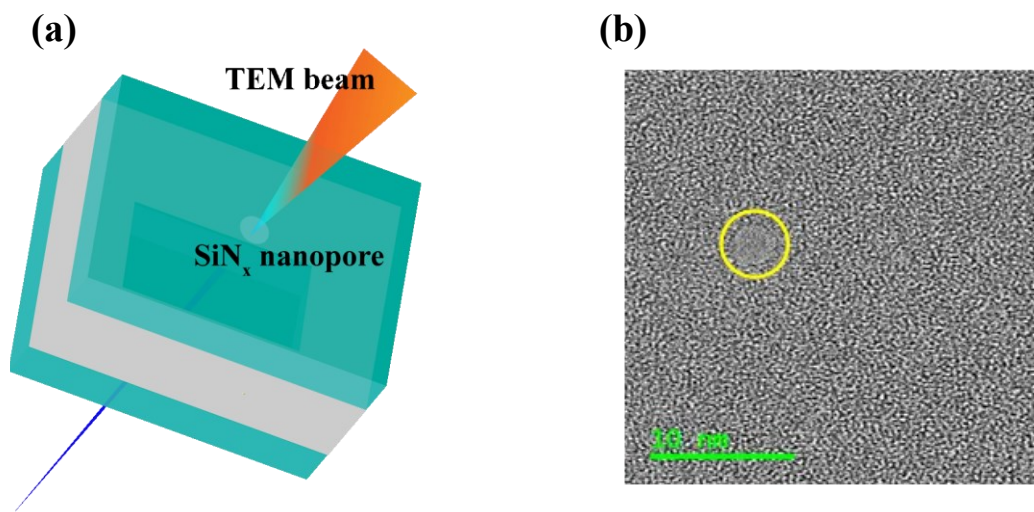


**Figure 3.4.** (a) Schematic for STEM drilling of nanopore drilling on free-standing SiN<sub>x</sub> membrane and (b) TEM image of a STEM fabricated SiN<sub>x</sub> nanopore.

### 3.1.2 Fabrication of MoS<sub>2</sub> nanopores

#### 3.1.2.1 MoS<sub>2</sub> substrate

The free-standing SiN<sub>x</sub> membranes fabricated previously (see **Section 3.1.1** and **Figure 3.3.(d)**) were used for MoS<sub>2</sub> nanopore fabrication. For MoS<sub>2</sub> membranes, low defect density highly oriented 2H- phase MoS<sub>2</sub> single crystal procured from 2D semiconductors Inc. was used.

#### 3.1.2.2 Patterning of the nitride membranes

A 200 nm diameter circle was patterned at the center of the SiN<sub>x</sub> membrane by using Electron beam lithography. PMMA bilayer positive tone resist was then spin coated on the membrane. First the membranes were dehydrated by baking it at 180 °C for 2 min and left to cool for about 2-3 min. Then PMMA 495 was spread at 500 rpm for 10 sec and spin coated at 4000 rpm for 45 sec. Then it was baked at 180 °C for about 5 min and then left to cool for 2-3 min. Then PMMA 950 was spread at 500 rpm for 10 sec and spin coated at 4000 rpm for 50 sec. Then it was again baked at 180 °C for about 5 min and then left to cool for 2-3 min. After spin coating the PMMA bilayer, the membranes were taken for exposure in Raith-Two Electron Beam Lithography (EBL) system. First the 200 nm diameter circle was patterned at the centre of SiN<sub>x</sub> membrane by coordinate correction in scanning electron microscopy (SEM) mode of EBL. Then the pattern was exposed using a 10-micron aperture at 30 keV voltage with an area dose of 120 μC/cm<sup>2</sup>. After exposure, it was developed for 60 sec at room temperature using 1:3 MIBK/IPA solution followed by an IPA rinse for 20 sec. Then the membrane was dried thoroughly. Since the size of the patterned circle was 200 nm, which is not possible to be viewed under microscope, the chip after development was viewed under SEM mode of EBL again to ensure it is properly patterned. Then the patterned membranes are then dry etched by RIE to remove the exposed free-standing nitride part, thus resulting in a 200 nm hole. The free-standing SiN<sub>x</sub> with 200 nm hole was then piranha cleaned

again following the same procedure as stated in **Section 3.1.1** of wafer cleaning. Then it was imaged under Helium ion Microscope (HiM) to ensure the membrane was not broken after piranha clean and the diameter of the hole fabricated by EBL and RIE is close to what was desired (i.e. 200 nm). Then it was taken for MoS<sub>2</sub> deposition. **Figure 3.5.(a)** and **Figure 3.5.(b)** shows a schematic and HiM image of a 200 nm hole fabricated on free-standing SiN<sub>x</sub> membrane.

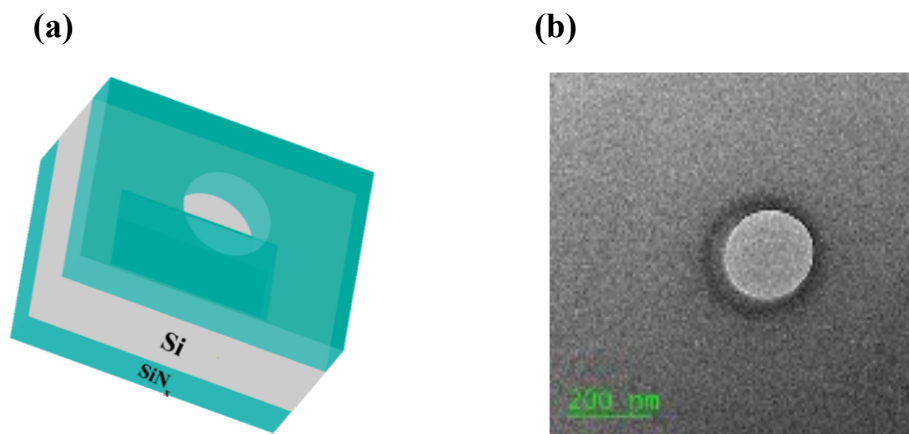


**Figure 3.5.** (a) Schematic and (b) HiM image of a 200 nm hole fabricated by EBL and RIE on free-standing SiN<sub>x</sub> membrane.

### 3.1.2.3 Mechanical exfoliation of MoS<sub>2</sub> membranes

A piece of scotch tape was taken and treated with a swab dipped in acetone to reduce its stickiness. Thin layers of MoS<sub>2</sub> were then mechanically exfoliated from the MoS<sub>2</sub> bulk crystal onto the scotch tape. The SiN<sub>x</sub> membranes with 200 nm hole was mounted on the bottom stage of a dual-stage microscope with XYZ stage adjustments. The scotch tape was then mounted on the upper stage of the microscope. The MoS<sub>2</sub> on scotch tape and the centre of the SiN<sub>x</sub> membrane (where the 200 nm hole is fabricated) were aligned while watching it under the microscope. After alignment the two stages were brought together such that they are pressed against each other transferring MoS<sub>2</sub> onto the hole on SiN<sub>x</sub> membrane. It was found that the thickness of the MoS<sub>2</sub> transferred first on the

scotch tape is crucial for obtaining monolayer or bilayer MoS<sub>2</sub> on the SiN<sub>x</sub>. The device was imaged under JEOL JEM-ARM200CF S/TEM in TEM mode to ensure that the 200 nm hole is fully covered by one or two uniform MoS<sub>2</sub> layers. **Figure 3.6.(a)** shows the free-standing MoS<sub>2</sub> membrane transferred by mechanical exfoliation to the 200 nm hole on SiN<sub>x</sub>. **Figure 3.6.(b-d)** show the TEM images of three typical bilayer MoS<sub>2</sub> membranes with the free-standing part clearly differentiated from the part supported by SiN<sub>x</sub>. The free-standing MoS<sub>2</sub> membranes were used for nanopore fabrication.

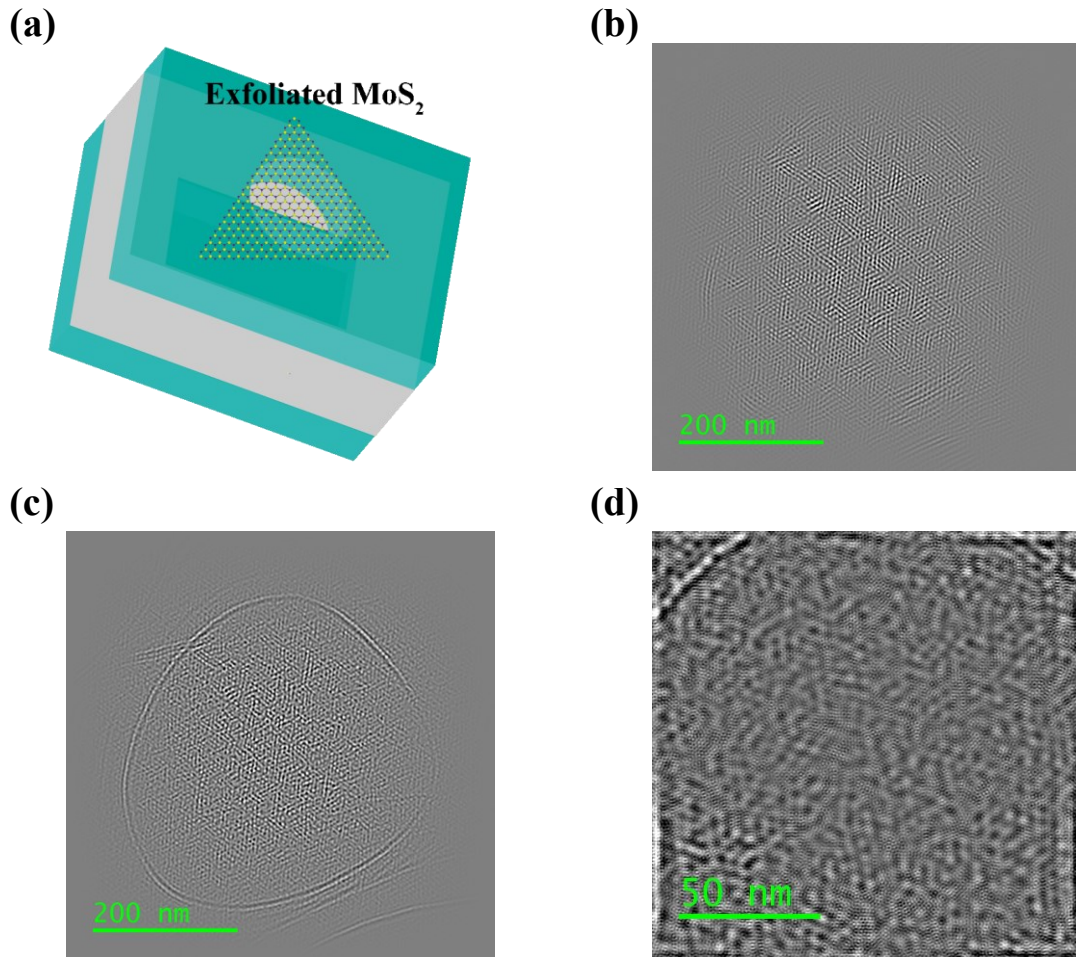


**Figure 3.6.** (a) Schematic of a free-standing MoS<sub>2</sub> membrane transferred by mechanical exfoliation to the 200 nm hole on SiN<sub>x</sub> after being aligned properly by using a dual-stage

microscope and (b-d) TEM images of three typical bilayer MoS<sub>2</sub> membranes with the free-standing part clearly distinguished from the part supported by SiN<sub>x</sub>, as observed by the difference in contrast with the lighter part showing the free-standing portion of the membrane. It looks lighter due to its thinness allowing higher light transmission.

### 3.1.2.4 Fabrication of MoS<sub>2</sub> nanopores

The nanopores were fabricated using JEOL JEM-ARM200CF S/TEM in STEM mode right after imaging the membranes using a 40 mrad corrected aberration probe at 200 keV with 0.1 nm resolution. The nanopore drilling occurred almost instantly (in < 5 sec) and 2.5-3.5 nm pores were obtained from it. Further exposure in STEM mode was avoided to prevent unnecessary expansion of the nanopore (owing to thinness of MoS<sub>2</sub>). Then the nanopore was imaged in TEM mode and further taken for sensing. **Figure 3.7.(a)** and **Figure 3.7.(b)** show schematic of STEM drilling of MoS<sub>2</sub> nanopore and HRTEM (High Resolution TEM) image of a STEM fabricated MoS<sub>2</sub> nanopore, respectively.

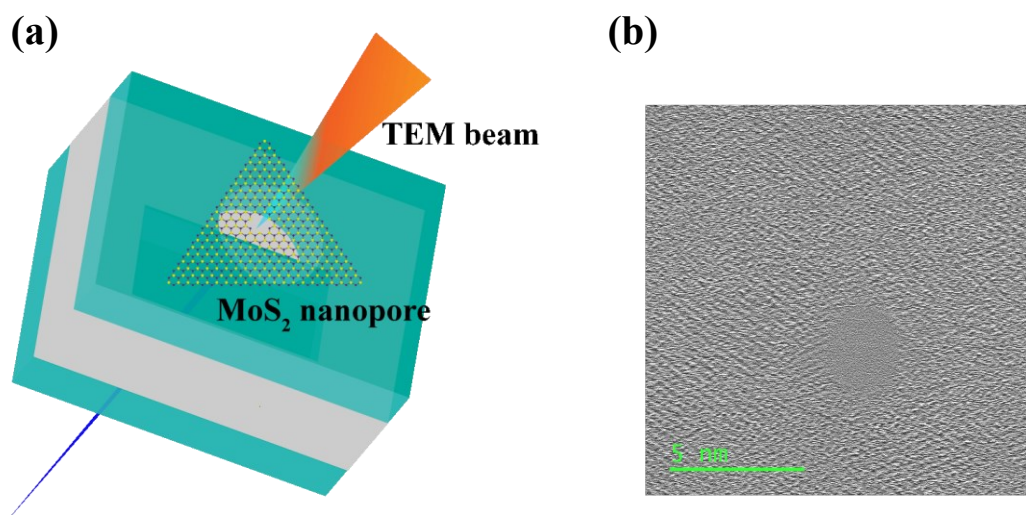


**Figure 3.7.** (a) Schematic diagram of STEM drilling of MoS<sub>2</sub> nanopore and (b) HRTEM (High Resolution TEM) image of a STEM fabricated bilayer MoS<sub>2</sub> nanopore.

## **3.2 Ionic conductance-based characterization of nanopores**

### **3.2.1 Electrolyte preparation**

300 mM filtered KCl solution was prepared and buffered with 3 mM Tris-HCl was prepared (pH=8) and stored (to be used for measurement of ionic conductance). The latter solution was diluted with DI water for lower concentration, if and when required for sensing. The stored KCl solution was degassed for 90 minutes in vacuum. Before experiments, the degassed KCl solution was ensured to be at room temperature.

### **3.2.2 Nanopore Cleaning**

#### ***3.2.2.1 For SiN<sub>x</sub> nanopores***

The SiN<sub>x</sub> nanopores were first cleaned in a piranha bath (prepared as described in **Section 3.1.1**) for about 2 hours to remove debris left after drilling, environment particulates and organic materials which may block the pore. About 5 ml of H<sub>2</sub>O<sub>2</sub> are added to the bath every 30 min to keep the bath reactive for a fresh supply of nascent oxygen and the fumes to flow even through the small nanopores. The nanopore was taken out of the piranha bath and thoroughly clean with degassed (for 90 min) DI water to avoid to almost eliminate the chance of any nanobubble for water blocking the pore. The pore was dipped in ethanol and left for about 3 hours in vacuum to pull ethanol through the pore making it clean for ionic conduction. The nanopore was taken for being mounted in the measurement cell for sensing.

#### ***3.2.2.2 For MoS<sub>2</sub> nanopores***

The MoS<sub>2</sub> nanopores were cleaned three times by pulling acetone under vacuum for 30 minutes each, with the acetone solution being replaced by a new solution every time to avoid drying up of

acetone at the nanopore. The same process was repeated four times using IPA and once using ethanol, each cycle was carried out for 20 minutes. During initial measurements, 4 cycles of IPA clean was found to be optimum for removing all acetone and achieve a low noise level by avoiding residues. The nanopore was taken for being mounted in the measurement cell for further experiments.

### **3.2.3 Custom-designed cell assembly and cleaning**

Half cells made of Poly-tetra-fluoro-ethylene (Teflon) were used as electrolytic chambers. Teflon having a good electro-chemical resistance and hydrophobicity helps maintain clean and insulated environment, required for accurate sensing. Polydimethylsiloxane (PDMS) gaskets were used to seal the half cells in order to prevent cross flow of electrolyte in between cells other than through nanopore. PDMS gaskets reduce capacitive noise during ionic current measurements. For ionic current measurements the clean nanopore was mounted onto the cell by sandwiching them between the PDMS gaskets. Sonication-assisted thorough cleaning of half cells was done before each experiment to remove any particulates or KCl residue (in between experiments). The cells were fastened together in a way tight enough to prevent electrolyte leak but loose enough to prevent the membranes from breaking. The cells were filled with ethanol and kept in vacuum for about 2-3 hours to create an uninterrupted wetted nanopore. The cell chambers were filled with KCl solution (previously prepared electrolyte- see **Section 3.2.1**). The KCl solution was refluxed to efficiently replace ethanol with KCl. This step was also found to benefit faster conduction through the nanopores along with the vacuum pulling process. Bias across the membrane was applied using Ag/AgCl electrodes dipped in the electrolyte contained in the half cells. Electrodes were functionalized with chloride by treating them with ethanol, DI water and dipping them in bleach for about 1 hour. Electric interference was prevented by isolating the entire assembly in a Faraday

cage purchased from Warner instruments. **Figure 3.8** shows the sensing cell setup used for all experiments.

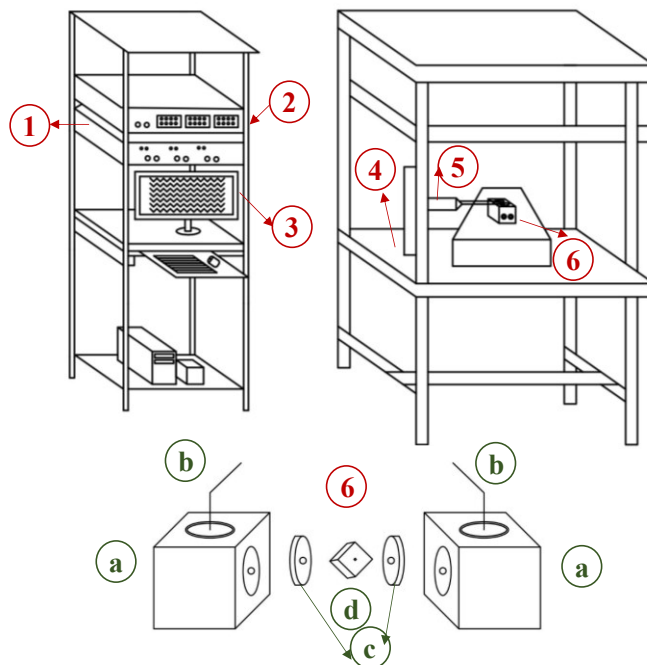


**Figure 3.8.** Schematic representation of custom-designed cell assembly for sensing [1. Amplifier, 2. Digitizer, 3. User interface, 4. Faraday cage, 5. Amplifier head, 6. Cell set up (a. Teflon cell containing KCl, b. Ag/AgCl electrodes, Gaskets to hold membrane, d. Membrane bearing nanopore)].

Single channel recordings were then obtained to characterize the nanopores. The ionic blockades induced by translocating analytes were filtered by Warner 8-pole Bessel filter, amplified by Axon MultiClamp 700B amplifier and finally digitized by Digidata 1550B. The digitized traces were then viewed and recorded in real-time by using Clampex 10.6. The files were then saved as .abf files and stored for further analysis.

### 3.3 COMSOL Multiphysics simulation

The following section explains the details of defined geometry, meshing and physics behind the model used for simulating ionic conductance and DNA translocation electro-kinetics through different sized nanopores on 50 nm SiN<sub>x</sub> and 1-6 layers MoS<sub>2</sub> membranes.

#### 3.3.1 Geometry and parameters involved

A geometry mimicking the cell-set up used for experiments was considered for the simulation. A two-dimensional axis-symmetric representative geometry of the two reservoirs separated by a membrane was considered for all nanopore conductance measurements. For simulating DNA translocation kinetics, a polynucleotide strand defined as a 1 nm thick and 10 nm long cylinder was introduced into the geometry at a distance of 5 nm away (along the longitudinal axis) from the centre of the nanopore. An electrolyte (KCl) concentration of 300 mM was considered for the simulations. Debye length for 300 mM KCl was calculated to be 1.8 Å (considering room temperature of 23 °C). Hence a mesh size of less than 1 Å for nanopores and membranes, and 0.5 Å for the rest of the geometry were considered to consider the Electrical Double Layer (EDL) and to achieve a good accuracy of results.

A potential difference was applied across the reservoir with the electrodes considered at the reservoir ends. The electric field hence induced, generates an ionic current through the nanopore and also draws the negatively charged nanoparticle through the pore. Thus, it blocks a portion of the ionic current based on its surface charge and electric field interactions, physical and chemical properties of the particle and the system containing it.

The detailed geometry and meshing process adopted for ionic conductance and DNA translocation simulation through MoS<sub>2</sub> and SiN<sub>x</sub> nanopores is explained in detail in **Chapter 4**. **Table 3.1** shows the geometry dimensions and values of parameters considered for the simulations.

**Table 3.1.** Geometry dimensions and parameter values used for simulation

<i>Parameters</i>	<b>Values</b>
<i>DNA dimensions</i>	1 nm × 10 nm
<i>Diffusivity of K<sup>+</sup></i>	1.95E-9 m <sup>2</sup> /s
<i>Diffusivity of Cl<sup>-</sup></i>	2.032E-9 m <sup>2</sup> /s
<i>Universal gas constant</i>	8.314 J/K/mol
<i>Temperature</i>	298 K
<i>Relative permittivity</i>	80
<i>Medium viscosity</i>	0.001 Pa-s
<i>Water density</i>	1000 kg/m <sup>3</sup>
<i>Transmembrane bias</i>	0.2 V
<i>DNA surface charge</i>	-0.015 C/m <sup>2</sup>
<i>Silicon nitride surface charge</i>	-0.02 C/m <sup>2</sup>
<i>MoS<sub>2</sub> surface charge</i>	-0.031 C/m <sup>2</sup>
<i>KCl concentration</i>	300 mM
<i>DNA (dA) density</i>	1600 kg/m <sup>3</sup>

For repeatability study, the nanopore geometry was assumed to be hour-glass. An hour-glass shape with an upper conical zone (Zone 1), a 10 nm long cylindrical body (Zone 2) and a lower conical zone (Zone 3) was considered for all pore sizes simulated (as shown in **Figure 3.9**). A constant

cylindrical zone thickness was assumed since the shape of the pore is governed by the way electron beam passes through a membrane. Since a constant thickness of the silicon nitride membrane (50 nm) was used for fabrication of all pores, cylindrical region can be assumed to have same thickness for all pores. However, the upper and lower conical parts were considered to have different volumes and half angles to precisely represent the practical scenario. The detailed simulation method will be discussed in **Chapter 4**.

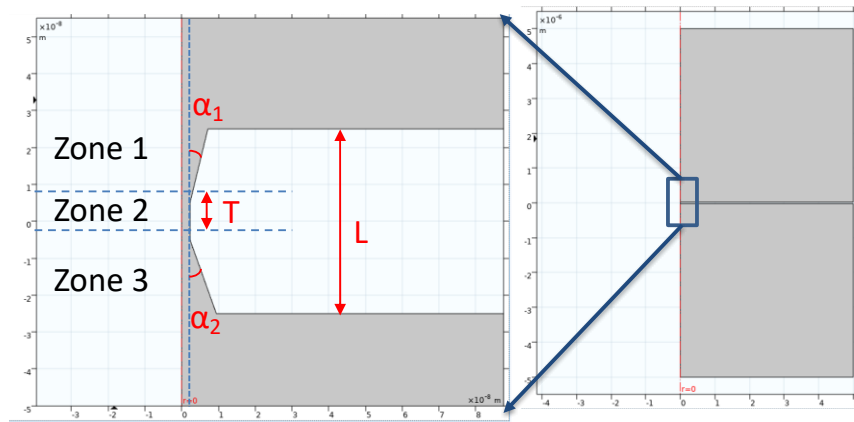


**Figure 3.9.** Geometry of COMSOL Multiphysics simulation model showing an hour-glass shaped pore with a cylindrical body;  $L$  = thickness of membrane/pore height = 50 nm,  $T$  = thickness of cylindrical part of pore = 10 nm,  $\alpha_1$  = half-angle of the top conical portion and  $\alpha_2$  = half-angle of the bottom conical portion of the pore

### 3.3.2 Mathematical modelling

#### 3.3.2.1 For steady-state analysis of blank nanopore conductance (ionic conductance without any DNA)

The ionic current through the nanopore was calculated from the potential distribution determined from Poisson's equation; by feeding the ionic concentration gradient from the Transport of dilute

physics and velocity from the Stokes' law, since Reynold's number for KCl in water falls in the laminar flow regime.

*Laminar flow (Navier-Stokes equation)*

The fluid flow velocity profile in the laminar flow regime was determined by the Navier Stokes equation (**Equation 3.1**) with the potential distribution and concentration gradient fed as input.

**Equation 3.1:**  $\rho(u \cdot \nabla)u = \nabla \cdot [-PI + \mu(\nabla u + (\nabla u)^T)] + V_F$

$$\rho \nabla \cdot u = 0 \quad \text{for stationary flow}$$

Volume force components,  $V_{Fx} = -F(c_1 - c_2)V_x$  and  $V_{Fy} = -F(z_1c_1 + z_2c_2)V_y$

Where  $\rho$  = fluid density,  $u$  = fluid velocity,  $P$  = Pressure,  $\mu$  = fluid dynamic viscosity,  $V$  = applied potential,  $z_1$  = charge number of  $K^+$  ion = 1,  $z_2$  = charge number of  $Cl^-$  ion = -1,  $c_1$  = concentration of  $K^+$  ion and  $c_2$  = concentration of  $Cl^-$  ion (obtained from **Equation 3.3** presented later) and  $F$  = Faraday's constant.

The concentrations  $c_1$  and  $c_2$  were obtained from transport of dilute species physics, which will be explained later in this section.

- Boundary conditions for the flow:

The cell wall, nanopore wall and membrane were kept at no-slip condition. The bottom (electrolyte inlet) and top (electrolyte outlet) cell boundaries and DNA were kept at zero pressure conditions.

**Figure 3.10** shows the different boundary conditions defined in this physics.

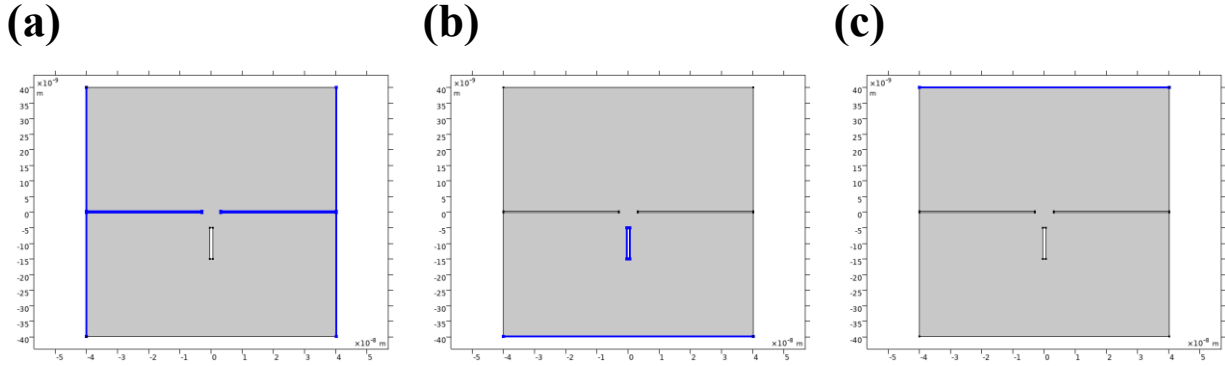


**Figure 3.10.** (a) Boundaries in blue kept at no-slip condition, (b) Inlet and (c) Outlet boundaries kept at zero pressure conditions.

We obtained the fluid velocity profile ( $u$ ) from this physics to be used for further simulations.

*Electrostatics (Poisson's equation)*

The potential distribution as a result of the induced electric field and charge interactions due to the ionic transport through the nanopore was simulated from the Poisson's equation (**Equation 3.2**).

**Equation 3.2:**  $\nabla^2 V = -\frac{\rho_{vf}}{\epsilon_0 \epsilon_r}$  and Surface charge density,  $\rho_{vf} = F(z_1 c_1 + z_2 c_2)$

Where  $V$  = applied potential,  $\epsilon_0$  = vacuum permittivity,  $\epsilon_r$  = relative permittivity,  $z_1$  = charge number of  $K^+$  ion = 1,  $z_2$  = charge number of  $Cl^-$  ion = -1,  $c_1$  = concentration of  $K^+$  ion and  $c_2$  = concentration of  $Cl^-$  ion (obtained from **Equation 3.3** presented later) and  $F$  = Faraday's constant.

➤ Electrostatic boundary conditions:

The electrodes were considered at the two ends of the cell, the top boundary was given a bias of  $V$  and the bottom boundary was grounded to generate a potential difference and hence an induced electric field to electrophoretically drag the electrolyte ions. **Figure 3.11** shows the different boundary conditions defined in this physics.

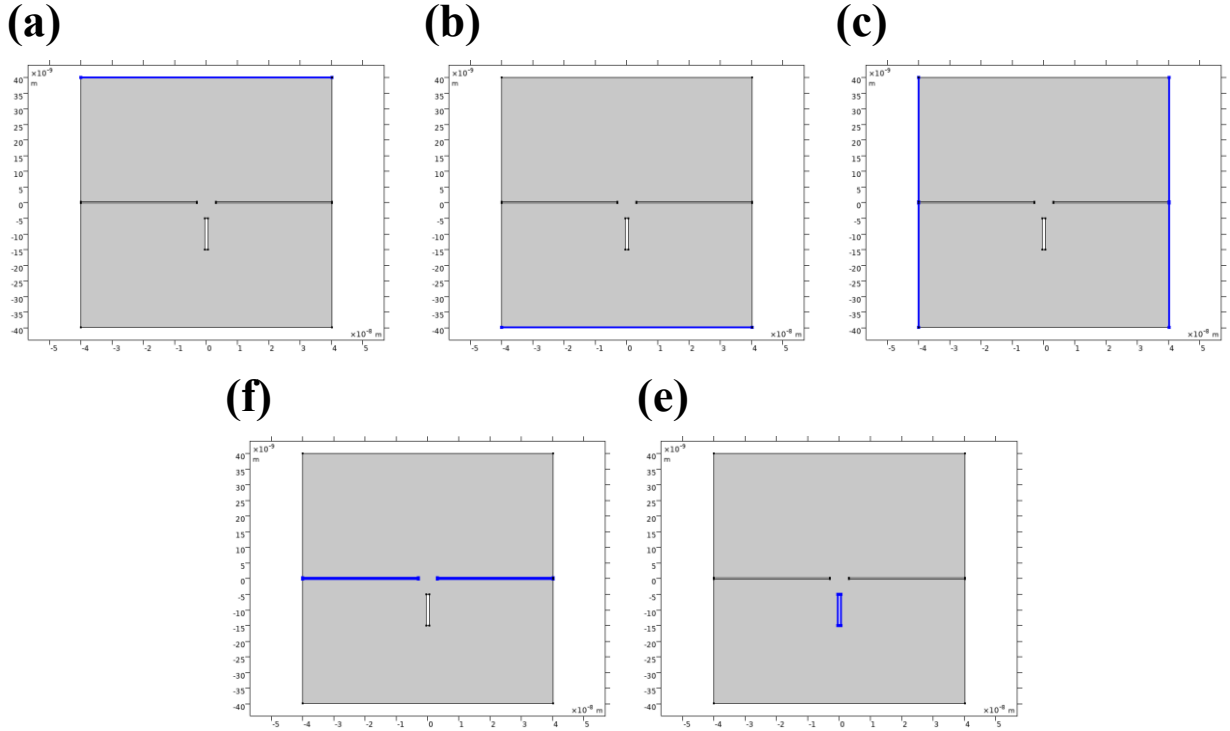


**Figure 3.11.** (a) Boundary representing electrode where a potential of 200 mV was applied, (b) Boundary representing the ground electrode, (c) Boundaries at zero charge, (d) Boundaries at a surface charge of  $-0.031 \text{ C/m}^2$  for  $\text{MoS}_2$  membranes and  $-0.02 \text{ C/m}^2$  for  $\text{SiN}_x$  membranes and (e) DNA boundaries at a surface charge of  $-0.015 \text{ C/m}^2$ .

The electric potential (V) profile was obtained from this physics which was used for further simulations.

*Transport of dilute species (Nernst-Planck equation)*

The ionic transport through the nanopore in response to the applied bias at a particular bulk electrolytic concentration was represented and simulated by Nernst-Planck equation (**Equation 3.3**).

$$\text{Equation 3.3: } N_i = D_i \nabla c_i - z_i \left( \frac{D_i}{RT} \right) F c_i \nabla V + u c_i, \quad i = 1 (\text{for } K^+ \text{ ion}), 2 (\text{for } Cl^- \text{ ion})$$

Where  $N_i$  = ionic flux,  $D_i$  = diffusivity of  $i^{\text{th}}$  ion,  $z_i$  = charge number of  $i^{\text{th}}$  ion,  $c_i$  = concentration of  $i^{\text{th}}$  ion,  $F$  = Faraday's constant,  $u$  = fluid velocity (obtained from **Equation 3.1**),  $R$  = Universal gas constant,  $T$  = ambient temperature and  $V$  = applied potential (obtained from **Equation 3.2**),

Transport boundary conditions: The two ends of the cell were kept at bulk concentration for both  $K^+$  and  $Cl^-$  ions. **Figure 3.12** shows the different boundary conditions defined for this physics.

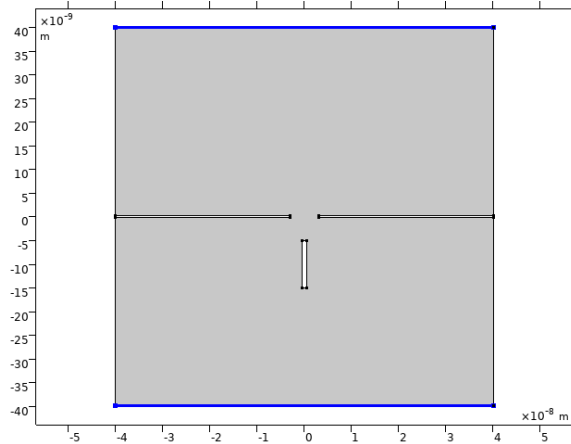


**Figure 3.12.** Boundaries conditions kept at 300 mM KCl (electrolyte) concentration

The concentration profiles of both the ions were obtained from this physics, which were fed to **Equation 3.1** and **Equation 3.2** for calculating volume force and space charge density respectively. Thus, all the three equations were coupled to simulate the nanopore conductance. Then based on the simulation results the ionic conductance through nanopore was evaluated according to **Equation 3.4**. For that, first a cut plane was defined at the nanopore surface and the ionic flux was integrated over the pore surface to obtain the ionic current which was then divided by the applied bias to get the ionic conductance (G).

$$\text{Equation 3.4: } G = \frac{1}{V} \oint F(z_1 N_1 + z_2 N_2) \cdot \hat{n} dS$$

Where,  $G$  = ionic conductance,  $V$  = Applied bias,  $F$  = Faraday's constant,  $z_1$  = charge number of  $K^+$  ion = 1,  $z_2$  = charge number of  $Cl^-$  ion = -1,  $N_1$  and  $N_2$  =  $K^+$  and  $Cl^-$  ionic flux through the nanopore.

### 3.3.2.2 For transient analysis of molecular translocation

The ionic blockade due to the particle transport is influenced by the particle position and surface charge as well as nanopore size and material. The particle's negative surface charge as mentioned in **Table 3.1** and shown with red boundaries around the particle in **Figure 3.13.a**, and initial orientation (see **Table 3.1**) with respect to the centerline of the nanopore significantly affect both the dynamics of the particle translocation and the modulation of the ionic current through a nanopore. Under an applied electric field, electroosmotic fluid flow is generated and an electrical double layer (EDL) is formed, as seen in **Figure 3.13.a**. An EDL (shown with green circles representing positive charge concentration in **Figure 3.13.a**) is formed on both sides of the membranes (having negative surface charge as represented by red boundaries in **Figure 3.13.a**). An EDL is also formed around the particle (also shown by green circles as seen in **Figure 3.13.a**) created by induced dipoles based on the surface charge of particle. The fluid flow velocity (as calculated from Navier-Stokes equation) is then used to evaluate the viscous drag on the particle (see **Figure 3.13.a**). The resultant hydrodynamic force  $F_{Hy}$  (see **Equation 3.5**) on the particle is therefore defined as the negative of viscous drag (VD) as shown in **Figure 3.13.a** which is evaluated by integrating the hydrodynamic stress tensor over the particle surface ( see **Equation 3.5**).

$$\text{Equation 3.5: } Y\text{-component of hydrodynamic force, } F_{Hy} = - \int \mu \left( \frac{\partial u}{\partial y} + \frac{\partial v}{\partial x} \right) \cdot \hat{n} dS$$

Where,  $\mu$  = fluid dynamic viscosity,  $u$  and  $v$  are the X-component and Y-component of fluid velocity.

The electrostatic force (EF as shown in **Figure 3.13.a**) acting on the particle due to the applied electric potential was then evaluated by integrating the electrostatic stress tensor.

**Equation 3.6:**

Y-component of electrostatic force,  $F_{Ey} = \int \epsilon_0 \epsilon_r [E_x E_y + E_y E_y - 0.5(E_y^2)] \cdot \hat{n} dS$

$$F_{Ey} = \int \epsilon_0 \epsilon_r \left[ \frac{\partial V_x}{\partial y} \frac{\partial V_y}{\partial y} + \frac{\partial V_y}{\partial y} \frac{\partial V_y}{\partial y} - 0.5 \left( \left( \frac{\partial V_y}{\partial y} \right)^2 \right) \right] \cdot \hat{n} dS$$

Where  $E_x$  and  $E_y$  = X and Y components of the electric field,  $V_x$  and  $V_y$  = X and Y components of the electric potential,  $\epsilon_0$  = vacuum permittivity and  $\epsilon_r$  = relative permittivity.

The electrophoretic (EP as shown in **Figure 3.13.a**) force on the particle therefore is the summation of the hydrodynamic and electrostatic forces (EF as shown in **Figure 3.13.a**). Due to the induced dielectrophoretic effect (generated as a result of electroosmosis and electrophoresis), a relatively high electric field tends to pull the analyte towards the positively biased chamber (trans) from the grounded (cis) chamber. To evaluate the particle velocity, a force balance was conducted on the particle (from particle frame of reference) immersed in an electrolyte under an applied potential. **Figure 3.13.b** shows the force balance on the particle. The forces were defined as integration coupled boundary probes over the particle surface. The translational velocities were calculated from the total force balance on the particle, with the equations being fed using Global ODEs physics. The initial values of all variable (at time = 0) was assumed to be zero.

**Equation 3.7:** Force balance along Y-axis,  $m_p \frac{dv_p}{dt} = F_{Hy} + F_{Ey} + F_{Vy}$

Where,  $m_p$  is the mass of the translocating particle,  $v_p$  is the longitudinal velocity of the translocating particle and  $F_{Hy}$  and  $F_{Ey}$  are the hydrodynamic and electrostatic forces as obtained from **Equation 3.5** and **Equation 3.6**.

Only Y-component of these forces were considered here as we wanted to compare only the linear (longitudinal) acceleration and retardation of the particle and corresponding current blockade occurring in response to the applied bias during its translocation through the nanopore system. For capturing such translational dynamics, we used the physics explained for ionic conductance simulation along deformed geometry physics which allowed the mesh to be deformed at a pace defined within the physics.

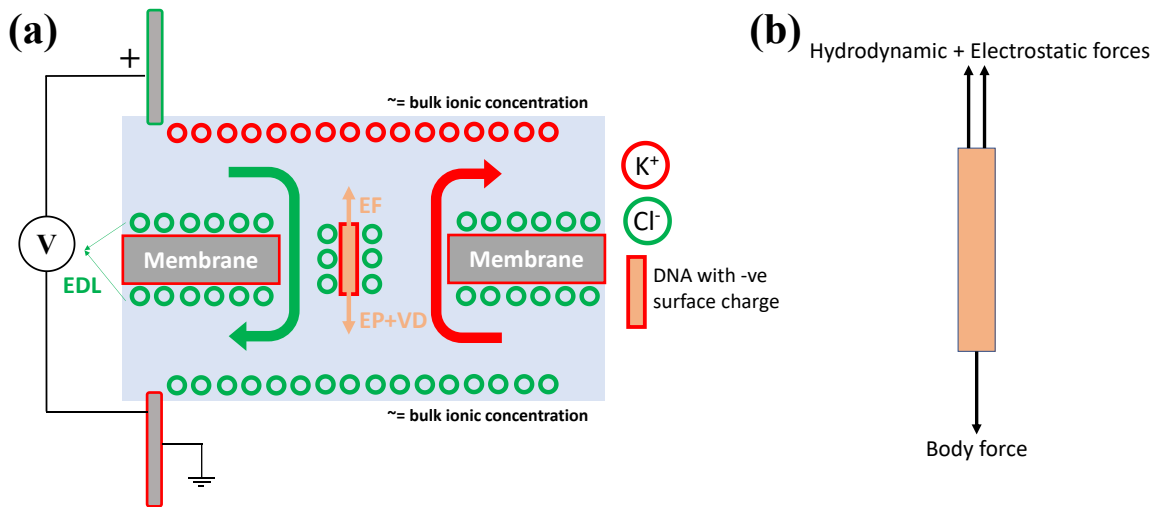


**Figure 3.13.** (a) Schematic showing the major phenomena occurring in and around the nanopore under an applied electric potential involving electroosmotic fluid flow; viscous drag (VD), Electrostatic and resultant Electrophoretic forces acting on the translocating particle immersed in an electrolyte. The red and green circles indicate negatively and positively charged ions and the red and green boundaries represent negative and positive surface charge which gives rise to Electrical Double layer (EDL) due to counter-charge concentration around both the membranes

and the particle and (b) Primary forces acting on the particle dispersed in an electrically biased compartment containing an electrolytic fluid

The deformed geometry physics was used to move the particle with the calculated velocity and the simulation of the next time instant was carried out from the updated particle position (as can be calculated from **Equation 3.8**).

**Equation 3.8:**  $Y_p = Y_{p0} + \int_0^t v_p dt$

where,  $Y_p$  and  $Y_{p0}$  are the previous and updated particle positions respectively.

**In case of multilayer (>1-layer) MoS<sub>2</sub> only:**

van der Waals force ( $F_{vy}$ ) acting between every two layers of multilayer MoS<sub>2</sub> is defined as integration coupled variables as presented in **Equation 3.9**.

**Equation 3.9:**

Y-component of van der Waals force [183],  $F_{Vy} = \int H \left[ \frac{1}{l^2} + \frac{1}{(l+nd)^2} - \frac{2}{(l+d)^2} \right] \cdot \hat{n} dS$

Where H is the Hamaker constant [183] for MoS<sub>2</sub>, d is the membrane/layer thickness, n is the number of layers, l is the interlayer spacing.

**In case of MoS<sub>2</sub> only:**

The ionic conductance (G) through the nanopore was first simulated by following **Equation 3.4**.

The resistivity ( $\sigma$ ) of KCl was then calculated from **Equation 3.10**.

**Equation 3.10:**  $\sigma = G \frac{L}{\pi R_p^2}$

Where L is the nanopore length and  $R_p$  is the nanopore radius.

For ultrathin nanopore, the access resistance ( $R_a$ ) [184] has a dominant role on the ionic conductance. The total resistance ( $R_{total}$ ) can be calculated from **Equation 3.11**.

$$\textit{Equation 3.11: } R_{total} = R_p + R_{acc} = \frac{\sigma L}{\pi R_p^2} + \frac{\sigma}{2R_p}$$

The blank pore ionic conductance was thereby calculated from the reciprocal of the total resistance as the calculated from **Equation 3.11**.

## Chapter 4 <sup>1</sup>(Paper 1)

**This chapter** presents a simulation study to investigate the factors influencing reproducibility of nanopore sensors. Silicon nitride nanopores were used for this study because it is till date the most studied material which allows easy fabrication and hence suitable for initial selections.

### **4 Predicting geometry and size repeatability of silicon nitride nanopores**

*Payel Sen and Manisha Gupta\**

Payel Sen

Department of Chemical and Materials Engineering

University of Alberta

Edmonton, Canada

Email: [payel@ualberta.ca](mailto:payel@ualberta.ca)

Manisha Gupta

Department of Electrical and Computer Engineering

University of Alberta

Edmonton, Canada

Email: [mgupta1@ualberta.ca](mailto:mgupta1@ualberta.ca)

---

<sup>1</sup> Manuscript under preparation and will be submitted by May 2021

## 4.1 Keywords

Silicon nitride nanopores, COMSOL Multiphysics simulation, nanopore geometry, noise analysis, nanopore size repeatability.

## 4.2 Abstract

Solid-state nanopores have been used extensively for biomolecular sensing, particular for its stability and scalability. Geometry of a nanopore affects the sensing of the analyte significantly. Therefore, the nanopore geometry should be closely monitored for repeatable measurements. Ionic conductance measurements through silicon nitride nanopores of different sizes were measured and the noise was analysed for obtaining a stable and refined signal. In this study, we propose a COMSOL Multiphysics model to predict the geometry (diameter and shape) of a nanopore from the measured nanopore conductance. We further extended the model to monitor effective change in nanopore diameter from the variation of ionic conductance for multiple measurements obtained for each nanopore. We observe that silicon nitride nanopores with diameter less than 4 nm demonstrate very good size repeatability, but as the size increases the repeatability was found to deteriorate. The results signify the suitability of silicon nitride nanopores with less than 4 nm diameter for formulating a reusable and reliable sensor.

## 4.3 Introduction

Solid-state nanopores have been used extensively as potential biomolecular sensors [138]. A small pore having dimension in the nanoscale is fabricated on solid-state membranes (eg. SiN<sub>x</sub> [158], [185]–[187], SiO<sub>2</sub> [47], Al<sub>2</sub>O<sub>3</sub> [80], [188], MoS<sub>2</sub> [51], [52], Graphene [54], [189]–[191], BN [98]). The membrane with the nanopore is then sandwiched between two electrolyte-filled cells, such

that on application of a bias across the membrane, the electrolyte-filled nanopore acts as the only conducting channel connecting the two chambers [160]. The resultant ionic conductance therefore is a characteristic of the nanopore size and shape [13], [160]. This conductance acts as the basis (baseline) for all nanopore-based sensing methods. For sensing, the analyte is introduced in one of the chambers and dragged electrophoretically to the other. The number of ions blocked in the path is manifested as ionic current drop, which helps identify the analyte. The current blockade is a factor of the pore size (baseline current) and analyte size (ionic blockade). Therefore, achieving a suitable and stable nanopore geometry is essential for reliable sensing [13], [160].

Different nanofabrication techniques have been employed for making a nanopore. The commonly used methods include direct drilling of pore by sputtering techniques using a highly focussed ion beam [159], [192]–[196] or electron beam [162], [197]. Wet etch and plasma etch [82], [157], [198] have also been extensively used, especially for pore array fabrication due to their ease of pattern transfer. In order to get a pore tuned to suitable size and shape, sometimes pore opening techniques are assisted with material deposition [199] and thermal treatments [200], [201]. The sensing reliability and resolution is directly dependent on the size of the nanopore, which is related with the fabrication efficiency of the techniques used. Silicon nitride has been by-far the most widely used nanopore material due to its robustness, handling ease and compatibility with standard fabrication techniques [158], [185]–[187], [202]. However, the conventionally used membrane thickness lies in the range of 20-50 nm. Pore fabrication using commonly used beam or ion drilling techniques can lead to pore shapes (cylindrical, hourglass, conical and so on) with variable aspect ratios even for the same fabrication parameters used (aperture size, exposure time, etc.) due to minute change in focussing [203]–[206]. The sensing accuracy immensely depends upon accurate knowledge of the nanopore size and shape. Due to small size of the nanopore, even 5% change in

size can lead to a large change in ionic conductance, thus perturbing the accuracy of the sensed signal for the same analyte type. As a result, pore size and shape estimation form the foundation of all sensing analysis. The fastest and easiest method measure the pore size is via image analysis of the fabricated pore. The advantage of solid-state nanopores is the thermomechanical stability of the membranes which allows large-scale production of portable and reusable biosensors. However, even solid-state nanopores are prone to pore expansion and shrinkage due to cleaning by harsh chemicals, unnecessary sputtered material redeposition, exposure to high-energy beams and accelerated ions. Therefore, precise knowledge of the pore size and shape during every experiment is essential to account for the possible changes in pore geometry after repeated sensing and to note the diameter at which the pore boundaries attain the stability required for molecular detection.

In this work, we have conducted experiments to understand the sensing repeatability by observing the change in the size of the  $\text{SiN}_x$  solid state nanopores via conductance measurements. We have also proposed a COMSOL Multiphysics simulation approach to precisely predict nanopore geometry which can be used to monitor pore size change.

## **4.4 Methods**

### **4.4.1 Experimental section**

4-inch both side 50 nm thick low stress, LPCVD silicon nitride ( $\text{SiN}_x$ ) coated  $525 \pm 25 \mu\text{m}$  thick,  $\langle 100 \rangle$  silicon wafers were used as the starting substrate.  $\text{SiN}_x$  is patterned using standard contact photolithography and the exposed nitride is etched by Reactive Ion Etch (RIE) to fabricate 50  $\mu\text{m}$  nitride windows. The exposed silicon is wet etched by KOH to obtain the free-standing  $\text{SiN}_x$  membranes on silicon support. JEOL JEM-ARM200CF Scanning/ Transmission Electron Microscope (S/TEM) was used to fabricate 2-3 nm nanopores on the  $\text{SiN}_x$  membranes.

The fabricated nanopore is cleaned for 30 min in heated piranha at 85 °C and then rinsed well in degassed DI water to avoid entrapment of any nanobubbles. The nanopore is then refluxed with degassed electrolyte (KCl) for pore wetting before conducting the conductance measurements. The two Teflon half cells and PDMS gaskets are cleaned with Acetone and rinsed with IPA. The membrane with the pore is then sandwiched between the two half cells with supporting gaskets. The two cell compartments are filled with equal volume of KCl. Two Ag/AgCl electrodes are treated with ethanol and DI water and then finally with bleach for re-chlorination. The electrodes are then introduced in the KCl filled compartments for applying bias across the nanopore. The entire set-up was placed inside a Faraday cage for electromagnetic isolation. The resultant ionic current in response to the applied voltage is then recorded by an Axon Patch assembly assisted by Axopatch 700B amplifier and Digidata 1550B digitizer.

Each pore was measured multiple times with intermediate cleaning steps to analyse its size stability for sensing applications.

#### **4.4.2 Simulation section**

An axisymmetric model was used to setup the system (see **Figure 4.1**). Based on the obtained linear I-V profiles two pore shapes are probable: cylindrical or hourglass (conical shaped silicon nitride nanopores display Ion current rectification). Considering the thickness of the membrane, hourglass shape is assumed as the pore geometry.

An hour-glass shape with an upper conical zone (Zone 1), a 10 nm long cylindrical body (Zone 2) and a lower conical zone (Zone 3) is considered for all pore sizes simulated (as shown in **Figure 4.1**). A constant cylindrical zone thickness is assumed since the shape of the pore is governed by the way electron beam passes through a membrane. Since a constant thickness of the silicon nitride

membrane (50 nm) is used for fabrication of all pores, cylindrical region can be assumed to have same thickness for all pores. However, the upper and lower conical parts were considered to have different volumes and half angles to precisely represent the practical scenario.

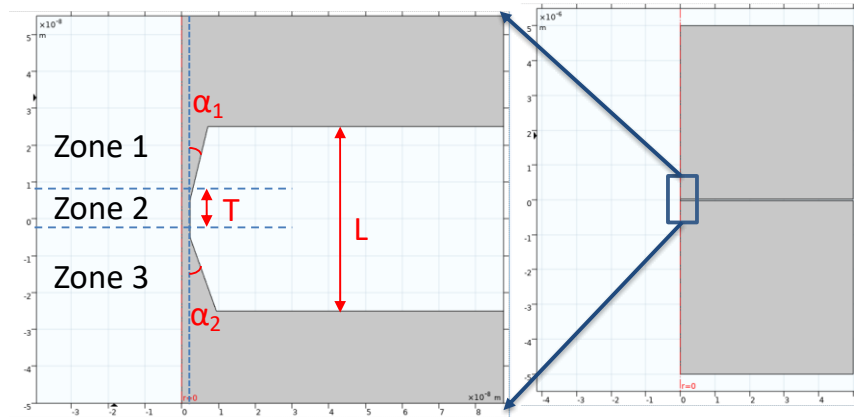


**Figure 4.1.** Geometry of COMSOL Multiphysics simulation model showing an hour-glass shaped pore with a cylindrical body;  $L$  = thickness of membrane/pore height = 50 nm,  $T$  = thickness of cylindrical part of pore = 10 nm,  $\alpha_1$  = half-angle of the top conical portion and  $\alpha_2$  = half-angle of the bottom conical portion of the pore

Step 1: Simulations are first done for  $\alpha_1 = \alpha_2$ , each varied from  $0^\circ$  to  $90^\circ$  in increment of  $10^\circ$  (if both  $\alpha_1$  and  $\alpha_2$  is equal to zero, the pore is cylindrical)

Say in case of a typical nanopore, for  $\alpha_1 = \alpha_2 = a$ , simulated conductance is A

for  $\alpha_1 = \alpha_2 = b$ , simulated conductance is B

Step 2: If measured conductance for that pore is M, then the values of A and B closest (low error) to M are taken such that  $A < M < B$ .

Step 3: The simulations are repeated by varying  $\alpha_2$  between to  $a$  and  $b$  at an increment of  $1^\circ$  at constant  $\alpha_1 = a$

Step 4: Step 2 is repeated. The new values obtained are  $\alpha_2 = u_2$  and  $\alpha_2 = l_2$ .

Step 5: The volume of the pore for  $\alpha_1 = a$  and  $\alpha_2 = u_2$  is then calculated in MATLAB = UV.

The volume of the pore for  $\alpha_1 = 0^\circ$  and  $\alpha_2 = l_2$  is then calculated in MATLAB = LV.

where, V= volume of Zone 1 ( $V_{z1}$ ) + Zone 2 ( $V_{z2}$ ) + Zone 3 ( $V_{z3}$ )

Considering d as the pore diameter,

$$V_{z1} = \frac{1}{3} * \pi * \left[ \frac{d}{2} + \left\{ \left( \frac{L}{2} - \frac{T}{2} \right) * (\tan \alpha_1) \right\} \right]^2 * \left( \frac{L}{2} - \frac{T}{2} \right)$$

$$V_{z2} = \pi * \left( \frac{d}{2} \right)^2 * T$$

$$V_{z3} = \frac{1}{3} * \pi * \left[ \frac{d}{2} + \left\{ \left( \frac{L}{2} - \frac{T}{2} \right) * (\tan \alpha_2) \right\} \right]^2 * \left( \frac{L}{2} - \frac{T}{2} \right)$$

Step 7: Pore volumes are also calculated in MATLAB for  $\alpha_1$  varying from  $a$  to  $b$  and  $\alpha_2$  varying from  $a$  to  $b$  at an increment of  $0.5^\circ$ . The pore volumes lying within the range bounded by UV and LV (see Step 6) are short-listed.

Step 8: The simulation is re-run for  $\alpha_1$  and  $\alpha_2$  values of the short-listed volumes. The simulated conductance closest to the experimental value gives the geometry of the pore.

Ionic conductance was then simulated by using coupled Laminar equation, Nernst-Planck equation, and Poisson's equation for different pore geometries to predict the measured pore geometry. **Table 4.1** summarizes the process flow used in this study.

**Table 4.1** Process flow followed in this work

$\alpha_1$	$\alpha_2$	Cone-angle variation	Simulated conductance for $\alpha_1$	Simulated conductance for $\alpha_2$	Experimental conductance	Selection condition	Volume
Equal		$0^\circ : 10^\circ : 90^\circ$	A for $\alpha_1 = a$	B for $\alpha_2 = b$	M	$A < M < B$	—
$a$	Varied	$\alpha_2 ( a : 1^\circ : b )$	Repeated				—
$a$	Varied	$\alpha_2 ( a1 : 0.5^\circ : b1 )$	Repeated				—
$( a , b2 )$		With smallest error between experimental and simulated conductance					V
<b>MATLAB program</b>							
Varied	Varied	$(\alpha_1, \alpha_2)$ values for while pore volume is closest (10% error) to V are all short-listed					
<b>Simulation</b>							
Ionic conductance is simulated for these $(\alpha_1, \alpha_2)$ values							
Values with smallest error between experimental and simulated conductance are selected and presented							

## 4.5 Results

SiN<sub>x</sub> pores were fabricated on 50 nm silicon nitride membranes using TEM. **Figure 4.2** shows the TEM images of the pores.

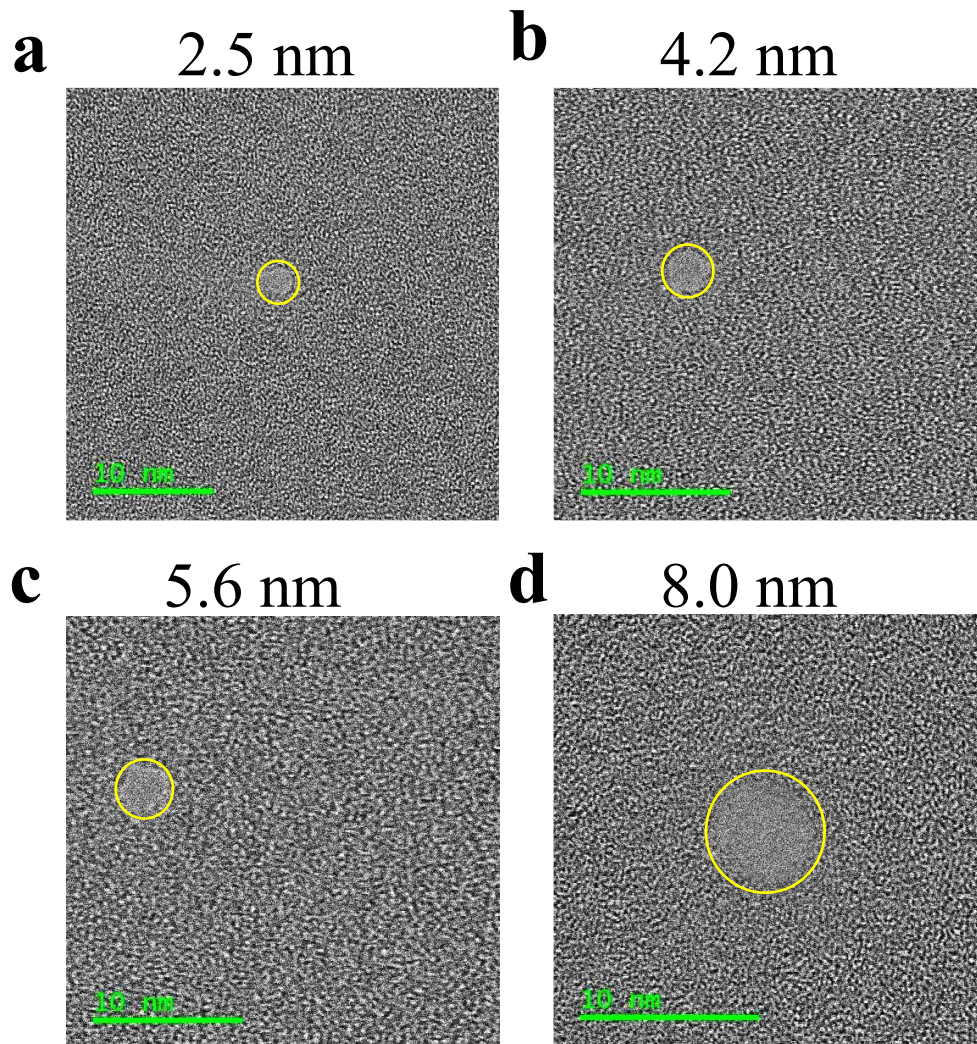


**Figure 4.2.** TEM fabricated solid-state nanopores on free-standing 50 nm thick 5×5 mm silicon nitride on silicon windows: Pore diameters of (a) 2.5 nm, (b) 4.2 nm, (c) 5.6 nm and (d) 8.0 nm. The yellow circle in each image just shows the nanopore locations and is not used for size calculation.

The fabricated pores are characterized by measuring the ionic conductance for which bias across the pore was varied from -200 to 200 mV and the ionic current change is noted (detailed procedure is described in the methods: experimental section). The pore is cleaned and electrically conditioned till a stable base current is obtained. **Figure 4.3.a-b** shows ionic current for a voltage sweep of -200 mV to 200 mV, through a partially blocked pore vs a properly clean pore. The current observed clearly shows higher noise fluctuations for a blocked pore. To confirm about the noise reduction, we normalized the current traces (as presented in **Figure 4.3.c**) to eliminate the voltage-effect. Pore blockade can be caused due to entrapment of nanobubbles at the pore mouth (caused due to insufficient degassing of electrolyte) which results in an unstable baseline current as observed from **Figure 4.3.c**. We further analysed the noise spectra (**Figure 4.3.d**) and observed a significant reduction of both low frequency (<1000 Hz) noise after cleaning. Pore can also be clogged by solvent residues and nanobubbles created during sensing procedures. Nanobubbles can be caused due to insufficient degassing of electrolyte or liquids involved in the cleaning process. Therefore, proper degassing and complete removal of residues is essential for resolved sensing. In case of nanopore sensing, high frequency noise is usually influenced by presence of bigger particulates in and around the nanopore. Since particulate-blockade is unlikely after piranha cleaning, we do not observe any significant reduction of high-frequency noise (>1000 Hz) between the clean and blocked pore.

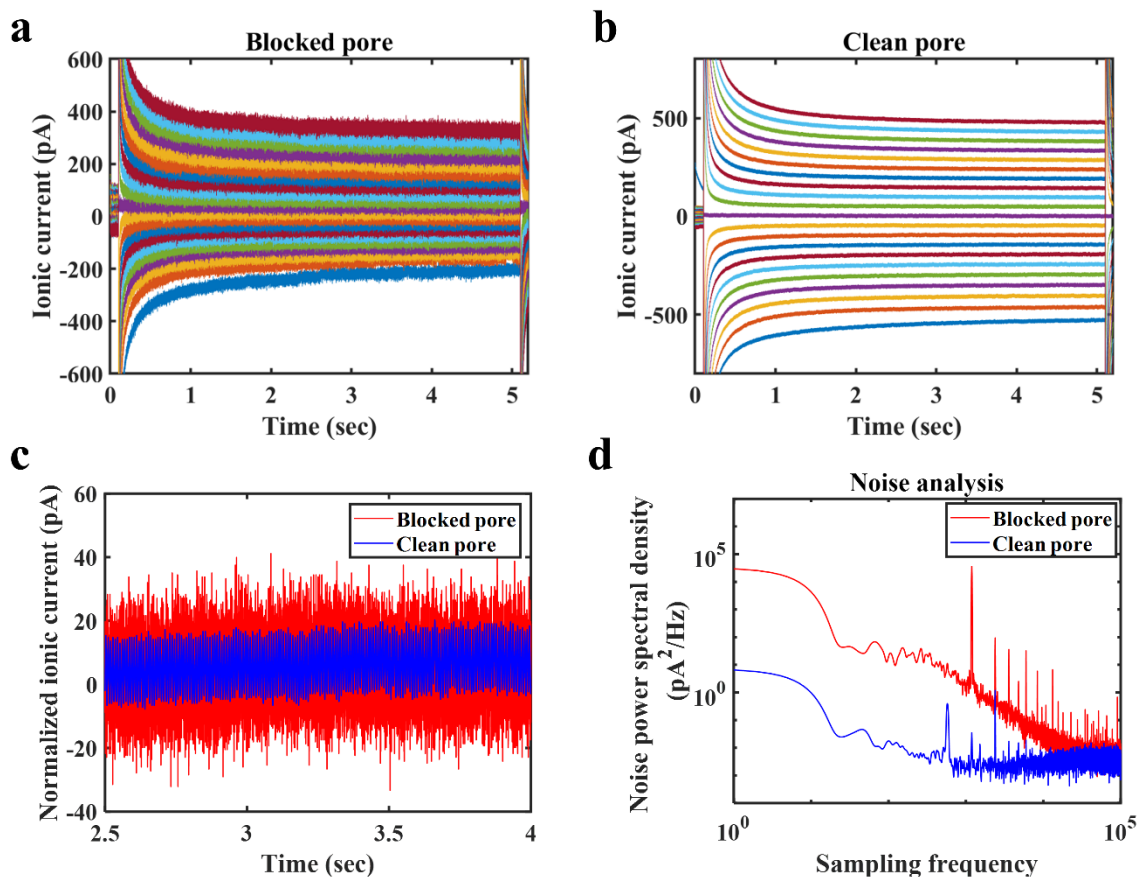


**Figure 4.3.** Ionic current for -200 mV to 200 mV voltage sweep for (a) a blocked pore and (b) a clean pore, (c) Normalized ionic current showing lower noise fluctuation amplitude for clean pore and (d) noise power spectra for the blocked and clean pore showing reduced low frequency noise for the clean pore, which may be caused by solvent residues or nanobubbles created during measurements.

A COMSOL geometry mimicking the original measurement cell assembly is modelled for accurate prediction of nanopore structure. Detailed information about the simulation process is discussed in methods: simulation section. The pore current is measured 20 times on each pore and the experimental I-V is plot against the simulated I-V for the predicted pore geometry. The experimental I-V profile was compared with simulated profiles of different pore geometries. For

a single comparison, the smallest pore diameter is kept constant and top ( $\alpha_1$ ) and bottom ( $\alpha_2$ ) cone angles are varied for a constant 10 nm thick cylindrical zone. **Figure 4.4.a-f** presents the experimental and simulated I-V fit, denoting the prediction accuracy.

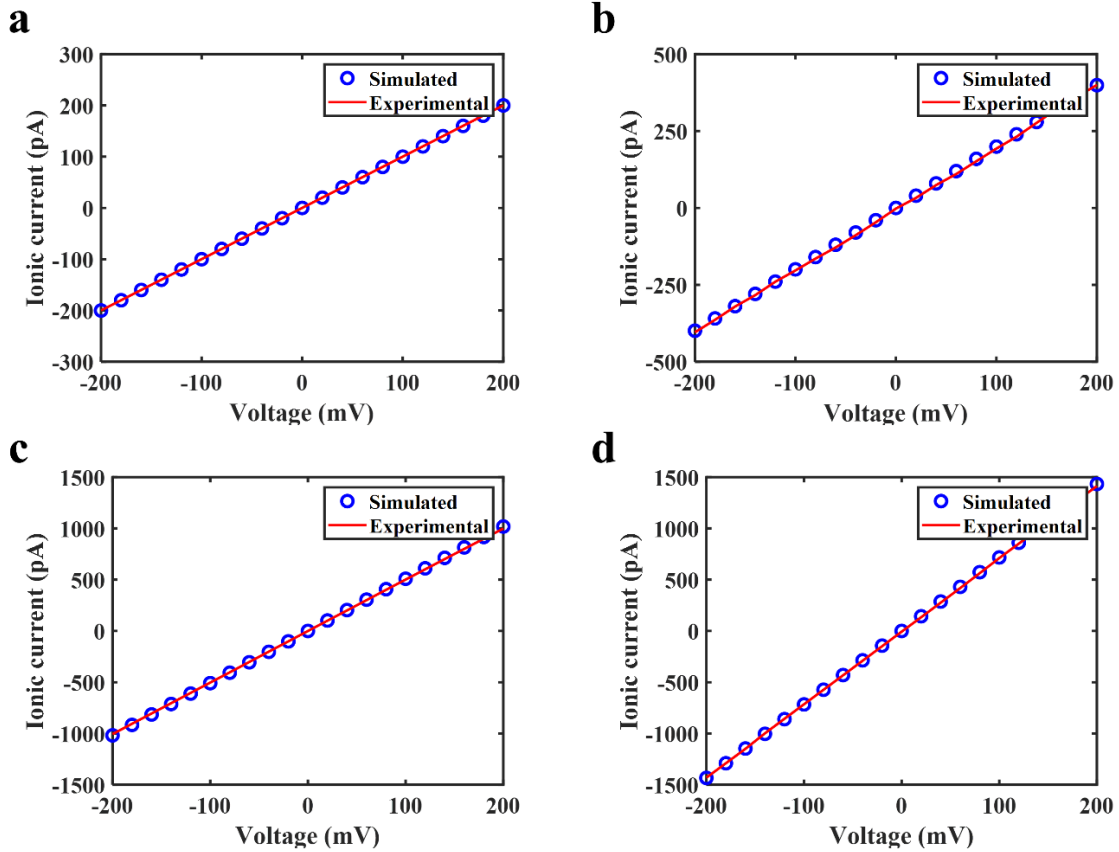


**Figure 4.4.** Experimental (first reported measurement) and simulated IV plots for (a) 2.5 nm, (b) 4.2 nm, (c) 5.6 nm and (d) 8.0 nm showing a good fit for the experimental to simulated conductance and ionic response.

**Table 4.2.** shows the conductance of the pores, extracted from the slope of experimental and simulated curves. The small deviation (error) can be due to difference in surface charge values.

<b>Experimentally measured starting pore diameter (nm)</b>	<b>Top cone angle, <math>\alpha_1</math> (degree)</b>	<b>Bottom cone angle, <math>\alpha_2</math> (degree)</b>	<b>Simulated conductance (nS)</b>	<b>Experimental conductance (nS)</b>	<b>Error (%)</b>
2.5	6.0	5.5	1.00025	1.000186	-0.006%
4.2	9.5	11.0	1.996	2.00147	-0.27%
5.6	8.0	7.0	5.092	5.00923	-1.65%
8.0	20	15.5	7.168	7.0801	-1.24%

Multiple ionic current measurements are conducted on each pore to analyse its repeatability. Before every measurement the pore is cleaned in hot piranha and wetted (under vacuum) in ethanol and then KCl, to analyse the effect of chemical treatment on the pore geometry. At the simulated angles, the radius is then varied to figure out the change in pore size corresponding to the pore conductance changes owing to multiple treatments. The measured ionic conductance for each pore after repeated cleaning were then matched with simulated conductance for different pore diameters keeping top ( $\alpha_1$ ) and bottom ( $\alpha_2$ ) cone angles constant for a single pore. This was done to determine the change in the pore diameter each pore suffers due to repeated chemical cleaning and measurement steps. **Figure 4.5** shows the measured ionic conductance over 20 cleaning steps. The

variation of diameter for the same pore was obtained by comparing the measured and the simulated conductance.

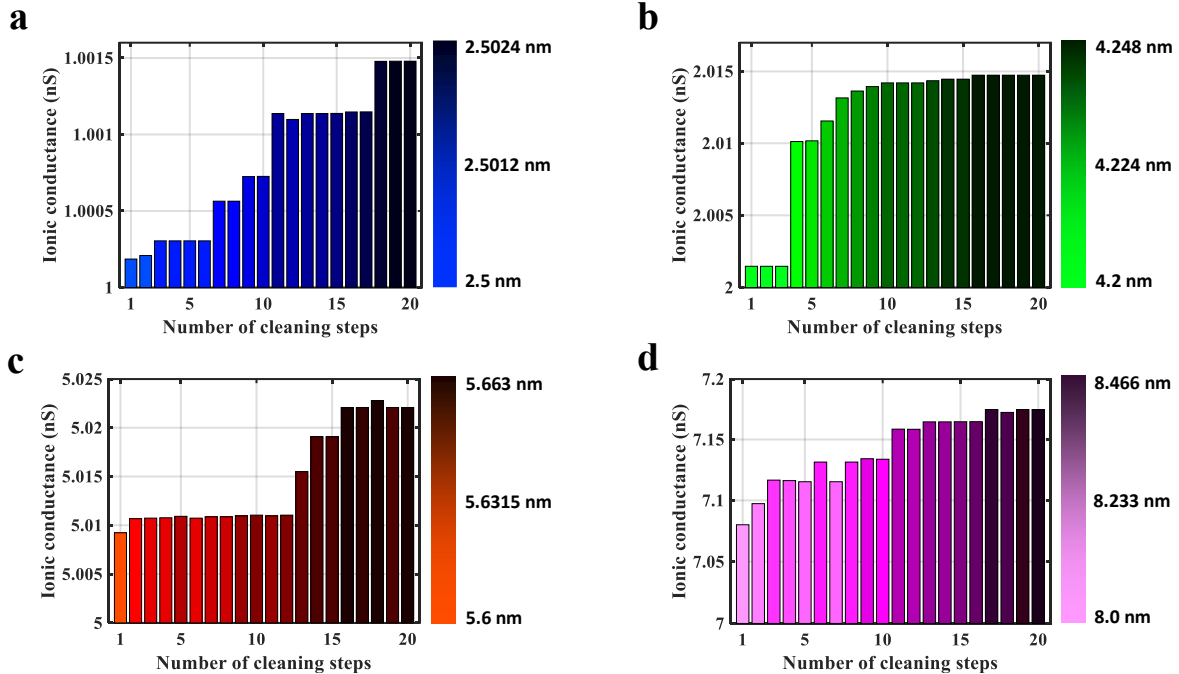


**Figure 4.5.** Measured ionic conductance after repeated pore cleaning and measurements through nanopores having (a) 2.5 nm, (b) 4.2 nm, (c) 5.6 nm and (d) 8.0 nm diameters. The bar plots show experimentally measured ionic conductance variation for each pore across 20 repeated measurements, each bar being mapped according to the color bar presented on the right of each plot showing the variation of characteristic nanopore diameter as estimated and extracted from simulation study. The color-bars show the nanopore diameter variation corresponding to the color gradation represented in the bar plots.

The corresponding change in nanopore diameter as deduced from the comparative simulation study is then analysed. **Table 4.3** shows the experimental and simulated starting diameters and change in diameter after 20 measurements for each of the four reported nanopores.

**Table 4.3.** Variation of nanopore diameter after 20 repeated pore cleaning and ionic conductance measurements.

<b>Experimentally measured starting pore diameter (nm)</b>	<b>Top cone angle, <math>\alpha_1</math> (degree)</b>	<b>Bottom cone angle, <math>\alpha_2</math> (degree)</b>	<b>Simulated pore diameter after first conductance measurement</b>	<b>Largest diameter after 20 measurements</b>	<b>Increase in nanopore diameter</b>
2.5	6.0	5.5	2.5	2.5024	0.4%
4.2	9.9	11.2	4.2	4.248	1.13%
5.6	8.0	7.0	5.6	5.663	1.112%
8.0	20	15.8	8.0	8.466	5.43%

We observe an increasing trend for the change in ionic conductance and therefore nanopore diameter with repeated cleaning steps. The increase in pore diameter is observed to be the least ( $<0.1 \text{ \AA}^0$ ) for the smallest pore (Starting diameter: 2.5 nm). For 4.2 nm and 5.6 nm pores, the increase is found to be greater than  $0.1 \text{ \AA}^0$  but less than  $1 \text{ \AA}^0$ . However, a huge variation of diameter ( $\sim 5 \text{ \AA}^0$ ) is observed for the 8 nm nanopore. The results suggest that the nanopore suffers from higher size change for the same number of cleaning steps, with increase in pore diameter.

## 4.6 Discussions

Fabricating and maintaining a thermo-mechanically stable and clean nanopore is crucial for developing a reusable and cost-effective nanopore sensor. We observed that while piranha clean

can reduce high frequency noise due to bigger particulates. However, degassing and residue-removal is also essential to remove low frequency noise for obtaining a well-resolved signal. The sensing resolution and analysis accuracy also depends highly upon the nanopore geometry and effective cross-sectional diameter. Silicon nitride nanopores despite having amazing thermo-mechanical stability, are prone to size (and therefore ionic conductance) variation due to TEM beam irradiation, piranha etching, applied bias and erosion or deposition in salt-solution. Studies show that closer the nanopore size to the TEM beam resolution, higher is the mechanical stability of the nanopore. This is because as the TEM beam irradiates to create a nanopore, it also creates a nitrogen-depleted defect ring around the nanopore [43]. Larger the nanopore, the irradiation may create a silicon-rich wider ring which dissolves in electrolyte solution. This increases the probability of nanopore expansion along the weak boundaries due to etching or dissolution [43], [207]. This may be the reason behind increased expansion of the larger nanopores, as seen from **Table 4.3**. Our inference matches previous study [43] conducted on testing pore stability by leaving it in salt solution for long period of time. Our study mimics the sensing scenario by taking into consideration piranha cleaning and conductance measurement steps, which are essential before detection to ensure a clean, conducting and electrically conditioned pore. Our results therefore suggest that using smaller ( $<3$  nm) nanopores not only can increase spatial resolution of sensing but also improve its pore reusability and sensing repeatability.

## Chapter 5 <sup>2</sup>(Paper 2)

**This chapter** presents a simulation study to compare the performance of Silicon nitride and MoS<sub>2</sub> (monolayer and multilayer) nanopores in sensing DNA and therefore select membrane and sensor properties suitable for realizing a sensor capable of molecular sensing with high spatial and temporal resolution.

### **5 Understanding molecular electrokinetic behaviour through monolayer and multilayer MoS<sub>2</sub> nanopores**

*Payel Sen and Manisha Gupta\**

Payel Sen

Department of Chemical and Materials Engineering

University of Alberta

Edmonton, Canada

Email: [payel@ualberta.ca](mailto:payel@ualberta.ca)

Manisha Gupta

Department of Electrical and Computer Engineering

University of Alberta

Edmonton, Canada

---

<sup>2</sup> Manuscript under preparation (Preprint: P. Sen, H. Hoi, D. Nandi, and M. Gupta, “Highly accurate random DNA sequencing using inherent interlayer potential traps of bilayer MoS<sub>2</sub> nanopores,” 2020, doi: 10.1101/2020.04.21.053595)

Email: [mgupta1@ualberta.ca](mailto:mgupta1@ualberta.ca)

## 5.1 Keywords

Sensing resolution, Membrane material, Molecular kinetics, Alignment, Blockade conductance

## 5.2 Introduction

Nanopore integrated biosensors have emerged as a new technology in molecular sensing. It involves blockade current identification of the molecule caused by obstruction at the nanopore during its translation. Target molecules are electrophoretically driven through nanopores and are electrically detected from the ionic current fluctuations during their entry and passage through the nanopore. Considering DNA sequencing, each nucleotide (nt) base (adenine, thymine, cytosine, and guanine) have distinct chemical properties. These distinguishable characteristics lead to difference in electrical current measurement that offers a base-specific information readout of the DNA [208].

In contrast to biological nanopores, DNA sequencing is faster using solid-state nanopores. For solid-state nanopores, DNA sequencing optimally occurs at  $1\text{-}50\text{ nt ms}^{-1}$ . The higher sequencing speed in solid-state nanopores is due to the lower pore size range (2-25 nm) and the applied bias voltage (100-800 mV) [51]. The increased sequencing speed limits the sensing resolution, which is the major bottleneck of solid-state DNA sequencing [116], [187], [209]. Relatively controlled DNA transport was achieved with nanopores engineered via mutagenesis, targeted chemical functionalization and enzyme incorporation [156], [210], [211].

Diverse challenges need to be addressed for effective detection, of which size-controlled membrane fabrication, nanopore drilling and velocity modulation of translocating molecules are

crucial for high-quality sensing [95], [212]. Single nucleotide resolution is limited by a number of factors including membrane thickness, nanopore size, membrane-biomolecule interaction, and translocation speed of the biomolecular strand. The membrane thickness is inversely proportional to its capacitance, which determines its ability to separate charges efficiently [95]. Moreover, the membrane thickness governs the pore height which in turn dictates the sensing length. Hence, thinner the membranes, better is the spatial resolution and signal to noise ratio. A thinner membrane also offers an easier platform for nanopore drilling of size as small as a single nucleotide, thus improving the detection accuracy. These thinner membranes can be achieved using the insulating materials like silicon nitride and silicon oxide but can also be achieved using 2D materials like graphene, MoS<sub>2</sub>.

Silicon nitride, the most commonly used bio-compatible semiconductor membrane material is compatible for a wide range of nanopore sizes improving the production scalability for multiplexed devices. Several methods have been proposed to overcome this challenge such as exonuclease-assisted which can detect 5'-monophosphate molecules with 99.8% averaging accuracy and hybridization-assisted sequencing [52], [116], [213]. These methods involved improvement of biocompatibility of the nanopores by enzyme or oligonucleotide modification. However, higher thickness of the membranes compared to molecular dimensions (~1 nm), makes highly resolved and sensitive detection difficult. Fabrication of SiN<sub>x</sub> membranes as low as 3 nm thickness by polycrystalline silicon sacrificial layer method has been reported [90], [214]. However, decreased nitride thinning leads to increased probability of membrane damage and thickness non-uniformity. This hindrance to detections calls for strong yet thinner materials like 2D materials.

2D materials are materials with interlayers separated by weak van der Waals force. They can thus be implemented as a membrane material to resolve the single-nucleotide resolution issues due to

monolayer separation properties offering thinner yet robust membranes with greater size reproducibility of the nanopore [215]–[217]. The passage of a biomolecule hence creates a significant change in the ionic current density through the nanopore, with the change in density increasing with decrease in membrane thickness.

Graphene, as a 2D material has continued to get attention in nanopore sequencing as a membrane material due to its atom-thick membrane fabrication feasibility to distinguish single nucleotides, and its mechanical strength and durability. Activities of graphene transistors and biosensors have been achieved. The adhesion of proteins with graphene at the nanopore due to dangling bonds and the interference of conductive nature of graphene with ionic current however pose challenges in smooth DNA translocation and detection [161], [209], [218], [219]. On the other hand, transition metal dichalcogenides or TMDs ( $\text{MX}_2$  type) have a transition metal ( $\text{M} = \text{Mo}, \text{W}, \text{We}, \text{etc.}$ ) layer sandwiched between two chalcogen ( $\text{X} = \text{S}, \text{Se}, \text{T}, \text{etc.}$ ) layers. They inherit all basic 2D material properties but differ from graphene by a finite bandgap making them suitable for semiconductor-based studies at room temperature [128], [215]–[217], [220], [221].

A good sensitivity is achieved if a single molecule can be sensed in presence of contaminants. The sensitivity or signal to noise ratio mainly depends upon the surface property interaction of membrane and analytes as well as the membrane thickness, which decides the sensing length. Hence, selection of a suitable biocompatible semiconducting membrane is crucial. In this work, COMSOL Multiphysics Simulation was performed to affirm 2D materials to be a good material for sensitivity improvement compared to  $\text{SiN}_x$  [216]. Electrophoretic movement of nanoparticles like organic polymers, proteins, and DNA through a nanopore in response to an external electric field can distinctly change the ionic current through the nanopore. This current modulation provides a platform for detection of these nanoparticles for bioanalysis. Molecular dynamics (MD)

simulations are commonly performed to provide insights into atomic-level dynamics and hence change in molecular conformations (such as DNA) during its translocation through the nanopore. They are suitable for simulation molecular configurations, chemical interactions and capturing events occurring within the nanopore, usually instantaneous or over a short span of time ( $\sim$ ns- $\mu$ s). On the other hand, COMSOL Multiphysics simulation with a continuum-based approach is a faster and more suitable approach for monitoring dynamics of molecular translocation through and away from the nanopore i.e. simulate data over a longer time range ( $\sim$  $\mu$ s-ms). Model definition by COMSOL is also simpler and perfect for initial estimations and comparative studies. Moreover, the translocation phenomenon is highly influenced by the imposed electric field which may cause sudden molecular accelerations and velocity fluctuations, which are better captured through a broader scope of COMSOL Multiphysics as found in previous literature [128], [210], [219], [222], [223].

The effect of change in membrane thickness, surface charge and electric field interactions are simulated on the electro-kinetics of DNA and flow properties of the system. This offers an insight into the various factors that affect the sensing resolution of nanopore sequencing. These factors were compared for 50 nm Silicon nitride ( $\text{SiN}_x$ ) and 1-5 layers of Molybdenum disulphide ( $\text{MoS}_2$ ) and a material and thickness suitable for obtaining a good sensing resolution (spatial and temporal) was selected through step-wise optimizations.

### **5.3 Methods**

The DNA translocation velocity can be determined along the nanopore axis, by a quasi-static approach from the force balance on the particle during its electrokinetic transport. In this study,

steady state and transient continuum-based models are developed, taking into consideration the translational dynamics of the molecule.

### 5.3.1 Model definition

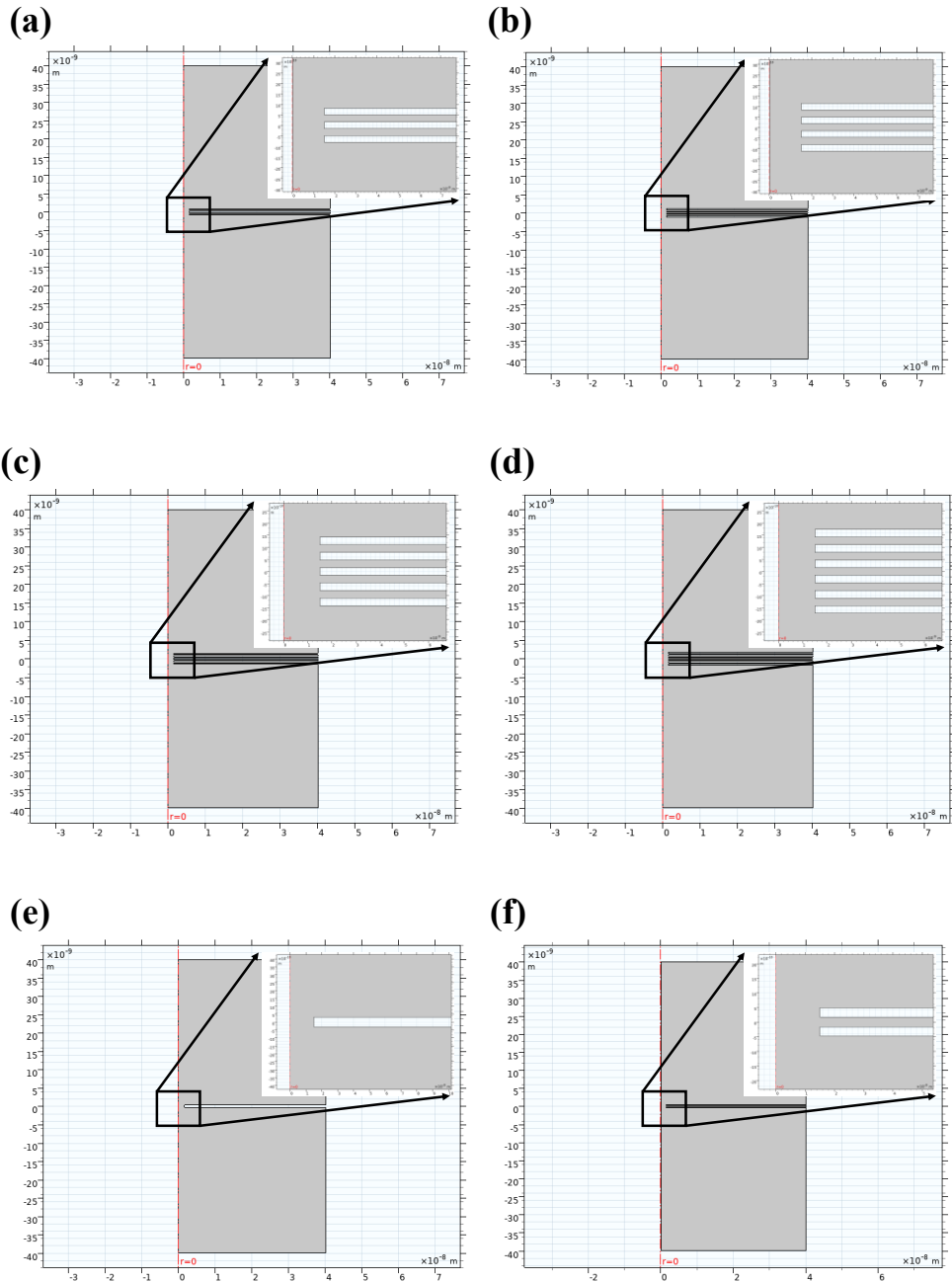
#### 5.3.1.1 For blank pore ionic conductance simulation

A 2D axisymmetric model is used to evaluate the ionic conductance through nanopores defined on  $\text{SiN}_x$  and different layer  $\text{MoS}_2$  membranes, owing to the axisymmetric behaviour of the nanopore electrochemical system. In addition, axisymmetric model helps in realizing a 3D revolved geometry for accurate calculation of the ionic conductance over the nanopore plane.

For  $\text{MoS}_2$ , different (1-6 layers) membranes are defined with each layer having a thickness of 0.314 nm and interlayer distance of 0.336 nm i.e. monolayer having one 0.314 nm layer, 3-layers having 3 layers of 0.314 nm thickness and 0.336 nm interlayer distance; and so on till 6 layers. Cylindrical nanopores having uniform diameter of 3 nm are considered on the membrane for ionic conductance calculation through it. Two reservoirs containing the electrolyte, each having a size of  $80 \times 80$  nm is considered. **Figure 5.1.(a-f)** shows simulation models used for 1-6 layers of  $\text{MoS}_2$  nanopores.

For  $\text{SiN}_x$ , hour-glass shaped nanopores are defined on 50 nm thick membrane. Two reservoirs containing the electrolyte, each having a size of  $5 \times 5$   $\mu\text{m}$  is considered. A conical geometry is considered for the nanopore with diameter progressively increasing from 3 nm in steps of 1.5 nm every 10 nm pore thickness. This is done because mainly two types of geometries are probable for thick membranes like  $\text{SiN}_x$ , hour-glass shape and conical. Conical nanopores provide comparatively higher conductance due ion current rectification. Therefore, for the purpose of selecting the material with the highest conductance, we selected  $\text{SiN}_x$  nanopore with the geometry

choice providing the highest conductance. **Figure 5.1.(g)** shows simulation models used for 50 nm  $\text{SiN}_x$  nanopore.



(g)

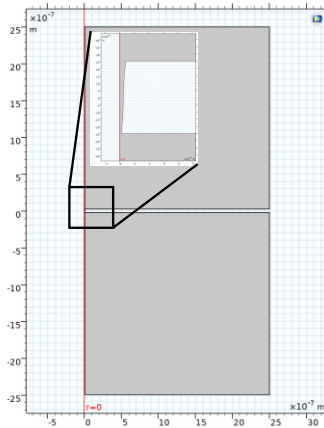


**Figure 5.1.** 2D axis-symmetric models used for simulations representing (a) 1-layer, (b) 2-layers, (c) 3-layers, (d) 4-layers, (e) 5-layers, (f) 6-layers MoS<sub>2</sub>, and (g) 50 nm SiN<sub>x</sub> nanopores each having a characteristic diameter of 3 nm with each having an inset figure showing the membrane area zoomed in.

### 5.3.1.2 For DNA electrokinetic simulation

A 2D model (no symmetry assumed) is adopted to simulate the electrokinetic behaviour of the nanoparticle (DNA in this study) towards, through and away from the nanopore realized on different membranes. The symmetry axis of an axis-symmetric model fails to capture the scenario and the mesh distortion which occurs during particle translocation. Therefore, a full 2D model is required for accurate replication of the particle motion, in this case. **Figure 5.2** shows simulation models used for 1-4 layers of MoS<sub>2</sub> nanopores having a diameter of 3 nm with the leading end of the polynucleotide defined 10 nm away from the nanopore at the compartment kept grounded.

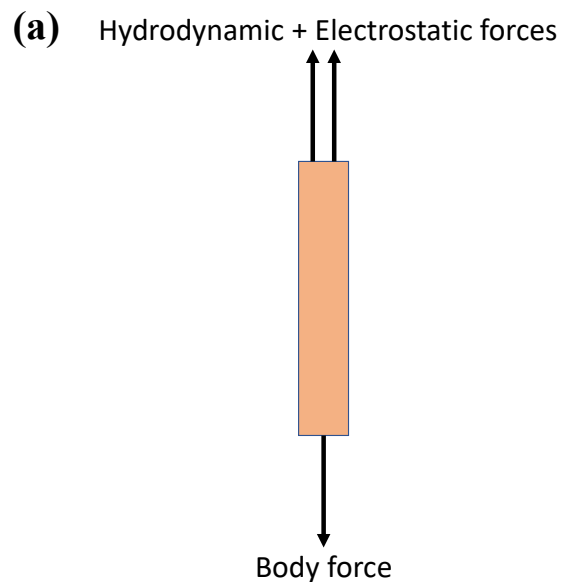


In this study, a transient continuum-based model is employed. The physics is captured by considering Nernst Planck equations for ionic (electrolyte) transport, Navier Stokes for the laminar fluid flow (for low Reynold's number considering water as a solvent), Poisson's equation to evaluate the effect of external electric field; followed by geometry deformation to represent the particle translational and simultaneously calculate translocation dynamics.

The parameter values used, and physics is explained in detail in **Chapter 3**.

## 5.4 Results and Discussions

Ionic conductance through 1-10 nm diameter pores was first simulated using COMSOL Multiphysics 5.4, for different membrane types: 1-6 layers MoS<sub>2</sub> (0.65-4 nm thick), 50 nm SiN<sub>x</sub> and 76-layers MoS<sub>2</sub> having thickness (49.4 nm) similar to that of SiN<sub>x</sub> membrane. This was carried out using the geometry presented in **Figure 5.1**.



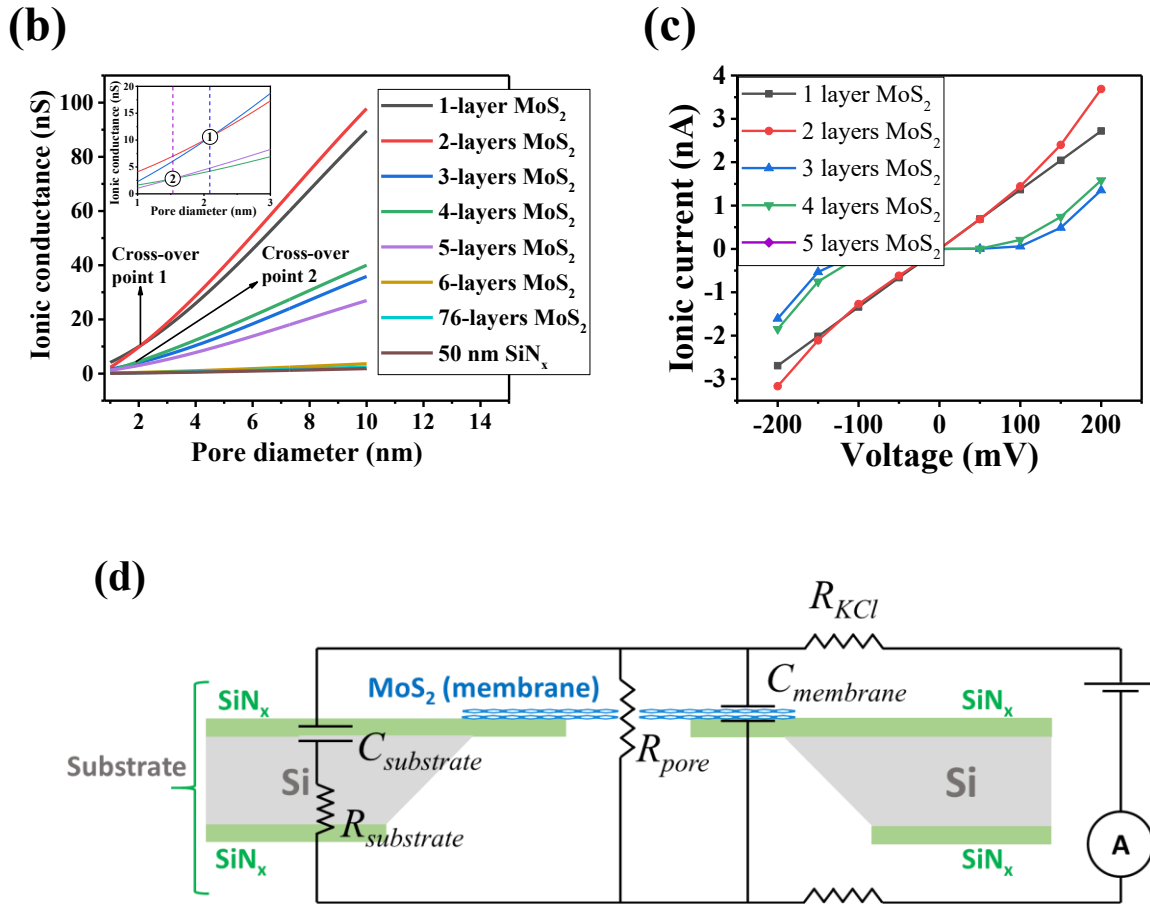


**Figure 5.3.** (a) Simple schematic representation of the force balance used for simulating DNA translocation electro-kinetics through nanopores, (b) Simulated ionic conductance of 1-6 layers MoS<sub>2</sub> (thickness range: 0.65-4 nm), 50 nm thick SiN<sub>x</sub> and 76-layers MoS<sub>2</sub> (thickness: 49.4 nm), showing cross-over points, Cross-over 1 indicates the diameter beyond which ionic conductance for 2-layers thick MoS<sub>2</sub> nanopore is higher than 1-layer thick MoS<sub>2</sub>. Similarly, above cross-over point 2, the ionic conductance through 4-layers thick MoS<sub>2</sub> pore is found to be greater than that for 3-layers thick MoS<sub>2</sub>; inset showing the cross-over points clearly: data reported for -200 mV to 200 mV trans bias and 300 mM KCl (c) Simulated I-V profile for 1-4 layers thick MoS<sub>2</sub> (shortlisted from ionic conductance comparison) for 2.5 nm pore diameter (greater than cross-over point 1), showing highest non-linearly varying I-V response demonstrated by 2-layers thick MoS<sub>2</sub>:

simulation conducted for -200 mV to 200 mV bias range and 300 mM KCl, (d) Representative nanopore circuit showing the active capacitance and resistances.

**Figure 5.3.(a)** shows the primary forces acting on the translocating particle, which are considered for evaluating its velocity and blockade conductance. Ionic conductance of 1-5 layers thick MoS<sub>2</sub> 2.5 nm diameter nanopore is found to be ~14 times higher than same sized pore on 50 nm thick SiN<sub>x</sub> membrane (**Table 5.1**). Thus, there is better surface charge interaction along thinner pore walls, stating that a better signal can be anticipated by using MoS<sub>2</sub> nanopores. The ionic conductance of MoS<sub>2</sub> nanopores is seen to decrease with increase in the number of layers and beyond 5-layers, the ionic conductance is found to be very close to that of 50 nm SiN<sub>x</sub>. The comparison suggests that 1-4 layers thick MoS<sub>2</sub> nanopores with diameters > 2 nm are good alternatives to SiN<sub>x</sub> for maximizing ionic conductance (**Table 5.1**).

**Table 5.1.** Simulation results for drawing an ionic conductance-based comparison between different type of nanopores (1-6 layers thick MoS<sub>2</sub>, 76-layers thick MoS<sub>2</sub> and 50 nm thick SiN<sub>x</sub>) for 200 mV bias and 300 mM KCl. The ionic conductance for different nanopore types having 2.5 nm diameter are listed. The diameters at cross-over points 1 and 2 (extracted from **Figure 5.3.(b)**) are also numerically mentioned below.

Nanopore type	Membrane thickness	Cross-over points	Ionic conductance
1-layer thick MoS <sub>2</sub>	0.65 nm	Point 1: 2 nm diameter	13.48 nS
2-layers thick MoS <sub>2</sub>	1.3 nm		14.12 nS
3-layers thick MoS <sub>2</sub>	1.9 nm	Point 2: 1.5 nm diameter	5.39 nS

4-layers thick MoS <sub>2</sub>	2.6 nm		6.33 nS
5-layers thick MoS <sub>2</sub>	3.8 nm		4.05 nS
6-layers thick MoS <sub>2</sub>	5.2 nm	—	0.57 nS
76-layers thick MoS <sub>2</sub>	49.4 nm	—	0.37 nS
50 nm thick SiN <sub>x</sub>	50 nm	—	0.28 nS

The I-V behaviour for the selected 1- 4 layers thick MoS<sub>2</sub> pores with applied bias from -200 mV to 200 mV in 300 mM KCl was then simulated. 1-layer thick MoS<sub>2</sub> pores demonstrate a linear I-V curve as compared to the 2-4 layers thick MoS<sub>2</sub> pores show non-linear behaviour (see **Figure 5.3.(c)**). It was found that I-V profile tends to become more non-linear with increasing number of layers. The ionic conductance trend and I-V response (**Figure 5.3.(b-c)**) observed by COMSOL Multiphysics simulation can be best explained by utilising a Resistance (R) – Capacitance (C) equivalent model for the nanopore (**Figure 5.3.(d)**). The nanopore acts as a resistance (R) and membrane along with the electrolyte is the capacitance (C). The current variation with respect to resultant impedance (Z) can therefore be studied (see **Equation 5.1**).

**Equation 5.1.**  $Z^2 = R^2 + \frac{1}{(\omega C)^2}$ , where,  $\omega$  is the phase change

The Cross-over points 1 and 2 indicate the diameters above which the capacitance is dominant as compared to the pore resistance, which reduces the impedance, thus causing a rise in ionic conductance. It is also important to note that this behaviour is highly dependent on the applied bias (greater than 50 mV in this case as seen in **Figure 5.3.(c)**). In case of 1-layer thick MoS<sub>2</sub>, the pore resistance dominates the impedance producing a linear I-V (**Figure 5.3.(c)**). For smaller pores (~1-

2 nm diameter), due to higher pore resistance, the impedance increases, thus reducing the ionic current (**Figure 5.3.(c)**). With increase in the number of layers, an interlayer potential gradient along the MoS<sub>2</sub> interfaces causes accumulation of ions therefore producing a capacitance [224], [225]. Hence, the resultant impedance has a contribution from the membrane-based interlayer and intralayer charge storage, electro-activity caused by pseudo-capacitance and the pore resistance [224], [225]. As a result, an increase in I-V is observed above a certain applied voltage indicating an increased conductance (**Figure 5.3.(c)**).

Then, to understand sensing performance of 1-4 layers MoS<sub>2</sub> nanopores, the kinetics for translocation of the same analyte DNA were then simulated using 300 mM KCl electrolyte using geometry presented in **Figure 5.4**.

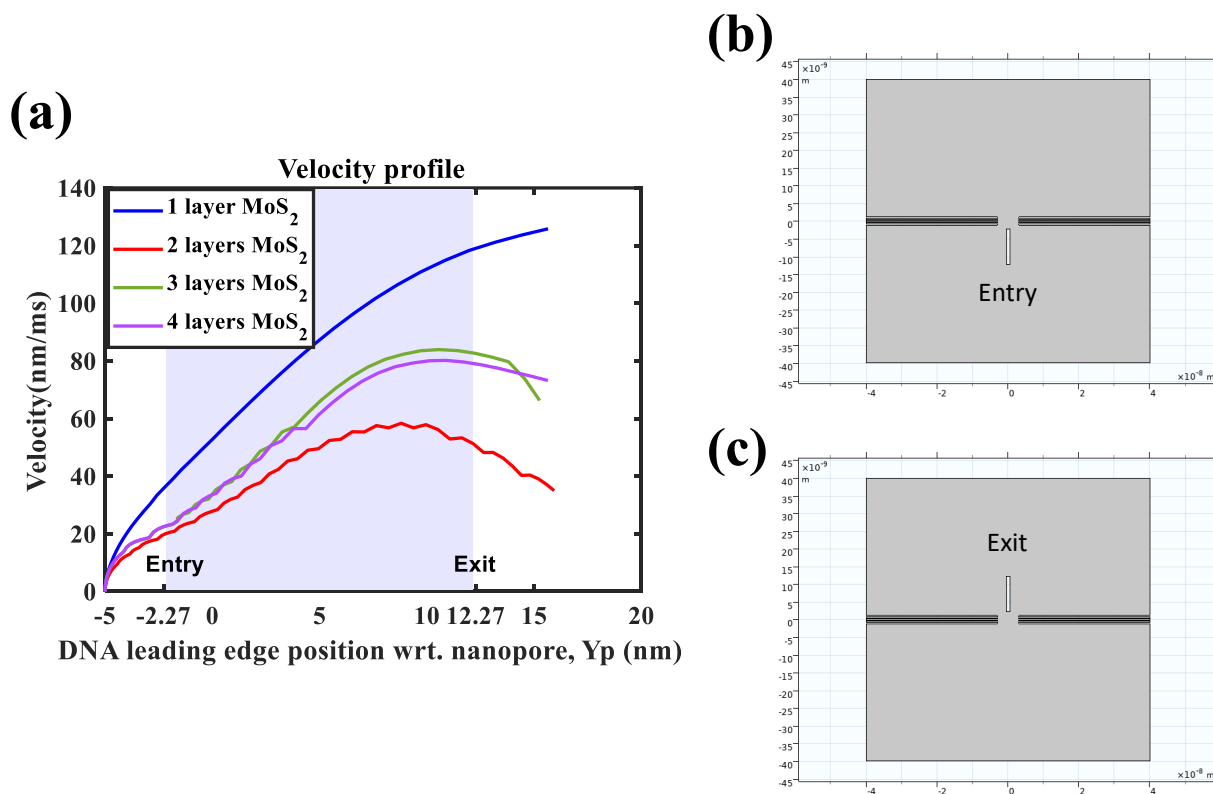


**Figure 5.4.** (a) Velocity profiles of the translocating 10 nm long polyadenine molecule through 1-4 layers MoS<sub>2</sub> nanopores, with the highest possible nanopore area (i.e. for 4 layers) marked

according to (b-c) which presents corresponding geometry showing the DNA position at its entry and exit to/from the nanopore.

First the velocity profile of the translocating polyadenine molecule is analysed. **Figure 5.4.(a)** shows the velocity variation with respect to the DNA position ( $Y_p$ ) and **Figure 5.4.(b-c)** show the position of the DNA at its entry and exit to/from the nanopore for 4 layers (which is the highest membrane thickness when 1-4 layers MoS<sub>2</sub> nanopores are compared). According to **Figure 5.4.(b-c)**, the nanopore area is marked in blue in **Figure 5.4.(a)**. It is observed that the peak velocity varies as 1 layer > 3-layer > 4-layer > 2-layer suggesting that translocation is slowest for BL MoS<sub>2</sub> nanopore. This may be due to the best electric field confinement offered by two biased MoS<sub>2</sub> layers compared to >2-layers. 1 layer, on the other hand shows the highest velocity, which may be due to the least surface charge interaction occurring at the ultrathin nanopore (thickness  $\ll$  nucleotide dimension). However, it is found that the velocity profile attains its peak far quite later to DNA entry into the nanopore. To better understand the role of nanopore charge interaction in slowing down DNA translocation, the rate at which velocity varies within the nanopore needs to be analysed.

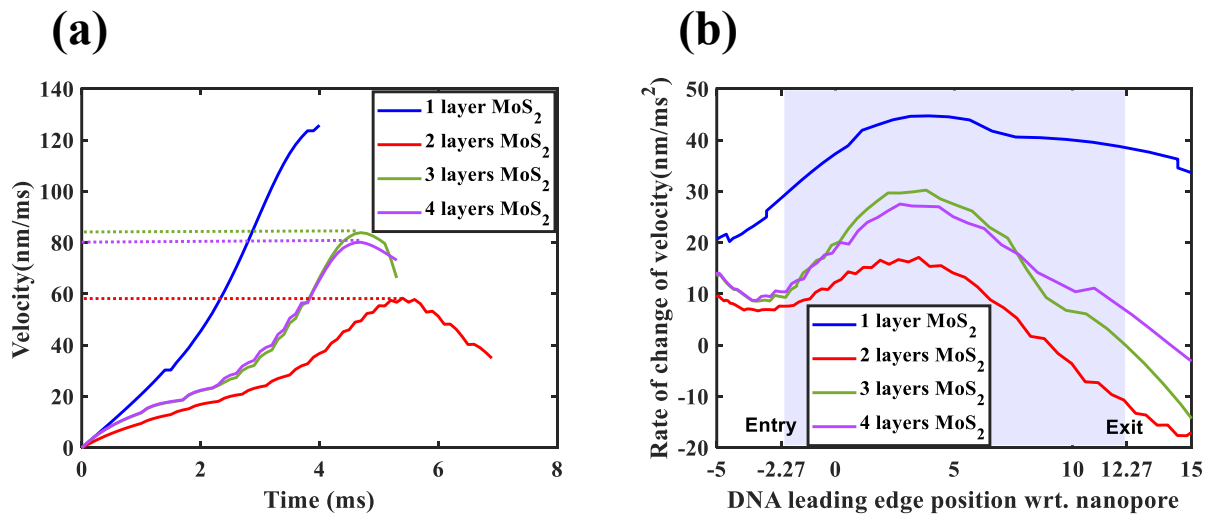


**Figure 5.5.** (a) DNA velocity vs translocation time plot showing 2-layers MoS<sub>2</sub> nanopore demonstrating least velocity and (b) Evaluated rate of change of velocity plot with respect to DNA position showing the effect of nanopore on the reduction of DNA velocity.

We therefore first plot the velocity vs the translocation time (**Figure 5.5.(a)**) and then evaluated the acceleration/retardation experienced by the DNA during its passage through the nanopore. **Figure 5.5.(b)** shows that for all (1-4 layers) MoS<sub>2</sub> nanopores, DNA is retarded as soon as it enters the nanopore, as depicted by the reduction in rate of change of velocity. However, in case of 1-layer MoS<sub>2</sub> nanopore, the retardation is the least whereas 2 layers nanopore provided the most retardation. From these results, we can confidently infer that 2 layers MoS<sub>2</sub> nanopore can successfully slow down DNA translocation compared to 1 layers or > 2 layers nanopores. To comment on the effect of number of MoS<sub>2</sub> layers on dwell time/ time resolution of molecular detection, we analysed the blockade current produced by the translocating DNA.

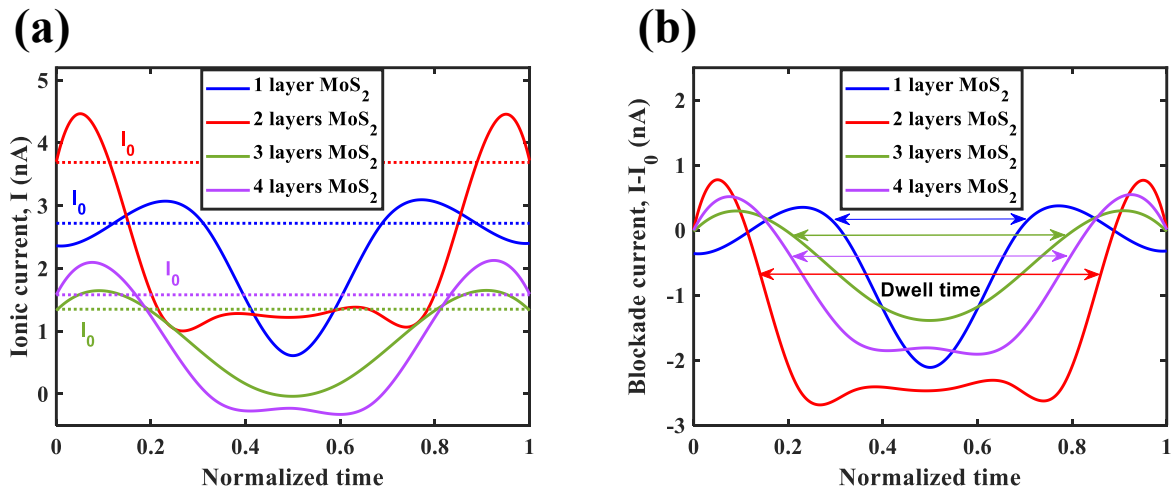


**Figure 5.6.** (a) Ionic current,  $I$  vs normalized time trace for DNA translocation through 1-4 layers MoS<sub>2</sub> nanopores, and (b) Blockade current (evaluated as Ionic current,  $I$  – Baseline current,  $I_0$ ) vs normalized time plot showing blockade current magnitude varying as 3 layers < 4 layers < 1 layer < 2 layers and dwell time varying as 1 layers < 3 layers < 4 layer < 2 layers.

First we plot the obtained ionic current ( $I$ ) vs translocation time trace (during DNA entry and exit), as presented in **Figure 5.6.(a)**. We observed different magnitudes of baseline current ( $I_0$ ) for the different nanopores ( $I_0 = 2.72$  nA for 1 layer, 3.69 nA for 2 layers, 1.35 nA for 3 layers and 1.58 nA for 4 layers MoS<sub>2</sub>), as shown by dotted lines in **Figure 5.6.(a)**. The magnitude of baseline current,  $I_0$  is found to differ (in the same way as observed in **Figure 5.3.(b)**), which makes direct comparison of blockade current from **Figure 5.6.(a)** difficult. In order to infer on the molecular blockade current resolution, we evaluated the blockade current ( $I-I_0$ ) variation and also noted the dwell times for each, as plot in **Figure 5.6.(b)**. Blockade current magnitude is found to vary as 3 layers < 4 layers < 1 layer < 2 layers MoS<sub>2</sub> whereas dwell time is found to vary as 1 layers < 3 layers < 4 layer < 2 layers MoS<sub>2</sub> nanopores. From the simulation results, it is clearly seen that 2 layers MoS<sub>2</sub> nanopore can improve the temporal resolution (due to highest dwell time) of sensing while producing signals with a good signal-to-noise ratio (due to highest blockade current).

## 5.5 Discussions

The simulation comparison drawn between the behaviour of different membrane materials provide the necessary support behind the choice of MoS<sub>2</sub> as the membrane material. Molecular immobilization and residence at the nanopore and ionic current change specific to single molecule can be studied from the simulation results.

Blank nanopore ionic conductance study showed that 2.5 nm diameter nanopore demonstrate ~14 times higher conductance than 2.5 nm pore on 50 nm thick SiN<sub>x</sub> membrane. This can be directly related to the higher surface charge of MoS<sub>2</sub> (-0.031 C/m<sup>2</sup> at pH~7) compared to that of SiN<sub>x</sub> (-0.02 C/m<sup>2</sup>) and also thinness of MoS<sub>2</sub> nanopores compared to SiN<sub>x</sub>. Normally, in case of 3D membranes the ionic conductance reduces with increase in membrane thickness. However, the

behaviour is different for 2D materials like MoS<sub>2</sub>. This is because of its layered property. van der Waals force also acts only at the interface of two layers, so is active only for more than a single layer. The membranes being free-standing, van der Waals has no role for 1-layer MoS<sub>2</sub> nanopore. This prominently distinguishes multilayer from monolayer nanopores. So, for 3 layers MoS<sub>2</sub> nanopore (for example), the membrane is not a 2.6 nm (theoretical thickness of 4 layers MoS<sub>2</sub>) thick continuous membrane; instead it is a membrane composed of four 0.314 nm thick membranes with 0.336 nm van der Waals gap between every two layers. This 0.336 nm nanochannels in between the layers, present within the nanopore distinguish their behaviour from continuous 3D membranes. When normally for 3D membranes, the nanopore only acts as a resistance, for 2D membranes the interlayer electric field gradient gives rise to capacitive nanochannels favouring ionic conduction (**.a-d**). However, with increase in the number of layers the resistance increases. On the other hand, the capacitive power of even layers is found to be better than the preceding odd layers (i.e. 2 layers better than 1 layer, 4 layers better than 3 layers and so on) due to greater positive potential than the negative (**Figure A- 1.a-d**). Therefore 2 and 4 layers is found to provide better ionic conductance than 1 and 3 layers respectively. We also looked into the total co-ion and counter-ion flux through the nanopore which influences nanopore conductance. We also found that the total flux (**Figure A- 2.a-d**) varies as 3 layers < 4 layers < 1 layer < 2 layers, similar to the ionic current variation trend. We therefore believe, that for 2-layers, the impedance is optimum for giving rise to maximum ionic conduction compared to most resistive 1-layer and less capacitive 3-4 layers. The ionic current trend is also found to agree with the generated potential gradient along the translocation direction (**Figure A- 3.a-d**). As a result, the generated electrostatic force is also found to vary as 3 layers < 4 layers < 1 layer < 2 layers MoS<sub>2</sub> nanopore (see **Table A- 1**). The particle (DNA) translocation velocity (which is a function of electrostatic and hydrodynamic

forces) is found to vary differently than electrostatic force. However, the hydrodynamic force (as well as the total force) varies as 1 layers < 3 layers < 4 layer < 2 layers. This is because both co-ionic and counter-ionic flow is permitted through the interlayer nanochannels as the size of  $K^+$  and  $Cl^-$  ions are less than the interlayer nanogap, which permits horizontal ionic cross-talk too. The influence of this horizontal fluid velocity component becomes more prominent with more field confinement at the nanopore. This horizontal flow is found to be greater for even layers than odd layers. We therefore believe, the improved dwell time within the nanopore is due to increased resistance offered by horizontal and vertical co-ionic repulsion to the translocating DNA. All our results conclusively suggest that 2-layer  $MoS_2$  nanopores can produce improved blockade current magnitude and temporal resolution suitable for molecular sensing and DNA sequencing.

## Chapter 6 <sup>3</sup>(Paper 3)

**This chapter** presents experimental comparison of DNA sequencing efficiency and single nucleotide detection efficiency demonstrated by monolayer MoS<sub>2</sub> and bilayer MoS<sub>2</sub> nanopores. The size, thickness, and material of the nanopores used in this chapter are as optimized by the previous two chapters i.e. **Chapter 4** and **Chapter 5**. Data relevant to this chapter outside the published work is given as **Appendix B**.

### **6 Single nucleotide detection using bilayer MoS<sub>2</sub> nanopores with high efficiency**

*Payel Sen and Manisha Gupta\**

Payel Sen

Department of Chemical and Materials Engineering

University of Alberta

Edmonton, Canada

Email: [payel@ualberta.ca](mailto:payel@ualberta.ca)

Manisha Gupta

Department of Electrical and Computer Engineering

University of Alberta

Edmonton, Canada

---

<sup>3</sup> A version of the manuscript is published as P. Sen and M. Gupta, “Single nucleotide detection using bilayer MoS<sub>2</sub> nanopores with high efficiency†,” *RSC Advances*, vol. 11, no. M1, pp. 6114–6123, 2021, doi: 10.1039/d0ra10222a.

Email: [mgupta1@ualberta.ca](mailto:mgupta1@ualberta.ca)

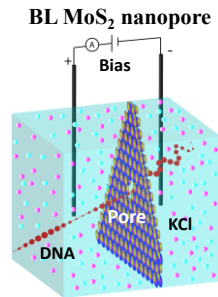
## 6.1 Keywords

MoS<sub>2</sub> nanopores, single nucleotide sensing, DNA sequencing, dwell time, efficiency

## 6.2 Abstract

Single nucleotide detection is important for early detection of diseases and for DNA sequencing. Monolayer (ML) MoS<sub>2</sub> nanopores have been used to identify and distinguish single nucleotides with good signal-to-noise ratio in the recent past. Here, we use a bilayer (BL) MoS<sub>2</sub> nanopore (~1.3nm thick) to detect distinct single nucleotides with high spatial resolution and longer dwell time. In this study, the performance of similar sized (< 4 nm) ML and BL MoS<sub>2</sub> nanopores for detection of single nucleotide has been compared. Both single nucleotide and single stranded DNA translocations through them are studied. For single nucleotide detection, we observe that BL MoS<sub>2</sub> nanopores demonstrate twice the dwell time as compared to ML MoS<sub>2</sub> nanopores with 95% confidence. Single nucleotide detection rate for BL MoS<sub>2</sub> nanopores (50-60 nucleotides/s) is five-fold higher as compared to ML MoS<sub>2</sub> nanopores (10-15 nucleotides / sec) in 10 pM analyte concentration. For single stranded DNA, we observe 89% (for 60 DNA molecules detected) single nucleotide detection efficiency with BL MoS<sub>2</sub> nanopores as compared to 85% for ML MoS<sub>2</sub>. The DNA sequencing efficiency through BL MoS<sub>2</sub> nanopore is also found to be 8-10 % better than ML MoS<sub>2</sub> nanopore, irrespective of DNA sequencing orientation. Thus, owing to improved analyte/nanopore charge interaction BL MoS<sub>2</sub> nanopores can be used for single nucleotide detection with high resolution due to longer dwell time, detection rate and efficiency.

## Table of contents



This study demonstrates the improved ability of BL MoS<sub>2</sub> nanopores in sequencing DNA with 8 - 10 % higher efficiency, two-times temporally resolved single-nucleotide current signatures and five-times higher detection rate, compared to ML MoS<sub>2</sub> nanopores.

### 6.3 Introduction

DNA sequencing data can be used for detecting hereditary diseases based on genetic information and also determine health effects of a microbial strain. DNA sequencing performed with nanopores is an important technique as it is label free and can be conducted real-time with relatively low-cost and long-read without amplification [1]. Solid-state nanopores are used extensively for DNA sequencing due to nanopore stability and ease of fabrication [2-6]. However, the sensing efficiency and resolution depend upon a lot of factors including the solid-state membrane thickness, nanopore size and material properties. A variety of materials like silicon [7], silicon oxide [8], silicon nitride [9], aluminium dioxide [10], hafnium oxide [11] have been used for sequencing DNA. In spite of being mechanically stable, sensing suffers from poor spatial resolution making them incapable of properly distinguishing four DNA bases. 2D material nanopores are rapidly emerging as a solution to improve spatial resolution due to their ultra-thinness for identifying single nucleobase [12-27].

Molybdenum disulphide ( $\text{MoS}_2$ ) is a type of 2D metal dichalcogenide that has been used in the last decade for nanopore fabrication. These  $\text{MoS}_2$  nanopores have demonstrated good DNA sequencing with low sticking of the DNA and high signal-to-noise ratio [12, 16, 20, 21]. High molybdenum (Mo) around  $\text{MoS}_2$  nanopore is favorable for the analyte/nanopore wall surface charge interactions as this minimizes the noise. Thus, this is a promising material for nanopore fabrication.

Van der Waals force separate the layers of 2D materials like  $\text{MoS}_2$ . Thus, the number of layers of  $\text{MoS}_2$  separated can be controlled, which allows tunability of the membrane thickness. Single nucleotide and polynucleotide translocation through monolayer  $\text{MoS}_2$  nanopores have been previously demonstrated experimentally [13]. However,  $\text{MoS}_2$  nanopores also suffer from high translocation velocity similar to other solid-state nanopores. Although different techniques have been employed to slow down DNA translocation through solid state nanopore [28-31], the control of translocation speed is still challenging. The thickness of monolayer (ML)  $\text{MoS}_2$  (0.65 nm) is less than a single nucleotide (1.6-1.8 nm). Thus, the charge interaction along DNA/nanopore interface for ML  $\text{MoS}_2$  gets compromised making DNA translocation fast. Molecular translocation through ML  $\text{MoS}_2$  nanopore has been slowed down by using transmembrane viscosity gradient for producing temporally resolved current blockades capable of distinguishing different types of DNA nucleotides [13].

In this work, we experimentally investigated the role of 2D material membrane properties on the translocation speed of DNA. It is found that the behavior of monolayer (ML) and bilayer (BL)  $\text{MoS}_2$  is different under a vertical electrical field applied using the cis and trans electrodes [32]. The strong interlayer coupling in the BL  $\text{MoS}_2$  leads to a gradation in potential throughout the thickness as each layer will experience a different electric potential [32]. Due to this potential

gradient the phosphate groups are trapped and detrapped by the Molybdenum atoms in the membrane. An additional pull is created because of the increased negative (analyte DNA) - positive (Mo atoms lining the nanopore surface) charge interaction. This can help immobilize molecules at the nanopore for longer time producing highly resolved signals. Molecular dynamics simulation study conducted previously concluded that BL MoS<sub>2</sub> can slow down peptide translocation producing stepwise distinguishable current blockades for single nucleotide sensing [22]. Thus, we have conducted detailed single and poly nucleotide translocation experimental studies through ML and BL MoS<sub>2</sub> nanopores. The translocations were conducted using picomolar concentration and the dwell times were then extracted from these measurements for further analysis.

## 6.4 Experimental

Standard microfabrication techniques were used to fabricate free-standing solid-state silicon nitride (SiN<sub>x</sub>) membranes on silicon support. Electron Beam Lithography (EBL) was used along with Reactive Ion Etching (RIE) to fabricate a 50 nm pore at the centre of the previously fabricated SiN<sub>x</sub> membrane. Then, monolayer (ML) and bilayer (BL) MoS<sub>2</sub> flakes were transferred on the pore via exfoliation using scotch tape. A dual-stage microscope was used to ensure a properly aligned and centred MoS<sub>2</sub> transfer. *Figure B- 1.a* presents the detailed fabrication flowsheet of MoS<sub>2</sub> nanopores. 20 μm sized MoS<sub>2</sub> flakes were obtained repeatedly by this method. The membranes were first characterized to determine and ensure the number of MoS<sub>2</sub> layers using JEOL JEM-ARM200CF Scanning/ Transmission Electron Microscope (STEM). The nanopore was STEM drilled on the free standing MoS<sub>2</sub> membrane. Nanopores with diameters between 2.5-3 nm were obtained repeatedly and were suitable for our application. To prevent nanopore expansion or

material redeposition due to prolonged beam exposure, intense imaging on the same nanopore was avoided.

300 mM filtered KCl solution at pH=7 was prepared by adding 3 mM Tris-HCl buffer. The solution was then degassed in vacuum for 90 minutes and used for the experiments after attaining room temperature. 0.5 mM solutions of single nucleotides (deoxyadenosine triphosphate: dA, deoxythymidine triphosphate: dT, deoxycytidine triphosphate: dC and deoxyguanosine triphosphate: dG) were procured from Integrated DNA technologies for nanopore translocation and dwell-time analysis thereof. 5 mM solution of single stranded (ss) customized DNA oligos (3'-ATCGATCGATCGATCGATCGATCG-5') were procured from Integrated DNA technologies to evaluate the efficiency of ML and BL MoS<sub>2</sub> nanopores for detection of single nucleotides from a DNA strand. Analyte solutions at 10 pM concentration were then prepared by dilution of the purchased single nucleotide and ssDNA solutions.

Custom-made teflon half-cells were used to contain the electrolyte (KCl). As teflon or Poly-tetrafluoro-ethylene are both hydrophobic polymers, they help in maintaining a clean environment. They also have high chemical resistance which ensures a well-insulated sensing environment. The half cells were sealed with Polydimethylsiloxane (PDMS) to ensure that the electrolytic exchange between the chambers is only via the nanopore. PDMS, also reduces capacitive noise which helps in obtaining improved signals. The half-cells were thoroughly cleaned by ultra-sonication before each experiment. The nanopores/membranes were dipped in acetone and kept in vacuum for 30 min. The nanopore was cleaned by gradually pulling the acetone through it. The cleaning steps include three acetone-cleaning repeats followed by four IPA washes in vacuum (20 min each) to remove acetone residue. Fresh solvent is used for every cycle of acetone and IPA treatment. The membrane with the embedded nanopore was then mounted between the half cells. Two Ag/AgCl

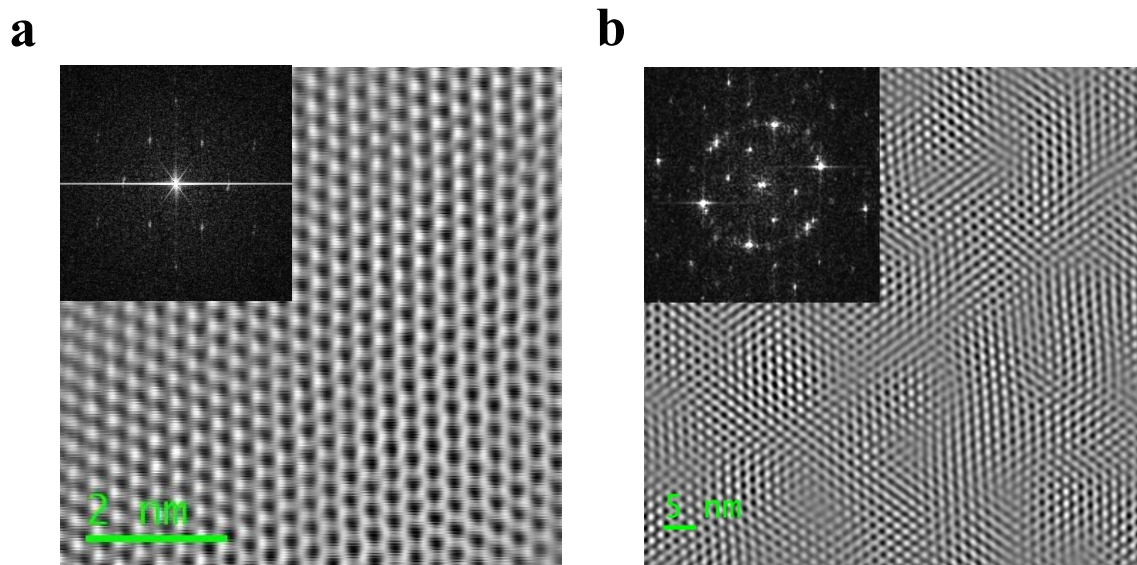
electrodes were cleaned using ethanol and DI water and re-chlorinated by treating them with bleach for an hour. The electrodes were then dipped in each half-cell to apply a voltage across the nanopore bearing membrane. The entire cell-assembly was enclosed in a Faraday cage (Warner instruments) to prevent electrical interference. Filtered and buffered 300 mM KCl solution (previously prepared) was introduced in both chambers and the ionic current at varying voltage (-200 mV to 200 mV) was recorded to evaluate the channel conductance. The nanopore was electrically conditioned at a constant 100 mV bias to obtain a stable baseline. The analytes were then added to the trans chamber and pulled electrophoretically to the cis chamber through the nanopore under a constant bias of 200 mV. Single blockade recording obtained from translocating nucleotides and DNA were amplified using Axon MultiClamp 700B and digitized using Axon Digidata 1550B. The raw data was separately filtered using an 8-pole Bessel filter using Clampfit software and resampled by a factor of 100. The events in filtered data and resampled were compared and the events showing dwell time greater than twice the transition time for the filtered data were selected. The dwell times of those events from the resampled data were collected and reported. This was done to prevent blockade current and dwell time value change induced by filtering and to obtain more accurate results. *Figure B- 1.b* presents schematic of the sensing assembly.

A customized MATLAB algorithm was used to identify translocation peaks. The raw traces were first loaded as an .abf file. The peaks were identified as change points and the blockade current was calculated by subtracting the mean blockade current from the mean baseline current. The mean was calculated for the 100 samples before and after the peak to account for shift in baseline during the translocation. The dwell time was calculated from the difference of the initial and final changepoint indices multiplied by the sampling frequency. The mean and median of the dwell time

were then compared to test whether the distribution is normal or not. We then assumed a null hypothesis that the dwell times for ML and BL MoS<sub>2</sub> nanopore is the same and then tested the hypothesis by conducting T-test at 95% confidence on the dwell time data. All statistical analysis was performed for a population of 300 nucleotides. For the mixed DNA, a MATLAB algorithm was built to first truncate the data at each molecular entry and exit. Then the dwell time and blockade current at each individual current drop steps within a molecular translocation event were obtained. The individual nucleotides were then identified by comparing the blockades with that obtained from single nucleotide translocation performed earlier through the same nanopore.

## 6.5 Results and Discussions

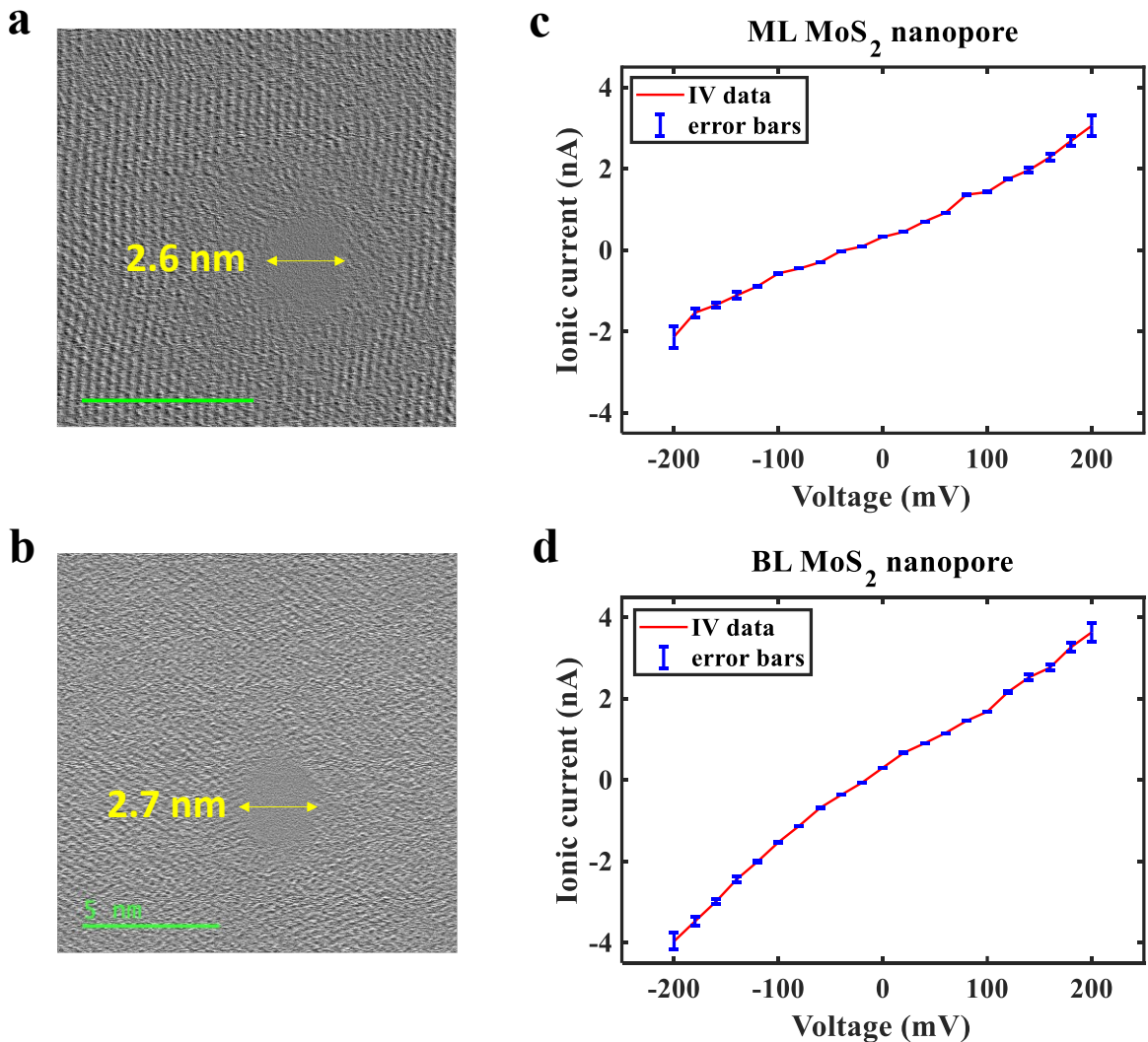
The free-standing ML and BL MoS<sub>2</sub> membranes were first characterized by High Resolution TEM (HRTEM) microscopy to confirm number of layers. **Figure 6.1.a** shows STEM image of molecular arrangement of a ML MoS<sub>2</sub> membrane. **Figure 6.1.b** shows STEM image of an AA' stacked BL MoS<sub>2</sub> membrane showing Moiré pattern of two overlapped domains rotated by 60°. The TEM structure obtained for ML MoS<sub>2</sub> and Moiré patterns observed for BL MoS<sub>2</sub> are in agreement with the literature [33-35]. All the HRTEM images are low pass filtered using Gatan Microscope software to remove noise for prominent visualization of the molecular structure. No additional artifacts were produced from the simple filtering. **Figure B- 2.a-b** shows the profilometric studies of ML and BL MoS<sub>2</sub> on SiN<sub>x</sub> support showing the corresponding membrane thicknesses. **Figure B- 2.c-d** shows additional STEM images of the MoS<sub>2</sub> membranes.



**Figure 6.1.** a. HRTEM image of a typical exfoliated free-standing ML MoS<sub>2</sub> membrane on SiN<sub>x</sub> support with the inset diffraction pattern showing a single hexagon corresponding to monolayer and b. HRTEM image of AA' stacked BL MoS<sub>2</sub> membrane with the inset diffraction pattern showing two hexagonal domains twisted by 60° (image was filtered to remove noise).

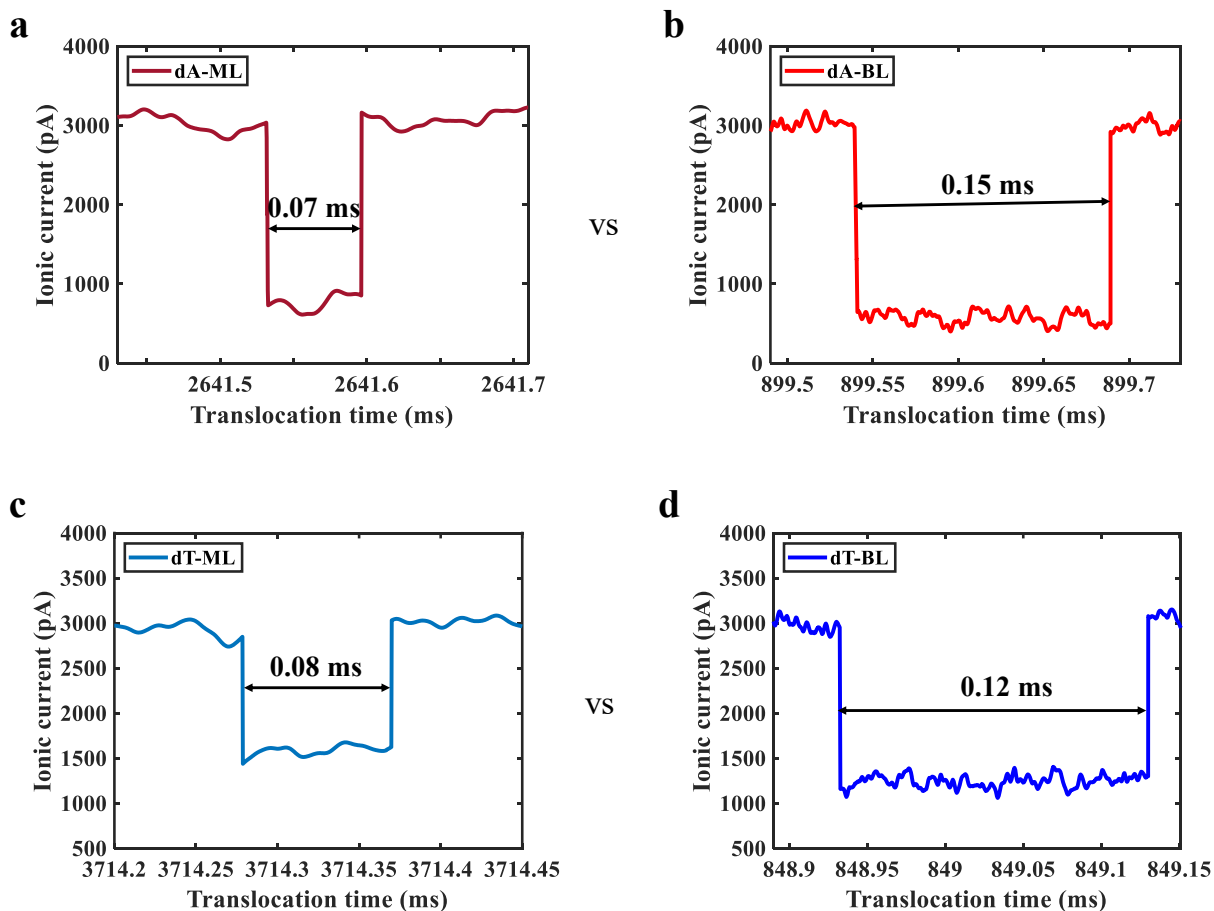
The ionic conductance of the fabricated ML and BL MoS<sub>2</sub> nanopores were measured following the procedure described in the methods section to ensure properly cleaned and conducting nanopores. **Figure 6.2.a-b** shows MoS<sub>2</sub> nanopores with diameters of 2.6 nm for ML and 2.7 nm for BL respectively. Ionic current through each nanopore was measured by applying a trans bias in the range of -200 mV to 200 mV in 300 mM KCl. 4 consecutive ionic conductance measurements were conducted through the nanopore along with intermediate cleaning steps. Here, we have reported the average conductance for each pore. **Figure 6.2.c-d** shows the IV plot for both the nanopores. The mean of ionic current recorded at each bias is displayed as scatter plot, with the error bars showing the current variation between the 4 measurements at each voltage. The mean nanopore conductance (calculated as the average of the ratio of ionic current and voltage at each

bias value) was found to be  $10.5 \pm 0.016$  nS for 2.6 nm ML MoS<sub>2</sub> nanopore and  $17.2 \pm 0.023$  nS for 2.7 nm BL MoS<sub>2</sub> nanopore.



**Figure 6.2.** a. HRTEM image of 2.6 nm STEM fabricated ML MoS<sub>2</sub> nanopore, b. HRTEM image of a 2.7 nm STEM fabricated BL MoS<sub>2</sub> nanopore, c. IV plot for ML MoS<sub>2</sub> nanopore showing an ionic conductance 10.5 nS and d. IV plot for BL MoS<sub>2</sub> nanopore showing an ionic conductance 17.2 nS. The ionic conductance is determined from the average of the ratio of ionic current to bias value at each voltage. The error bars shown in IV plots correspond to the deviation obtained from 4 pore conductance measurements.

To study the effect of ML and BL MoS<sub>2</sub> on single nucleotide translocation and sensing, 10pM concentration of dA, dT, dC and dG were electrophoretically pulled through the above-mentioned ML and BL MoS<sub>2</sub> nanopores. For these nucleotide translocations 200 mV bias was applied and the and translocation traces were recorded. **Figure B- 3.a-h** shows the recorded data for single nucleotide (for each of dA, dT, dC and dG) translocation for 5 sec and 1.5 secs through ML MoS<sub>2</sub> and BL MoS<sub>2</sub> nanopores respectively. We also observe a detection rate of 10-15 nucleotides / sec and 50-60 nucleotides / sec for ML and BL MoS<sub>2</sub> nanopores respectively (see **Figure B- 3.a-h**). The five-fold higher detection rate obtained for BL nanopores may be due to faster capture of the translocating nucleotides at the nanopore due to stronger electrophoretic pull towards the layered BL MoS<sub>2</sub>.



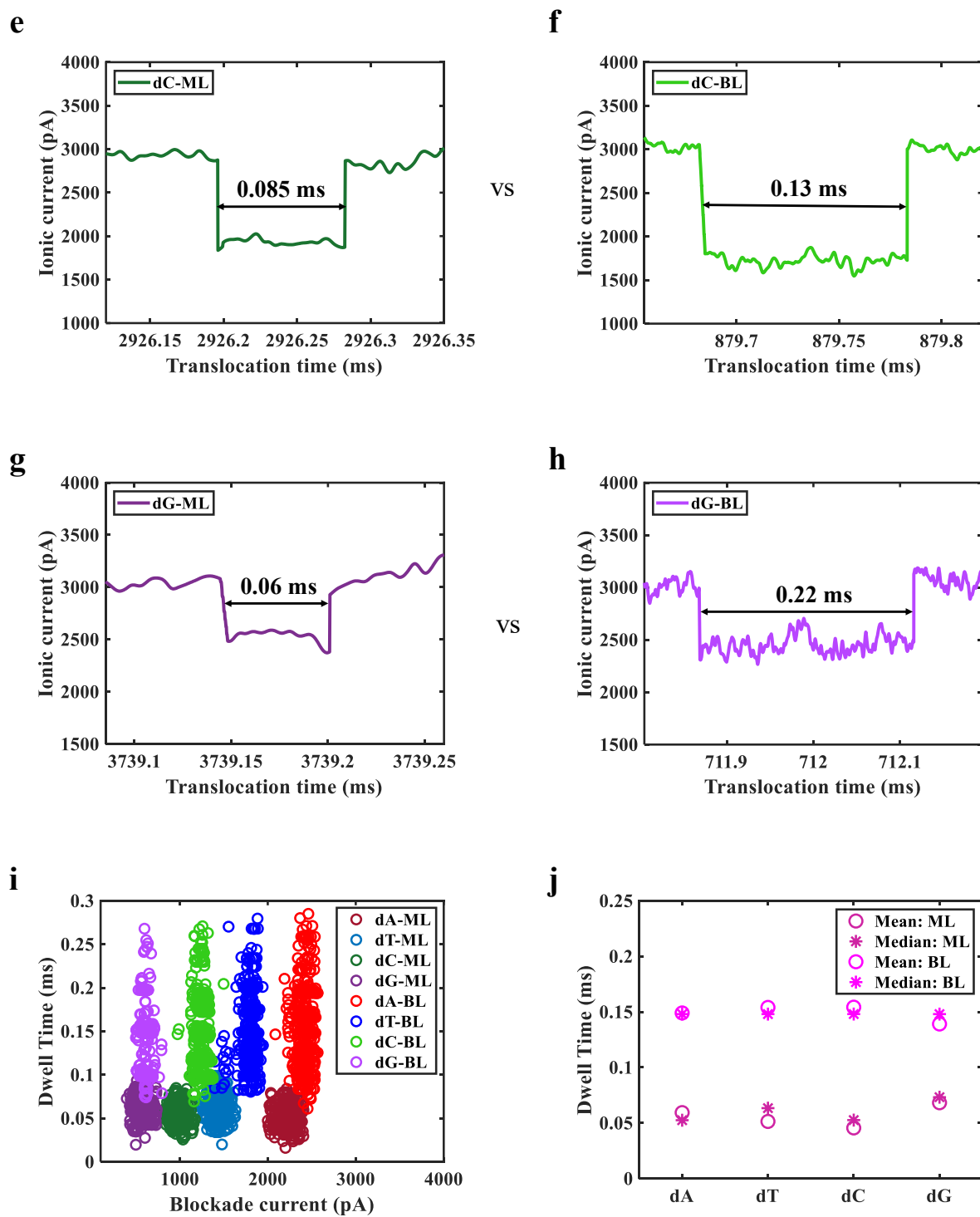


**Figure 6.3.** Truncated typical single nucleotide peaks for a-b. dA, c-d. dT, e-f. dC and g-h. dG translocations through ML and BL MoS<sub>2</sub> nanopores respectively at 200 mV bias showing characteristic dwell time and blockade current values. i. Scatter plots of 3000 translocation events

(unfiltered and 100-fold resampled) showing four different levels for each nucleotide for both ML and BL MoS<sub>2</sub> nanopores and distinctly higher dwell times for BL MoS<sub>2</sub> compared to ML MoS<sub>2</sub> nanopores and j. Plots showing mean and median dwell time values to be similar for each of the four nucleotides through ML and BL MoS<sub>2</sub> nanopores, suggesting a normal distribution.

**Figure 6.3.a-h** presents truncated single nucleotide peaks obtained for ML and BL MoS<sub>2</sub> nanopores for a direct comparison of dwell times. It is observed that the dwell times are higher for BL as compared for the ML MoS<sub>2</sub> nanopores for all the different nucleotides. Blockade current is plotted as a function of dwell time for 3000 single nucleotide transport events in **Figure 6.3.i**. We observe four distinct blockade current regions for the different nucleotides. Thus, we can conclude that both ML and BL MoS<sub>2</sub> nanopores are capable of detecting single nucleotides. The blockade current for the nucleotide translocation is plotted as histograms to observe their distribution (**Figure B- 4**). We observe normal distribution for all the nucleotides for both ML and BL nanopores. Thus, the mean blockade current values along with their standard deviations can be obtained.

**Table 6.1.** Blockade current and dwell time for the single nucleotide translocation for both ML and BL MoS<sub>2</sub> nanopores along with the deviation.

Analyte	ML MoS <sub>2</sub> nanopore		BL MoS <sub>2</sub> nanopore	
	Blockade current	Dwell time	Blockade current	Dwell time
<i>dG</i>	0.595±0.057 nA	0.0529±0.0092 ms	0.608±0.036 nA	0.1409±0.0424 ms
<i>dC</i>	0.987±0.066 nA	0.0577±0.0102 ms	1.256±0.048 nA	0.1430±0.0424 ms
<i>dT</i>	1.454±0.076 nA	0.0610±0.0110 ms	1.809±0.07 nA	0.1422±0.0405 ms

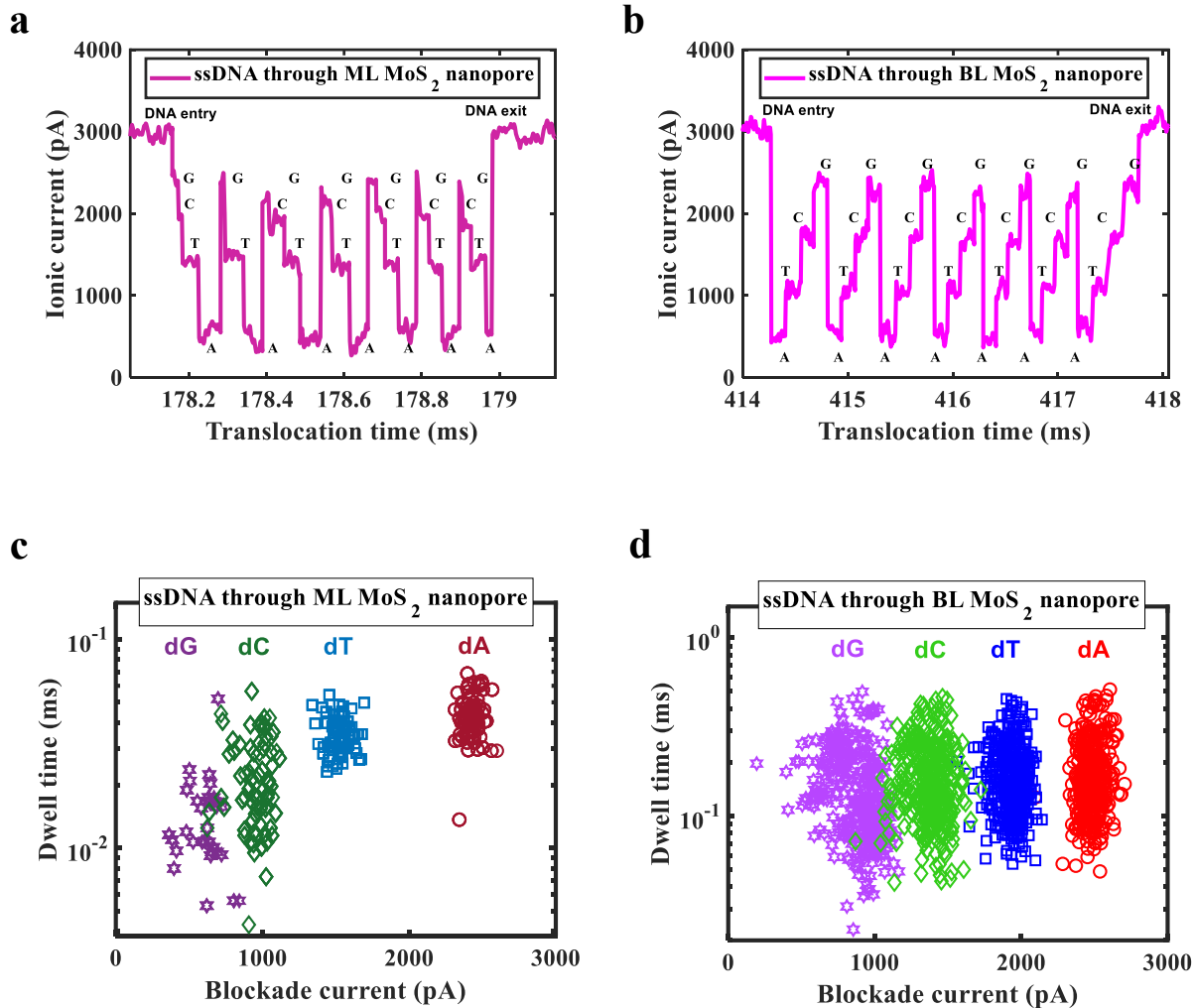
$dA$	$2.245 \pm 0.079$ nA	$0.0615 \pm 0.0122$ ms	$2.434 \pm 0.06$ nA	$0.1412 \pm 0.0401$ ms
------	----------------------	------------------------	---------------------	------------------------

---

**Table 6.1** lists the dwell time and blockade current values for all single nucleotides sensed using ML and BL MoS<sub>2</sub> nanopores. The blockade current magnitudes measured are found to be the dA, dT, dC and dC in decreasing order which agrees with previous study [13]. The mean blockade current obtained through BL MoS<sub>2</sub> is found to be slightly higher than or comparable to ML MoS<sub>2</sub>, which may be due to better charge interaction at the Van der Waals separated nanopore interface. Based on these numbers we can conclude that the current resolution obtained for ML is preserved in BL MoS<sub>2</sub> nanopores. On the other hand, it was observed that the dwell time values of the translocations for BL nanopore are spread over a larger range as compared to the ML nanopore. The events detected through ML nanopores show mean dwell times in range of 0.053-0.061 ms with a 17-20% of deviation. For BL nanopore detection the mean dwell time range is 0.141 – 0.143 ms with a deviation of 28-30 % (see **Table 6.1** and **Figure B- 5**). The mean and median dwell time values were then evaluated for ML and BL nanopores (see **Figure 6.3.j**) and the values were found to be pretty close to each other, supporting an assumption of a normal distribution. Therefore, T-tests were done on the values for a statistical comparison. T-tests thus performed, indicate that for all the nucleotides, the dwell times for ML and BL nanopores are different at a 95% confidence level (shown in Error! Reference source not found.). The sample mean of the dwell time for the BL nanopore is approximately twice that of the ML nanopore. A higher dwell time indicates an improvement in sensing.

To demonstrate the single nucleotide detection capability of ML and BL MoS<sub>2</sub> nanopores mixed nucleotide translocations through ML and BL MoS<sub>2</sub> nanopores were conducted. **Figure B- 6.a-b** show translocation traces for 5 sec and 1.5 sec through ML and BL MoS<sub>2</sub> nanopores respectively.

The nucleotide distinction is made based on the current blockades obtained for individual nucleotides sensed separately. The dwell time range for all nucleotides (as observed in the scatter plot in *Figure B- 6.c*) is found to be the same as that when detected separately through ML and BL MoS<sub>2</sub> nanopores.”



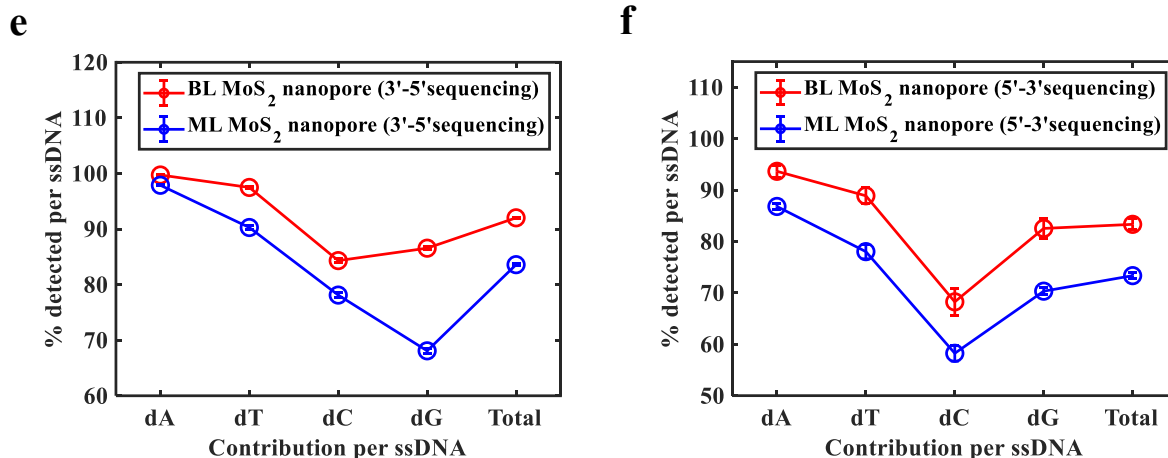


**Figure 6.4.** A typical truncated ssDNA translocation data (unfiltered and resampled) through a. ML MoS<sub>2</sub> nanopore and b. BL MoS<sub>2</sub> nanopore with single nucleotides being detected, Dwell time vs blockade current scatter plot for the single nucleotides detected from ssDNA translocation through c. ML MoS<sub>2</sub> nanopore and d. BL MoS<sub>2</sub> nanopore. and e-f. Percentage efficiency of individual nucleotide detection per ssDNA strand and ssDNA sequencing efficiency for 3'-5' and 5'-3' orientations respectively showing that BL MoS<sub>2</sub> nanopore demonstrates better sequencing efficiency than ML MoS<sub>2</sub> nanopore for both sequencing orientations.

To demonstrate that the BL MoS<sub>2</sub> improves the dwell time of the translocation and can detect single nucleotides, we used 10 pM single stranded (ss) DNA oligos with customized mixed sequence. The translocations were conducted using ML and BL nanopores. **Figure 6.4.a-b** show the translocation trace for a single ssDNA strand through the ML and BL MoS<sub>2</sub> nanopore respectively. For both the nanopores distinct molecular current blockades were observed. From careful inspection of each molecular blockade, it can be clearly understood that the discrete blockade steps correspond to the constituent nucleotides. All the translocations for the ML and BL were analysed using the code developed and dwell time as a function of blockade current for 3 sec translocations are plotted in **Figure 6.4.c-d**. For BL MoS<sub>2</sub> nanopore, we observe four different

current levels similar to observed for each nucleotide with dwell times ranging from 0.02-0.6 ms with the highest density obtained around 0.08-0.3 ms which is similar to what we obtained for single nucleotide translocations. On the other hand, for ML MoS<sub>2</sub> nanopore, four different nucleotides are also detected. However, the time resolution obtained for dC and dG are particularly low (0.004-0.04 ms for dC and 0.004-0.06 ms for dG) compared to dA and dT, the latter nucleotides showing dwell times in the range of 0.01-0.07 ms, with the mean ~ 0.05 ms, which is close to that obtained for single nucleotide triphosphates.

Based on the different dwell times and blockade current four different nucleotides can be distinctly identified. The blockade levels are then matched with the single nucleotide data recorded before to obtain and relate the DNA sequence. **Figure B- 7.a-b** shows the sequence of nucleotides detected and left undetected by ML and BL MoS<sub>2</sub> nanopore sensing in a color-coded format, thus representing the single nucleotide efficiency of detection in each case. ML MoS<sub>2</sub> nanopore is found to demonstrate a single nucleotide detection efficiency of 84.9% ((Total – undetected) / Total nucleotides) considering 60 DNA molecules translocation. Similarly, the experimental analysis shows that BL MoS<sub>2</sub> nanopore are capable of identifying single nucleotides with about 89.1% efficiency. For both ML and BL nanopores, it is observed that mostly dC and dG (especially at the tailing end or entering end of the DNA) are undetected or detected with poor time resolution. This may be due to the low density of these two nucleotides along with their low blockade current.

In addition, we have extracted the efficiency of ssDNA sequencing for both 3'-5' and 5'-3' orientations. BL MoS<sub>2</sub> nanopores demonstrate 83±1.07 % and 92±0.14 % for 5'-3' and 3'-5'-ssDNA sequencing efficiency respectively. These are 10 % better than ML MoS<sub>2</sub> for 5'-3'-orientation (73.35±0.55 %) and 8.4 % better for 3'-5' sequencing (83.6±0.16 %). **Figure B- 8** and

**Figure B- 9** shows sequencing events for 3'-5' and 5'-3' ssDNA translocations for ML and BL MoS<sub>2</sub> nanopores respectively.

**Figure 6.4.e-f** shows the efficiency of detection of individual molecules from ssDNA and ssDNA sequencing as a whole. It is found that the efficiency of BL MoS<sub>2</sub> nanopores is better in both cases. The role of BL MoS<sub>2</sub> is observed to be most prominent in improving the temporal resolution of the signature for dC and dG. It was observed that the 47/60 ssDNA translocations were in 3'-5' orientation for ML MoS<sub>2</sub> nanopore and 51/60 ssDNA translocations were in 3'-5' orientation for BL MoS<sub>2</sub> nanopore.

## 6.6 Discussions

Short dwell time or high translocation speed in a nanopore prevents precise sequencing of nucleotides. Different techniques have been used to slow down the DNA translocation using trans-membrane viscosity gradient, electric field tuning and surface charge modification of the nanopore/electrolyte interface [28-31]. DNA molecule sensing has been demonstrated through sub-5 nm nanopores on 25 nm thick SiN<sub>x</sub> membranes in 38 pM concentration solution [36]. The study demonstrated that unamplified dsDNA molecules (as opposed to single nucleotides) can be sensed by slowing down the translocation using 20-fold salt gradient [36]. A ML MoS<sub>2</sub> nanopore-based viscosity gradient system has also been used for improved DNA sequencing by slowing down the translocation by two orders of magnitude [13]. A simulation study has also been used to demonstrate improved peptide dwell times for BL MoS<sub>2</sub> nanopores [22].

In this study, we experimentally explore the unaided capacity of BL MoS<sub>2</sub> nanopores in improving real-time sensing resolution, detection rate and efficiency for ssDNA sequencing. We first analysed the blockade current obtained for single nucleotide using ML and BL MoS<sub>2</sub> nanopores.

Our ML MoS<sub>2</sub> nanopore current signatures are similar to that obtained in previous study [13]. However, we observed geometry defying blockade signatures for Guanine. This may be due to the increased hydrogen bonding potential of Guanine or increased physical adsorption energy of Guanine on MoS<sub>2</sub> which may increase the pore conductance, thus producing a lower overall ionic blockade event [37]. For ssDNA sequencing, we also observed lower time resolution of guanine base of the ssDNA compared to other bases, which may indicate that the effect of surrounding A and C over nanopore blockade are dominant over G. Few studies have shown exceptions to the geometry-determined blockade when larger A and G have produced lower blockades than C and T, for both single nucleotide and polynucleotide sensing [13, 20, 38].

We also obtain higher blockade current levels for BL MoS<sub>2</sub> nanopore as compared to ML MoS<sub>2</sub> nanopore. In general, for 3D bulk materials like SiN<sub>x</sub>, the conductance decreases with increase in pore/membrane thickness [39]. However, in our study we find that 2D MoS<sub>2</sub> nanopores do not demonstrate this behaviour. Unlike 3D bulk material nanopores, in 2D material nanopores interlayer charge storage, electro-activity and field confinement between the van der Waals coupled monolayers increases the capacitance of the pore [40]. COMSOL Multiphysics simulation study indicates that the ionic conductance of MoS<sub>2</sub> nanopores demonstrates the following trend 2-layers > 1-layer > 4-layers > 3-layers > 6-layers > 5-layers and so on above 2 nm diameter nanopore [41]. Few studies on 2D materials nanopores like graphene also demonstrate similar behaviour [18, 42, 43].

We further observe nearly double the dwell time for BL MoS<sub>2</sub> as compared to ML MoS<sub>2</sub> nanopore, with 95% confidence. To observe the effect of the bias on the blockade current we measured the blockade current for three different voltages. **Figure B- 11** shows blockade current vs dwell time scatter plot for single nucleotide translocations through ML and BL MoS<sub>2</sub> nanopores for varying

transmembrane bias values (100 mV, 150 mV and 200 mV). However, significant change in dwell times is not observed for either of ML or BL MoS<sub>2</sub> nanopore sensing. This further proves that the events considered are indeed translocation events and strengthens the inference drawn about improved ability of BL MoS<sub>2</sub> nanopores in providing better resolution for single nucleotide sensing.

The effect of the temporal resolution improvement offered by BL MoS<sub>2</sub> nanopore on sequencing single-stranded DNA oligos was investigated next. From these experiments, we found that the capability of BL MoS<sub>2</sub> nanopores can resolve the nucleotide blockade currents and hence can distinguish single distinct nucleotides. Thus, we observed an overall single nucleotide (for 1800 nucleotides in 60 ssDNA strands) detection efficiency of 89 % using BL MoS<sub>2</sub> nanopore, a 4 % improvement compared to that for ML MoS<sub>2</sub> nanopores. We also observed an 8-10 % improved ssDNA sequencing efficiency for both 3'-5' and 5'-3' ssDNA orientations. The interlayer potential gradient for BL MoS<sub>2</sub> offers improved capture of analytes inside the nanopore even at low (picomolar) concentration leading to 5X better detection rate. Previous studies have shown that improved nanopore/DNA interaction can result in faster capture of DNA within the nanopore and also cause longer residence of DNA at the nanopore [44]. We believe that the improved capture rate and nanopore dwell time is a result of the enhanced DNA/nanopore interaction experienced in BL MoS<sub>2</sub> nanopore as compared to ML MoS<sub>2</sub> nanopore.

Moreover, the behaviour of even and odd layers of MoS<sub>2</sub> is found to differ under an applied vertical electrical field [45]. The electric field confinement within the layers is more for odd-numbered layers than even-numbers, which thus improves the ionic conduction for even layers. Moreover, the BL MoS<sub>2</sub> thickness is close to nucleotide size which helps maintain a good spatial resolution. However, >2 layers can hamper the spatial resolution. Additionally, our simulation results also

show a reduction in blockade signal amplitude above two layers. All things considered; we believe > 2-layers MoS<sub>2</sub> may not be a better choice for DNA sequencing. The results conclusively suggest that BL MoS<sub>2</sub> nanopores can distinguish four type of nucleotides with significantly higher dwell time. Thus, BL MoS<sub>2</sub> nanopores can be a suitable choice for more efficient and faster DNA sequencing.

## **6.7 Conclusion**

In summary, we experimentally demonstrate that BL MoS<sub>2</sub> nanopores are capable of detecting distinct single nucleotides with twice the dwell time as compared to ML MoS<sub>2</sub> nanopores. The van der Waals separated layers of BL MoS<sub>2</sub> experience different potentials when a bias is applied across them creating an interlayer potential gradient. This makes each individual molecule experience an increased charge interaction and stronger immobilization at the nanopore, leading to prominently sharp and broad translocation events. The translocation profiles through BL MoS<sub>2</sub> nanopores show distinct peaks for each type of DNA nucleobase of 10pM concentration. Thus, we have been able to detect nucleotides at 89% efficiency using BL MoS<sub>2</sub> nanopores for 60 detected DNA molecules. Furthermore, we observed an 8-10 % improved sequencing efficiency by using BL MoS<sub>2</sub> nanopores. The BL MoS<sub>2</sub> nanopore can resolve single-nucleotide signals temporally, while maintaining a good spatial resolution as well. This high detection rate, efficiency and dwell time makes BL MoS<sub>2</sub> nanopores promising for high-speed detections in low concentration analyte solutions which is essential for several biosensing applications.

## **Corresponding Authors**

[mgupta1@ualberta.ca](mailto:mgupta1@ualberta.ca) (MG)

## Author Contributions

P. S. conducted all the simulations, fabrication, and experiments on the nanopores. P. S. and M.G. analyzed and wrote the manuscript.

## Funding Sources

This work was funded by Natural Sciences and Engineering Research Council of Canada award # 06096 and Alberta Innovates.

## References

- [1] J. J. Kasianowicz, E. Brandin, D. Branton and D. W. Deamer, Characterization of Individual Polynucleotide Molecules Using a Membrane Channel, *Proc. Natl. Acad. Sci. U. S. A.*, 1996, 93, 13770–13773.
- [2] F. Haque, J. Li, H. C. Wu, X. J. Liang and P. Guo, Solid-state and biological nanopore for real-time sensing of single chemical and sequencing of DNA, *Nano Today*, 2013, 8, 56–74.
- [3] F. Sawafta, A. T. Carlsen and A. R. Hall, Membrane thickness dependence of Nanopore formation with a focused helium ion beam, *Sensors*, 2014, 14, 8150–8816.
- [4] Y. H. Lanyon, G. D. Marzi, Y. E. Watson, A. J. Quinn, J. P. Gleeson, G. Redmond and D. W. M. Arrigan, Fabrication of nanopore array electrodes by focused ion beam milling, *Anal. Chem.*, 2007, 79, 3048–3055.
- [5] H. M. Kim, M. H. Lee and K. B. Kim, Theoretical and experimental study of nanopore drilling by a focused electron beam in transmission electron microscopy, *Nanotechnology*, 2011, 22(27), 275303.

- [6] O. K. Zahid and A. R. Hall, Helium ion microscope fabrication of solid-state nanopore devices for biomolecule analysis, in *NanoScience and Technology*, ed. G. Hlawacek and A. Götzhauser, Springer, Cham, 2016, pp. 447–470.
- [7] T. Schmidt, M. Zhang, I. Sychugov, N. Roxhed and J. Linnros, Nanopore arrays in a silicon membrane for parallel single molecule detection: fabrication, *Nanotechnology*, 2015, 26(31), 314001.
- [8] J. Storm, J. H. Chen, H. W. Zandbergen and C. Dekker, Translocation of double-strand DNA through a silicon oxide nanopore, *Phys. Rev. E: Stat., Nonlinear, Soft Matter Phys.*, 2005, 71(5), 051903.
- [9] K. Briggs, H. Kwok and V. Tabard-Cossa, Automated fabrication of 2-nm solid-state nanopores for nucleic acid analysis, *Small*, 2014, 10, 2077–2086.
- [10] B. M. Venkatesan, B. Dorvel, S. Yemenicioglu, N. Watkins, I. Petrov and R. Bashir, Highly sensitive, mechanically stable nanopore sensors for DNA analysis, *Adv. Mater.*, 2009, 21, 2771–2776.
- [11] J. Larkin, R. Henley, D. C. Bell, T. Cohen-Karni, J. K. Rosenstein and M. Wanunu, Slow DNA transport through nanopores in hafnium oxide membranes, *ACS Nano*, 2013, 7, 10121–10128.
- [12] K. Liu, J. Feng, A. Kis and A. Radenovic, Atomically thin molybdenum disulfide nanopores with high sensitivity for dna translocation, *ACS Nano*, 2014, 8, 2504–2511.
- [13] J. Feng, K. Liu, R. D. Bulushev, S. Khlybov, D. Dumcenco, A. Kis and A. Radenovic, Identification of single nucleotides in MoS<sub>2</sub> nanopores, *Nat. Nanotechnol.*, 2015, 10, 1070–1076.

- [14] A. B. Farimani, K. Min and N. R. Aluru, DNA base detection using a single-layer MoS<sub>2</sub>, *ACS Nano*, 2014, 8, 7914–7922.
- [15] H. Chen, L. Li, T. Zhang, Z. Qiao, J. Tang and J. Zhou, Protein Translocation through a MoS<sub>2</sub> Nanopore: A Molecular Dynamics Study, *J. Phys. Chem. C*, 2018, 122, 2070–2080.
- [16] M. Graf, M. Lihter, D. Altus, S. Marion and A. Radenovic, Transverse Detection of DNA in a MoS<sub>2</sub> Nanopore, *Nano Lett.*, 2019, 19(12), 9075–9083.
- [17] Y. Deng, Q. Huang, Y. Zhao, D. Zhou, C. Ying and D. Wang, Precise fabrication of a 5 nm graphene nanopore with a helium ion microscope for biomolecule detection, *Nanotechnology*, 2017, 28(4), 045302.
- [18] C. A. Merchant, K. Healy, M. Wanunu, V. Ray, N. Peterman, J. Bartel, M. D. Fischbein, K. Venta, Z. Luo, A. T. C. Johnson and M. Drndić, DNA translocation through graphene nanopores, *Nano Lett.*, 2010, 10, 2915–2921.
- [19] B. Luan and R. Zhou, Spontaneous Transport of Single-Stranded DNA through Graphene-MoS<sub>2</sub> Heterostructure Nanopores, *ACS Nano*, 2018, 12, 3886–3891.
- [20] A. D. Carral, S. C. Sarap, K. Liu, A. Radenovic and M. Fyta, 2D MoS<sub>2</sub> nanopores: ionic current blockade height for clustering DNA events, *2D Mater.*, 2019, 6(4), 045011.
- [21] J. Shim, S. Banerjee, H. Qiu, K. K. H. Smithe, D. Estrada, J. Bello, E. Pop, K. Schulten and R. Bashir, Detection of methylation on dsDNA using nanopores in a MoS<sub>2</sub> membrane, *Nanoscale*, 2017, 9, 14836–14845.
- [22] A. Nicolai, M. D. B. Pérez, P. Delarue, V. Meunier, M. Drndić and P. Senet, Molecular Dynamics Investigation of Polylysine Peptide Translocation through MoS<sub>2</sub> Nanopores, *J. Phys. Chem. B*, 2019, 123, 2342–2353.

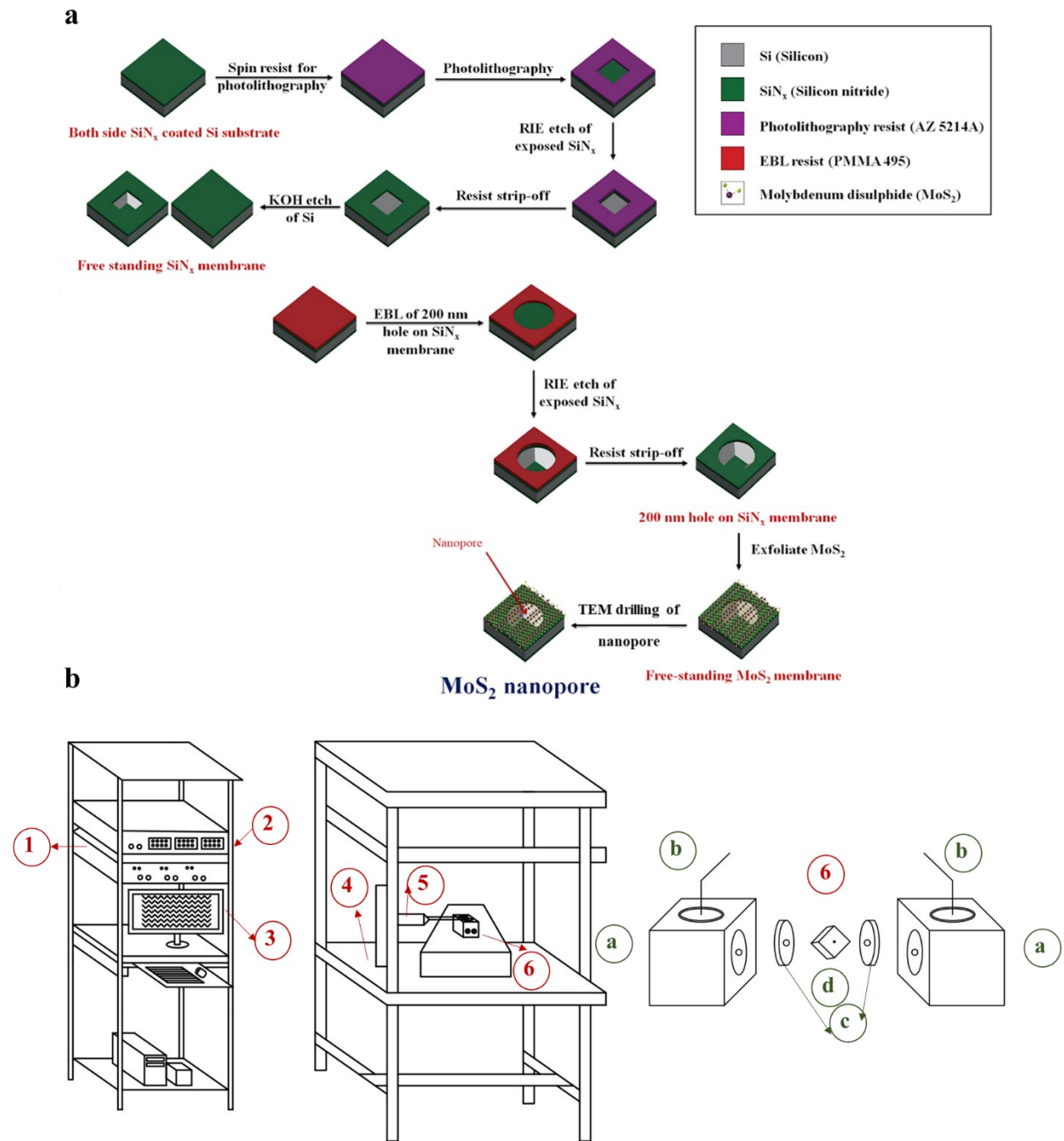
- [23] A. Smolyanitsky, B. I. Yakobson, T. A. Wassenaar, E. Paulechka and K. A. Kroenlein, A MoS<sub>2</sub>-Based Capacitive Displacement Sensor for DNA Sequencing, *ACS Nano*, 2016, 10, 9009–9016.
- [24] G. Danda, P. M. Das, Y. C. Chou, J. T. Mlack, W. M. Parkin, C. H. Naylor, K. Fujisawa, T. Zhang, L. B. Fulton, M. Terrones, A. T. C. Johnson and M. Drndi'c, Monolayer WS<sub>2</sub> Nanopores for DNA Translocation with Light- Adjustable Sizes, *ACS Nano*, 2017, 10, 9009–9016.
- [25] H. Arjmandi-Tash, L. A. Belyaeva and G. F. Schneider, Single molecule detection with graphene and other two dimensional materials: nanopores and beyond, *Chem. Soc. Rev.*, 2016, 45, 476–493.
- [26] W. Chen, G. C. Liu, J. Ouyang, M. J. Gao, B. Liu and Y. D. Zhao, Graphene nanopores toward DNA sequencing: a review of experimental aspects, *Sci. China: Chem.*, 2017, 60, 721–729.
- [27] G. F. Schneider, Q. Xu, S. Hage, S. Luik, J. N. H. Spoor, S. Malladi, H. Zandbergen and C. Dekker, Tailoring the hydrophobicity of graphene for its use as nanopores for DNA translocation, *Nat. Commun.*, 2013, 4(1), 2619.
- [28] B. Luan, G. Stolovitzky and G. Martyna, Slowing and controlling the translocation of DNA in a solid-state nanopore, *Nanoscale*, 2012, 4, 1068–1077.
- [29] D. V. Melnikov, J. P. Leburton and M. E. Gracheva, Slowing down and stretching DNA with an electrically tunable nanopore in a p-n semiconductor membrane, *Nanotechnology*, 2012, 23(25), 255501.

- [30] R. Akahori, T. Haga, T. Hatano, I. Yanagi, T. Ohura, H. Hamamura, T. Iwasaki, T. Yokoi and T. Anazawa, Slowing single-stranded DNA translocation through a solid-state nanopore by decreasing the nanopore diameter, *Nanotechnology*, 2014, 25(27), 275501.
- [31] M. Waugh, A. Carlsen, D. Sean, G. W. Slater, K. Briggs, H. Kwok and V. Tabard-Cossa, Interfacing solid-state nanopores with gel media to slow DNA translocations, *Electrophoresis*, 2015, 36, 1759–1767.
- [32] Q. Liu, L. Li, Y. Li, Z. Gao, Z. Chen and J. Lu, Tuning electronic structure of bilayer MoS<sub>2</sub> by vertical electric field: a first-principles investigation, *J. Phys. Chem. C*, 2012, 116, 21556–21562.
- [33] P. Yang, X. Zou, Z. Zhang, M. Hong, J. Shi, S. Chen, J. Shu, L. Zhao, S. Jiang, X. Zhou, Y. Huan, C. Xie, P. Gao, Q. Chen, Q. Zhang, Z. Liu and Y. Zhang, Batch production of 6-inch uniform monolayer molybdenum disulfide catalyzed by sodium in glass, *Nat. Commun.*, 2018, 9, 1–10.
- [34] H. Qiu, T. Xu, Z. Wang, W. Ren, H. Nan, Z. Ni, Q. Chen, S. Yuan, F. Miao, F. Song, G. Long, Y. Shi, L. Sun, J. Wang and X. Wang, Hopping transport through defect-induced localized states in molybdenum disulphide, *Nat. Commun.*, 2013, 4, 2642.
- [35] S. Hussain, J. Singh, D. Vikraman, A. K. Singh, M. Z. Iqbal, M. F. Khan, P. Kumar, D. C. Choi, W. Song, K. S. An, J. Eom, W. G. Lee and J. Jung, Large-area, continuous and high electrical performances of bilayer to few layers MoS<sub>2</sub> fabricated by RF sputtering via post-deposition annealing method, *Sci. Rep.*, 2016, 6, 1–13.
- [36] M. Wanunu, W. Morrison, Y. Rabin, A. Y. Grosberg and A. Meller, Electrostatic focusing of unlabelled DNA into nanoscale pores using a salt gradient, *Nat. Nanotechnol.*, 2010, 5(2), 160–165.

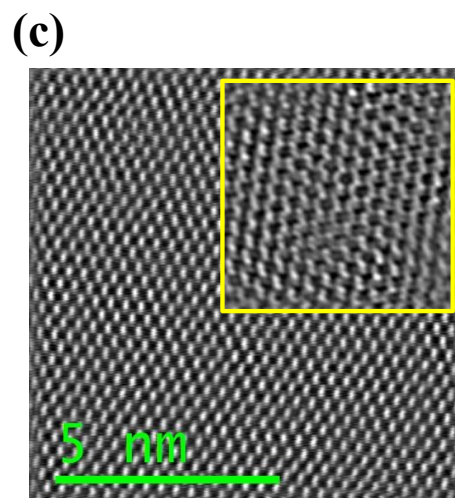
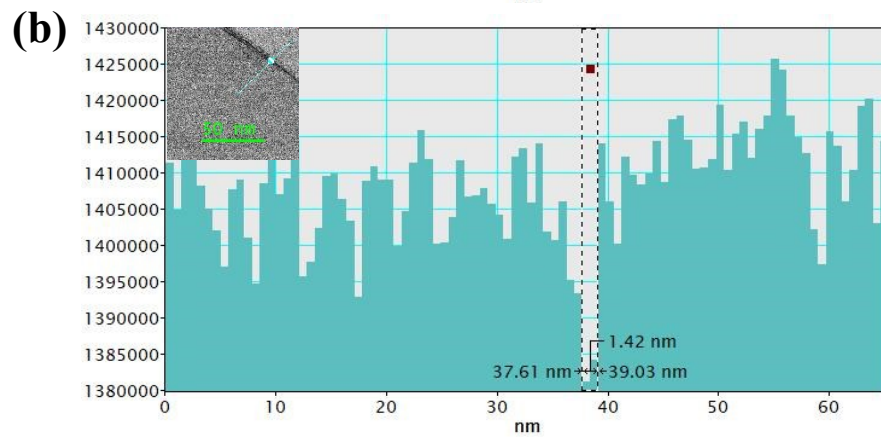
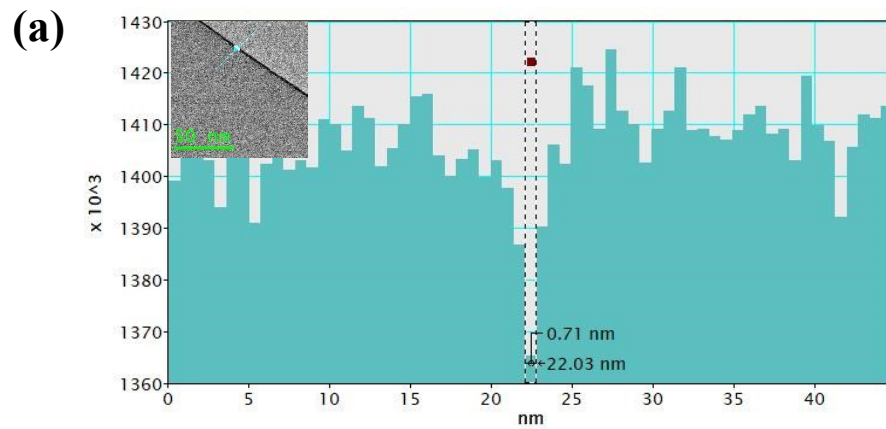
- [37] N. M. Luscombe, R. A. Laskowskia and J. M. Thornton, Amino acid-base interactions: a three-dimensional analysis of protein-DNA interactions at an atomic level, *Nucleic Acids Res.*, 2001, 29, 2860–2874.
- [38] S. Bhattacharya, J. Yoo and A. Aksimentiev, Water Mediates Recognition of DNA Sequence via Ionic Current Blockade in a Biological Nanopore, *ACS Nano*, 2016, 10, 4644–4651.
- [39] S. W. Kowalczyk, A. Y. Grosberg, Y. Rabin and C. Dekker, Modeling the conductance and DNA blockade of solid state nanopores, *Nanotechnology*, 2011, 22, 315101.
- [40] J. Bard and L. R. Faulkner, *Electrochemical Methods: Fundamentals and Applications*, Department of Chemistry and Biochemistry, University of Texas, Austin, Second edn, 2001.
- [41] P. Sen, H. Hoi, D. Nandi and M. Gupta, Highly accurate random DNA sequencing using inherent interlayer potential traps of bilayer MoS<sub>2</sub> nanopores, *bioRxiv*, 2020, DOI: 10.1101/2020.04.21.053595.
- [42] G. F. Schneider, S. W. Kowalczyk, V. E. Calado, G. Pandraud, H. W. Zandbergen, L. M. K. Vandersypen and C. Dekker, DNA Translocation through Graphene Nanopores, *Nano Lett.*, 2010, 10, 3163–3167.
- [43] W. Lv, M. Chen and R. Wu, The impact of the number of layers of a graphene nanopore on DNA translocation, *Soft Matter*, 2013, 9, 960–966, DOI: 10.1039/C2SM26476E.
- [44] D. Wang, S. Harrer, B. Luan, G. Stolovitzky, H. Peng and A. Afzali, Regulating the Transport of DNA through Biofriendly Nanochannels in a Thin Solid Membrane, *Sci. Rep.*, 2014, 4, 3985, DOI: 10.1038/srep03985.

- [45] H. Zhong, R. Quhe, Y. Wang, Z. Ni, M. Ye, Z. Song, Y. Pan, J. Yang, L. Yang, M. Lei, J. Shi and J. Lu, Interfacial Properties of Monolayer and Bilayer MoS<sub>2</sub> Contacts with Metals: Beyond the Energy Band Calculations, *Sci. Rep.*, 2016, 6, 21786, DOI: 10.1038/srep21786.

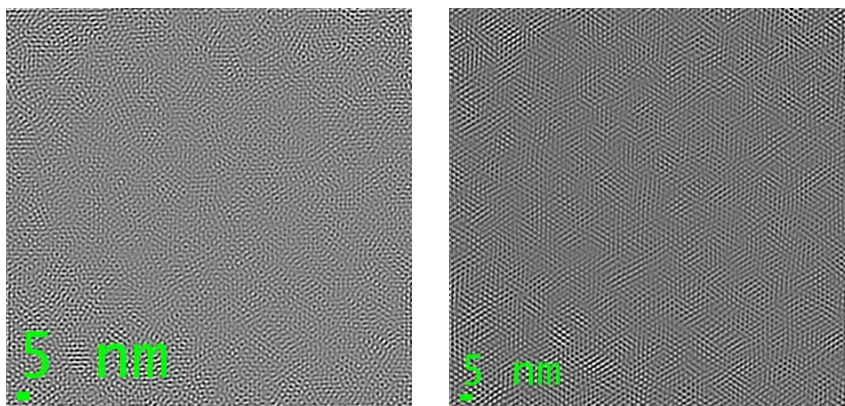
## 6.8 Supplementary information



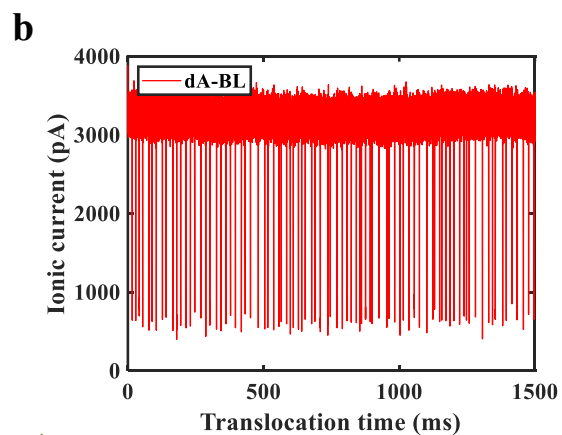
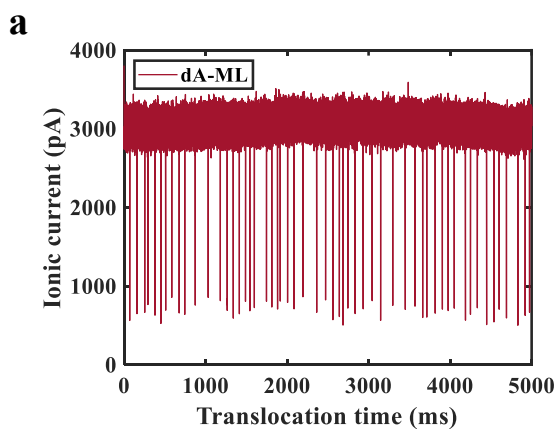
5. Amplifier head, 6. Cell set up (a. Teflon cell containing KCl, b. Ag/AgCl electrodes, Gaskets to hold membrane, d. Membrane bearing nanopore)].

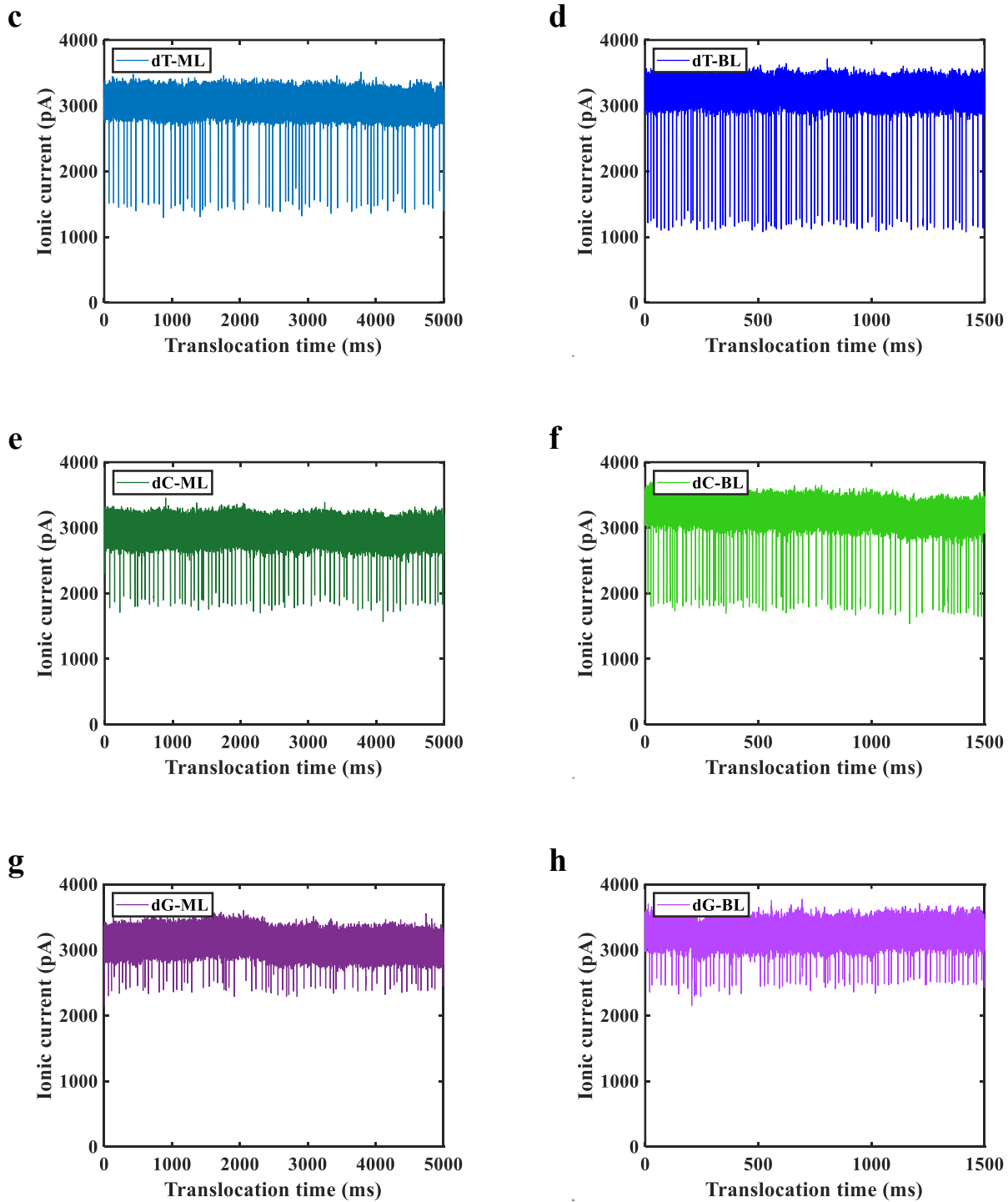


(d)

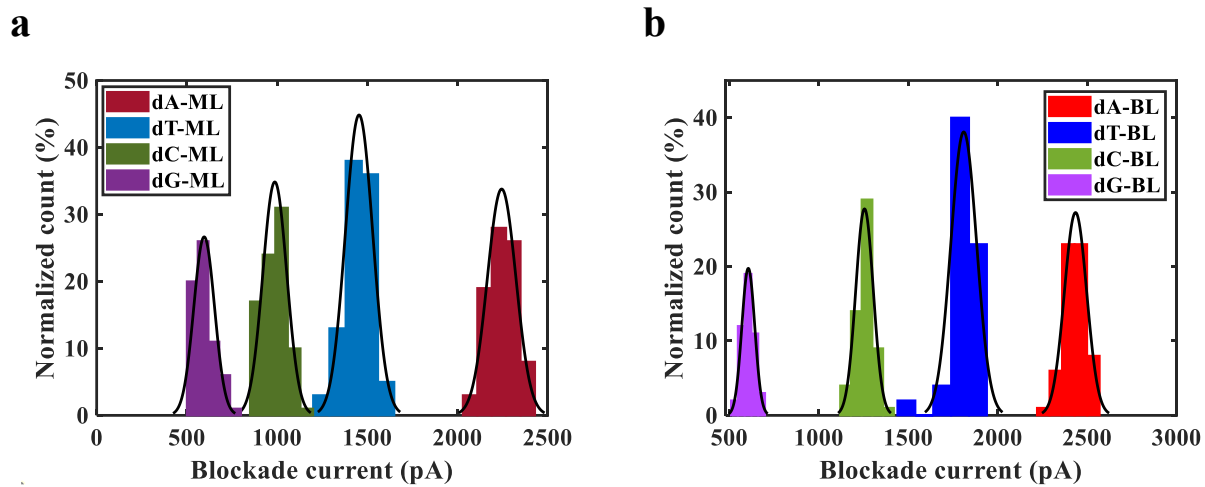


**Figure B- 2.** (a) TEM line profile of ML MoS<sub>2</sub> with an inset raster plot of the same region showing the layer thickness of 0.71 nm, characteristic to a ML MoS<sub>2</sub>, (b) TEM line profile of BL MoS<sub>2</sub> with the inset showing its raster plot, showing the layer thickness of 1.42 nm, characteristic to a BL MoS<sub>2</sub>, TEM raster profiles of (c) ML MoS<sub>2</sub> and (d) (left) AB stacked BL MoS<sub>2</sub> and (right) AA' stacked BL MoS<sub>2</sub>.

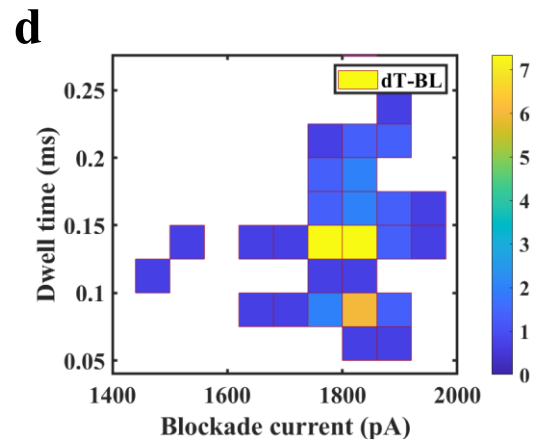
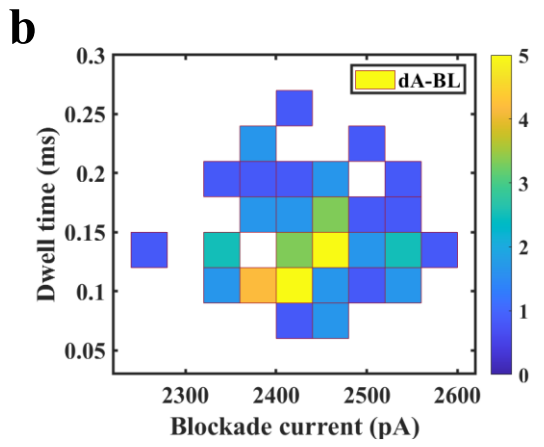
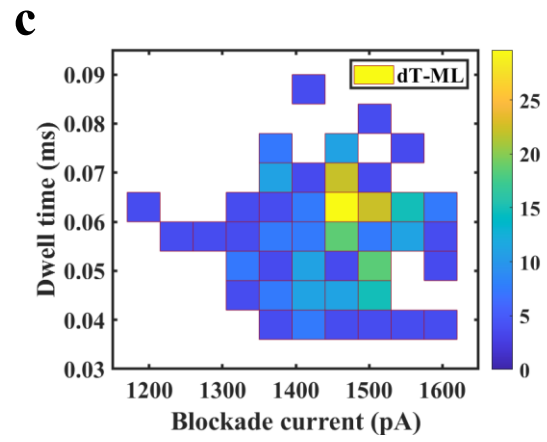
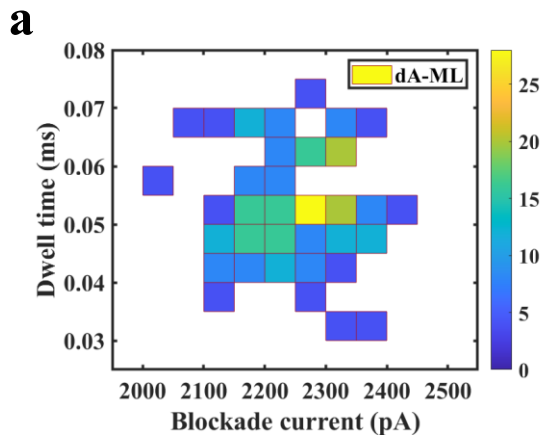




**Figure B- 3.** Recorded data for single nucleotide (for each of dA, dT, dC and dG) translocation for 5 sec and 1.5 secs through ML MoS<sub>2</sub> and BL MoS<sub>2</sub> nanopores respectively.



**Figure B- 4.** Normalized histogram of the recorded dA, dT, dC and dG translocation events through (a) ML and (b) BL MoS<sub>2</sub> nanopores with respect to the blockades current produced for each type of analyte.



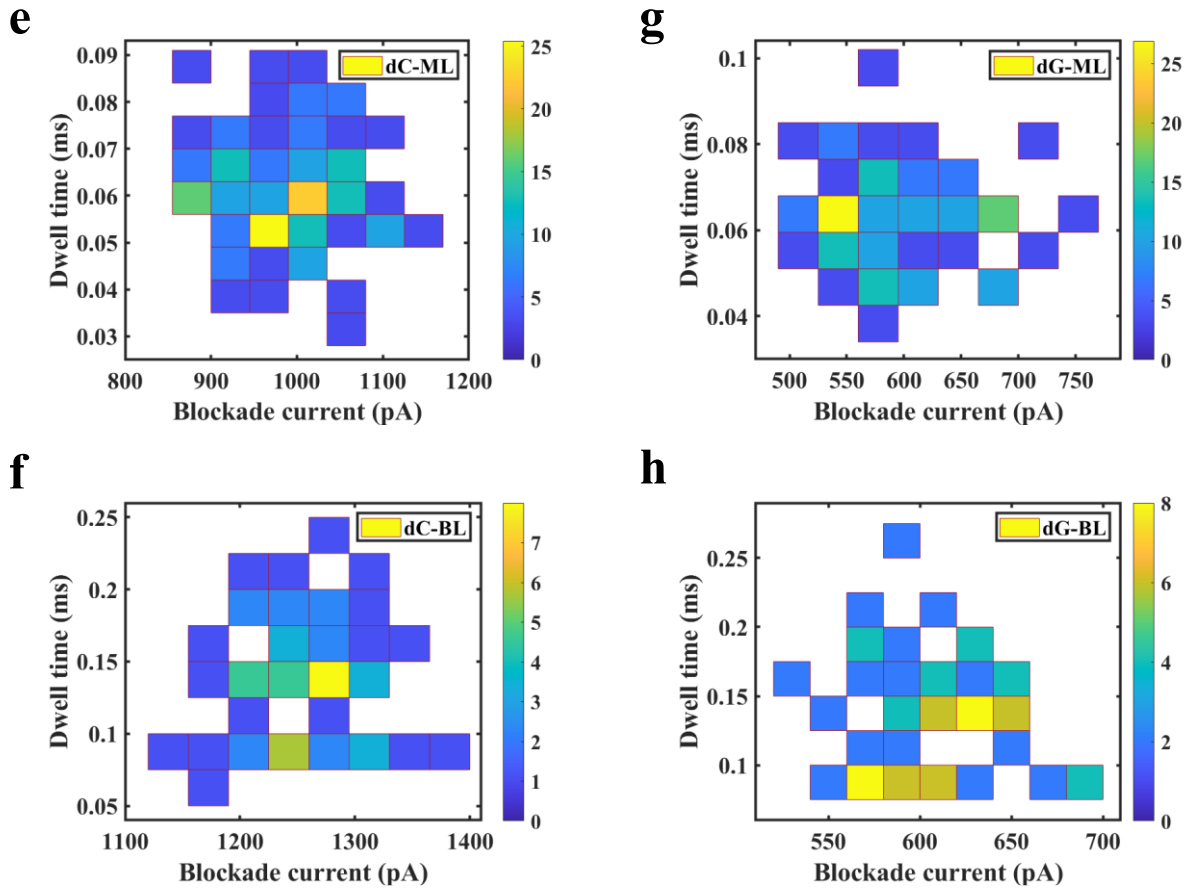


**Figure B- 5.** 2D flat density plots showing distribution of polynucleotide traces with respect to both blockade current and dwell time with ML pores demonstrating highest density of peaks at 0.05-0.07 ms dwell time and BL pores showing highest density of peaks at 0.06-0.14 ms.

**Table B- 1.** T-test results conducted on ~300 nucleotides (each for dA, dT, dG and dC) and polynucleotide molecules (dA30, dT30, dC30) translocated through ML and BL MoS<sub>2</sub> nanopores.

Analyte type	Dwell time difference (ms)	Confidence interval (ms)	p-value
--------------	-------------------------------	-----------------------------	---------

dA	0.0879	0.0785 - 0.0973	1.10E-39 (<0.05)
dT	0.0853	0.0764 - 0.0942	7.65E-43 (<0.05)
dC	0.0813	0.0720 - 0.0905	1.37E-36 (<0.05)
dG	0.0797	0.0691 - 0.0902	2.81E-28 (<0.05)

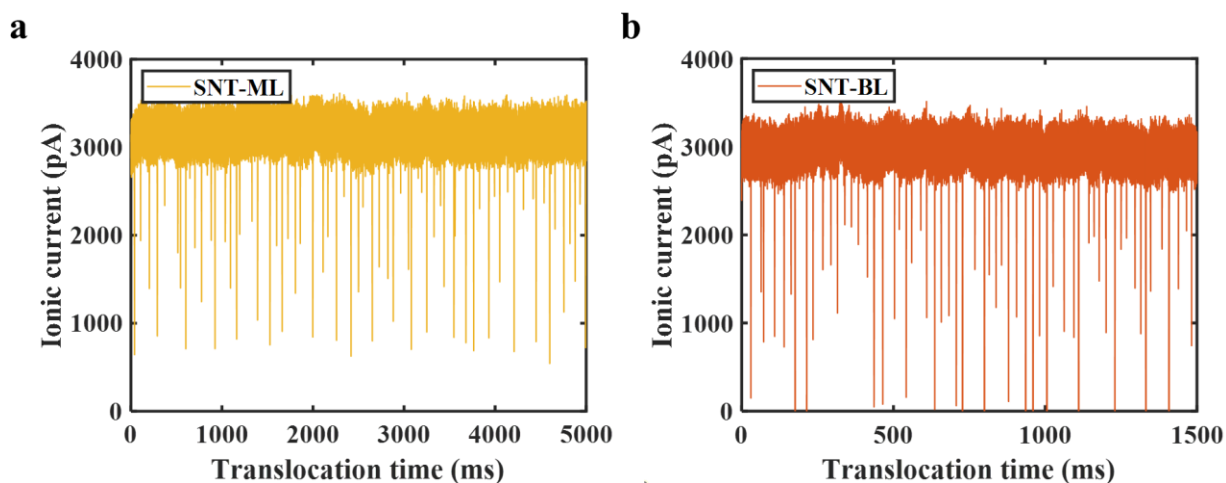


**Figure B- 6.** Translocation traces for a mixture of the four nucleotides through (a) ML and (b) BL MoS<sub>2</sub> nanopores and (c) dwell time vs blockade current plot for the same.

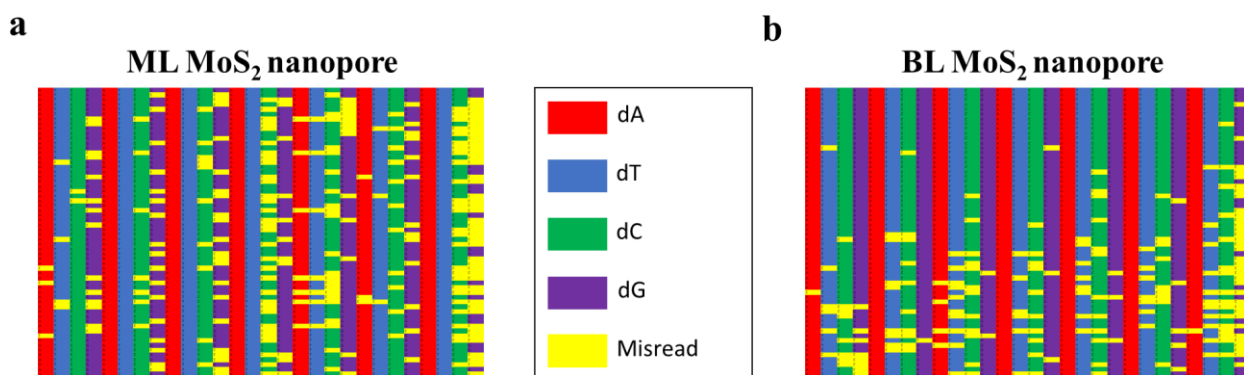


**Figure B- 7.** Color coded sequence for 60 ssDNA molecules (1800 nucleotides) detected through (a) ML and (b) BL MoS<sub>2</sub> nanopore: dA (red), dT (blue), dC (green), dG (violet) and undetected (yellow).

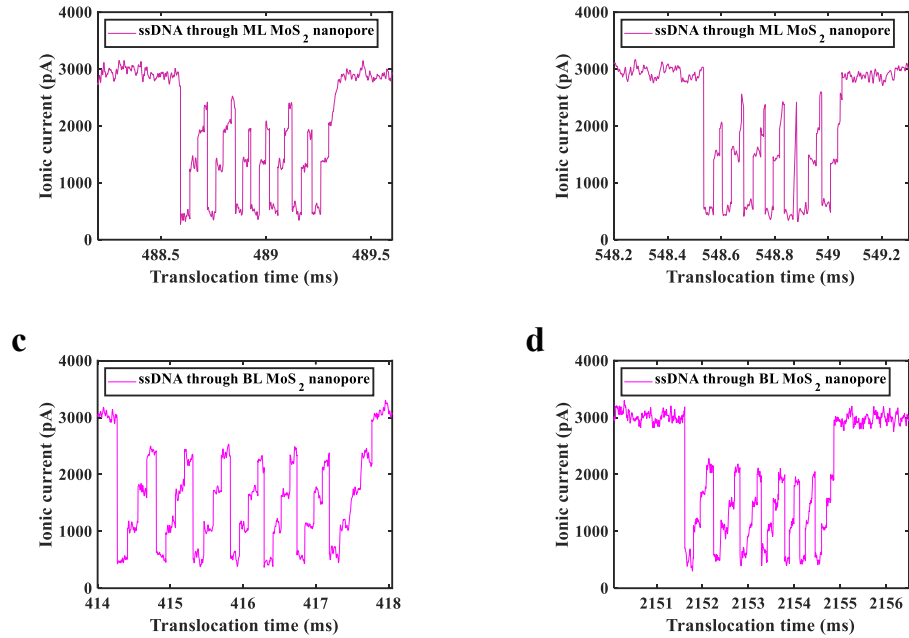


**Figure B- 8.** Few instances of 3'-5' sequencing of ssDNA translocation through (a-b) ML and (c-d) BL MoS<sub>2</sub> nanopores

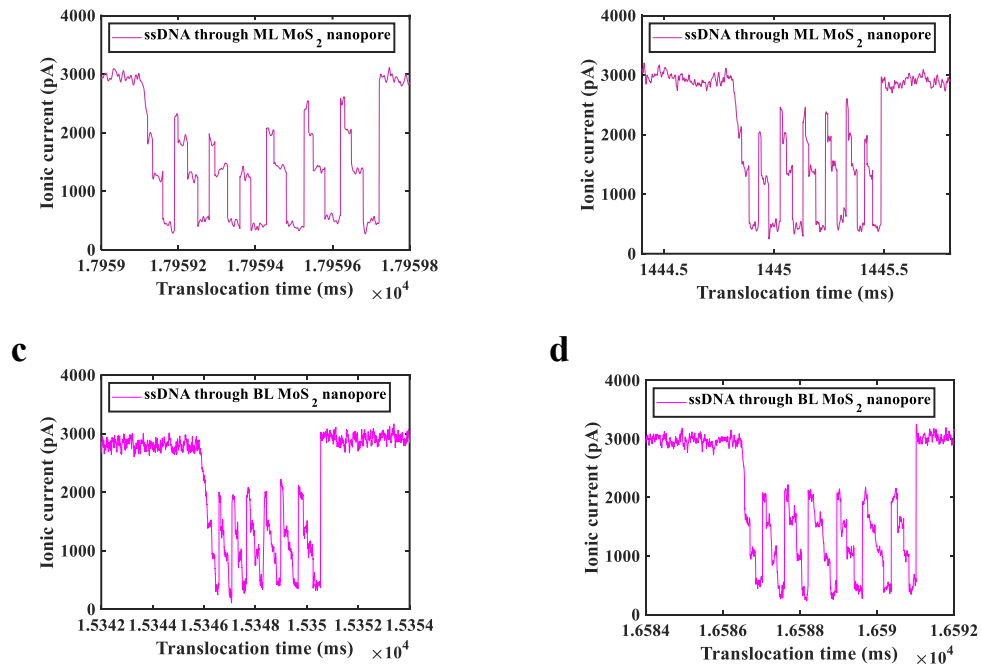


**Figure B- 9.** Few instances of 5'-3' sequencing of ssDNA translocation through (a-b) ML and (c-d) BL MoS<sub>2</sub> nanopores

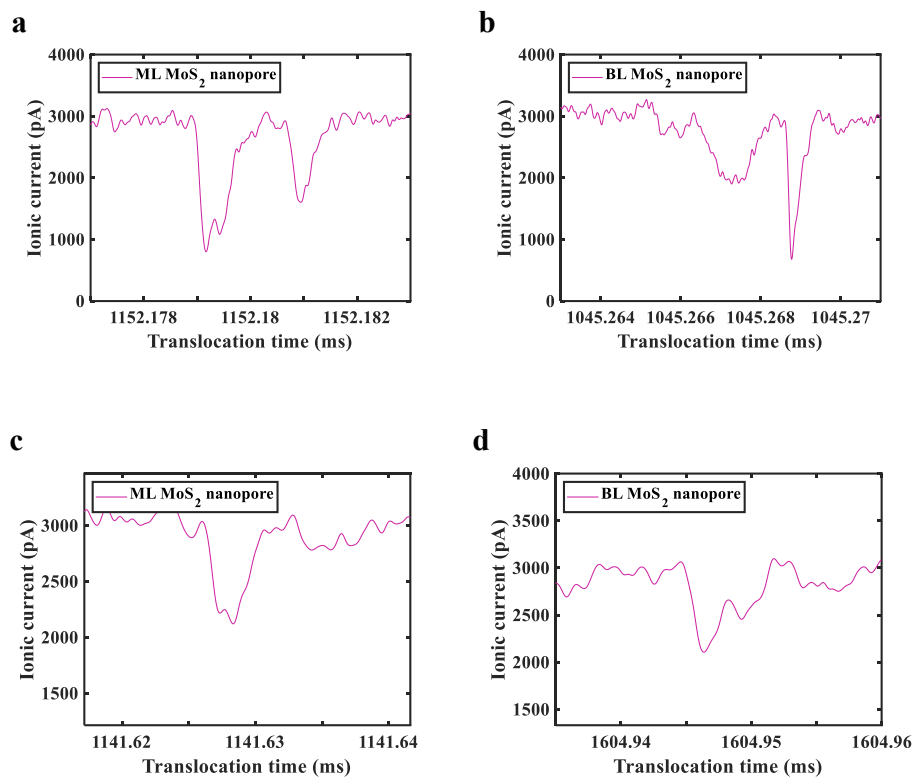


**Figure B- 10.** Transient ssDNA bouncing events observed for (a) ML MoS<sub>2</sub> and (b) BL MoS<sub>2</sub> nanopore and single nucleotide non-translocation interactions observed for (c) ML MoS<sub>2</sub> and (d) BL MoS<sub>2</sub> nanopore.

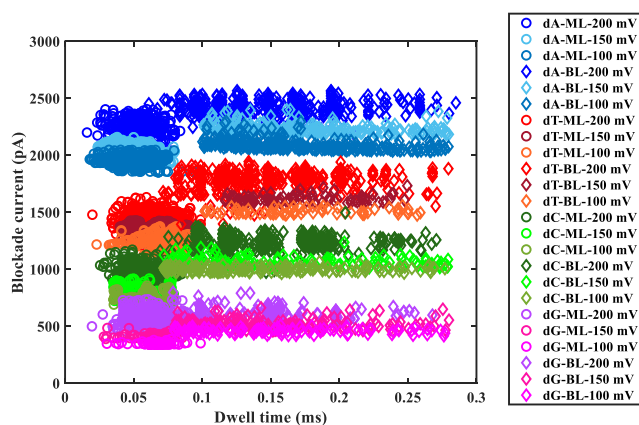


**Figure B- 11.** Blockade current vs dwell time scatter plot for single nucleotide translocations through ML and BL MoS<sub>2</sub> nanopores for 100 mV, 150 mV and 200 mV transmembrane bias.

## Chapter 7 <sup>4</sup>(Paper 4)

**This chapter** discusses the study on development of a hybrid nanopore formed by combining outer membrane porin G (biological nanopore) in solid-state bilayer MoS<sub>2</sub>, having a suitable size for easy and stable hybrid nanopore formation. The reason for using bilayer MoS<sub>2</sub> as the solid-state nanopore is discussed in **Chapter 6**. This chapter also discusses the reason and process of modifying the porin in order to reduced pH-dependent gating and reduce low-frequency noise. Polyadenine strands (length- 30 nucleotides) were then translocated through the hybrid pore and this chapter discusses the complete analysis to infer on the role of hybrid nanopore on DNA molecule sensing with improved temporal resolution and signal-to-noise ratio.

### **7 Low noise engineered OmpG and bilayer MoS<sub>2</sub> hybrid nanopore**

*Payel Sen, Hiofan Hoi, Manisha Gupta\**

Payel Sen

Department of Chemical and Materials Engineering

University of Alberta

Edmonton, Canada

Email: [payel@ualberta.ca](mailto:payel@ualberta.ca)

---

<sup>4</sup> Manuscript under review in ACS Applied Biomaterials

Hiofan Hoi

Department of Chemical and Materials Engineering

University of Alberta

Edmonton, Canada

Email: [hiofan@ualberta.ca](mailto:hiofan@ualberta.ca)

Manisha Gupta

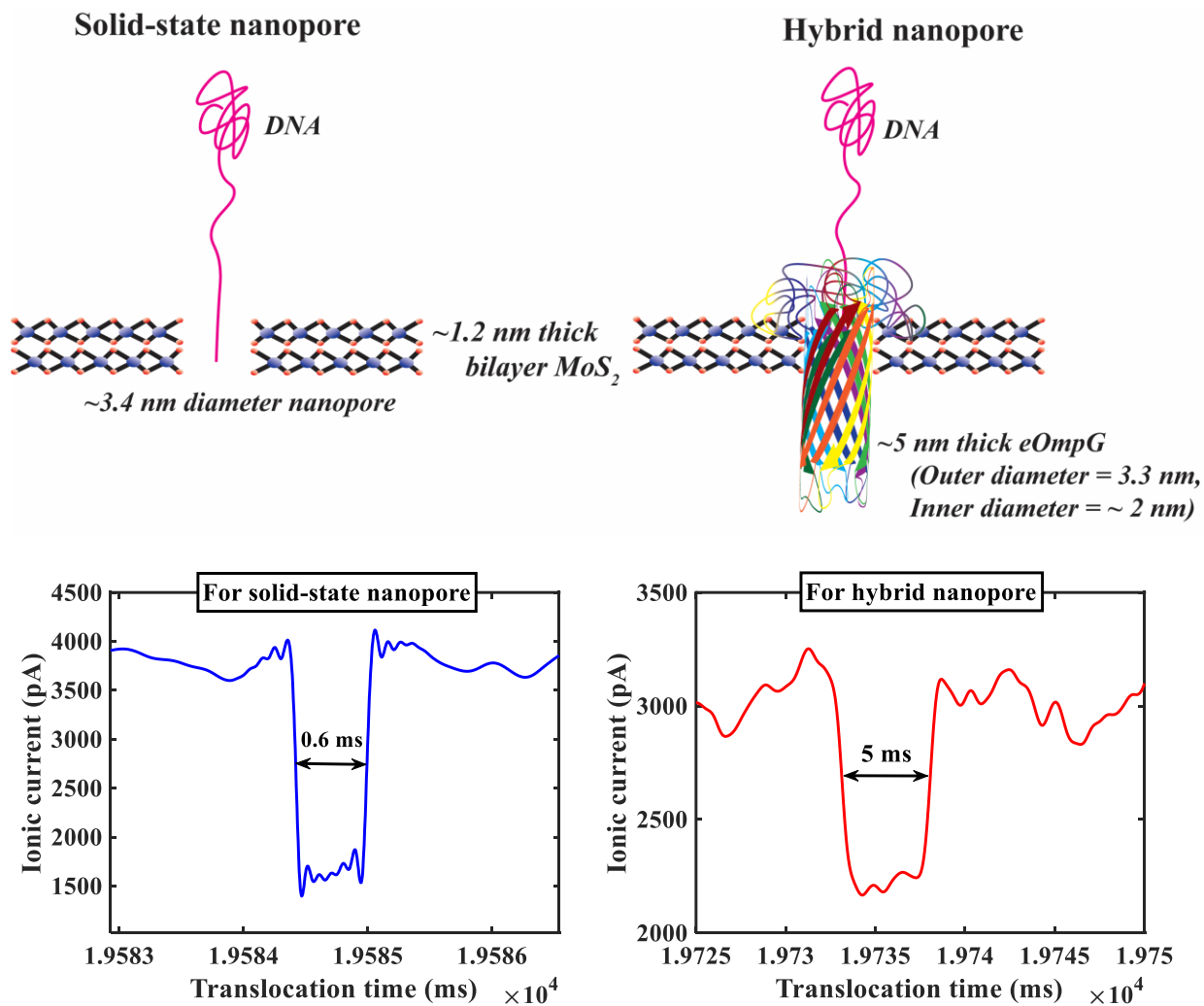
Department of Electrical and Computer Engineering

University of Alberta

Edmonton, Canada

Email: [mgupta1@ualberta.ca](mailto:mgupta1@ualberta.ca)

## Graphical Abstract



### 7.1 Keywords

Hybrid nanopore, bilayer  $\text{MoS}_2$ , outer Membrane Porin G, DNA sensing, noise analysis

## 7.2 Abstract

Hybrid nanopore combine the durability of the solid-state nanopore with the precise structure of the biological nanopore. When a DNA strand is pulled electrophoretically through a solid-state nanopore it can be sensed from the ionic blockades current produced by each translocating molecule. However, owing to the lack of chemical specificity and pore size reproducibility, solid-state nanopore sensing suffers from poor repeatability. Biological nanopores which have a constant geometry ensures sensitive and repeatable sensing. In this study, hybrid nanopores were formed by insertion of engineered outer membrane porin G (eOmpG) in a molybdenum disulfide ( $\text{MoS}_2$ ) solid-state nanopore. Engineered outer membrane porin G (eOmpG) is used as the biological counterpart of the hybrid nanopore due to its uniform cylindrical geometry and controlled gating useful for specific detection of label-free analytes. Bilayer (BL)  $\text{MoS}_2$  is used as the solid-state support for the hybrid construct owing to its surface charge and 2D layered properties, which ensures a stable support with low capacitive noise, favourable for precise sensing. Single eOmpG was electrophoretically pulled through a 3.4 nm solid-state BL  $\text{MoS}_2$  nanopore at neutral pH and +80 mV trans bias, to realize the hybrid nanopore. Hybrid BL  $\text{MoS}_2$  - eOmpG nanopore was found to demonstrate 32% lower noise levels with nearly 1.9 times improvement in the signal to noise ratio (SNR) and 6.5 times longer dwell times for dA30 molecular sensing compared to solid-state BL  $\text{MoS}_2$  nanopore. The low-noise biocompatible platform of hybrid BL  $\text{MoS}_2$  - eOmpG nanopore can thus be used for highly resolved biomolecular sensing.

## 7.3 Introduction

Nanopore sensing is a technique by which single analyte molecules can be detected from the ionic current blockade they induce during their translocation through the nanopore [13], [51], [52], [54],

[125], [187], [189], [226]. An application of nanopore sensing is sequencing biopolymers like Deoxy-ribonucleic acid (DNA) and Ribonucleic acid (RNA). Mainly, three types of nanopores are being explored for molecular sensing (DNA sequencing in this case) i.e., biological, solid-state, and hybrid nanopore. Solid-state nanopores with strong pore walls are ideal for making reusable and portable sensors [51], [96], [98], [227]–[235]; however, they often fail to reproduce sensed signals due to inconsistency in pore geometry. Ionic current fluctuations observed in solid-state nanopores are typically a result of high frequency noise which is characteristic to the pore material and low-frequency  $1/f$  noise which is subject to differ depending on the ion type and concentration, nanopore size, mechanical stability of membranes and ionic cross-flow [118], [188]. On the other hand, biological nanopores have a constant pore size producing highly repeatable signals. The sensitivity of a biological nanopore is influenced by both analyte interactions at the nanopore interface along with blockade events due to analyte translocations which results in improved single molecular sensitivity. It also results in improved manifestation of the weak and reversible analyte interaction with the nanopore producing easily distinguishable and prominent signals [236], [237]. Previous studies have reported that the mutant biological nanopores have shown better performance, sensitivity and temporal resolution compared to the wild pore [238], [239]. The controlled charge interaction and transport offered for biological nanopores also produce lesser electrical noise compared to solid-state nanopores [236], [237]. According to previous studies biological pores demonstrate better signal-to-noise ratio and lower noise levels as compared to the solid-state nanopores [20], [61], [64], [154], [236], [237] However, biological nanopores are thermo-mechanically unstable and have low durability [54], [118], [188], [189], [236]–[239]. A hybrid nanopore (combination of solid-state and biological nanopore) helps achieve repeatable blockade current with strong device framework [61], [64], [154].

In hybrid nanopore, the sensing is conducted primarily through the biological part which is inserted in a solid-state nanopore. Thus, the spatial resolution does not get affected by the thickness of the solid-state membrane. The spatial resolution in hybrid nanopore is mainly governed by the diameter and height of the biological nanopore. However, if the thickness of solid-state membrane is high, it increases the capacitive noise [20], [240] reducing the signal to noise ratio (SNR). The solid-state nanopore material and size is also important to ensure a spontaneous biological nanopore insertion and a stable hybrid assembly, two factors essential for cost-effective and prompt detection. Considering these factors, 2D material Molybdenum disulphide ( $\text{MoS}_2$ ) [221], [230], [231] forms a suitable solid-state membrane in terms of geometry and charge interactions to form a hybrid nanopore.

Different types of biological nanopores have been explored for developing a hybrid nanopore [20], [61], [64], [130], [154]. Alpha hemolysin is commonly used as the biological counterpart of the hybrid nanopore [64], [127]–[129], [131]. A  $\sim 2$  nm inner diameter and hydrophilic inner walls makes it a promising sensor for small molecules. The non-uniform mushroom-structure ensures its stable insertion in a solid-state nanopore [64], [127]. Recently, Outer Membrane Porin G (OmpG) is emerging as a biological pore for sensing analytes over a wide size range [151], [153], [172]. OmpG is a 32 kDa, 14 stranded monomeric porin that has a uniform barrel-shaped structure allowing easy insertion in the solid-state nanopore [153]. The symmetry also allows uniform surface charge interaction with the translocating or binding analyte. Another advantage of OmpG nanopore is its gating phenomenon by which the permeability of the pore to analytes and ions can be regulated. This can be attained by changing the OmpG environment. OmpG has 7 extracellular loops, which respond differently with change in pH, ionic or electric conditions. The discrete changes in protein dynamics induces more specific ionic current signals for analyte identification,

without additional functionalization. The gating effect depends on a lot of factors including the proximity of the analyte with OmpG; charge interactions between OmpG and analyte and conformation changes of the flexible groups. Such flexibility of the loops leads to high selectivity and sensitivity of OmpG nanopores which is an advantage. OmpG switches between open (permeable) and closed (non-permeable) states with change in voltage or solution pH, thus making fine tuning of the nanochannel possible. However, OmpG can experience spontaneous gating due to minute changes in sensing environment, which may lead to unnecessary fluctuations during sensing [151], [172]. Therefore, to ensure controlled gating, OmpG may require additional structural and chemical modifications. Fortunately, OmpG allows easy adaptation of the loops by introducing mutations in the amino acid sequence, which provides easy and better control on the signal stability and resolution required for molecular sensing.

One of the common techniques of achieving a stable and aligned insertion of the biological nanopore in the solid-state nanopore is by using a DNA guide, tethered to the biological nanopore [127]. Research showed coaxial alignment of alpha hemolysin with the solid-state nanopore is hindered without a tethered DNA [130]. In this work, we observed the ability of lone eOmpG to self-direct, insert into and align with the solid-state bilayer (BL) MoS<sub>2</sub> nanopore without any attached DNA [154]. Here, we have explored the hybrid nanopore stability using MoS<sub>2</sub> solid-state pore and eOmpG. BL MoS<sub>2</sub> has been used owing to its thickness to obtain a more stable solid-state support for the hybrid nanopore formation. A short single stranded (ss) polyadenine (dA<sub>30</sub>) strand containing 30 nucleotides was sensed through the hybrid nanopore. This hybrid nanopore demonstrates much lower noise than its solid-state counterpart. This study presents a novel approach towards unfunctionalized and stable hybrid BL MoS<sub>2</sub> nanopore based biosensing at picomolar analyte concentration.

## 7.4 Results and Discussions

Hybrid nanopores were obtained using BL MoS<sub>2</sub> and engineered OmpG (eOmpG). 2D materials owing to their thickness provide pore fabrication with repeatable size with an error of  $< 2\text{\AA}$  using Transmission Electron Microscopy. **Figure C-1** shows a few examples of four different fabricated pores having  $\sim 3.4$  nm diameter, showing the fabrication repeatability and controllability of BL MoS<sub>2</sub> nanopores. These nanopores were fabricated using an exposure time of 5 sec using 40 mrad corrected probe at 200 kV in the STEM mode. The complete fabrication and characterization procedure of bilayer MoS<sub>2</sub> membranes used for our study is presented in our previous work [241]. Our previous study confirms the structure of the BL MoS<sub>2</sub> membrane through HRTEM characterization and the corresponding diffraction pattern showing two overlapped hexagons. **Section 7.5** explains the details of the OmpG modifications and characterizations carried out before using it for the pore application. **Figure 7.1.a** shows the HRTEM (High Resolution TEM) image of the fabricated 3.4 nm diameter BL MoS<sub>2</sub> nanopore. In order to ensure a single eOmpG is inserted, MoS<sub>2</sub> nanopore diameter is kept just greater than the outer diameter of a single eOmpG nanopore. A single eOmpG was pulled through the MoS<sub>2</sub> nanopore to observe the ionic conductance before and after hybrid pore formation. **Figure 7.1.b** shows a schematic of the hybrid eOmpG-BL MoS<sub>2</sub> nanopore.

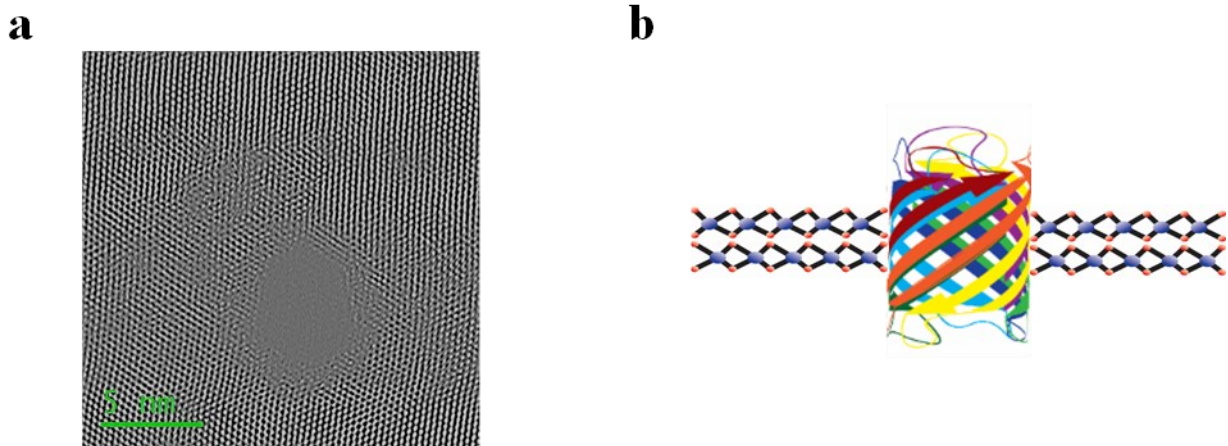
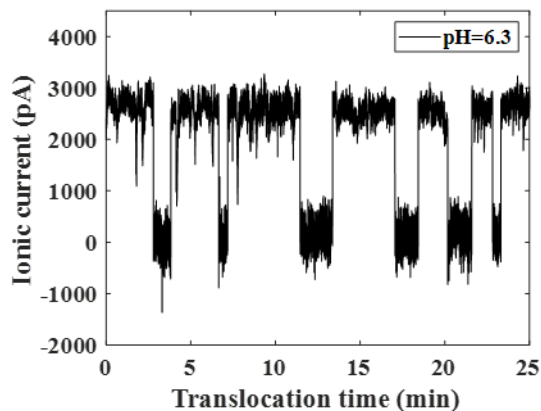


**Figure 7.1.** (a) HRTEM image of a  $\sim 3.4$  nm diameter solid-state pore on BL ( $\sim 1.2$  nm thick) MoS<sub>2</sub> membrane and (b) simple schematic of eOmpG integrated BL MoS<sub>2</sub> hybrid nanopore.

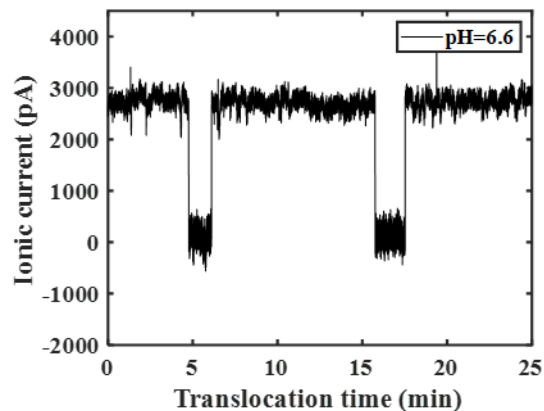
The open probability of the eOmpG in the pH range of 6.3-7.4 was tested using Tris-HCl. It was found that the time for which eOmpG remains open after its insertion into the nanopore reduces with increase in acidity. **Figure 7.2.a-d** shows spontaneous gating of single eOmpG through BL MoS<sub>2</sub> nanopore at varying pH for a time span of 25 min. The opening time of the eOmpG was measured with different pH and this is plotted in **Figure 7.2.e** as a function of pH. The eOmpG open probability (as extracted from **Figure 7.2.e**) is  $0.68 \pm 0.11$  for pH = 6.3,  $0.9 \pm 0.07$  for pH = 6.6,  $0.99 \pm 0.0084$  for pH = 7.0 and  $0.94 \pm 0.08$  for pH = 7.4. The close probability of eOmpG is found to be significantly low at neutral pH. There can be a few explanations for such the varying open probabilities of OmpG. OmpG has seven extracellular loops of which the configuration and flexibility of loop 6 (L6) controls its gating. The dynamics of L6 can cause the channel to open or close depending upon whether it is drawn inside the lumen or repelled from it. This motion is influenced by the protonation and deprotonation of the outer loops of OmpG. Acidic pH unlike neutral pH necessarily can be directly related to an increased protonation resulting in increased instability of the  $\beta$ -strand leading to comparatively more gating at pH < 7. Previous studies

conducted have also demonstrated that the open probability of OmpG depends strongly on the energy of the system [242], [243]. At pH = 7 the open configuration of eOmpG is found to be at the lowest energy compared to acidic or alkaline pH thus restricting loop relaxation and showing the least gating frequency [242], [243].

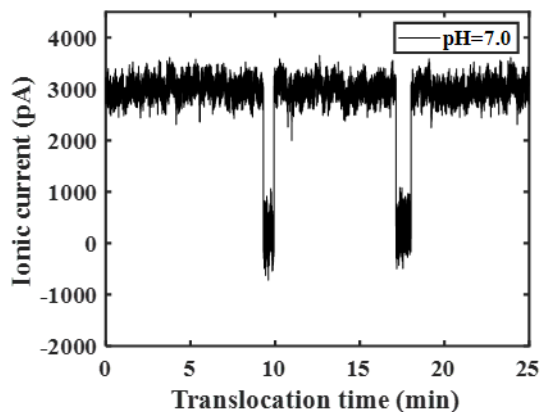
**a**



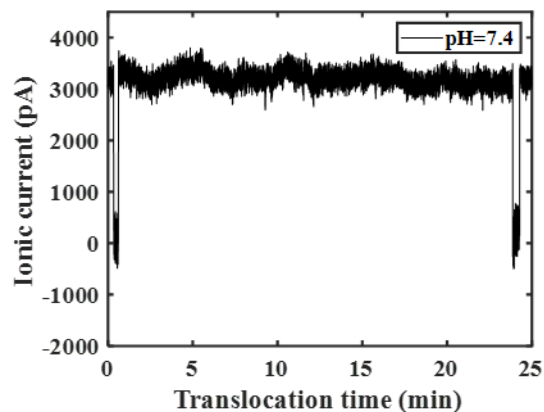
**b**



**c**



**d**



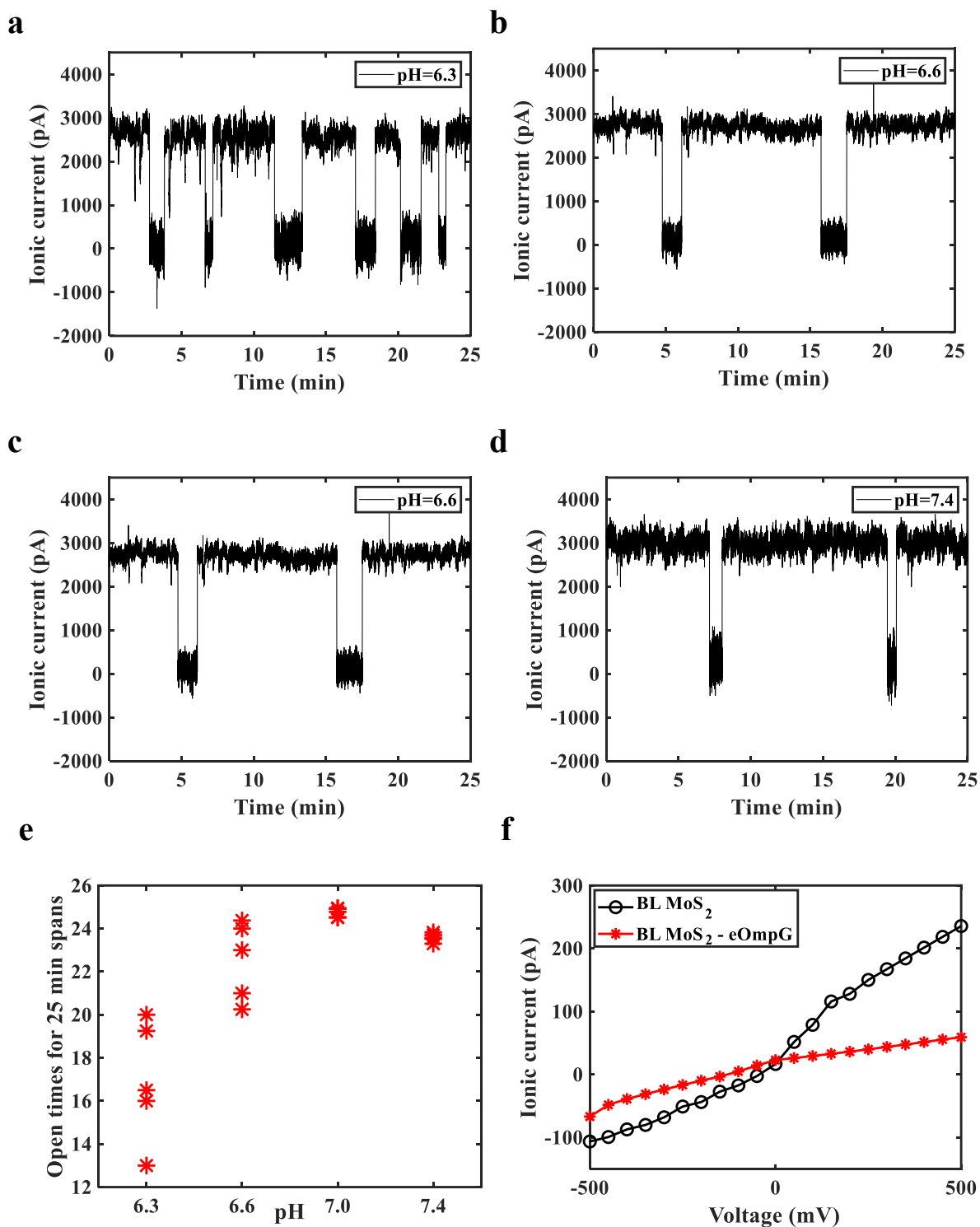


**Figure 7.2.** (a-d) eOmpG spontaneous gating at a constant voltage of 200 mV, through BL MoS<sub>2</sub> at pH = 6.3, pH = 6.6, pH = 7.0 and pH = 7.4 respectively using 10 mM KCl, (e) scatter plot for

eOmpG open times for five traces noted for 25 min each, showing improved hybrid nanopore stability at pH = 7 with an open probability of 99 % and (f) Ionic current vs voltage plot using 10 mM KCl before and after eOmpG insertion into the fabricated BL MoS<sub>2</sub> nanopore at neutral pH showing that the pore exhibits stable attachment at positive voltages and detaches at negative voltages.

To further test hybrid nanopore stability at positive and negative voltages before and after eOmpG insertion the ionic current was recorded for a trans bias of -200 mV to 200 mV and after eOmpG insertion the ionic current was recorded for a trans bias of -200 mV to 200 mV using 10 mM (Figure 7.2.f) and 100 mM KCl (Figure C- 2). The I-V profiles for ionic conduction through solid-state and hybrid MoS<sub>2</sub> nanopores are shown in Figure 7.2.f. From the curves we can observe that the hybrid assembly shows good stability at positive voltages but becomes unstable at negative voltages. Beyond -100 mV trans bias, the ionic current of the hybrid nanopore becomes similar to a solid-state nanopore indicating detachment of eOmpG. Thus, a positive bias of 80 mV was maintained on the trans to ensure that eOmpG was inserted in the nanopore. 10 pM dA30 was added to the cis side solution and pulled electrophoretically at 100 mV bias. Then after hybrid pore formation, bias is increased slowly to 200 mV to record the DNA translocation traces.

Translocation traces were recorded for 60 min.

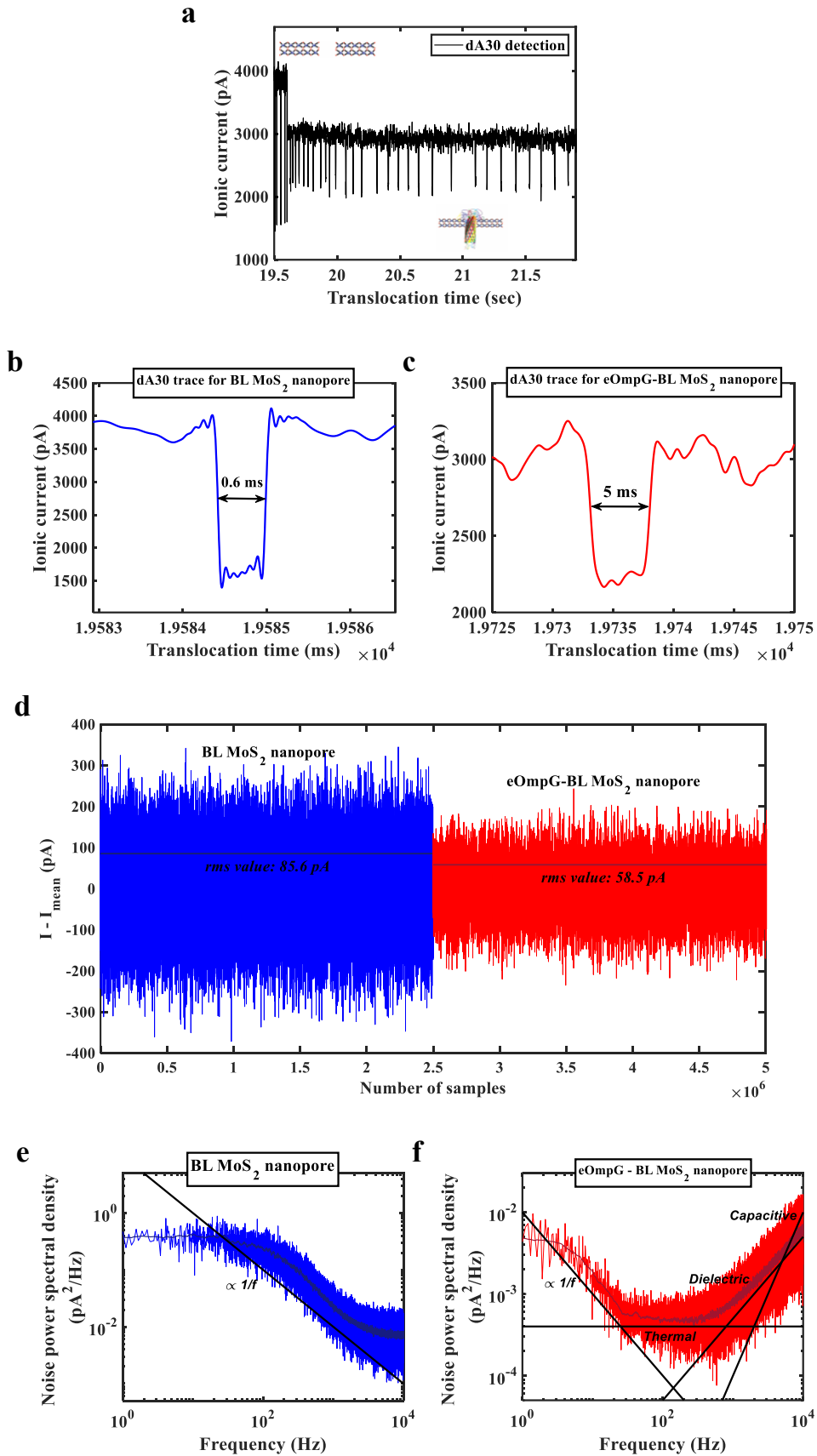


**Figure 7.3.** (a) Single dA30 molecule translocation traces through 3.4 nm diameter solid-state BL MoS<sub>2</sub> pore showing a steep drop of 1 nA at around 20 sec indicating single eOmpG insertion, insets showing schematics of solid-state and hybrid pore, (b) dA30 molecular sensing event through BL MoS<sub>2</sub> nanopore showing a molecular dwell time of about 6 ms, (c) dA30 molecular sensing event through hybrid eOmpG-BL MoS<sub>2</sub> nanopore showing a molecular dwell time of about 50 ms (6.5 times larger than the solid-state BL MoS<sub>2</sub> nanopore with 95% confidence), (d) Noise traces ( $I - I_{\text{mean}}$ ) of 2.5E6 samples that is 12.5 sec data at a sampling frequency of 20 kHz for solid-state (with 3.4 nm diameter) and hybrid (with 2.2 nm inner diameter) eOmpG-BL MoS<sub>2</sub> nanopores. A reduction in the noise level is observed after hybrid nanopore formation.  $I$  and  $I_{\text{mean}}$  are the ionic and the mean ionic current respectively., (e-f) Noise power spectral density (evaluated by pwelch method at cut-off frequency of 1 Hz) for 1.25E7 samples that is for ~1 min data of at a sampling frequency of 20 kHz (after the traces are high-pass filtered at 1 Hz for eliminating baseline fluctuations) for solid-state and hybrid nanopore. The dark blue and dark red traces showing moving average of the noise spectra for solid-state and hybrid nanopores respectively. The plots show reduction of low-frequency noise after hybridization, but the high frequency noise (>1 kHz) remains almost similar, although the trend and contributions differ.

**Figure 7.3.a** shows transient current drops for single dA30 translocation through solid-state and eOmpG hybridized MoS<sub>2</sub> nanopore. The initial phase shows molecular blockades through the solid-state nanopore. eOmpG insertion is found to occur after 30-40 min of dA30 introduction every time. A 1 nA drop in ionic current indicates eOmpG integration inside the MoS<sub>2</sub> nanopore. We also observed r molecular (dA30) dwell time of ~0.6 ms for solid-state BL MoS<sub>2</sub> nanopore (**Figure 7.3.b**) and ~5 ms for hybrid eOmpG-BL MoS<sub>2</sub> nanopore (**Figure 7.3.c**). A capture rate of 14-18 nucleotides per second was obtained for the hybrid nanopore, which is about three-fold

lower than what was observed for a solid-state bilayer MoS<sub>2</sub> nanopore [241]. **Table C- 1** shows the results of T-test performed on a sample population of 1000 events for both solid-state and hybrid sensing. The dwell time with hybrid nanopore is 6.5 times longer than that of the solid state nanopore with 95% confidence. This provides an improved time resolution along with an improved sensitivity as the translocation speed is reduced.

Now, to obtain detection with good reliability and confidence, it is necessary to reduce noise interference and the other sources of current deviations. We therefore analyzed the noise before and after eOmpG integration. The signal is filtered using a high pass Butterworth filter (MATLAB) to eliminate baseline drift. We estimated the cut-off frequency to be 1 Hz for which the baseline shift is removed without significantly affecting the noise spectrum. The mean ionic current ( $I_{\text{mean}}$ ) is then subtracted from the obtained ionic current ( $I$ ) and plot in **Figure 7.3.d** to analyze the noise traces for both solid-state and hybrid nanopore systems. Solid-state pore is seen to produce higher deviations around the baseline current (RMS noise: 85.6 pA), whereas hybrid pore produces a quieter signal (RMS noise: 58.5 pA), inferring a 31.7 % reduction in noise levels by eOmpG insertion (see **Figure 7.3.d**). Nanopore noise can have contributions of low frequency ( $1/f$ ) and high-frequency (dielectric, thermal and capacitive) noises [20], [215].

**Equation 7.1.**

$$\text{Noise} = c_1 \frac{1}{f} (\text{low frequency}) + c_2 (\text{thermal}) + c_3 f (\text{dielectric}) + c_4 f^2 (\text{capacitive})$$

The noise power spectral density of solid-state and hybrid nanopores is then evaluated by pwelch method for ~1 min data (1.25E7 samples) and plotted in **Figure 7.3.e** and **Figure 7.3.f** respectively. The noise spectra are then intercepted with low and high frequency noise components indicated in **Equation 7.1**, to understand their contributions to the resultant noise. As can be seen from

**Equation 7.1**, thermal noise is independent of frequency whereas the  $1/f$  noise, dielectric and capacitive noise are functions of frequency.  $1/f$  noise therefore becomes dominant at lower frequencies whereas dielectric and capacitive noises being proportional to the frequency becomes appreciable at high frequency regimes.

To understand the noise contributions for the BL MoS<sub>2</sub> solid-state nanopore, the noise spectra obtained was intercepted with  $1/f$  curve as shown in **Figure 7.3.e**. It is observed that the noise is predominantly due to the  $1/f$  component. The high quality SiN<sub>x</sub> substrate used along with a small free-standing area of 200 nm reduces parasitic capacitive noise. Additionally, low dielectric constant and small thickness of BL MoS<sub>2</sub> results in low membrane capacitance and dielectric loss. Thus, for the solid-state BL MoS<sub>2</sub> nanopore the high frequency noise is very low levels (Power spectral density (PSD) is  $<10^{-2}$  above 1000 Hz with negligible capacitance and dielectric noise contributions) as shown in **Figure 7.3.e**. With the incorporation of eOmpG in the BL MoS<sub>2</sub> nanopore the noise signature changes. For the hybrid nanopore we observe significant contribution of dielectric and capacitive noise (as seen from the high frequency domain of **Figure 7.3.f**), which primarily is characteristic to the nanopore type used and usually remains the same for a particular type of nanopore. Therefore, for obtaining a good SNR one needs to control and reduce the low frequency noise. Particularly, for biological nanopore, the  $1/f$  noise has major influence of protonation/deprotonation occurring at the nanopore interface. Specific structural modifications of the biological nanopores can reduce electrokinetic noise response to the charge fluctuations, thus reducing the low frequency noise and improving the SNR. The H231E mutation introduced in the eOmpG reduces its spontaneous gating [152] which ensures a stable behavior and reduction of low-frequency protonation noise [20], [244]. Additionally, the deletion of Loop 6 (by changing W217 to A217) also contributes to the  $1/f$  noise reduction [245] of the protein during sensing. This

reduces the low frequency (1-20 Hz)  $1/f$  noise spectral density of the hybrid nanopore by 2 orders of magnitude as can be observed from **Figure 7.3.f**. The resultant RMS noise for hybrid nanopore is also found to be lower as compared to the solid-state nanopore (RMS value: 85.6 pA, as mentioned earlier). The SNR was then calculated from the ratio of the blockade signal value and the RMS noise values [20], [246]. SNR values for the solid-state pore is found to be  $\sim 12.4$  whereas for the hybrid pore is found  $\sim 23.3$ , showing a 1.9 times improvement of SNR for dA30 sensing through the eOmpG-BL MoS<sub>2</sub> hybrid.

The blockade current spectra were then analyzed to obtain the translocation event distribution. A unimodal normal distribution of events is observed with respect to current blockades (**Figure 7.4.a**), with a mean blockade current of  $725 \pm 185$  pA (25% deviation). The signal deviation obtained from the hybrid nanopore sensing is found to be 8 % lower than that observed through solid-state BL MoS<sub>2</sub> nanopore. The unimodal curve also suggests minimal leakage current along the protein boundaries creating a great hybrid pore for DNA sensing. On the other hand, the distribution shows a bimodal fit with respect to dwell time (**Figure 7.4.b**) with lower density of peaks between 2-4 ms and highest between 4-7 ms. Bimodal dwell time distribution for biological and hybrid interfaces can happen due to the considerable length of the biological (OmpG in our case) nanopore. During analyte translocation and sensing, another molecule may or may not be at the mouth of the OmpG pore thus varying the translocation speed of the sensed analyte by varying electrostatic interactions. 2D material solid-state nanopores due to their thinness do not face competition from other molecule at the same time an analyte is sensed leading to unimodal distribution [241].

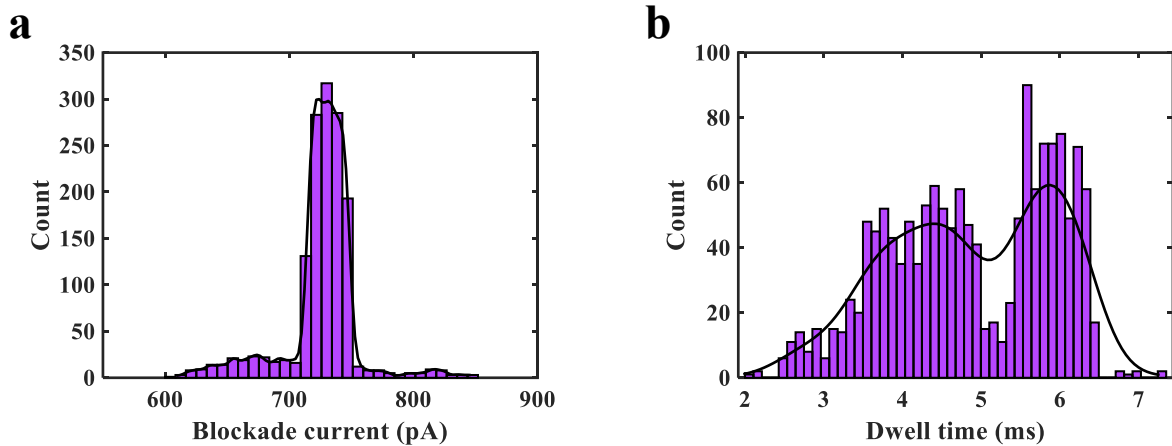


**Figure 7.4.** (a) Unimodal distribution of 1488 dA30 translocation events with respect to blockade current with blockades ranging between 600 to 850 pA having the highest density between 700-750 pA, (b) Bimodal distribution of dA30 events with respect to dwell times with molecular dwell times ranging between 2-7 ms having two closely placed peaks centered at 4.5 ms and 5.8 ms.

**Table 7.1** summarizes the relevant results for solid state, biological and hybrid nanopores from literature. The nanopore diameter, thickness, SNR, RMS noise and low frequency PSD are presented in the table. Hybrid nanopore thickness shown in the table is for the thickest component which could be either the solid-state membrane or the biological nanopore. The SNR, RMS noise and low frequency noise are strongly dependent on the nanopore type/material [20], [246], size/thickness [20], [246], free-standing area of the membrane [72], [74] and the electrolyte/concentration [72]. Thus, we are comparing nanopores of sizes similar to ours (1-5nm in diameter) here. It is observed that the electrolyte (KCl) concentration plays an important role in the nanopore SNR with it reducing with reduction of electrolytic concentration. Whereas the RMS noise of the nanopores has a reverse trend and increases with reduction of the electrolyte concentration.

**Table 7.1.** Comparison of SNR and RMS noise obtained for solid-state and hybrid nanopore with previous studies. Solid state, biological and hybrid nanopores from literature are shown here.

Type of nanopore	Pore diameter (nm)	Pore thickness (nm)	SNR	RMS noise (pA)	KCl concentration	Low frequency PSD (pA <sup>2</sup> /Hz)
<b><i>Solid state nanopores</i></b>						
Silicon nitride	3 [244]	20 [244]	~5 [244] ~45 [244]	—	0.1 M [244] 1 M [244]	—
	1.4 [20]	5 [20]	37 [20]	130 [20]	1 M [20]	
Graphene	4 [72]	0.35 [72]	—	115.39 [72], [246]	1 M [72]	~10 <sup>3</sup> [72]
	10 [74]	0.35 [74]	—	104.93 [74], [246]	1 M [74]	~10 <sup>3</sup> [74]
hBN	2.5 [215]	1.4 [215]	20 [215]	35 [215]	1 M [215]	—
ML MoS <sub>2</sub>	1.4 [20]	0.7 [20]	5 [20]	100 [20]	1 M [20]	—
	~2 [51]	0.65 [51]	>10 [51]	—	0.1 M [51]	—
BL MoS <sub>2</sub> [our study]	3.4	1.3	12	85.6	0.1 M	0.1-1
<b><i>Biological nanopores</i></b>						
Alpha hemolysin	1.4 [20]	5 [20]	11 [20]	8.8 [20]	0.1 M [20]	10 <sup>-3</sup> -10 <sup>-2</sup> [20]
MspA	1.2 [20]	0.6 [20]	4 [20]	40.2 [20]	0.1 M [20]	10 <sup>-4</sup> -10 <sup>-3</sup> [20]
<b><i>Hybrid nanopores</i></b>						

Alpha hemolysin-SiN <sub>x</sub>	1.4 [64]	20 [64]	—	—	1 M [64]	~10 <sup>-5</sup> [64]
Natural DNA pore - SiN <sub>x</sub>	2.3 [62]	30 [62]	—	—	n/a	10 <sup>-2</sup> -10 <sup>-1</sup> [62]
Hybrid BL MoS <sub>2</sub> - OmpG [our study]	2.2	5	23	58.5	0.1 M	10 <sup>-3</sup> -10 <sup>-2</sup>

A 9-fold reduction in the SNR of the SiN<sub>x</sub> nanopores is observed when the electrolyte, KCl, concentration is reduced from 1M to 100 mM [244]. The SNR for our BL MoS<sub>2</sub> nanopore 3.4 nm diameter is twice as compared to the 3 nm diameter SiN<sub>x</sub> nanopores at 100 mM KCl concentration [244]. As compared to 2D material nanopores, our 3.4 nm diameter BL MoS<sub>2</sub> nanopores (for 100 mM KCl) demonstrate ~1.35 times lower RMS noise compared to 4 nm diameter graphene nanopores (for 1M KCl). Also, 2.5 nm diameter hBN nanopore [215] demonstrate an SNR of 20 with an RMS noise of 35 pA for 1M KCl. For 1.4 - 2.5 nm ML MoS<sub>2</sub> nanopores, SNR is found to be ~5 for 1M KCl [129] and 10-16 (2-3 times better) for 100 mM KCl [51]. As the RMS noise levels increase and SNR reduces with lower KCl concentration we observe that BL MoS<sub>2</sub> nanopores demonstrate noise performance better than SiN<sub>x</sub> and graphene. Also, the performance of the BL MoS<sub>2</sub> nanopores is comparable to hBN and ML MoS<sub>2</sub> nanopores in terms of RMS noise and SNR. Also, for understanding, we have added the biological nanopore noise. The eOmpG-BL MoS<sub>2</sub> hybrid nanopore is found to demonstrate higher SNR as compared to both alpha hemolysin [20], [72] and MspA [20] biological nanopores. Additionally, our hybrid nanopore

noise PSD levels are found to be comparable with existing hybrid nanopores [62], [64] which are being used for DNA sensing.

This work introduces the advantage of using eOmpG hybrid with MoS<sub>2</sub> in creating a stable and reusable nanopore device which can be scaled to arrays for parallel sensing. Future work can be further conducted on the device for sensing single nucleotides by attaching a complementary DNA strand to the eOmpG nanopore. The low noise assembly of this hybrid nanopore can also ameliorate ionic fluctuation noise created due to dangling DNA strand. Thus, the eOmpG-BL MoS<sub>2</sub> hybrid nanopore can lead the way for low-noise, time-resolved and repeatable molecular sensing.

Here, we present the first realization of a hybrid BL MoS<sub>2</sub> nanopore. In our work, outer membrane protein G (OmpG) is used as the biological counterpart due to its unique gating properties along with low noise behavior which allows controlled detection of single DNA molecules. However, owing to the spontaneous gating tendencies of OmpG, the pore was engineered to reduce its gating dependency on the pH or ionic changes. A BL MoS<sub>2</sub> was used as the solid-state support owing to its stability and low capacitive noise due to its thickness which is good for low-noise detection.

The major contribution of lower noise obtained in this study is due to controlled and less turbulent ionic and analyte flow through OmpG. However, the surface charge interaction between positively charge molybdenum atoms at the surface of BL MoS<sub>2</sub> nanopore and the interlayer potential gradient also can neutralize some of the negative charge repulsion at the OmpG interface thus producing lower ionic current fluctuations as well. Therefore, we do believe that BL MoS<sub>2</sub> along with OmpG has a significant contribution towards hybrid nanopore stability and low-noise levels demonstrated by it.

In this work, we also demonstrate the unique ability of the untethered engineered OmpG (eOmpG) with outer diameter of 3.3 nm, to form a stable and well aligned hybrid nanopore within a suitably sized (3.4 nm) solid-state BL MoS<sub>2</sub> frame. We have employed a pore size of 3.4 nm in diameter for this work. As the outer diameter of eOmpG is ~3.3 nm we do not expect multiple OmpG insertions into the nanopore at the same time. However, an improper fit between eOmpG and BL MoS<sub>2</sub> nanopore is probable which can give rise to leakage current. Although this leakage current cannot be eliminated completely, we can observe very low leakage ionic current of ~20-40 pA for 100 mM KCl when the eOmpG is inserted into the nanopore and is closed (see **Figure 7.2**). Thus, the leakage current is very small and what we observe is the ionic current through the hybrid pore. The high conductance through the eOmpG may be due to many reasons. One of the reasons may be E163C/E229A/H231E modifications carried out on wild OmpG, which increases cationic contribution reducing loop repulsion and pore relaxation, thus making OmpG mutant more rigid allowing larger ionic flux [243]. Again, the behaviour is expected to be different for hybrid pore constructed from thicker silicon nitride and thin 2D materials like MoS<sub>2</sub> as well. Since the thickness of BL MoS<sub>2</sub> is lesser than the OmpG pore, the functionalization occurs at the mouth of the nanopore only. We therefore anticipate a significant contribution of BL MoS<sub>2</sub> and the way it concentrates electric potential at the nanopore to the ionic flux through the hybrid pore. Previous studies on DNA origami nanopores has also shown higher conductance within a graphene-based hybrid construct compared to one on lipid bilayers [61]. Also, biological pores on lipid bilayers are operated at low voltages (+50 mV) compared to higher 200 mV bias used for our work.

However, we agree that it requires further study to draw a direct correlation between the OmpG composition, relaxation, and ionic conductance, and confidently comment on the ionic

conductance of the resultant hybrid pore and the contribution of solid-state membrane, which will be explored in future.

We demonstrated 10 pM single dA30 polynucleotide molecular detection through the hybrid nanopore at +80 mV bias and neutral pH with highly time-resolved (>2 ms) signals, 31.7 % reduced noise, 8 % lower current deviation and 1.9 times improved SNR compared to solid-state BL MoS<sub>2</sub> nanopore acting alone. Our analysis also leads the way for highly reliable low-noise biomolecular detection over a wide size range.

## 7.5 Methods

Double-side LPCVD (low stress) silicon nitride (SiN<sub>x</sub>) coated 4 inch, 525 ± 25 μm, <100> silicon wafers were purchased from Rogue Valley Microdevices. Low defect, high purity, MoS<sub>2</sub> crystal (15×10 mm) was purchased from 2D semiconductors. Rest of the reagents were obtained from Fisher Sci. 25.5 n-moles single-stranded (ss) polyadenine (dA30) strand containing 30 dA nucleotides in 250 μl solution was bought from Integrated DNA technologies.

### 7.5.1 Protein engineering and characterization

Engineered OmpG-Δ216-228/E163C/E230A/H231E (eOmpG) was created to minimize pH-change dependent spontaneous gating and ensure that OmpG remains open and stable above its open-channel voltage. A single cysteine mutation was made at E163, several amino acid residues 216-228 were deleted, glutamate 230 was changed to Alanine and Hystidine 231 was changed to glutamate. **Figure C- 3** shows the sequence of wild-type OmpG (wOmpG) and engineered OmpG (eOmpG). For refolding, the pooled protein was mixed with the refolding buffer (20 mM Tris–HCl, 2 mM DTT, 3.25% OG, pH 9.0) at 2:3 volume ratios and incubated with gentle shaking at 37 °C overnight. Refolding was confirmed by the band shift as observed on SDS-PAGE (**Figure**

C- 4). The refolded OmpG was then buffer exchanged into the storage buffer (20 mM Tris-HCl, 2 mM DTT, 150 mM NaCl, 10% (v/v) glycerol, 0.7%OG, pH 8.0 using desalting column.

eOmpG was characterized in lipid bilayers (DPhPC and POPG/POPE). Gating activity was observed at a positive applied bias of 50 mV using 1 M NaCl buffer (pH 8.0).

### **7.5.2 Experiment protocol**

Engineered OmpG (eOmpG) having an outer diameter of 3.3 nm and dA30 was introduced in cis chamber. Bias across the nanopore was then slowly increased to 80 mV in steps of 10 mV to pull eOmpG through the nanopore and for the DNA translocation. OmpG has a symmetric cylindrical macromolecular structure. Therefore, its stability essentially depends upon the gating potential, charge interaction with the nanopore, nanopore size relative to outer OmpG diameter and pH of the analyte solution. So, fabricating a suitable sized solid-state nanopore and prevention of spontaneous gating is crucial for its subsequent stability during sensing procedure. A solid-state nanopore size just bigger than the eOmpG diameter (3.3 nm) is required to hold the porin at the pore owing to surface charge interactions and to avoid multiple protein insertion at a time. Lesser the difference between the outer eOmpG diameter and inner solid-state nanopore diameter, higher is the stability of the hybrid assembly. BL MoS<sub>2</sub> solid-state nanopores were therefore fabricated having a diameter around 3.4 nm. Nanopore fabrication, cell assembly (set-up for measurement), pore and cell cleaning, reagent and analyte solution preparation were carried out following the same procedure as described in our previous work [241].

Single channel recordings were obtained to characterize the solid-state nanopores, test protein (eOmpG) insertion and analyse the sensing profile through the hybrid nanopores. Signal alterations due to eOmpG insertion and translocating analyte induced ionic blockades were amplified by

Axopatch 200B and finally digitized by Digidata 1500B. 100 mM KCl solution buffered with 25 mM Tris-HCl was poured in each chamber separated by the membrane bearing nanopore. A pH value of 7.0 was used to conduct the experiments to minimize any spontaneous closing of eOmpG pore and a constant positive bias was applied [153]. After measuring signal from the pore, 1 ng/ml of eOmpG was introduced in the cis chamber and mixed thoroughly. For ionic current measurement, voltage sweep from -200 to 200 mV with 20 mV steps was applied to trans side and the cis chamber was grounded. Ionic current was recorded for 10 sec for each applied voltage for solid-state nanopores fabricated on BL MoS<sub>2</sub>. Hybrid nanopores were produced by pulling eOmpG through nanopore by applying a positive voltage of +80 mV to the trans chamber (**Figure C- 5**). After complete eOmpG insertion, applied bias was slowly increased to +200 mV and dA30 translocation was conducted at that voltage. Translocation data is reported after baseline stabilization.

### **Signal acquisition and analysis**

In this work, we acquired translocation traces using Axopatch 200B amplifier and Digidata 1500B digitizer. The signals were acquired at a sampling rate of 20 kHz. In-built low-pass filters were bypassed for all the measurements. This was done to obtain a broader bandwidth of raw data. This helped us in overcoming access resistance issues of MoS<sub>2</sub> before and sequencing DNA in our previous work [241]. Hence, the same procedure was adopted for this work. Bypassing the in-built filter also helped us in preventing alterations of blockade and dwell time values and monitoring attenuations.

Two different techniques were used to analyze the data:

- 1) The data was low-pass filtered at 2 kHz cut-off using 8-pole Bessel filter in Clampfit 10.6 software. The unfiltered raw data and filtered data were then compared to identify translocation events. The translocation parameters were calculated of the selected events using the unfiltered data, to ensure accuracy. Events attenuated after filtering were not considered in the analysis.
- 2) For power spectral density analysis and comparison, the traces were filtered using a high-pass Butterworth filter (using MATLAB) at a cut-off frequency of 0.1 Hz to eliminate baseline fluctuations to obtain spectra for 1 Hz to 10 kHz bandwidth.

Ionic conductance (I-V) measurements were conducted first for a low (10 mM) concentration (see **Figure 7.2.f**) of KCl to avoid ionic turbulence shock to the OmpG nanopore during a voltage sweep. However, at 10 mM KCl the signal-to-noise ratio for DNA sensing was highly compromised. Therefore, a higher KCl concentration of 100 mM was used to obtain better signals. I-V measurements were then repeated for 100 mM KCl concentration (see **Figure C- 2**) and all translocation and gating response tests were conducted using 100 mM KCl.

## **Data availability**

The data that support the findings of this study are available from the corresponding author upon reasonable request.

## **Corresponding Authors**

[mgupta1@ualberta.ca](mailto:mgupta1@ualberta.ca) (MG)

## **Author Contributions**

P. S. conducted all fabrication and experiments on the solid-state and hybrid nanopores. H. H. performed all protein purification, engineering, and characterization. P. S. and M.G. analyzed and wrote the manuscript.

## **Funding Sources**

This work was funded by Natural Sciences and Engineering Research Council of Canada award # 06096 and Alberta Innovates.

## **Competing Interests**

The authors declare that there are no competing interests.

## Chapter 8 <sup>5</sup>(Paper 5)

**In this chapter** I demonstrate the use of hybrid nanopore developed previously (as explained in Chapter 7) for sensing  $\Delta^9$ -THC molecules. THC, which is the primary psychoactive element in marijuana is responsible for determining the toxicity and its effect on passive or active users of marijuana. So, monitoring  $\Delta^9$ -THC levels closely and accurately can help control THC usage, reap medical benefits of marijuana in correct amounts and prevent adverse health effects due to overdose. The chemical sensitivity of eOmpG interface can also help in further using it for distinguishing between the toxic and non-toxic components for accurately predicting the consequences on human health.

### **8 Monitoring THC levels using highly sensitive engineered OmpG and bilayer MoS<sub>2</sub> hybrid nanopore**

*Payel Sen, Manisha Gupta\**

Payel Sen

Department of Chemical and Materials Engineering

University of Alberta

Edmonton, Canada

Email: [payel@ualberta.ca](mailto:payel@ualberta.ca)

---

<sup>5</sup> Manuscript under preparation

Manisha Gupta

Department of Electrical and Computer Engineering

University of Alberta

Edmonton, Canada

Email: [mgupta1@ualberta.ca](mailto:mgupta1@ualberta.ca)

**Keywords:** Hybrid nanopore, bilayer MoS<sub>2</sub>, outer Membrane Porin G, THC sensing, sensitivity

## 8.1 Abstract

Prevention of Cannabis overuse has been one of the primary objectives after its legalization in different countries. Active detection and monitoring the dose of Delta(9)-Tetrahydrocannabinol ( $\Delta^9$ -THC) in individuals is crucial to determine tolerance level and to avoid severe health effects due to overdose. Detection in saliva matrix allows accurate long-term sensing of THC due to long lifetime ( $\sim 34$  hours) in saliva. Nanopore sensing provides a highly sensitive fast detection platform for single molecule THC sensing in real-time. However, owing to fast translocation of neutral  $\Delta^9$ -THC molecules, solid-state nanopore sensing produce events with very low temporal resolution, thus making it unsuitable for being used as a reliable sensor. A hybrid eOmpG-BL MoS<sub>2</sub> nanopore with its eOmpG interface slows down THC translocation, thus amplifying the charge interaction and producing well-resolved detection events. In this work, we conducted  $\Delta^9$ -THC sensing at different concentration (1 pM to 100 nM). eOmpG with its unique gating properties and sensitivity to localized charge alterations, responds to both bound and free  $\Delta^9$ -THC, thus showing an ability to detect very minute (cut-off limit of 1 pM) changes in  $\Delta^9$ -THC concentration in the saliva buffer used. We additionally also obtained signatures specific (with respect to dwell times) to the

orientation at which  $\Delta^9$ -THC molecules approach and translocate through the nanopore, the specificity caused due to difference in chemical interactions to for different configurations. This leads the way for determining the level of toxicity of marijuana by distinguishing between its non-toxic and toxic components, which forms scope of future work.

## 8.2 Introduction

Drug use and abuse is a matter of prime concern in Canada and worldwide. According to Canadian Alcohol and Drug Use Monitoring Survey (CADUMS) 2012, 21.6% Canadians i.e. 8 million population in Canada suffer from drug addiction [247]. Cannabis or marijuana is one of the most popularly used psychoactive herbal drug, which has medicinal benefits but also used for recreational purposes [248]. Marijuana (Cannabis) was first legalized for medical purposes in Canada in 2001 [249]. It can be used as an analgesic, bronchodilator, blood-pressure controller, muscle relaxant and appetite stimulator [250]–[252]. Topical application has its anti-inflammatory and pain killing effect [173], [174]. It shows its localized effect in minutes and can last for hours. Sublingual cannabis sprays also have proved to be safe apart from a few side effects [253]. Oral cannabis intake and inhalation in low doses has been found to cause euphoric feelings, hallucinations, panic, sleepiness, etc. [254]. In 2018, Canada became the second country (after Uruguay) to legalize recreational and medical use of Marijuana and its by-products under the Cannabis Act [249]. Delta(9)-Tetrahydrocannabinol ( $\Delta^9$ -THC) is the chief psychoactive element in Cannabis which affects the concentration of released neurotransmitters thus inducing mood changes and sense of awareness [57]. THC can have short-term or long-term health effects depending on the extent of its usage [178]. Low intake has been found to cause euphoric feelings and sleepiness [178]. Overdosing above psychotropic level can cause hallucinations and panic

attacks. Although fatality due to cannabis overdose has not been reported, long-drawn usage can intensely harm memory, intellect or even majorly affect lungs and heart. Cannabis use during pregnancy can even affect fetus health [178], [179], [255]. Individuals are found to display withdrawal symptoms after regular use of the drug [179]. Hence, it is extremely essential to monitor cannabis level in body and its effect to avoid major health issues.

Marijuana can either be smoked or ingested orally. When inhaled, THC can manifest itself in a few minutes and its effect can last to 2-3 hours [181], [256]. Oral administration shows its effects after 30-90 minutes and can last for as long as 12 hours [181]. Urine, blood, saliva and sweat are the fluid mediums mostly used for testing THC intake. THC can be detected for 34 hours in saliva with a cut off limit of 0.5 ng/ml [182], which is 20-30 times lower than that of blood and urine [181], [182]. This also suggests that detection in saliva matrix can actively identify more recent consumption of THC.

Since Cannabis legalization in Canada, a spike in Cannabis consumption has been witnessed. According to National Cannabis Survey (2019), cannabis consumption has increased from 14% in 2018 to 18% in 2019 [257]. This poses an increased risk of accident and psychotic behaviour due to continuous and overdosed consumption.  $\Delta^9$ -THC not only determines the degree of toxicity, but the concentration of  $\Delta^9$ -THC also can be directly correlated with the time since last cannabis smoke or ingestion. Cannabis Sensors Inc. has been working in developing breath-based and saliva-based cannabis sensors using multiple strategies. Cannabisense, an aptamer nanopore has been recently developed by Cannabis Sensors Inc. for sensing THC using a target-induced strand release (TISR) strategy [258].

Solid-state nanopores have been used as potential small molecule sensors due to its steady pore current [138], [226]. Analytes can be detected by their translocation-based ionic blockade. Thin

2D semiconducting membranes have proved to be a good solution by slowing down molecular translocation and improving detection resolution [51], [52], [54], [189]. The change in ionic current generated through solid-state pores is molecular size dependent leading to lack of specificity for detection of similar-sized analytes. Biological pores have structural precision and high sensitivity to chemical and electronic modifications but lack the necessary structural strength for good repeatability and stability of sensing [13]. Hybrid nanopores offer an amalgamation of the favorable properties of both synthetic and bio pores preferably by inserting a single protein pore in a solid-state nanopore [61], [64], [154]. A combination of alpha haemolysin and solid-state silicon nitride pores has been successfully created for sensing proteins and dsDNA [64]. The solid-state pore diameter is ensured sufficient to permit the beta barrel of OmpG into the pore, whereas the broader cap sits on the pore and prevents it from moving out. The bio-pore orientation therefore governs detection of the molecules electrophoretically pulled through the hybrid barrel pore. Unlike alpha haemolysin, OmpG is a 32 kDa 14 stranded monomeric beta barrel-shaped porin [153]. OmpG has 7 flexible extracellular loops, loop 6 being the most flexible [153]. These loops respond to different pH, ionic or electric conditions in different ways producing a discrete analyte binding changing the protein dynamics and ionic current differently in each case. These current fluctuations or gating are characteristic to the bound analyte helping its identification [151], [172]. The gating effect depends on a lot of factors including the proximity of the analyte with OmpG, charge interactions between OmpG, conformation changes of the flexible groups [151], [172]. The flexibility of the loops leads to high selectivity and sensitivity of OmpG pores unlike other rigid bio pores. It has been demonstrated that gating activity at positive potential is lower than negative (**Chapter 7**). But a reduced noise is obtained for positive potential, making it more favorable for sensing purpose [151], [153], [172]. A high electrolyte concentration is found to hinder binding

and detection of analytes through hybrid pores due to Debye screening [259]. As a result, a low electrolyte concentration is usually used for biosensing of small molecules. Owing to the cylindrical shape, the probability of OmpG sitting at the pore reduces. TMD-based 2D materials like MoS<sub>2</sub> have high electrochemical activity at the surface allowing enhanced attachment of bio pores to their solid-state pores.

In this work, OmpG hybridized bilayer MoS<sub>2</sub> nanopore is used for detection of neutral  $\Delta^9$ -THC molecules with high temporal resolution and repeatability. In our previous work we performed DNA sensing through solid-state and hybrid MoS<sub>2</sub> nanopores to demonstrate the improvement in signal-to-noise ratio and ionic current stability after OmpG hybridization. OmpG has flexible outer loops which respond differently due to variation of localized surface charge. As a result, pH and analytes present in the sensing medium can therefore alter OmpG loop dynamics giving rise to varying gating events, which can identify the analyte type. Our study demonstrates that THC molecule can be detected by the sharp signals produced by electrostatic interaction induced gating of the hybrid OmpG pore. We also present a dose (concentration) dependent sensor response which can help build a sensitive tool for  $\Delta^9$ -THC tracking. Hybrid nanopores were used to detect  $\Delta^9$ -THC molecules in saliva buffer for 1 pM to 100 nM concentrations.

### **8.3 Material and methods**

Prime 4-inch diameter silicon wafers having a thickness of  $525 \pm 25$   $\mu\text{m}$  and cut along  $\langle 100 \rangle$  plane with both sides coated with 50 nm thick LPCVD (low stress) silicon nitride was purchased from Rogue Valley Microdevices. MoS<sub>2</sub> crystal (15 $\times$ 10 mm) was purchased from 2D semiconductors. Rest of the reagents were procured from Fisher Sci. Engineered OmpG (eOmpG) having an outer diameter of 3.3 nm was prepared following the same procedure as **Chapter 7**. Potential was then

slowly increased in steps of 10 mV to 50 mV to pull OmpG and DNA through the pore. A pore size just bigger than the OmpG outer diameter (3.3 nm) is required to hold the porin at the pore owing to surface charge interactions. The smallest the difference between the outer OmpG diameter and inner solid-state pore diameter, higher is the stability of the hybrid assembly. BL MoS<sub>2</sub> solid-state pores were therefore fabricated having a diameter of ~3.4 nm. Nanopore fabrication, cleaning, reagent and analyte solution preparation were carried out following the procedure described in our previous work [241].

Single channel recordings were obtained to characterize the solid-state nanopores, observe protein (eOmpG) insertion and analyse the sensing profile through the hybrid pores. Signal alterations due to eOmpG insertion and translocating analyte induced ionic blockades were filtered by 2kHz Bessel filter, amplified by Axopatch 1500B and finally digitized by Digidata. Artificial saliva buffer is prepared with composition similar to real saliva except for the protein constituents. The buffer was made following the same procedure as used by *Wanklyn et al.*, 2016 [260]. All reagents were purchased from Sigma Aldrich.  $\Delta^9$ -THC solution having different concentration were prepared by diluting 1 mM solution of  $\Delta^9$ -THC in methanol with suitable amount of saliva buffer. The resultant pH of the solution is found to be in the range of 6.3-6.5.

1 ng/ml of eOmpG was introduced in the cis chamber and mixed thoroughly. Hybrid nanopores were produced by pulling eOmpG through nanopore by applying a positive voltage to the trans chamber. Protein insertion was observed as potential was slowly increased above 80 mV. Different concentration of  $\Delta^9$ -THC was sensed by pulling from cis to trans chamber at 100 mV through the hybrid nanopore after OmpG insertion following the protocol described previously, to determine the detection rate for each concentration. Concentration was varied for a range of 1 pM to 100 nM

and current blockade was recorded for 15 min for each concentration. No parameters were changed in between recordings for the same concentration.

## 8.4 Results and Discussions

The constructed eOmpG hybrid nanopore is seen to be stable for >5 hours under a bias of 100 mV, until a negative potential is applied to the trans chamber to remove the protein out of the pore. Different concentrations of  $\Delta^9$ -THC are introduced in the cis chamber and a transmembrane bias of 100 mV is applied. The eOmpG hybrid displays a high affinity towards the  $\Delta^9$ -THC molecules producing detectable gating events due to analyte binding and non-cognate analyte translocations through the pore. We first determined the blank pore ionic current in presence of a saliva medium. We varied the voltage over a range of -200 mV to 200 mV at a step-size of 10 mV and recorded the ionic current for 12 sec. **Figure 8.1.a** shows the recorded nanopore current in presence of the prepared saliva buffer medium. At 200 mV the mean current value is observed to be around 450 pA. We first tried to obtain THC sensing events by pulling 1 nM  $\Delta^9$ -THC in saliva medium through the solid-state BL MoS<sub>2</sub> nanopore. **Figure 8.1.b** shows current traces in presence of analyte  $\Delta^9$ -THC. We observed that in spite of showing current fluctuations, the events obtained are not sufficiently resolved for being confidently recognized as  $\Delta^9$ -THC blockades. This may be because of very fast translocation of the neutral THC molecules through the solid-state nanopore hindering sufficient surface charge interaction and identifiable drops.

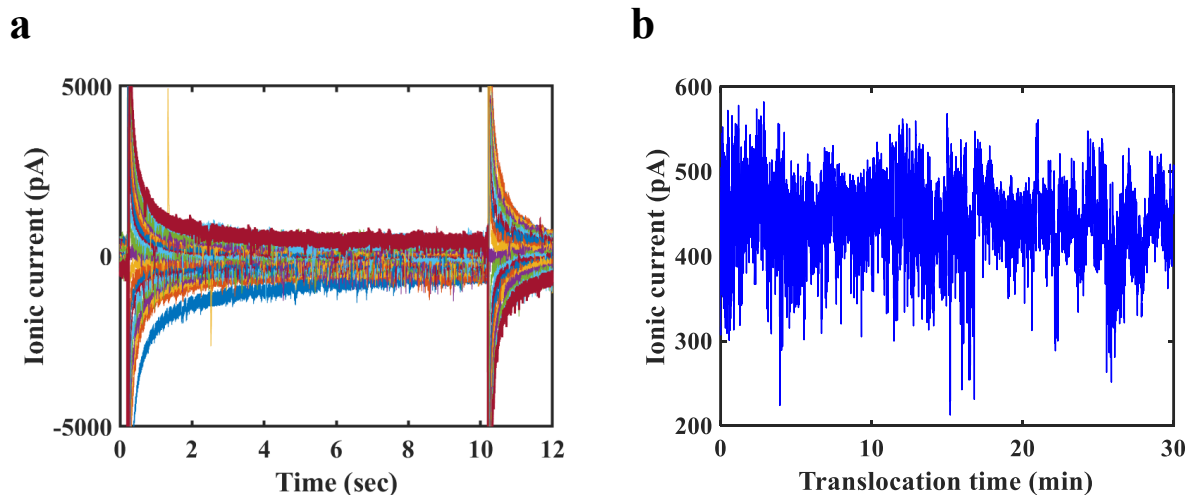


**Figure 8.1.** a. Ionic current recorded in a saliva medium for 12 sec for a transmembrane voltage varied from -200 mV to 200 mV, showing a blank current of  $\sim 450$  pA for a bias of 200 mV and b. Ionic current traces recorded at a bias of 200 mV through solid-state BL MoS<sub>2</sub> nanopore in presence of  $\Delta^9$ -THC showing that  $\Delta^9$ -THC translocation events obtained are not sufficiently resolved for reliable molecular sensing.

eOmpG is introduced in the cis chamber and after a wait time of about 40 min, eOmpG incorporation into BL MoS<sub>2</sub> nanopore is observed. First the open pore current in absence of any analyte is recorded to note the open pore current through the hybrid nanopore. **Figure 8.2** also shows an open pore current of  $\sim 415$  pA (maximum current obtained after eOmpG insertion) after eOmpG incorporation into the solid-state BL MoS<sub>2</sub> nanopore. The eOmpG is found to open fully in steps after insertion into the MoS<sub>2</sub> nanopore, as seen from **Figure 8.2**. Two partially open current levels of eOmpG are also observed with 393 pA denoting a 95% open eOmpG and 360 pA denoting an 87% open eOmpG. This stepwise opening observed in a saliva buffer unlike a KCl medium may be due to mixed contribution of different counterions constituting the saliva buffer.

These counterions require time to attain a diffusive equilibrium (constant baseline current) thus quenching the effect of surrounding ions on loop configuration of eOmpG.

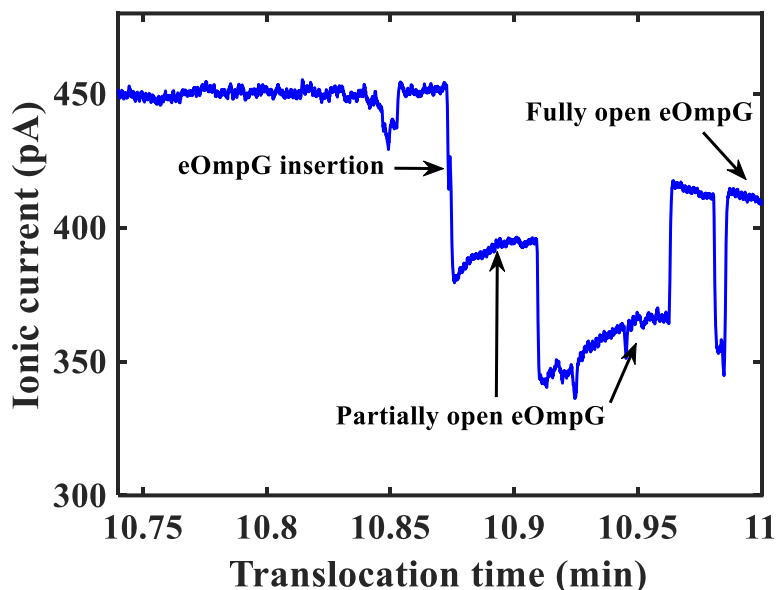


**Figure 8.2.** Traces showing eOmpG insertion into solid-state BL MoS<sub>2</sub> and stepwise eOmpG opening with a fully open pore current of 415 pA.

After achieving a fully open-state of eOmpG,  $\Delta^9$ -THC (at different concentrations, as mentioned above) is introduced in the cis chamber and pulled electrophoretically through the hybrid nanopore.  $\Delta^9$ -THC when sensed through the hybrid pore is found to display prominent temporally resolved events, unlike when sensed through the solid-state nanopore. **Figure 8.3** presents sensing events at different  $\Delta^9$ -THC concentrations (100 nM, 10 nM, 1 nM, 100 pM, 10 pM and 1 pM). Events with dwell time greater than 20  $\mu$ s are considered only as we are using a 20 kHz filter for analysis (rise time  $\sim$  17  $\mu$ s). Two types of events were observed; First, events manifested as change in baseline current are caused due to eOmpG gating induced by localized charge variation owing to analyte  $\Delta^9$ -THC binding to eOmpG; resulting in rearrangement of the inner loops, changing the

open pore volume and thus the nanopore current; Second, intermittent blockade events caused due to translocation of free THC through the eOmpG hybrid.

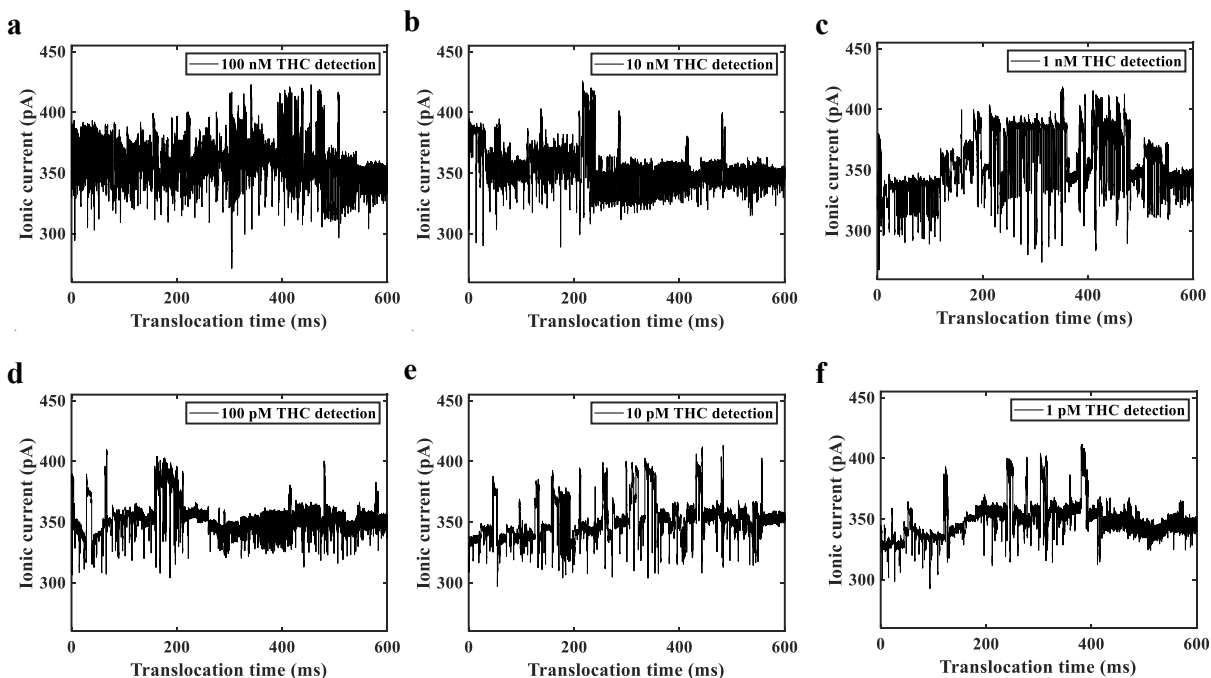


**Figure 8.3.** THC traces sensed through hybrid eOmpG-BL MoS<sub>2</sub> nanopore at different THC concentrations: a. 100 nM, b. 10 nM, c. 1 nM, d. 100 pM, e. 10 pM and f. 1 pM.

$\Delta^9$ -THC mainly consists of three domains: phenol, cyclohexene and a pyran ring. The aromatic rings are prone to resonating and inductive effects. Furthermore, electronic interactions of other entities with the phenolic group gives rise to conformational change of the THC molecules. The dimensions of a  $\Delta^9$ -THC molecule are about  $1.8 \times 2$  nm whereas inner diameter of eOmpG is about 2.2 nm, which indicates that  $\Delta^9$ -THC can translocate through eOmpG hybrid in any orientation varying between the linear (Orientation 1) and transverse (Orientation 2) configurations, as indicated in **Figure 8.4**.

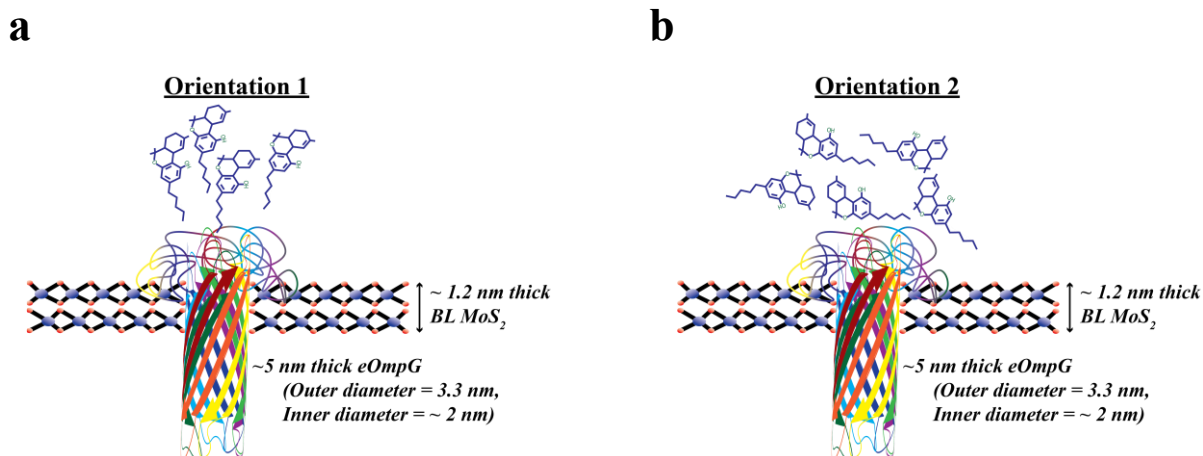


**Figure 8.4.** Schematic diagram of a. Orientation 1 denoting THC translocation in its linear orientation which should produce characteristically smallest ionic blockade current and b. Orientation 2 denoting THC translocation in its transverse orientation which should produce characteristically highest ionic blockade current.

To further analyse the translocation events, we plot density plots of blockade current vs dwell time information of the events (see **Figure 8.5**).

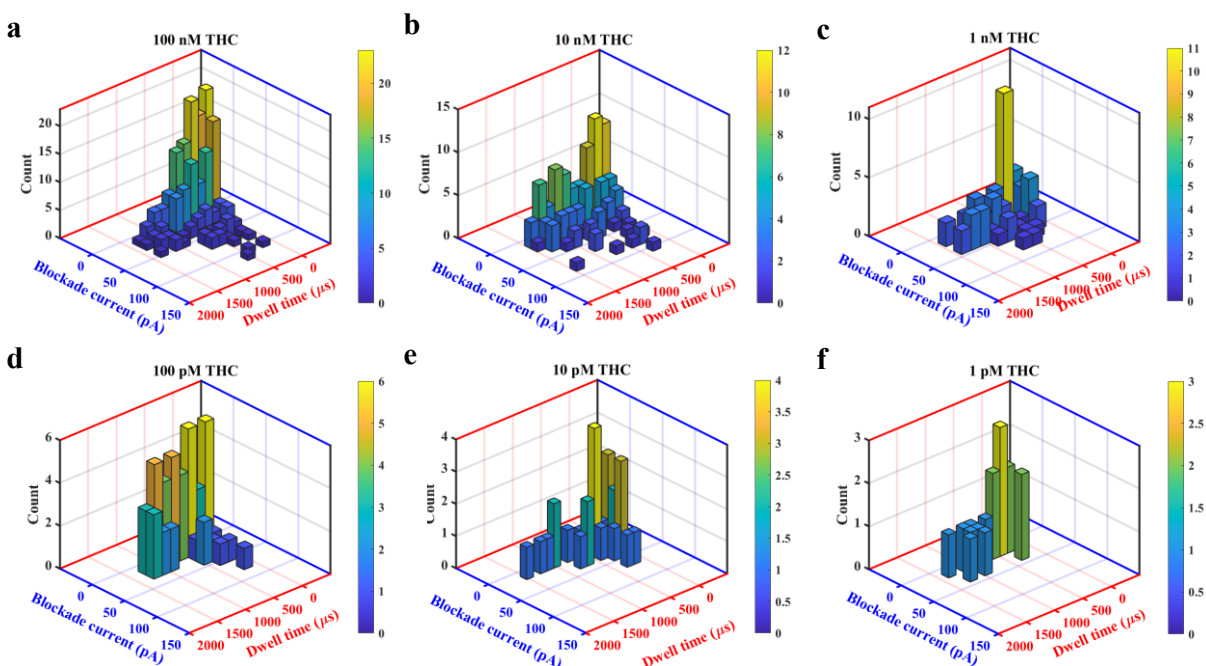


**Figure 8.5.** 3D density plot of THC translocation events recorded for 600 ms, for concentrations of a. 100 nM, b. 10 nM, c. 1 nM, d. 100 pM, e. 10 pM and f. 1 pM showing highest density of peaks around 100-600  $\mu$ s dwell time and 10-40 pA blockade values. These signatures are obtained for 87% open eOmpG, which theoretically should have a characteristic opening of 1.9 nm which is just enough for letting in single THC molecules in linear orientation (Orientation 1). Therefore, we believe, these signatures correspond to single THC molecule translocation for Orientation 1.

We observed highest density of events for blockades in the range of 10-40 pA and dwell time range of 100-600  $\mu$ s (**Figure 8.5**). As observed from **Figure 8.3**, these events are seen to happen through an 87% open eOmpG, which theoretically should have an inner diameter of 1.9 nm. This opening is just sufficient for allowing THC translocations in linear fashion (Orientation 1 of **Figure 8.4**). Also, relatively lower dwell times (< 600  $\mu$ s) are obtained for these events. This may be due to weak dipole-dipole interactions caused due to the leading -CH<sub>3</sub> group of linearly oriented THC molecules. Other events are also observed with blockades greater than 40 pA and dwell times greater than 600  $\mu$ s, which correspond to a baseline current indicating 95% and 99% open eOmpG. These signatures are obtained because, with increase in eOmpG volume (open gating), transverse orientations (Orientation 2 of **Figure 8.4**) of THC molecules are also permitted in, thus resulting in higher blockades. Additionally, transverse orientations cause stronger -OH interactions to dominate resulting in higher dwell times (> 600  $\mu$ s).

The sensor response was evaluated for varying THC concentration by noting the number of single THC molecules detected per sec as a function of THC concentration (see **Figure 8.6**).

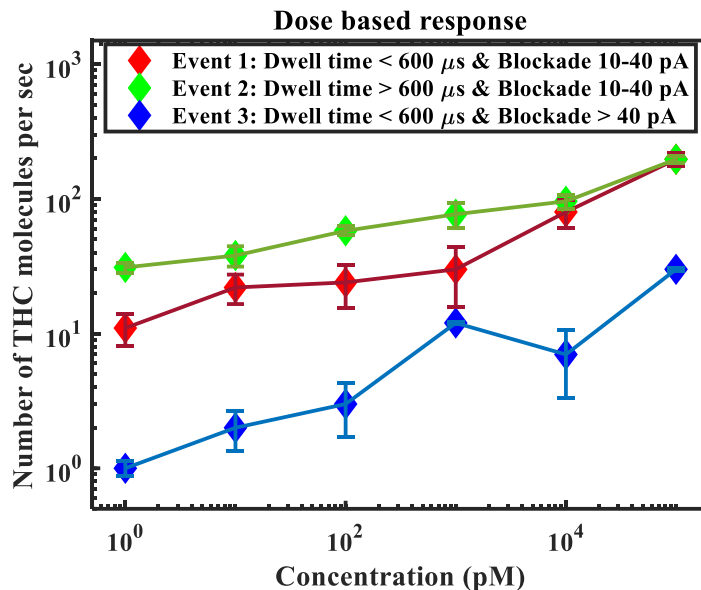


**Figure 8.6.** Concentration based response of a THC molecule sensing demonstrated by hybrid eOmpG-BL MoS<sub>2</sub> nanopore in a saliva medium.

The sensor is found to be sensitive to THC concentration change with a cut-off limit of 1 pM, which suggests that minute (picomolar) concentration changes in THC levels in saliva can be detected by this sensor. The results pave the way for efficient and proactive control of THC dosage and simultaneous prevention of serious health concerns.

This study demonstrates the ability of eOmpG-BL MoS<sub>2</sub> hybrid nanopore sensor in recognizing minute (1 pM) change in THC level in saliva. Our study leads the way for sensitive and instant detection of THC levels in saliva helping in control and monitoring of its dose and subsequent health effects. It can also increase awareness of individuals towards their intake and help avoid overdose symptoms and health hazards due to active and passive marijuana usages.

## Chapter 9

### 9 Summary of results

Nanopores are extensively used as biomolecular sensor due to their real-time low-cost amplification free sensing platform. Nanopore sensing mainly depend on blockade current produced by translocating analyte molecules as dictated by Coulter-counter principle. So, the efficiency, reproducibility, sensitivity, and resolution of nanopore sensing is influenced by nanopore volume (nanopore diameter and membrane thickness), analyte translocation velocity, analyte charge, surface charge of the membrane and noise contributions. In this work, these factors were addressed one by one to design a reusable, repeatable and scalable sensor capable of efficiently detecting single charged and uncharged molecules with good spatial and temporal resolution, with sensitivity high enough to detect analytes at low concentrations. Solid-state nanopore fabricated on synthetic insulating or semiconducting membranes are good choice for such biomolecular sensors primarily due to their durability and scalability. Of all the solid-state materials, silicon nitride is by-far the most-used and standardized material.

In this work, the influence of nanopore geometry on the reproducibility of sensed ionic current was first tested using silicon nitride nanopore. It is also important to monitor nanopore diameter during multiple nanopore measurements, for improving signal accuracy and reliability. The ionic current/conductance was repeatedly recorded through nanopores having variable diameters. A COMSOL Multiphysics model was built to first predict the nanopore geometry from the measured ionic conductance and to evaluate the size change experienced by each nanopore due to multiple measurements. Since the nanopore size is directly related to ionic conductance, change in nanopore

size indicates change in signal amplitude due to multiple measurements. So, the nanopore size undergoing the least size change can be listed as the most repeatable and reliable. We observed that nanopores having  $< 4$  nm diameter demonstrate the best reproducibility. We therefore continued our studies using  $\sim 3$  nm diameter nanopores.

Next, research was carried out in improving spatial resolution of sensing. Standard 50 nm silicon nitride senses multiple molecules at a time, thus reducing spatial resolution for molecular sensing. So, it is essential to select a stable and thin nanopore material suitable for fabricating  $\sim 3$  nm sized nanopores, which can sense single molecules with high spatial resolution. DNA sensing and sequencing are two of the primary applications of nanopore sensors. So, a COMSOL Multiphysics simulation approach was adopted to first compare the DNA sensing performance and spatial resolution of 3 nm diameter nanopores on 50 nm  $\text{SiN}_x$  with similar sized nanopores on 1-6 layers and  $\sim 50$  nm  $\text{MoS}_2$  nanopores. When the results clearly indicated improvement in ionic current magnitude and spatial resolution by employing few layers of  $\text{MoS}_2$  instead of 50 nm  $\text{SiN}_x$ , the effect of number of  $\text{MoS}_2$  layers in improving the temporal resolution of sensing was investigated. Comparison of DNA translocation electro-kinetics through 3 nm diameter (as selected from **Chapter 4**) nanopores on 1-6 layers  $\text{MoS}_2$  showed the potential of bilayer  $\text{MoS}_2$  nanopore in slowing down translocation; i.e. demonstrating time resolution better than monolayer  $\text{MoS}_2$  nanopore while maintaining a good spatial resolution. To conclusively infer on the prospects of bilayer  $\text{MoS}_2$  nanopore sensors, monolayer and bilayer  $\text{MoS}_2$  nanopores having 2.5-3 nm diameters were fabricated and single nucleotide sensing and DNA sequencing experiments were performed through them to compare their performances. In the recent past, monolayer (ML)  $\text{MoS}_2$  nanopores have been used to detect and classify single nucleotides with good signal-to-noise ratio. Bilayer (BL)  $\text{MoS}_2$  nanopores were found to show double the dwell time offered by ML  $\text{MoS}_2$

nanopores for single nucleotide sensing. A 5X higher single nucleotide detection rate was also obtained for BL MoS<sub>2</sub> nanopores compared to ML MoS<sub>2</sub> for a low concentration of 10 pM, indicating an improved capture of nucleotide by BL MoS<sub>2</sub> nanopores. BL MoS<sub>2</sub> nanopore was also found to demonstrate 4% higher single nucleotide sensing efficiency and 8-10% better single-stranded DNA sequencing efficiency compared to ML MoS<sub>2</sub> nanopore. The results infer that BL MoS<sub>2</sub> nanopores can sequence DNA with high temporal resolution, detection rate and efficiency.

After achieving a solid-state nanopore capable of efficiently and rapidly determining the DNA sequence with good spatial and temporal resolution, work was focussed on reforming the sensor to make it durable, biocompatible as well as fit for sensing charged and neutral molecules with high signal-to-noise ratio (SNR). Therefore, a hybrid nanopore was constructed using outer membrane porin (OmpG) as the biological nanopore and BL MoS<sub>2</sub> as the solid-state nanopore. Due to its surface charge and 2D layered properties, BL MoS<sub>2</sub> was used for providing a robust solid-state support while minimizing capacitive noise required for precise sensing. The choice of OmpG as the biological nanopore also helped in further improving the SNR by reducing low-frequency noise. OmpG is very sensitive to localized charges and adapts its inner and outer loops in response to changes in its environment giving rise to gating (open/close) events. Such gating has its own advantages and limitations. The advantage of such gating is increased control over the nanopore volume, which can be suited to the particular analyte type being sensed. However, its sensitivity to surrounding charge fluctuations can lead to spontaneous gating (open and closing) of OmpG producing a noisy and unstable baseline current. To overcome the latter limitation, OmpG was modified to prevent spontaneous gating in response to ionic concentration or pH change of the buffer medium in presence or absence of the analyte. The engineered OmpG (eOmpG) was incorporated into the solid-state BL MoS<sub>2</sub> nanopore by pulling it electrophoretically

at 80 mV trans-bias. For charged molecule detection, work was continued on DNA sensing and single-stranded polyadenine having a length of 30 nucleotides (dA30) was translocated through the hybrid nanopore. With nearly 1.9 times increase in signal to noise ratio (32% lower noise levels) and 8 times longer dwell times for dA30 molecular sensing relative to solid-state BL MoS<sub>2</sub> nanopore, hybrid BL MoS<sub>2</sub> - eOmpG nanopore was found to be suitable for highly resolved charged biomolecular sensing.

Thus, solid-state BL MoS<sub>2</sub> nanopores capable of identifying individual nucleotides were achieved for fast, efficient, and well-resolved (spatially and temporally) DNA sequencing. A hybrid BL MoS<sub>2</sub> - eOmpG nanopore capable of sensing DNA with even more temporal resolution and signal-to-noise ratio (as obtained through solid-state BL MoS<sub>2</sub> nanopores) was also achieved. However, it is to be noted in this case that nanopore/analyte charge interaction which governs the analyte translocation velocity and resultant temporal resolution, differs immensely for charge and neutral analytes. So, the solid-state nanopores which are capable of sufficiently resolving charged analytes may not be suitable for resolving neutral molecule detection events too. However, hybrid nanopores are found to demonstrate even better temporal resolution for charged DNA molecules compared to its solid-state alternative. So, an increased probability of properly resolving neutral molecule sensing events by using hybrid nanopores can be anticipated. In order to look more into the truth behind this, a neutral analyte which can benefit health monitoring further was selected. Thus, the current issue on prevention of Cannabis overuse in Canada and worldwide was addressed. In order to assess the tolerance level and to prevent serious health consequences due to toxicity, successful identification, and control of THC dosage in individuals is very important. Detection in saliva buffer facilitates effective long-term detection of THC as it can be detected in saliva for as long as 34 hours. For single molecule THC sensing in real-time, nanopore sensing

offers a highly sensitive and rapid detection tool. Therefore, THC sensing at different concentrations (1 pM to 100 nM) was performed. eOmpG reacted to both bound and free THC with its special gating characteristics and susceptibility to localized charge shifts, thereby demonstrating the ability to detect as low as 1 pM change in THC levels in saliva. THC translocations in linear orientations led to blockades of 10-40 pA and dwell times of 100-600  $\mu$ s, while blockades of > 40 pA and dwell times of > 600  $\mu$ s corresponded to transversely directed THC translocations. Due to the variation in chemical interactions for various configurations, such orientation-specific signatures were acquired. This can offer a means for determining the extent of toxicity of marijuana by separating between its non-toxic and toxic elements, which form the scope of future work.

Thus, a versatile biocompatible nanopore sensor capable of identifying and distinguishing both charged and neutral analytes was achieved. Improved spatial and temporal resolution, signal-to-noise ratio, and efficiency for sensing and sequencing DNA, representing charged molecules and THC, representing neutral molecules, were also achieved. The sensor built can be further used to test chemical specificity by using target-specific tethers and functionalization, which can be scaled up by forming nanopore arrays for parallel sensing. Additionally, further work is required in testing the selectivity of THC in a mixture of Cannabinoids to determine the degree of toxicity by differentiating THC from non-toxic components like CBD and then estimating THC abundance from its detection rate as shown in our study. The study conducted can thus provide a good foundation for making significant contributions to betterment of health and environment.

A high efficiency was achieved for single nucleotide sensing and pseudo-random single-stranded short DNA sequencing having a length of 30 nucleotides by using  $\sim$  3 nm solid-state BL MoS<sub>2</sub> nanopores. The device can be further used for the following applications to influence genome

sequencing more significantly. The nanopore can be first used for double-stranded DNA sequencing to replicate the real scenario more closely. The nanopore can be tested for evaluating its read-lengths and the influence of DNA length on the sequencing efficiency. The nanopore can also be further utilized to sequence truly random DNA sequences to prepare it for healthy and mutated genome sequencing of human and microbes.

A hybrid nanopore designed by combining engineered OmpG with BL MoS<sub>2</sub> nanopore was also achieved, which enabled DNA sensing by temporally resolving the signals even more than what was obtained for solid-state nanopores and a good signal-to-noise ratio as well. Good sensitivity to neutral THC molecule sensing was also obtained and a strong foundation for THC level monitoring and control was also provided. This sensor can be further improved by using target-specific tether or functionalization to specifically detect molecules from a mixture or solution of other molecules. To further benefit THC dose control and monitoring, a mixture of CBD (non-toxic) and THC (toxic) and obtaining signals capable of differentiating these components so the effects of non-toxic elements can be eliminated for accurately monitoring the toxicity of marijuana and predicting its consequences.

## Reference

- [1] K. V, “DNA Biosensors-A Review,” *J. Bioeng. Biomed. Sci.*, vol. 07, no. 02, pp. 222(1–5), 2017, doi: 10.4172/2155-9538.1000222.
- [2] W. Vercoutere and M. Akeson, “Biosensors for DNA sequence detection,” *Current Opinion in Chemical Biology*, vol. 6, no. 6. pp. 816–822, 2002, doi: 10.1016/S1367-5931(02)00395-2.
- [3] S. R. Mikkelsen, “Electrochemical Biosensors for DNA Sequence Detection,” *Electroanalysis*, vol. 8, no. 1. pp. 15–19, 1996, doi: 10.1002/elan.1140080104.
- [4] D. Su, K. Wu, R. Saha, C. Peng, and J. P. Wang, “Advances in magnetoresistive biosensors,” *Micromachines*, vol. 11, no. 1. p. 34, 2020, doi: 10.3390/mi11010034.
- [5] A. Ramesh *et al.*, “Towards in vivo biosensors for low-cost protein sensing,” *Electron. Lett.*, vol. 49, no. 7, pp. 465–467, 2013, doi: 10.1049/el.2012.4283.
- [6] S. Neethirajan, X. Weng, A. Tah, J. O. Cordero, and K. V. Ragavan, “Nano-biosensor platforms for detecting food allergens – New trends,” *Sensing and Bio-Sensing Research*, vol. 18. pp. 13–30, 2018, doi: 10.1016/j.sbsr.2018.02.005.
- [7] S. Morais, L. A. Tortajada-Genaro, Á. Maquieira, and M. Á. Gonzalez Martinez, “Biosensors for food allergy detection according to specific IgE levels in serum,” *TrAC - Trends in Analytical Chemistry*, vol. 127. p. 115904, 2020, doi: 10.1016/j.trac.2020.115904.
- [8] X. Weng, G. Gaur, and S. Neethirajan, “Rapid detection of food allergens by microfluidics ELISA-based optical sensor,” *Biosensors*, vol. 6, no. 2, p. 24, 2016, doi: 10.3390/bios6020024.
- [9] J. F. Rusling, E. G. Hvastkovs, and J. B. Schenkman, “Toxicity screening using biosensors that measure DNA damage,” in *Current Opinion in Drug Discovery and Development*, 2007, vol. 10, no. 1, pp. 67–73.
- [10] J. Robbins, M. Maras, W. Laureyn, R. Blust, and W. De Coen, “Whole cell biosensors for (eco)toxicity screening: Alternatives for the future,” in *2005 NSTI Nanotechnology Conference and Trade Show - NSTI Nanotech 2005 Technical Proceedings*, 2005, pp. 497–

500.

- [11] S. S. Pathak and H. F. J. Savelkoul, "Biosensors in immunology: The story so far," *Immunol. Today*, vol. 18, no. 10, pp. 464–467, 1997, doi: 10.1016/S0167-5699(97)01124-9.
- [12] S. Prajapati, B. Padhan, B. Amulyasai, and A. Sarkar, "Nanotechnology-based sensors," in *Biopolymer-Based Formulations: Biomedical and Food Applications*, 2020, pp. 237–262.
- [13] F. Haque, J. Li, H. C. Wu, X. J. Liang, and P. Guo, "Solid-state and biological nanopore for real-time sensing of single chemical and sequencing of DNA," *Nano Today*, vol. 8, no. 1, pp. 56–74, 2013, doi: 10.1016/j.nantod.2012.12.008.
- [14] E. Beamish, H. Kwok, V. Tabard-Cossa, and M. Godin, "Fine-tuning the size and minimizing the noise of solid-state nanopores.," *J. Vis. Exp.*, vol. 80, p. e51081, 2013, doi: 10.3791/51081.
- [15] M. Muthukumar, C. Plesa, and C. Dekker, "Single-molecule sensing with nanopores," *Phys. Today*, vol. 68, no. 8, pp. 40–46, 2015, doi: 10.1063/PT.3.2881.
- [16] M. D. Graham, "The Coulter principle: Imaginary origins," *Cytom. Part A*, vol. 83, no. 12, pp. 1057–1061, 2013, doi: 10.1002/cyto.a.22398.
- [17] W. Shi, A. K. Friedman, and L. A. Baker, "Nanopore Sensing," *Anal. Chem.*, vol. 89, no. 1, pp. 157–188, 2017, doi: 10.1021/acs.analchem.6b04260.
- [18] B. N. Miles, A. P. Ivanov, K. A. Wilson, F. Dogan, D. Japrun, and J. B. Edel, "Single molecule sensing with solid-state nanopores: novel materials, methods, and applications," *ChemInform*, vol. 42, pp. 15–28, 2013, doi: 10.1002/chin.201316277.
- [19] S. Bearden, E. McClure, and G. Zhang, "Detecting and identifying small molecules in a nanopore flux capacitor," *Nanotechnology*, vol. 27, no. 7, p. 075503, 2016, doi: 10.1088/0957-4484/27/7/075503.
- [20] A. Fragasso, S. Schmid, and C. Dekker, "Comparing Current Noise in Biological and Solid-State Nanopores," *ACS Nano*, vol. 14, no. 2, pp. 1338–1349, 2020, doi: 10.1021/acsnano.9b09353.
- [21] A. Apetrei, A. Ciuca, J. kook Lee, C. H. Seo, Y. Park, and T. Luchian, "A Protein Nanopore-

- Based Approach for Bacteria Sensing,” *Nanoscale Res. Lett.*, vol. 11, no. 1, p. 501, 2016, doi: 10.1186/s11671-016-1715-z.
- [22] E. L. Moss, D. G. Maghini, and A. S. Bhatt, “Complete, closed bacterial genomes from microbiomes using nanopore sequencing,” *Nat. Biotechnol.*, vol. 38, no. 6, pp. 701–707, 2020, doi: 10.1038/s41587-020-0422-6.
- [23] A. Arima *et al.*, “Selective detections of single-viruses using solid-state nanopores,” *Sci. Rep.*, vol. 8, no. 1, p. 16305, 2018, doi: 10.1038/s41598-018-34665-4.
- [24] S. Oh, M. K. Lee, and S. W. Chi, “Single-Molecule-Based Detection of Conserved Influenza A Virus RNA Promoter Using a Protein Nanopore,” *ACS Sensors*, vol. 4, no. 11, pp. 2849–2853, 2019, doi: 10.1021/acssensors.9b01558.
- [25] Y. L. Ying, R. J. Yu, Y. X. Hu, R. Gao, and Y. T. Long, “Single antibody-antigen interactions monitored: Via transient ionic current recording using nanopore sensors,” *Chem. Commun.*, vol. 53, no. 61, pp. 8620–8623, 2017, doi: 10.1039/c7cc03927a.
- [26] T. J. Morin *et al.*, “A handheld platform for target protein detection and quantification using disposable nanopore strips,” *Sci. Rep.*, vol. 8, no. 1, p. 14834, 2018, doi: 10.1038/s41598-018-33086-7.
- [27] C. Cao *et al.*, “Single-molecule sensing of peptides and nucleic acids by engineered aerolysin nanopores,” *Nat. Commun.*, vol. 10, no. 1, p. 4918, 2019, doi: 10.1038/s41467-019-12690-9.
- [28] F. Piguet, H. Ouldali, M. Pastoriza-Gallego, P. Manivet, J. Pelta, and A. Oukhaled, “Identification of single amino acid differences in uniformly charged homopolymeric peptides with aerolysin nanopore,” *Nat. Commun.*, vol. 9, no. 1, p. 966, 2018, doi: 10.1038/s41467-018-03418-2.
- [29] A. B. Farimani, K. Min, and N. R. Aluru, “DNA base detection using a single-layer MoS<sub>2</sub>,” *ACS Nano*, vol. 8, no. 8, pp. 7914–7922, 2014, doi: 10.1021/nn5029295.
- [30] Z. Liu, Y. Wang, T. Deng, and Q. Chen, “Solid-State Nanopore-Based DNA Sequencing Technology,” *Journal of Nanomaterials*. p. 5284786, 2016, doi: 10.1155/2016/5284786.

- [31] M. Sultan and A. Kanavarioti, “Nanopore device-based fingerprinting of RNA oligos and microRNAs enhanced with an Osmium tag,” *Sci. Rep.*, vol. 9, no. 1, p. 14180, 2019, doi: 10.1038/s41598-019-50459-8.
- [32] N. Harel, M. Meir, U. Gophna, and A. Stern, “Direct sequencing of RNA with MinION Nanopore: Detecting mutations based on associations,” *Nucleic Acids Res.*, vol. 47, no. 22, p. e148, 2019, doi: 10.1093/nar/gkz907.
- [33] P. Y. Kwok and X. Chen, “Detection of single nucleotide polymorphisms,” *Curr. Issues Mol. Biol.*, vol. 5, no. 2, pp. 43–60, 2003.
- [34] Y. S. Ang and L. Y. L. Yung, “Rapid and label-free single-nucleotide discrimination via an integrative nanoparticle-nanopore approach,” *ACS Nano*, vol. 6, no. 10, pp. 8815–8823, 2012, doi: 10.1021/nn302636z.
- [35] Q. Zhao *et al.*, “Detecting SNPs using a synthetic nanopore,” *Nano Lett.*, vol. 7, no. 6, pp. 1680–1685, 2007, doi: 10.1021/nl070668c.
- [36] K. Tian *et al.*, “Single Locked Nucleic Acid-Enhanced Nanopore Genetic Discrimination of Pathogenic Serotypes and Cancer Driver Mutations,” *ACS Nano*, vol. 12, no. 5, pp. 4194–4205, 2018, doi: 10.1021/acsnano.8b01198.
- [37] S. Cornelis *et al.*, “Forensic STR profiling using Oxford Nanopore Technologies’ MinION sequencer,” *bioRxiv*. p. 433151, 2018, doi: 10.1101/433151.
- [38] S. Cornelis *et al.*, “Forensic tri-allelic SNP genotyping using nanopore sequencing,” *Forensic Sci. Int. Genet.*, vol. 38, pp. 204–210, 2019, doi: 10.1016/j.fsigen.2018.11.012.
- [39] J. Y. Choi *et al.*, “Nanopore sequencing-based genome assembly and evolutionary genomics of circum-basmati rice,” *Genome Biol.*, vol. 21, no. 1, p. 21, 2020, doi: 10.1186/s13059-020-1938-2.
- [40] A. Pomerantz *et al.*, “Real-time DNA barcoding in a rainforest using nanopore sequencing: Opportunities for rapid biodiversity assessments and local capacity building,” *Gigascience*, vol. 7, no. 4, pp. 1–14, 2018, doi: 10.1093/gigascience/giy033.
- [41] S. Johri *et al.*, “Mitochondrial genome to aid species delimitation and effective conservation

- of the Sharpnose Guitarfish (*Glaucostegus granulatus*),” *Meta Gene*, vol. 24, p. 100648, 2020, doi: 10.1016/j.mgene.2020.100648.
- [42] Q. Chen and Z. Liu, “Fabrication and applications of solid-state nanopores,” *Sensors (Switzerland)*, vol. 19, no. 8, p. 1886, 2019, doi: 10.3390/s19081886.
- [43] Y. C. Chou, P. Masih Das, D. S. Monos, D. S. Monos, and M. Drndić, “Lifetime and Stability of Silicon Nitride Nanopores and Nanopore Arrays for Ionic Measurements,” *ACS Nano*, vol. 14, no. 6, pp. 6715–6728, 2020, doi: 10.1021/acsnano.9b09964.
- [44] Y. Goto, K. Matsui, I. Yanagi, and K. I. Takeda, “Silicon nitride nanopore created by dielectric breakdown with a divalent cation: Deceleration of translocation speed and identification of single nucleotides,” *Nanoscale*, vol. 11, no. 30, pp. 14426–14433, 2019, doi: 10.1039/c9nr03563j.
- [45] L. Wu, H. Liu, Y. Liu, H. Chen, Q. Liu, and Z. Lu, “Fabrication and characterization of silicon nitride nanopore,” in *Proceedings of the 2013 6th International Conference on Biomedical Engineering and Informatics, BMEI 2013*, 2013, pp. 363–367, doi: 10.1109/BMEI.2013.6746964.
- [46] A. J. Storm, J. H. Chen, H. W. Zandbergen, and C. Dekker, “Translocation of double-strand DNA through a silicon oxide nanopore,” *Phys. Rev. E - Stat. Nonlinear, Soft Matter Phys.*, vol. 71, no. 5, p. 051903, 2005, doi: 10.1103/PhysRevE.71.051903.
- [47] H. Chang, F. Kosari, G. Andreadakis, M. A. Alam, G. Vasmatzis, and R. Bashir, “DNA-mediated fluctuations in ionic current through silicon oxide nanopore channels,” *Nano Lett.*, vol. 4, no. 8, pp. 1551–1556, 2004, doi: 10.1021/nl049267c.
- [48] L. J. Steinbock, R. D. Bulushev, S. Krishnan, C. Raillon, and A. Radenovic, “DNA translocation through low-noise glass nanopores,” *ACS Nano*, vol. 7, no. 12, pp. 11255–11262, 2013, doi: 10.1021/nn405029j.
- [49] J. A. Bafna and G. V. Soni, “Fabrication of low noise borosilicate glass nanopores for single molecule sensing,” *PLoS One*, vol. 11, no. 6, p. e0157399, 2016, doi: 10.1371/journal.pone.0157399.
- [50] H. Chen, L. Li, T. Zhang, Z. Qiao, J. Tang, and J. Zhou, “Protein Translocation through a

- MoS<sub>2</sub> Nanopore: A Molecular Dynamics Study,” *J. Phys. Chem. C*, vol. 122, no. 4, pp. 2070–2080, 2018, doi: 10.1021/acs.jpcc.7b07842.
- [51] J. Feng *et al.*, “Identification of single nucleotides in MoS<sub>2</sub> nanopores,” *Nat. Nanotechnol.*, vol. 10, no. 12, pp. 1070–1076, 2015, doi: 10.1038/nnano.2015.219.
- [52] K. Liu, J. Feng, A. Kis, and A. Radenovic, “Atomically thin molybdenum disulfide nanopores with high sensitivity for dna translocation,” *ACS Nano*, vol. 8, no. 3, pp. 2504–2511, 2014, doi: 10.1021/nn406102h.
- [53] M. Graf, K. Liu, A. Sarathy, J.-P. Leburton, and A. Radenovic, “Transverse Detection of DNA in a MoS<sub>2</sub> Nanopore,” *Biophys. J.*, vol. 114, no. 3, p. 180a, 2018, doi: 10.1016/j.bpj.2017.11.1005.
- [54] C. A. Merchant *et al.*, “DNA translocation through graphene nanopores,” *Nano Lett.*, vol. 10, no. 8, pp. 2915–2921, 2010, doi: 10.1021/nl101046t.
- [55] B. Luan and R. Zhou, “Spontaneous Transport of Single-Stranded DNA through Graphene-MoS<sub>2</sub> Heterostructure Nanopores,” *ACS Nano*, vol. 12, no. 4, pp. 3886–3891, 2018, doi: 10.1021/acsnano.8b01297.
- [56] Canadian Centre on Substance Use and Addiction, “Alcohol (Canadian Drug Summary),” *Gov. Canada*, 2017.
- [57] Z. Atakan, “Cannabis, a complex plant: Different compounds and different effects on individuals,” *Ther. Adv. Psychopharmacol.*, vol. 2, no. 6, pp. 241–254, 2012, doi: 10.1177/2045125312457586.
- [58] I. Jou and M. Muthukumar, “Effects of Nanopore Charge Decorations on the Translocation Dynamics of DNA,” *Biophys. J.*, vol. 113, no. 8, pp. 1664–1672, 2017, doi: 10.1016/j.bpj.2017.08.045.
- [59] J. Shim *et al.*, “Detection of methylation on dsDNA using nanopores in a MoS<sub>2</sub> membrane,” *Nanoscale*, vol. 9, no. 39, pp. 14836–14845, 2017, doi: 10.1039/c7nr03092d.
- [60] J. Bentin, S. Balme, and F. Picaud, “Polynucleotide differentiation using hybrid solid-state nanopore functionalizing with  $\alpha$ -hemolysin,” *Soft Matter*, vol. 16, no. 4, pp. 1002–1010,

- 2020, doi: 10.1039/c9sm01833f.
- [61] A. B. Farimani, P. Dibaieinia, and N. R. Aluru, “DNA origami-graphene hybrid nanopore for DNA detection,” *ACS Appl. Mater. Interfaces*, vol. 9, no. 1, pp. 92–100, 2017, doi: 10.1021/acsami.6b11001.
- [62] B. Cressiot, S. J. Greive, M. Mojtabavi, A. A. Antson, and M. Wanunu, “Thermostable virus portal proteins as reprogrammable adapters for solid-state nanopore sensors,” *Nat. Commun.*, vol. 9, no. 1, p. 4652, 2018, doi: 10.1038/s41467-018-07116-x.
- [63] N. A. W. Bell *et al.*, “DNA origami nanopores,” *Nano Lett.*, vol. 12, no. 1, pp. 512–517, 2012, doi: 10.1021/nl204098n.
- [64] A. R. Hall, A. Scott, D. Rotem, K. K. Mehta, H. Bayley, and C. Dekker, “Hybrid pore formation by directed insertion of  $\alpha$ -haemolysin into solid-state nanopores,” *Nat. Nanotechnol.*, vol. 5, no. 12, pp. 874–877, 2010, doi: 10.1038/nnano.2010.237.
- [65] G. M. Roozbahani, X. Chen, Y. Zhang, L. Wang, and X. Guan, “Nanopore Detection of Metal Ions: Current Status and Future Directions,” *Small Methods*, vol. 4, no. 10, p. 2000266, 2020, doi: 10.1002/smt.202000266.
- [66] L. Liu, Z. Fang, X. Zheng, and D. Xi, “Nanopore-Based Strategy for Sensing of Copper(II) Ion and Real-Time Monitoring of a Click Reaction,” *ACS Sensors*, vol. 4, no. 5, pp. 1323–1328, 2019, doi: 10.1021/acssensors.9b00236.
- [67] J. Larkin, R. Henley, D. C. Bell, T. Cohen-Karni, J. K. Rosenstein, and M. Wanunu, “Slow DNA transport through nanopores in hafnium oxide membranes,” *ACS Nano*, vol. 7, no. 11, pp. 10121–10128, 2013, doi: 10.1021/nn404326f.
- [68] K. Chuah *et al.*, “Nanopore blockade sensors for ultrasensitive detection of proteins in complex biological samples,” *Nat. Commun.*, vol. 10, no. 1, p. 2109, 2019, doi: 10.1038/s41467-019-10147-7.
- [69] Y. Luo, L. Wu, J. Tu, and Z. Lu, “Application of solid-state nanopore in protein detection,” *Int. J. Mol. Sci.*, vol. 21, no. 8, p. 2808, 2020, doi: 10.3390/ijms21082808.
- [70] Q. Li, Y. L. Ying, S. C. Liu, Y. Lin, and Y. T. Long, “Detection of Single Proteins with a

- General Nanopore Sensor,” *ACS Sensors*, vol. 4, no. 5, pp. 1185–1189, 2019, doi: 10.1021/acssensors.9b00228.
- [71] S. Ghosal, J. D. Sherwood, and H. C. Chang, “Solid-state nanopore hydrodynamics and transport,” *Biomicrofluidics*, vol. 13, no. 1, p. 011301, 2019, doi: 10.1063/1.5083913.
- [72] Z. Y. Zhang, Y. S. Deng, H. B. Tian, H. Yan, H. L. Cui, and D. Q. Wang, “Noise analysis of monolayer graphene nanopores,” *Int. J. Mol. Sci.*, vol. 19, no. 9, p. 2639, 2018, doi: 10.3390/ijms19092639.
- [73] K. B. Park *et al.*, “Highly reliable and low-noise solid-state nanopores with an atomic layer deposited ZnO membrane on a quartz substrate,” *Nanoscale*, vol. 9, no. 47, pp. 18772–18780, 2017, doi: 10.1039/c7nr05755e.
- [74] S. J. Heerema, G. F. Schneider, M. Rozemuller, L. Vicarelli, H. W. Zandbergen, and C. Dekker, “1/f noise in graphene nanopores,” *Nanotechnology*, vol. 26, no. 7, p. 074001, 2015, doi: 10.1088/0957-4484/26/7/074001.
- [75] W. E. Moerner, “Viewpoint: Single Molecules at 31: What’s Next?,” *Nano Letters*, vol. 20, no. 12, pp. 8427–8429, 2020, doi: 10.1021/acs.nanolett.0c04042.
- [76] A. Maghsodi, L. Adlnasab, M. Shabanian, and M. Javanbakht, “Optimization of effective parameters in the synthesis of nanopore anodic aluminum oxide membrane and arsenic removal by prepared magnetic iron oxide nanoparticles in anodic aluminum oxide membrane via ultrasonic-hydrothermal method,” *Ultrason. Sonochem.*, vol. 48, pp. 441–452, 2018, doi: 10.1016/j.ultsonch.2018.07.003.
- [77] A. Santos, T. Kumeria, and D. Losic, “Nanoporous anodic aluminum oxide for chemical sensing and biosensors,” *TrAC - Trends Anal. Chem.*, vol. 44, pp. 25–38, 2013, doi: 10.1016/j.trac.2012.11.007.
- [78] B. M. Venkatesan *et al.*, “Lipid bilayer coated Al<sub>2</sub>O<sub>3</sub> nanopore sensors: Towards a hybrid biological solid-state nanopore,” *Biomed. Microdevices*, vol. 13, no. 4, pp. 671–682, 2011, doi: 10.1007/s10544-011-9537-3.
- [79] R. Wang, T. Gilboa, J. Song, D. Huttner, M. W. Grinstaff, and A. Meller, “Single-Molecule Discrimination of Labeled DNAs and Polypeptides Using Photoluminescent-Free TiO<sub>2</sub>

- Nanopores,” *ACS Nano*, vol. 12, no. 11, pp. 11648–11656, 2018, doi: 10.1021/acsnano.8b07055.
- [80] B. M. Venkatesan, B. Dorvel, S. Yemenicioglu, N. Watkins, I. Petrov, and R. Bashir, “Highly sensitive, mechanically stable nanopore sensors for DNA analysis,” *Adv. Mater.*, vol. 21, no. 27, pp. 2771–2776, 2009, doi: 10.1002/adma.200803786.
- [81] B. C. Joshi, G. Eranna, D. P. Runthala, B. B. Dixit, O. P. Wadhawan, and P. D. Vyas, “LPCVD and PECVD silicon nitride for microelectronics technology,” *Indian J. Eng. Mater. Sci.*, vol. 7, no. 5–6, pp. 303–309, 2000.
- [82] D. V. Verschuere, W. Yang, and C. Dekker, “Lithography-based fabrication of nanopore arrays in freestanding SiN and graphene membranes,” *Nanotechnology*, vol. 29, no. 14, p. 145302, 2018, doi: 10.1088/1361-6528/aaabce.
- [83] Z. Tang, D. Zhang, W. Cui, H. Zhang, W. Pang, and X. Duan, “Fabrications, Applications and Challenges of Solid-State Nanopores: A Mini Review,” *Nanomaterials and Nanotechnology*, vol. 6, p. 35, 2016, doi: 10.5772/64015.
- [84] C. H. Chen, X. Chang, and C. S. Wu, “A novel shaped-controlled fabrication of nanopore and its applications in quantum electronics,” *Sci. Rep.*, vol. 9, no. 1, p. 18663, 2019, doi: 10.1038/s41598-019-55190-y.
- [85] S. Prakash, M. Pinti, and K. Bellman, “Variable cross-section nanopores fabricated in silicon nitride membranes using a transmission electron microscope,” *J. Micromechanics Microengineering*, vol. 22, no. 6, p. 067002, 2012, doi: 10.1088/0960-1317/22/6/067002.
- [86] O. K. Zahid and A. R. Hall, “Helium ion microscope fabrication of solid-state nanopore devices for biomolecule analysis,” in *NanoScience and Technology*, 2016, pp. 447–470.
- [87] Y. Deng, Q. Huang, Y. Zhao, D. Zhou, C. Ying, and D. Wang, “Precise fabrication of a 5 nm graphene nanopore with a helium ion microscope for biomolecule detection,” *Nanotechnology*, vol. 28, no. 4, p. 045302, 2017, doi: 10.1088/1361-6528/28/4/045302.
- [88] K. Briggs, H. Kwok, and V. Tabard-Cossa, “Automated fabrication of 2-nm solid-state nanopores for nucleic acid analysis,” *Small*, vol. 10, no. 10, pp. 2077–2086, 2014, doi: 10.1002/sml.201303602.

- [89] Z. Yuan, Y. Liu, M. Dai, X. Yi, and C. Wang, “Controlling DNA Translocation Through Solid-state Nanopores,” *Nanoscale Research Letters*, vol. 15, no. 1, p. 80, 2020, doi: 10.1186/s11671-020-03308-x.
- [90] I. Yanagi, T. Ishida, K. Fujisaki, and K. I. Takeda, “Fabrication of 3-nm-thick Si<sub>3</sub>N<sub>4</sub> membranes for solid-state nanopores using the poly-Si sacrificial layer process,” *Sci. Rep.*, vol. 5, p. 14656, 2015, doi: 10.1038/srep14656.
- [91] S. R. Gillmer *et al.*, “Predicting the failure of ultrathin porous membranes in bulge tests,” *Thin Solid Films*, vol. 631, pp. 152–160, 2017, doi: 10.1016/j.tsf.2017.04.004.
- [92] V. N. Do and T. H. Pham, “Graphene and its one-dimensional patterns: From basic properties towards applications,” *Adv. Nat. Sci. Nanosci. Nanotechnol.*, vol. 1, no. 3, p. 033001, 2010, doi: 10.1088/2043-6254/1/3/033001.
- [93] G. Yang, L. Li, W. B. Lee, and M. C. Ng, “Structure of graphene and its disorders: a review,” *Sci. Technol. Adv. Mater.*, vol. 19, no. 1, pp. 613–648, 2018, doi: 10.1080/14686996.2018.1494493.
- [94] Y. Ohno, K. Maehashi, and K. Matsumoto, “Chemical and biological sensing applications based on graphene field-effect transistors,” *Biosens. Bioelectron.*, vol. 26, no. 4, pp. 1727–1730, 2010, doi: 10.1016/j.bios.2010.08.001.
- [95] G. F. Schneider *et al.*, “Tailoring the hydrophobicity of graphene for its use as nanopores for DNA translocation,” *Nat. Commun.*, vol. 4, p. 2619, 2013, doi: 10.1038/ncomms3619.
- [96] Z. Zhou *et al.*, “DNA Translocation through hydrophilic nanopore in hexagonal boron nitride,” *Sci. Rep.*, vol. 3, p. 3287, 2013, doi: 10.1038/srep03287.
- [97] L. Zhang and X. Wang, “DNA sequencing by hexagonal boron nitride nanopore: A computational study,” *Nanomaterials*, vol. 6, no. 6, p. 111, 2016, doi: 10.3390/nano6060111.
- [98] S. Liu *et al.*, “Boron nitride nanopores: Highly sensitive DNA single-molecule detectors,” *Adv. Mater.*, vol. 25, no. 33, pp. 4549–4554, 2013, doi: 10.1002/adma.201301336.
- [99] S. Manzeli, D. Ovchinnikov, D. Pasquier, O. V. Yazyev, and A. Kis, “2D transition metal

- dichalcogenides,” *Nat. Rev. Mater.*, vol. 2, p. 17033, 2017, doi: 10.1038/natrevmats.2017.33.
- [100] K. Pandey, K. Paredis, T. Hantschel, C. Drijbooms, and W. Vandervorst, “The impact of focused ion beam induced damage on scanning spreading resistance microscopy measurements,” *Sci. Rep.*, vol. 10, no. 1, p. 14893, 2020, doi: 10.1038/s41598-020-71826-w.
- [101] G. Danda *et al.*, “Monolayer WS<sub>2</sub> Nanopores for DNA Translocation with Light-Adjustable Sizes,” *ACS Nano*, vol. 11, no. 2, pp. 1937–1945, 2017, doi: 10.1021/acsnano.6b08028.
- [102] A. P. Ivanov *et al.*, “DNA tunneling detector embedded in a nanopore,” *Nano Lett.*, vol. 11, no. 1, pp. 279–285, 2011, doi: 10.1021/nl103873a.
- [103] H. Liu, D. Gu, L. Wang, H. Wu, R. Wang, and Q. Liu, “A cross-scale method of fabricating transverse electrode-embedded nanopore,” *Nanosci. Nanotechnol. Lett.*, vol. 8, no. 8, pp. 641–646, 2016, doi: 10.1166/nnl.2016.2203.
- [104] K. Yokota, M. Tsutsui, and M. Taniguchi, “Electrode-embedded nanopores for label-free single-molecule sequencing by electric currents,” *RSC Adv.*, vol. 4, pp. 15886–15899, 2014, doi: 10.1039/c4ra00933a.
- [105] Y. H. Lanyon and D. W. M. Arrigan, “Top-Down Approaches to the Fabrication of Nanopatterned Electrodes,” in *Nanostructured Materials in Electrochemistry*, 2008, pp. 187–210.
- [106] V. Georgakilas *et al.*, “Functionalization of graphene: Covalent and non-covalent approaches, derivatives and applications,” *Chem. Rev.*, vol. 112, no. 11, pp. 6156–6214, 2012, doi: 10.1021/cr3000412.
- [107] J. Ryou, Y. S. Kim, K. C. Santosh, and K. Cho, “Monolayer MoS<sub>2</sub> Bandgap Modulation by Dielectric Environments and Tunable Bandgap Transistors,” *Sci. Rep.*, vol. 6, p. 29184, 2016, doi: 10.1038/srep29184.
- [108] K. F. Mak, C. Lee, J. Hone, J. Shan, and T. F. Heinz, “Atomically thin MoS<sub>2</sub>: A new direct-gap semiconductor,” *Phys. Rev. Lett.*, vol. 105, no. 13, p. 136805, 2010, doi: 10.1103/PhysRevLett.105.136805.

- [109] D. L. Duong, S. J. Yun, and Y. H. Lee, “Van der Waals Layered Materials: Opportunities and Challenges,” *ACS Nano*, vol. 11, no. 12, pp. 11803–11830, 2017, doi: 10.1021/acsnano.7b07436.
- [110] K. S. Novoselov, A. Mishchenko, A. Carvalho, and A. H. Castro Neto, “2D materials and van der Waals heterostructures,” *Science (80-. )*, vol. 353, no. 6298, p. 9439, 2016, doi: 10.1126/science.aac9439.
- [111] Y. Liu, N. O. Weiss, X. Duan, H. C. Cheng, Y. Huang, and X. Duan, “Van der Waals heterostructures and devices,” *Nat. Rev. Mater.*, vol. 1, p. 16042, 2016, doi: 10.1038/natrevmats.2016.42.
- [112] M. H. Doan *et al.*, “Charge Transport in MoS<sub>2</sub>/WSe<sub>2</sub> van der Waals Heterostructure with Tunable Inversion Layer,” *ACS Nano*, vol. 11, no. 4, pp. 3832–3840, 2017, doi: 10.1021/acsnano.7b00021.
- [113] A. Nourbakhsh, A. Zubair, M. S. Dresselhaus, and T. Palacios, “Transport properties of a MoS<sub>2</sub>/WSe<sub>2</sub> heterojunction transistor and its potential for application,” *Nano Lett.*, vol. 16, no. 2, pp. 1359–1366, 2016, doi: 10.1021/acs.nanolett.5b04791.
- [114] B. M. Venkatesan and R. Bashir, “Nanopore sensors for nucleic acid analysis,” *Nature Nanotechnology*, vol. 6, no. 10, pp. 615–624, 2011, doi: 10.1038/nnano.2011.129.
- [115] W. Van Drongelen, *Signal Processing for Neuroscientists*. 2007.
- [116] D. Fologea, J. Uplinger, B. Thomas, D. S. McNabb, and J. Li, “Slowing DNA translocation in a solid-state nanopore,” *Nano Lett.*, vol. 5, no. 9, pp. 1734–1737, 2005, doi: 10.1021/nl051063o.
- [117] B. Luan, G. Stolovitzky, and G. Martyna, “Slowing and controlling the translocation of DNA in a solid-state nanopore,” *Nanoscale*, vol. 4, no. 4, pp. 1068–1077, 2012, doi: 10.1039/c1nr11201e.
- [118] M. Wanunu, J. Sutin, B. McNally, A. Chow, and A. Meller, “DNA translocation governed by interactions with solid-state nanopores,” *Biophys. J.*, vol. 95, no. 10, pp. 4716–4725, 2008, doi: 10.1529/biophysj.108.140475.

- [119] L. Liang, P. Cui, Q. Wang, T. Wu, H. Ågren, and Y. Tu, “Theoretical study on key factors in DNA sequencing with graphene nanopores,” *RSC Adv.*, vol. 3, no. 7, pp. 2445–2453, 2013, doi: 10.1039/c2ra22109h.
- [120] B. Luan and A. Aksimentiev, “Electric and electrophoretic inversion of the DNA charge in multivalent electrolytes,” *Soft Matter*, vol. 6, no. 2, pp. 243–246, 2010, doi: 10.1039/b917973a.
- [121] Y. He, M. Tsutsui, C. Fan, M. Taniguchi, and T. Kawai, “Controlling DNA translocation through gate modulation of nanopore wall surface charges,” in *ACS Nano*, 2011, vol. 5, no. 7, pp. 5509–5518, doi: 10.1021/nn201883b.
- [122] Y. Zhang *et al.*, “Temperature effect on translocation speed and capture rate of nanopore-based DNA detection,” *Sci. China Technol. Sci.*, vol. 58, no. 3, pp. 519–525, 2015, doi: 10.1007/s11431-014-5674-2.
- [123] H. Zhang *et al.*, “Slowing down DNA translocation through solid-state nanopores by pressure,” *Small*, vol. 9, no. 24, pp. 4112–4117, 2013, doi: 10.1002/sml.201301263.
- [124] D. P. Hoogerheide, B. Lu, and J. A. Golovchenko, “Pressure-voltage trap for DNA near a solid-state nanopore,” *ACS Nano*, vol. 8, no. 7, pp. 7384–7391, 2014, doi: 10.1021/nn5025829.
- [125] N. Academy, N. Academy, and U. States, “Characterization of Individual Polynucleotide Molecules Using a Membrane Channel Author ( s ): John J . Kasianowicz , Eric Brandin , Daniel Branton and David W . Deamer Source : Proceedings of the National Academy of Sciences of the United States of Publi,” vol. 93, no. 24, pp. 13770–13773, 1996.
- [126] A. Pandey, K. Shin, R. E. Patterson, X. Q. Liu, and J. K. Rainey, “Current strategies for protein production and purification enabling membrane protein structural biology1,” *Biochem. Cell Biol.*, vol. 94, no. 6, pp. 507–527, 2016, doi: 10.1139/bcb-2015-0143.
- [127] S. Wang, Z. Zhao, F. Haque, and P. Guo, “Engineering of protein nanopores for sequencing, chemical or protein sensing and disease diagnosis,” *Current Opinion in Biotechnology*, vol. 51, pp. 80–89, 2018, doi: 10.1016/j.copbio.2017.11.006.
- [128] G. Maglia, M. R. Restrepo, E. Mikhailova, and H. Bayley, “Enhanced translocation of

- single DNA molecules through  $\alpha$ -hemolysin nanopores by manipulation of internal charge,” *Proc. Natl. Acad. Sci. U. S. A.*, vol. 105, no. 50, pp. 19720–19725, 2008, doi: 10.1073/pnas.0808296105.
- [129] N. N. Jetha, M. Wiggin, and A. Marziali, “Forming an alpha-hemolysin nanopore for single-molecule analysis,” *Methods Mol. Biol.*, vol. 544, pp. 113–127, 2009, doi: 10.1007/978-1-59745-483-4\_9.
- [130] R. M. A. Manara, S. Tomasio, and S. Khalid, “The nucleotide capture region of alpha hemolysin: Insights into nanopore design for DNA sequencing from molecular dynamics simulations,” *Nanomaterials*, vol. 5, no. 1, pp. 144–153, 2015, doi: 10.3390/nano5010144.
- [131] J. J. S. Júnior *et al.*, “Alpha-hemolysin nanopore allows discrimination of the microcystins variants,” *RSC Adv.*, vol. 9, no. 26, pp. 14683–14691, 2019, doi: 10.1039/c8ra10384d.
- [132] S. Y. Noskov, W. Im, and B. Roux, “Ion permeation through the  $\alpha$ -hemolysin channel: Theoretical studies based on Brownian dynamics and Poisson-Nernst-Planck electrodiffusion theory,” *Biophys. J.*, vol. 87, no. 4, pp. 2299–2309, 2004, doi: 10.1529/biophysj.104.044008.
- [133] G. Maglia, A. J. Heron, D. Stoddart, D. Japrun, and H. Bayley, “Analysis of Single Nucleic Acid Molecules with Protein Nanopores,” in *Methods in Enzymology*, 2010, pp. 591–623.
- [134] M. Akeson, D. Branton, J. J. Kasianowicz, E. Brandin, and D. W. Deamer, “Microsecond time-scale discrimination among polycytidylic acid, polyadenylic acid, and polyuridylic acid as homopolymers or as segments within single RNA molecules,” *Biophys. J.*, vol. 77, no. 6, pp. 3227–3233, 1999, doi: 10.1016/S0006-3495(99)77153-5.
- [135] S. Carson and M. Wanunu, “Challenges in DNA motion control and sequence readout using nanopore devices,” *Nanotechnology*, vol. 26, no. 7, p. 074004, 2015, doi: 10.1088/0957-4484/26/7/074004.
- [136] L. Rittié and B. Perbal, “Enzymes used in molecular biology: A useful guide,” *J. Cell Commun. Signal.*, vol. 2, pp. 25–45, 2008, doi: 10.1007/s12079-008-0026-2.
- [137] P. A. Mason and L. S. Cox, “The role of DNA exonucleases in protecting genome stability and their impact on ageing,” *Age (Omaha)*, vol. 34, no. 6, pp. 1317–1340, 2012, doi:

10.1007/s11357-011-9306-5.

- [138] L. Xue, H. Yamazaki, R. Ren, M. Wanunu, A. P. Ivanov, and J. B. Edel, “Solid-state nanopore sensors,” *Nat. Rev. Mater.*, vol. 5, pp. 931–951, 2020, doi: 10.1038/s41578-020-0229-6.
- [139] B. Juskowiak, “Nucleic acid-based fluorescent probes and their analytical potential,” in *Analytical and Bioanalytical Chemistry*, 2011, vol. 399, no. 9, pp. 3157–3176, doi: 10.1007/s00216-010-4304-5.
- [140] S. K. Silverman, R. Nutiu, L. P. Billen, and Y. Li, “Fluorescence-Signaling Nucleic Acid-Based Sensors,” in *Nucleic Acid Switches and Sensors*, 2006, pp. 49–72.
- [141] B. M. Venkatesan and R. Bashir, “Nanopore sensors for nucleic acid analysis,” *Nat. Nanotechnol.*, vol. 6, pp. 615–624, 2011, doi: 10.1038/nnano.2011.129.
- [142] D. Branton *et al.*, “The potential and challenges of nanopore sequencing,” *Nat. Biotechnol.*, vol. 26, pp. 1146–1153, 2008, doi: 10.1038/nbt.1495.
- [143] A. H. Laszlo *et al.*, “Detection and mapping of 5-methylcytosine and 5-hydroxymethylcytosine with nanopore MspA,” *Proc. Natl. Acad. Sci. U. S. A.*, vol. 110, no. 47, pp. 18904–18909, 2013, doi: 10.1073/pnas.1310240110.
- [144] Y. Ding, A. M. Fleming, and C. J. Burrows, “ $\alpha$ -Hemolysin nanopore studies reveal strong interactions between biogenic polyamines and DNA hairpins,” *Microchim. Acta*, vol. 183, no. 3, pp. 973–979, 2016, doi: 10.1007/s00604-015-1516-6.
- [145] I. M. Derrington *et al.*, “Nanopore DNA sequencing with MspA,” *Proc. Natl. Acad. Sci. U. S. A.*, vol. 107, no. 37, pp. 16060–16065, 2010, doi: 10.1073/pnas.1001831107.
- [146] I. Iacovache, S. De Carlo, N. Cirauqui, M. Dal Peraro, F. G. Van Der Goot, and B. Zuber, “Cryo-EM structure of aerolysin variants reveals a novel protein fold and the pore-formation process,” *Nat. Commun.*, vol. 7, p. 12062, 2016, doi: 10.1038/ncomms12062.
- [147] S. Köster, K. Van Pee, and Ö. Yildiz, “Purification, refolding, and crystallization of the outer membrane protein OmpG from *Escherichia coli*,” in *Methods in Enzymology*, 2015, pp. 149–166.

- [148] A. H. Laszlo, I. M. Derrington, and J. H. Gundlach, “MspA nanopore as a single-molecule tool: From sequencing to SPRNT,” *Methods*, vol. 105, pp. 75–89, 2016, doi: 10.1016/j.ymeth.2016.03.026.
- [149] K. W. Langford, B. Penkov, I. M. Derrington, and J. H. Gundlach, “Unsupported planar lipid membranes formed from mycolic acids of *Mycobacterium tuberculosis*,” *J. Lipid Res.*, vol. 52, no. 2, pp. 272–277, 2011, doi: 10.1194/jlr.M012013.
- [150] D. Wu, S. Bi, L. Zhang, and J. Yang, “Single-molecule study of proteins by biological nanopore sensors,” *Sensors (Switzerland)*, vol. 14, no. 10, pp. 18211–18222, 2014, doi: 10.3390/s141018211.
- [151] M. A. Fahie, B. Yang, M. Mullis, M. A. Holden, and M. Chen, “Selective Detection of Protein Homologues in Serum Using an OmpG Nanopore,” *Anal. Chem.*, vol. 87, no. 21, pp. 11143–11149, 2015, doi: 10.1021/acs.analchem.5b03350.
- [152] W. Grosse *et al.*, “Structure-based engineering of a minimal porin reveals loop-independent channel closure,” *Biochemistry*, vol. 53, no. 29, pp. 4826–4838, 2014, doi: 10.1021/bi500660q.
- [153] R. R. Sanganna Gari, P. Seelheim, B. Liang, and L. K. Tamm, “Quiet Outer Membrane Protein G (OmpG) Nanopore for Biosensing,” *ACS Sensors*, vol. 4, no. 5, pp. 1230–1235, 2019, doi: 10.1021/acssensors.8b01645.
- [154] U. Rengarajan, H. Hoi, M. Gupta, and C. Montemagno, “Hybrid Nanopore for Molecular Sensing Applications,” *Biophys. J.*, vol. 112, no. 3, p. 459a, 2017, doi: 10.1016/j.bpj.2016.11.2461.
- [155] Y. Wang, Q. Yang, and Z. Wang, “The evolution of nanopore sequencing,” *Front. Genet.*, vol. 5, p. 449, 2015, doi: 10.3389/fgene.2014.00449.
- [156] V. Mussi *et al.*, “DNA-functionalized solid state nanopore for biosensing,” *Nanotechnology*, vol. 21, no. 14, p. 145102, 2010, doi: 10.1088/0957-4484/21/14/145102.
- [157] T. Gilboa, E. Zvuloni, A. Zrehen, A. H. Squires, and A. Meller, “Automated, Ultra-Fast Laser-Drilling of Nanometer Scale Pores and Nanopore Arrays in Aqueous Solutions,” *Adv. Funct. Mater.*, vol. 30, no. 18, p. 1900642, 2020, doi: 10.1002/adfm.201900642.

- [158] K. Venta *et al.*, “Differentiation of short, single-stranded DNA homopolymers in solid-state nanopores,” *ACS Nano*, vol. 7, no. 5, pp. 4629–4636, 2013, doi: 10.1021/nn4014388.
- [159] D. Emmrich *et al.*, “Nanopore fabrication and characterization by helium ion microscopy,” *Appl. Phys. Lett.*, vol. 108, no. 16, p. 163103, 2016, doi: 10.1063/1.4947277.
- [160] J. Kong *et al.*, “Silicon nitride nanopores for nanoparticle sensing,” *J. Nanosci. Nanotechnol.*, vol. 13, no. 6, pp. 4010–4016, 2013, doi: 10.1166/jnn.2013.7141.
- [161] G. Goyal, Y. B. Lee, A. Darvish, C. W. Ahn, and M. J. Kim, “Hydrophilic and size-controlled graphene nanopores for protein detection,” *Nanotechnology*, vol. 27, no. 49, p. 495301, 2016, doi: 10.1088/0957-4484/27/49/495301.
- [162] M. Van Den Hout, A. R. Hall, M. Y. Wu, H. W. Zandbergen, C. Dekker, and N. H. Dekker, “Controlling nanopore size, shape and stability,” *Nanotechnology*, vol. 21, no. 11, p. 115304, 2010, doi: 10.1088/0957-4484/21/11/115304.
- [163] A. Diaz Carral, C. Shekar Sarap, K. Liu, A. Radenovic, and M. Fyta, “2D MoS<sub>2</sub> nanopores: Ionic current blockade height for clustering DNA events,” *2D Mater.*, vol. 6, no. 4, p. 045011, 2019, doi: 10.1088/2053-1583/ab2c38.
- [164] J. Hong, K. Li, C. Jin, X. Zhang, Z. Zhang, and J. Yuan, “Layer-dependent anisotropic electronic structure of freestanding quasi-two-dimensional Mo S<sub>2</sub>,” *Phys. Rev. B*, vol. 93, no. 7, p. 075440, 2016, doi: 10.1103/PhysRevB.93.075440.
- [165] A. Nicolai, M. D. Barrios Pérez, P. Delarue, V. Meunier, M. Drndić, and P. Senet, “Molecular Dynamics Investigation of Polylysine Peptide Translocation through MoS<sub>2</sub> Nanopores,” *J. Phys. Chem. B*, vol. 123, no. 10, pp. 2342–2353, 2019, doi: 10.1021/acs.jpcc.8b10634.
- [166] F. Sanger and A. R. Coulson, “A rapid method for determining sequences in DNA by primed synthesis with DNA polymerase,” *J. Mol. Biol.*, vol. 94, no. 3, pp. 441–446, 1975, doi: 10.1016/0022-2836(75)90213-2.
- [167] A. M. Maxam and W. Gilbert, “A new method for sequencing DNA,” *Proc. Natl. Acad. Sci. U. S. A.*, vol. 74, no. 2, pp. 560–564, 1977, doi: 10.1073/pnas.74.2.560.

- [168] E. S. Lander *et al.*, “Initial sequencing and analysis of the human genome,” *Nature*, vol. 409, no. 6822, pp. 860–921, 2001, doi: 10.1038/35057062.
- [169] J. M. Heather and B. Chain, “The sequence of sequencers: The history of sequencing DNA,” *Genomics*, vol. 107, no. 1, pp. 1–8, 2016, doi: 10.1016/j.ygeno.2015.11.003.
- [170] A. S. Mikheyev and M. M. Y. Tin, “A first look at the Oxford Nanopore MinION sequencer,” *Mol. Ecol. Resour.*, vol. 14, no. 6, pp. 1097–1102, 2014, doi: 10.1111/1755-0998.12324.
- [171] V. G. Leblanc and M. A. Marra, “Next-generation sequencing approaches in cancer: Where have they brought us and wherewill they take us?,” *Cancers (Basel)*, vol. 7, pp. 1925–1958, 2015, doi: 10.3390/cancers7030869.
- [172] M. A. Fahie, B. Yang, B. Pham, and M. Chen, “Tuning the Selectivity and Sensitivity of an OmpG Nanopore Sensor by Adjusting Ligand Tether Length,” *ACS Sensors*, vol. 1, no. 5, pp. 614–622, 2016, doi: 10.1021/acssensors.6b00014.
- [173] K. Rabgay, N. Waranuch, N. Chaiyakunapruk, R. Sawangjit, K. Ingkaninan, and P. Dilokthornsakul, “The effects of cannabis, cannabinoids, and their administration routes on pain control efficacy and safety: A systematic review and network meta-analysis,” *J. Am. Pharm. Assoc.*, vol. 60, no. 1, pp. 225–234, 2020, doi: 10.1016/j.japh.2019.07.015.
- [174] N. Bruni, C. Della Pepa, S. Oliaro-Bosso, E. Pessione, D. Gastaldi, and F. Dosio, “Cannabinoid delivery systems for pain and inflammation treatment,” *Molecules*, vol. 23, no. 10, p. 2478, 2018, doi: 10.3390/molecules23102478.
- [175] E. B. Russo, “Cannabinoids in the management of difficult to treat pain,” *Ther. Clin. Risk Manag.*, vol. 4, no. 1, pp. 245–259, 2008, doi: 10.2147/term.s1928.
- [176] L. Zuurman, A. E. Ippel, E. Moin, and J. M. A. Van Gerven, “Biomarkers for the effects of cannabis and THC in healthy volunteers,” *Br. J. Clin. Pharmacol.*, vol. 67, no. 1, pp. 5–21, 2009, doi: 10.1111/j.1365-2125.2008.03329.x.
- [177] M. L. Hudak *et al.*, “Neonatal drug withdrawal,” *Pediatrics*, vol. 129, no. 2, pp. e540–e560, 2012, doi: 10.1542/peds.2011-3212.

- [178] N. D. Volkow, R. D. Baler, W. M. Compton, and S. R. B. Weiss, “Adverse Health Effects of Marijuana Use,” *N. Engl. J. Med.*, vol. 370, no. 23, pp. 2219–2227, 2014, doi: 10.1056/nejmra1402309.
- [179] U. Bonnet and U. Preuss, “The cannabis withdrawal syndrome: current insights,” *Subst. Abuse Rehabil.*, vol. 8, pp. 9–37, 2017, doi: 10.2147/sar.s109576.
- [180] P. Sharma, P. Murthy, and M. M. S. Bharath, “Chemistry, metabolism, and toxicology of cannabis: Clinical implications,” *Iran. J. Psychiatry*, vol. 7, no. 4, pp. 149–156, 2012.
- [181] F. Grotenhermen, “Clinical pharmacokinetics of cannabinoids,” *Journal of Cannabis Therapeutics*, vol. 3, no. 1, pp. 3–51, 2003, doi: 10.1300/J175v03n01\_02.
- [182] M. A. Huestis and E. J. Cone, “Relationship of  $\Delta^9$ -tetrahydrocannabinol concentrations in oral fluid and plasma after controlled administration of smoked cannabis,” in *Journal of Analytical Toxicology*, 2004, vol. 28, no. 6, pp. 394–399, doi: 10.1093/jat/28.6.394.
- [183] B. Demé, M. Dubois, and T. Zemb, “Swelling of a lecithin lamellar phase induced by small carbohydrate solutes,” *Biophys. J.*, vol. 82, no. 1, 2002, doi: 10.1016/S0006-3495(02)75388-5.
- [184] C. Hyun, R. Rollings, and J. Li, “Probing access resistance of solid-state nanopores with a scanning-probe microscope tip,” *Small*, vol. 8, no. 3, pp. 385–392, 2012, doi: 10.1002/sml.201101337.
- [185] A. Balan *et al.*, “Improving signal-to-noise performance for DNA translocation in solid-state nanopores at MHz bandwidths,” *Nano Lett.*, vol. 14, no. 12, pp. 7215–7220, 2014, doi: 10.1021/nl504345y.
- [186] A. Balan, C. C. Chien, R. Engelke, and M. Drndic, “Suspended Solid-state Membranes on Glass Chips with Sub 1-pF Capacitance for Biomolecule Sensing Applications,” *Sci. Rep.*, vol. 5, p. 17775, 2015, doi: 10.1038/srep17775.
- [187] J. Li, M. Gershow, D. Stein, E. Brandin, and J. A. Golovchenko, “DNA molecules and configurations in a solid-state nanopore microscope,” *Nat. Mater.*, vol. 2, no. 9, pp. 611–615, 2003, doi: 10.1038/nmat965.

- [188] B. M. Venkatesan, A. B. Shah, J. M. Zuo, and R. Bashir, “DNA sensing using nanocrystalline surface-enhanced Al<sub>2</sub>O<sub>3</sub> nanopore sensors,” *Adv. Funct. Mater.*, vol. 20, no. 8, pp. 1266–1275, 2010, doi: 10.1002/adfm.200902128.
- [189] G. F. Schneider *et al.*, “DNA translocation through graphene nanopores,” *Nano Lett.*, vol. 10, no. 8, pp. 3163–3167, 2010, doi: 10.1021/nl102069z.
- [190] D. B. Wells, M. Belkin, J. Comer, and A. Aksimentiev, “Assessing graphene nanopores for sequencing DNA,” *Nano Lett.*, vol. 12, no. 8, pp. 4117–4123, 2012, doi: 10.1021/nl301655d.
- [191] A. Kumar, K. B. Park, H. M. Kim, and K. B. Kim, “Noise and its reduction in graphene based nanopore devices,” *Nanotechnology*, vol. 24, no. 49, p. 495503, 2013, doi: 10.1088/0957-4484/24/49/495503.
- [192] Y. H. Lanyon *et al.*, “Fabrication of nanopore array electrodes by focused ion beam milling,” *Anal. Chem.*, vol. 79, no. 8, pp. 3048–3055, 2007, doi: 10.1021/ac061878x.
- [193] B. Schiedt *et al.*, “Direct FIB fabrication and integration of ‘single nanopore devices’ for the manipulation of macromolecules,” *Microelectron. Eng.*, vol. 87, no. 5–8, pp. 1300–1303, 2010, doi: 10.1016/j.mee.2009.12.073.
- [194] J. Yang *et al.*, “Rapid and precise scanning helium ion microscope milling of solid-state nanopores for biomolecule detection,” *Nanotechnology*, vol. 22, no. 28, p. 285310, 2011, doi: 10.1088/0957-4484/22/28/285310.
- [195] F. Sawafta, A. T. Carlsen, and A. R. Hall, “Membrane thickness dependence of Nanopore formation with a focused helium ion beam,” *Sensors (Switzerland)*, vol. 14, no. 5, pp. 8150–8161, 2014, doi: 10.3390/s140508150.
- [196] A. T. Carlsen, O. K. Zahid, J. Ruzicka, E. W. Taylor, and A. R. Hall, “Interpreting the conductance blockades of DNA translocations through solid-state nanopores,” *ACS Nano*, vol. 8, no. 5, pp. 4754–4760, 2014, doi: 10.1021/nm501694n.
- [197] A. J. Storm, J. H. Chen, X. S. Ling, H. W. Zandbergen, and C. Dekker, “Fabrication of solid-state nanopores with single-nanometre precision,” *Nature Materials*, vol. 2, no. 8, pp. 537–540, 2003, doi: 10.1038/nmat941.

- [198] T. Gilboa, A. Zreben, A. Girsault, and A. Meller, “Optically-Monitored Nanopore Fabrication Using a Focused Laser Beam,” *Sci. Rep.*, vol. 8, no. 1, p. 9765, 2018, doi: 10.1038/s41598-018-28136-z.
- [199] P. Chen, T. Mitsui, D. B. Farmer, J. Golovchenko, R. G. Gordon, and D. Branton, “Atomic layer deposition to fine-tune the surface properties and diameters of fabricated nanopores,” *Nano Lett.*, vol. 4, no. 7, pp. 1333–1337, 2004, doi: 10.1021/nl0494001.
- [200] S. Pud, D. Verschueren, N. Vukovic, C. Plesa, M. P. Jonsson, and C. Dekker, “Self-Aligned Plasmonic Nanopores by Optically Controlled Dielectric Breakdown,” *Nano Lett.*, vol. 15, no. 10, pp. 7112–7117, 2015, doi: 10.1021/acs.nanolett.5b03239.
- [201] H. Kwok, K. Briggs, and V. Tabard-Cossa, “Nanopore fabrication by controlled dielectric breakdown,” *PLoS One*, vol. 9, no. 3, p. e92880., 2014, doi: 10.1371/journal.pone.0092880.
- [202] Z. Yuan, C. Wang, X. Yi, Z. Ni, Y. Chen, and T. Li, “Solid-State Nanopore,” *Nanoscale Research Letters*. p. 56, 2018, doi: 10.1186/s11671-018-2463-z.
- [203] C. M. Frament and J. R. Dwyer, “Conductance-based determination of solid-state nanopore size and shape: An exploration of performance limits,” *J. Phys. Chem. C*, vol. 116, no. 44, pp. 23315–23321, 2012, doi: 10.1021/jp305381j.
- [204] N. Patterson, D. P. Adams, V. C. Hodges, M. J. Vasile, J. R. Michael, and P. G. Kotula, “Controlled fabrication of nanopores using a direct focused ion beam approach with back face particle detection,” *Nanotechnology*, vol. 19, no. 23, p. 235304, 2008, doi: 10.1088/0957-4484/19/23/235304.
- [205] M. Y. Wu *et al.*, “Control of shape and material composition of solid-state nanopores,” *Nano Lett.*, vol. 9, no. 1, pp. 479–484, 2009, doi: 10.1021/nl803613s.
- [206] L. Petrossian *et al.*, “High aspect ratio cylindrical nanopores in silicon-on-insulator substrates,” *Solid. State. Electron.*, vol. 51, no. 10, pp. 1391–1397, 2007, doi: 10.1016/j.sse.2007.06.014.
- [207] D. G. Howitt, S. J. Chen, B. C. Gierhart, R. L. Smith, and S. D. Collins, “The electron beam hole drilling of silicon nitride thin films,” *J. Appl. Phys.*, vol. 103, no. 2, p. 024310, 2008, doi: 10.1063/1.2828157.

- [208] A. P. Alivisatos *et al.*, “Nanotools for neuroscience and brain activity mapping,” *ACS Nano*, vol. 7, no. 3, pp. 1850–1866, 2013, doi: 10.1021/nm4012847.
- [209] A. J. Storm, C. Storm, J. Chen, H. Zandbergen, J. F. Joanny, and C. Dekker, “Fast DNA translocation through a solid-state nanopore,” *Nano Lett.*, vol. 5, no. 7, pp. 1193–1197, 2005, doi: 10.1021/nl048030d.
- [210] S. Qian and Y. Ai, *Electrokinetic Particle Transport in Micro-/Nanofluidics*. 2012.
- [211] Y. He, M. Tsutsui, R. H. Scheicher, C. Fan, M. Taniguchi, and T. Kawai, “Mechanism of how salt-gradient-induced charges affect the translocation of DNA molecules through a nanopore,” *Biophys. J.*, vol. 105, no. 3, pp. 776–782, 2013, doi: 10.1016/j.bpj.2013.05.065.
- [212] S. Banerjee *et al.*, “Slowing DNA transport using graphene-DNA interactions,” *Adv. Funct. Mater.*, vol. 25, no. 6, pp. 936–946, 2015, doi: 10.1002/adfm.201403719.
- [213] W. Si, J. Sha, L. Liu, Y. Qiu, and Y. Chen, “Effect of nanopore size on poly(dT)<sub>30</sub> translocation through silicon nitride membrane,” *Sci. China Technol. Sci.*, vol. 56, no. 10, pp. 2398–2402, 2013, doi: 10.1007/s11431-013-5330-2.
- [214] A. M. Popa, P. Niedermann, H. Heinzelmann, J. A. Hubbell, and R. Pugin, “Fabrication of nanopore arrays and ultrathin silicon nitride membranes by block-copolymer-assisted lithography,” *Nanotechnology*, vol. 20, no. 48, p. 485303, 2009, doi: 10.1088/0957-4484/20/48/485303.
- [215] K. Liu *et al.*, “Geometrical Effect in 2D Nanopores,” *Nano Lett.*, vol. 17, no. 7, pp. 4223–4230, 2017, doi: 10.1021/acs.nanolett.7b01091.
- [216] W. gwi Kim and S. Nair, “Membranes from nanoporous 1D and 2D materials: A review of opportunities, developments, and challenges,” *Chemical Engineering Science*, vol. 104, pp. 908–924, 2013, doi: 10.1016/j.ces.2013.09.047.
- [217] K. S. Novoselov *et al.*, “Two-dimensional atomic crystals,” *Proc. Natl. Acad. Sci. U. S. A.*, vol. 102, no. 30, pp. 10451–10453, 2005, doi: 10.1073/pnas.0502848102.
- [218] M. Shankla and A. Aksimentiev, “Conformational transitions and stop-and-go nanopore transport of single-stranded DNA on charged graphene,” *Nat. Commun.*, vol. 5, p. 5171,

- 2014, doi: 10.1038/ncomms6171.
- [219] B. Wang *et al.*, “Electric Field Effect in Atomically Thin Carbon Films,” *Mater. Today*, vol. 60, no. 8, pp. 35–41, 2010, doi: 10.1063/1.2774096.
- [220] H. Qiu, A. Sarathy, K. Schulten, and J. P. Leburton, “Detection and mapping of DNA methylation with 2D material nanopores,” *npj 2D Mater. Appl.*, vol. 1, no. 1, p. 3, 2017, doi: 10.1038/s41699-017-0005-7.
- [221] J. Feng *et al.*, “Electrochemical reaction in single layer MoS<sub>2</sub>: Nanopores opened atom by atom,” *Nano Lett.*, vol. 15, no. 5, pp. 3431–3438, 2015, doi: 10.1021/acs.nanolett.5b00768.
- [222] M. Lepoitevin, P. E. Coulon, M. Bechelany, J. Cambedouzou, J. M. Janot, and S. Balme, “Influence of nanopore surface charge and magnesium ion on polyadenosine translocation,” *Nanotechnology*, vol. 26, no. 14, p. 144001, 2015, doi: 10.1088/0957-4484/26/14/144001.
- [223] X. Song *et al.*, “Origination, expansion, evolutionary trajectory, and expression bias of ap2/erf superfamily in brassica napus,” *Front. Plant Sci.*, vol. 7, p. 1186, 2016, doi: 10.3389/fpls.2016.01186.
- [224] E. Paek, A. J. Pak, and G. S. Hwang, “A Computational Study of the Interfacial Structure and Capacitance of Graphene in [BMIM][PF<sub>6</sub>] Ionic Liquid,” *J. Electrochem. Soc.*, vol. 160, no. 1, pp. A1–A10, 2013, doi: 10.1149/2.019301jes.
- [225] P. Lu, Q. Dai, L. Wu, and X. Liu, “Structure and capacitance of electrical double layers at the graphene-ionic liquid interface,” *Appl. Sci.*, vol. 7, no. 9, pp. 939–952, 2017, doi: 10.3390/app7090939.
- [226] D. Fologea, M. Gershow, B. Ledden, D. S. McNabb, J. A. Golovchenko, and J. Li, “Detecting single stranded DNA with a solid state nanopore,” *Nano Lett.*, vol. 5, no. 10, pp. 1905–1909, 2005, doi: 10.1021/nl051199m.
- [227] J. Geng, H. Fang, F. Haque, L. Zhang, and P. Guo, “Three reversible and controllable discrete steps of channel gating of a viral DNA packaging motor,” *Biomaterials*, vol. 32, no. 32, pp. 8234–8242, 2011, doi: 10.1016/j.biomaterials.2011.07.034.
- [228] F. Haque, J. Lunn, H. Fang, D. Smithrud, and P. Guo, “Real-time sensing and discrimination

- of single chemicals using the channel of Phi29 DNA packaging nanomotor,” *ACS Nano*, vol. 6, no. 4, pp. 3251–3261, 2012, doi: 10.1021/nm3001615.
- [229] K. B. Park *et al.*, “Noise and sensitivity characteristics of solid-state nanopores with a boron nitride 2-D membrane on a pyrex substrate,” *Nanoscale*, vol. 8, no. 10, pp. 5755–5763, 2016, doi: 10.1039/c5nr09085g.
- [230] P. Waduge *et al.*, “Direct and Scalable Deposition of Atomically Thin Low-Noise MoS<sub>2</sub> Membranes on Apertures,” *ACS Nano*, vol. 9, no. 7, pp. 7352–7359, 2015, doi: 10.1021/acsnano.5b02369.
- [231] S. Howorka, S. Cheley, and H. Bayley, “Sequence-specific detection of individual DNA strands using engineered nanopores,” *Nat. Biotechnol.*, vol. 19, no. 7, pp. 636–639, 2001, doi: 10.1038/90236.
- [232] D. Japrun, M. Henricus, Q. Li, G. Maglia, and H. Bayley, “Urea facilitates the translocation of single-stranded DNA and RNA through the  $\alpha$ -hemolysin nanopore,” *Biophys. J.*, vol. 98, no. 9, pp. 1856–1863, 2010, doi: 10.1016/j.bpj.2009.12.4333.
- [233] D. Wendell *et al.*, “Translocation of double-stranded DNA through membrane-adapted phi29 motor protein nanopores,” *Nat. Nanotechnol.*, vol. 4, no. 11, pp. 765–772, 2009, doi: 10.1038/nnano.2009.259.
- [234] P. Jing, F. Haque, D. Shu, C. Montemagno, and P. Guo, “One-way traffic of a viral motor channel for double-stranded DNA translocation,” *Nano Lett.*, vol. 10, no. 9, pp. 3620–3627, 2010, doi: 10.1021/nl101939e.
- [235] H. Fang, P. Jing, F. Haque, and P. Guo, “Role of channel lysines and the ‘push through a one-way valve’ mechanism of the viral DNA packaging motor,” *Biophys. J.*, vol. 102, no. 1, pp. 127–135, 2012, doi: 10.1016/j.bpj.2011.11.4013.
- [236] U. F. Keyser, S. Van Dorp, and S. G. Lemay, “Tether forces in DNA electrophoresis,” *Chem. Soc. Rev.*, vol. 39, no. 3, pp. 939–947, 2010, doi: 10.1039/b902072c.
- [237] S. H. Behrens and D. G. Grier, “The charge of glass and silica surfaces,” *J. Chem. Phys.*, vol. 115, no. 14, pp. 6716–6721, 2001, doi: 10.1063/1.1404988.

- [238] R. B. Schoch, J. Han, and P. Renaud, “Transport phenomena in nanofluidics,” *Rev. Mod. Phys.*, vol. 80, no. 3, pp. 839–883, 2008, doi: 10.1103/RevModPhys.80.839.
- [239] S. Garaj, W. Hubbard, A. Reina, J. Kong, D. Branton, and J. A. Golovchenko, “Graphene as a subnanometre trans-electrode membrane,” *Nature*, vol. 467, no. 7312, pp. 190–193, 2010, doi: 10.1038/nature09379.
- [240] M. H. Lee *et al.*, “A low-noise solid-state nanopore platform based on a highly insulating substrate,” *Sci. Rep.*, vol. 4, p. 7448, 2014, doi: 10.1038/srep07448.
- [241] P. Sen and M. Gupta, “Single nucleotide detection using bilayer MoS<sub>2</sub> nanopores with high efficiency†,” *RSC Adv.*, vol. 11, no. 11, pp. 6114–6123, 2021, doi: 10.1039/d0ra10222a.
- [242] A. Perez-Rathke, M. A. Fahie, C. Chisholm, J. Liang, and M. Chen, “Mechanism of OmpG pH-Dependent Gating from Loop Ensemble and Single Channel Studies,” *J. Am. Chem. Soc.*, vol. 140, no. 3, pp. 1105–1115, 2018, doi: 10.1021/jacs.7b11979.
- [243] S. Pezeshki, C. Chimerel, A. N. Bessonov, M. Winterhalter, and U. Kleinekathöfer, “Understanding ion conductance on a molecular level: An all-atom modeling of the bacterial porin OmpF,” *Biophys. J.*, vol. 97, no. 7, pp. 1898–1906, 2009, doi: 10.1016/j.bpj.2009.07.018.
- [244] R. M. M. Smeets, U. F. Keyser, N. H. Dekker, and C. Dekker, “Noise in solid-state nanopores,” *Proc. Natl. Acad. Sci. U. S. A.*, vol. 105, no. 2, pp. 417–421, 2008, doi: 10.1073/pnas.0705349105.
- [245] M. Yu *et al.*, “Mutation of the critical pH-gating residues histidine 231 to glutamate increase open probability of outer membrane protein G in planar lipid bilayer,” *Protein and Cell*, vol. 4, pp. 803–806, 2013, doi: 10.1007/s13238-013-3070-5.
- [246] S. Liang *et al.*, “Noise in nanopore sensors: Sources, models, reduction, and benchmarking,” *Nami Jishu yu Jingmi Gongcheng/Nanotechnology Precis. Eng.*, vol. 3, no. 1, pp. 9–17, 2020, doi: 10.1016/j.npe.2019.12.008.
- [247] Canadian Centre on Substance Abuse, “Canada ’ s low -risk alcohol drinking guidelines,” *Canadian Centre on Substance Abuse*, 2011. [www.ccsa.ca](http://www.ccsa.ca) (accessed Sep. 15, 2015).

- [248] M. B. Bridgeman and D. T. Abazia, “Medicinal cannabis: History, pharmacology, and implications for the acute care setting,” *P T*, vol. 42, no. 3, pp. 180–188, 2017.
- [249] “The Canadian Encyclopedia,” *Choice Rev. Online*, vol. 45, no. 08, pp. 45–4105, 2008, doi: 10.5860/choice.45-4105.
- [250] F. Grotenhermen, “Pharmacokinetics and pharmacodynamics of cannabinoids,” *Clinical Pharmacokinetics*, vol. 42, pp. 327–360, 2003, doi: 10.2165/00003088-200342040-00003.
- [251] H. B. Huson, T. M. Granados, and Y. Rasko, “Surgical considerations of marijuana use in elective procedures,” *Heliyon*, vol. 4, no. 9, p. e00779, 2018, doi: 10.1016/j.heliyon.2018.e00779.
- [252] N. M. Kogan and R. Mechoulam, “Cannabinoids in health and disease,” *Dialogues in Clinical Neuroscience*, vol. 9, no. 4, pp. 413–430, 2007, doi: 10.31887/dens.2007.9.4/nkogan.
- [253] S. A. Millar, N. L. Stone, A. S. Yates, and S. E. O’Sullivan, “A systematic review on the pharmacokinetics of cannabidiol in humans,” *Frontiers in Pharmacology*, vol. 9, p. 1365, 2018, doi: 10.3389/fphar.2018.01365.
- [254] L. Zuurman, A. E. Ippel, E. Moin, and J. M. A. Van Gerven, “Biomarkers for the effects of cannabis and THC in healthy volunteers,” *Br. J. Clin. Pharmacol.*, vol. 67, no. 1, pp. 5–21, 2009, doi: 10.1111/j.1365-2125.2008.03329.x.
- [255] D. Jutras-Aswad, J. A. DiNieri, T. Harkany, and Y. L. Hurd, “Neurobiological consequences of maternal cannabis on human fetal development and its neuropsychiatric outcome,” *European Archives of Psychiatry and Clinical Neuroscience*, vol. 259, no. 7, pp. 395–412, 2009, doi: 10.1007/s00406-009-0027-z.
- [256] D. G. Barrus *et al.*, “Tasty THC: Promises and Challenges of Cannabis Edibles,” *Methods Rep. RTI. Press.*, vol. 2016, pp. 1–22, 2016, doi: 10.3768/rtipress.2016.op.0035.1611.
- [257] Statistics Canada, “National Cannabis Survey, first quarter 201,” *Dly.*, p. 32098, 2019.
- [258] J. Yoshizumi, S. Kumamoto, M. Nakamura, and K. Yamana, “Target-induced strand release (TISR) from aptamer-DNA duplex: A general strategy for electronic detection of

- biomolecules ranging from a small molecule to a large protein,” *Analyst*, vol. 133, no. 3, pp. 323–325, 2008, doi: 10.1039/b719089c.
- [259] B. Luan and G. Stolovitzky, “An electro-hydrodynamics-based model for the ionic conductivity of solid-state nanopores during DNA translocation,” *Nanotechnology*, vol. 24, no. 19, p. 195702, 2013, doi: 10.1088/0957-4484/24/19/195702.
- [260] C. Wanklyn *et al.*, “Disposable screen printed sensor for the electrochemical detection of delta-9-tetrahydrocannabinol in undiluted saliva,” *Chem. Cent. J.*, vol. 10, p. 1, 2016, doi: 10.1186/s13065-016-0148-1.

# Appendices

## Appendix A

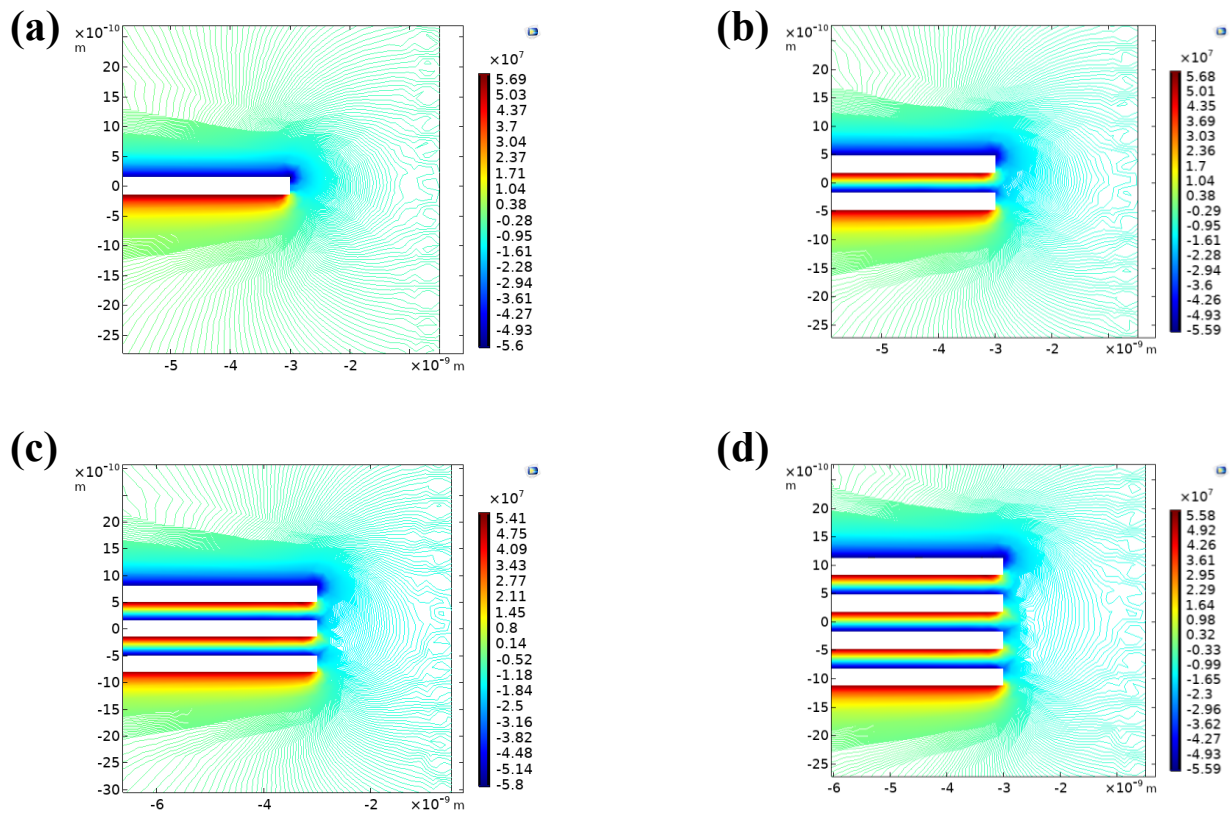


**Figure A- 1.** Electric field gradient contour plot (in V/m) obtained for (a) 1 layer, (b) 2 layers, (c) 3 layers and (d) 4 layers MoS<sub>2</sub> nanopores.

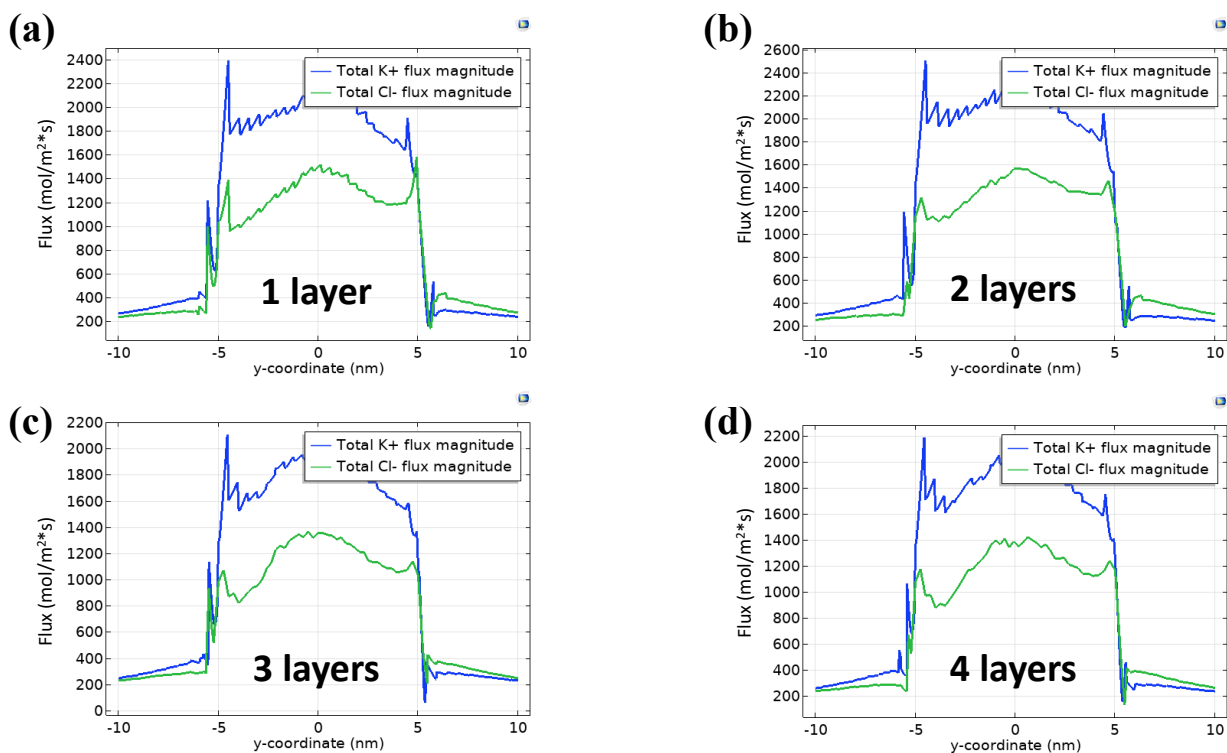


**Figure A- 2.**  $K^+$  and  $Cl^-$  total (diffusive, convective, and electrical) flux contributions to the nanopore conductance for (a) 1 layer, (b) 2 layers, (c) 3 layers and (d) 4 layers  $MoS_2$  nanopores.

**Table A- 1.** Hydrodynamic, electrostatic, and total force acting on the translocating DNA.

	Hydrodynamic force (N)	Electrostatic force (N)	Total force (N)
1 layer	20.273E-15	1.4509E-14	34.782E-15
2 layers	-8.4948E-15	2.5175E-14	16.6802E-15
3 layers	15.275E-15	1.2754E-14	28.029E-15
4 layers	-2.296E-15	1.924E-14	25.944E-15

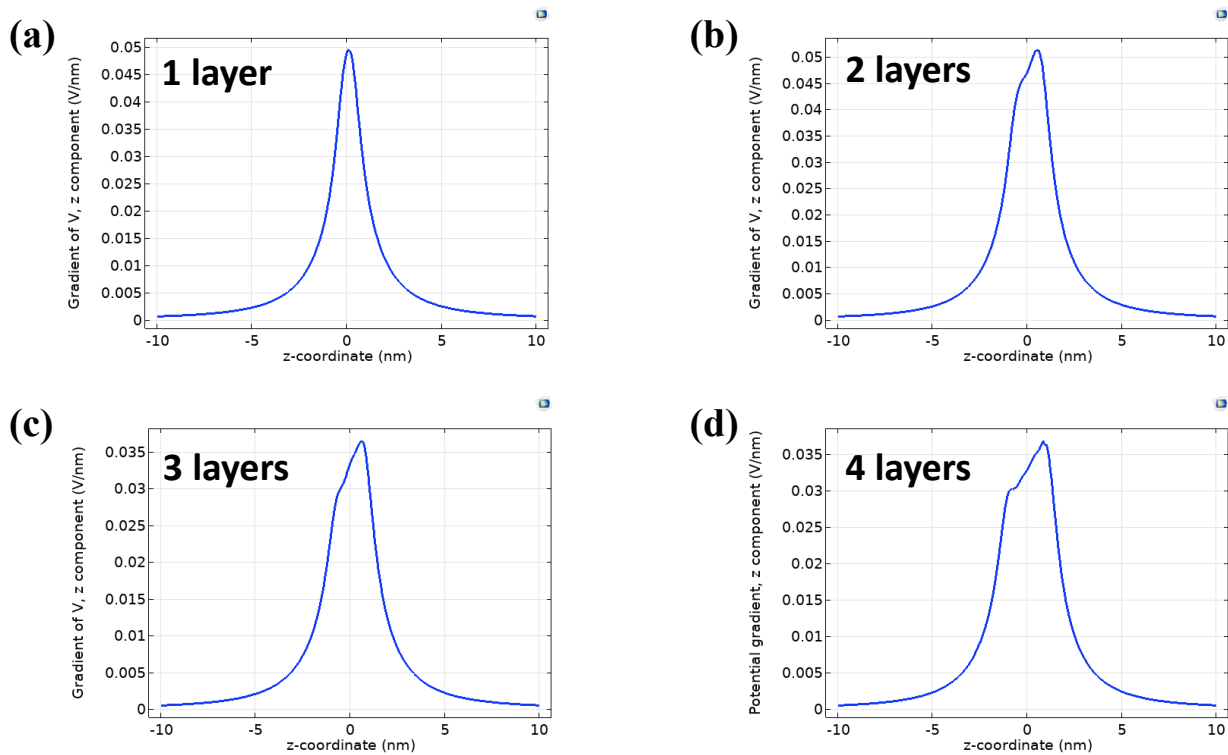


**Figure A- 3.** Potential gradient along the translocation axis for (a) 1 layer, (b) 2 layers, (c) 3 layers and (d) 4 layers MoS<sub>2</sub> nanopores.

## Appendix B

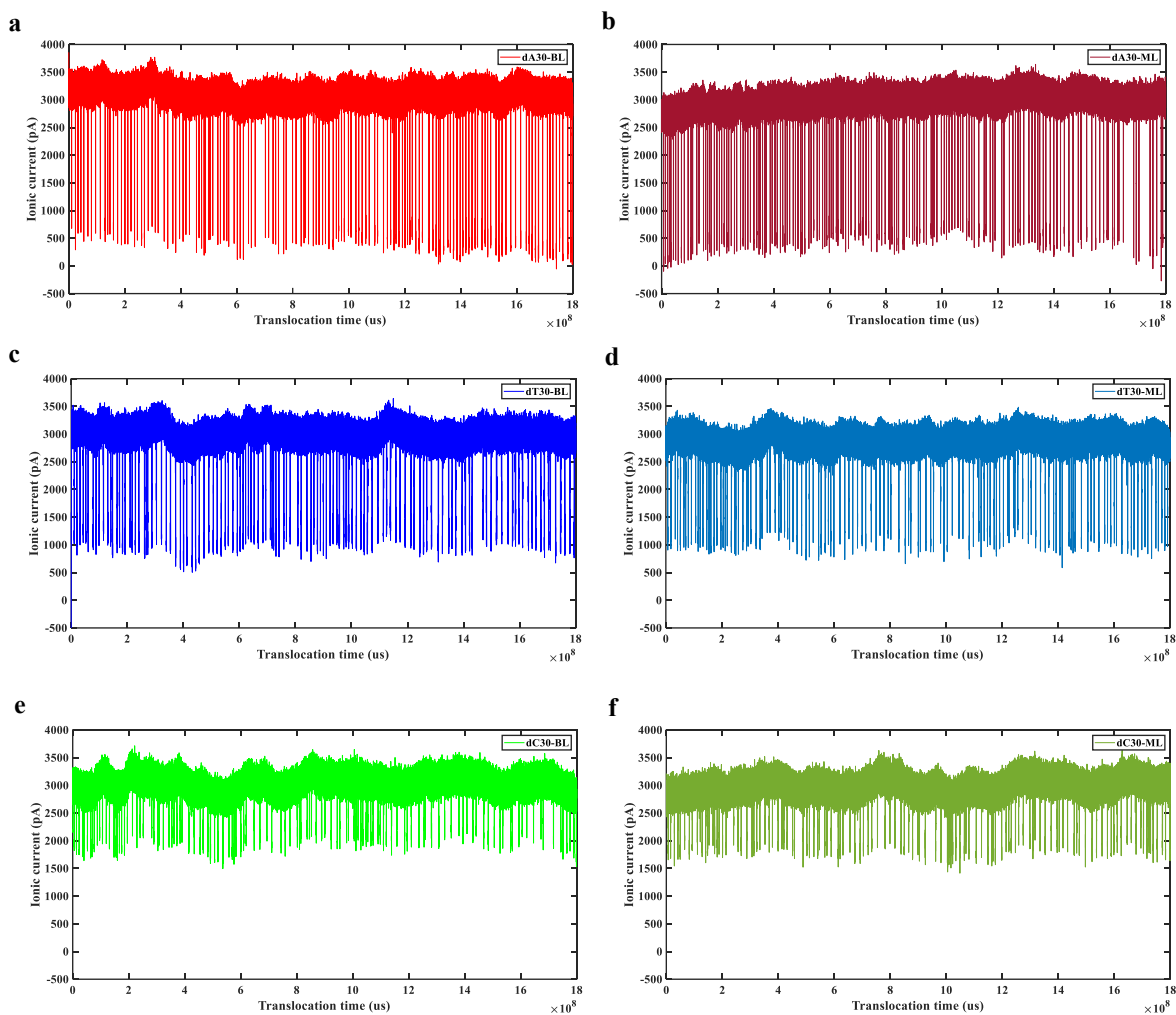


**Figure B- 12.** dA30 translocation traces through (a) ML and (b) BL MoS<sub>2</sub> nanopores, dT30 translocation traces through (c) ML and (d) BL MoS<sub>2</sub> nanopores and dC30 translocation traces through (e) ML and (f) BL MoS<sub>2</sub> nanopores. All traces recorded at 300 mM KCl and 200 mV trans bias.

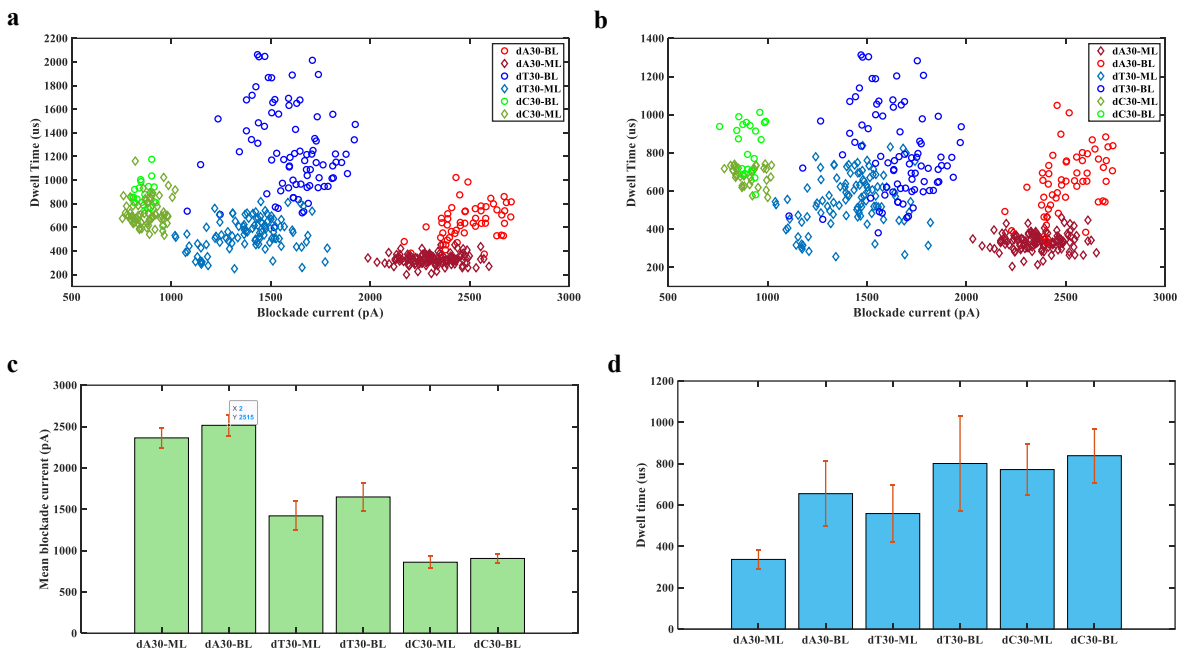


**Figure B- 13.** (a-b) Scatter plot of dA30, dT30 and dC30 sensing events through two different nanopores for each of ML and BL MoS<sub>2</sub>, bar plots showing (c) mean blockade current and (d) dwell time obtained for polynucleotide (dA30, dT30 and dC30) sensing through ML and BL MoS<sub>2</sub> nanopores.

## Appendix C

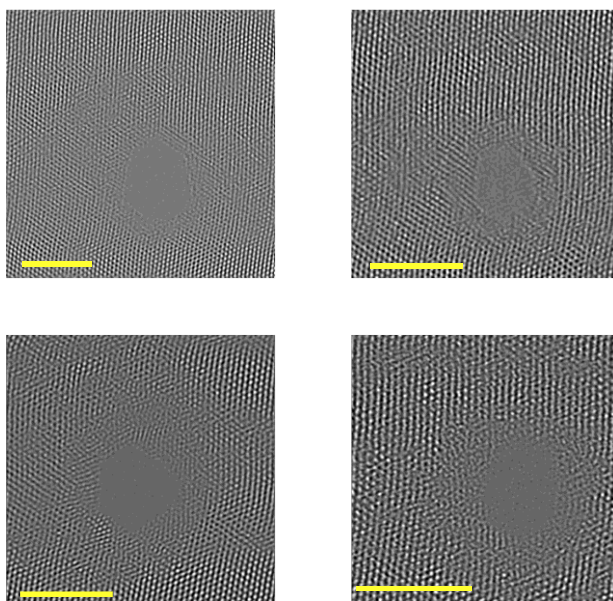


**Figure C- 1.** Four different STEM fabricated nanopores having  $\sim 3.4$  nm diameter, showing the pore fabrication repeatability and controllability of BL MoS<sub>2</sub> nanopores.

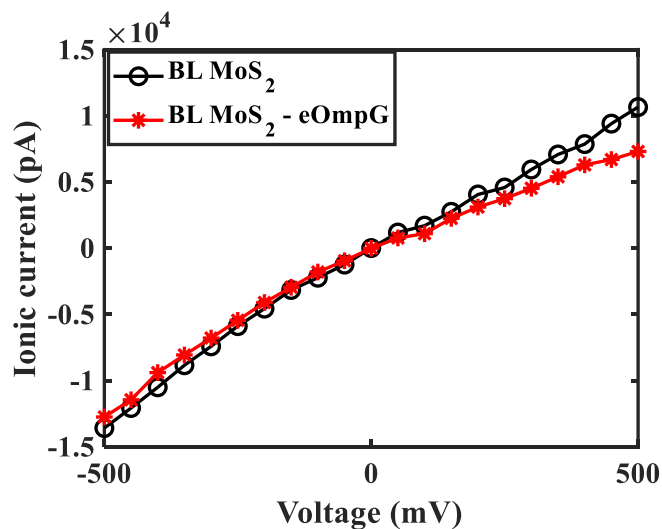


**Figure C- 2.** Ionic current vs voltage plot using 100 mM KCl before and after eOmpG insertion into the fabricated BL MoS<sub>2</sub> nanopore at neutral pH showing that the pore exhibits stable attachment at positive voltages and detaches at negative voltages.

## Protein purification and cell culture

The vector encoding eOmpG (pET-28a-eOmpG-6His) was transformed into C41 competent cells and the cells were plated on an agar plate supplemented with 5 ug/ml kanamycin. A fresh colony was grown in 2 ml SOC (Super Optimal broth with Catabolite repression) broth supplemented with 5 ug/ml kanamycin at 37°C and 250 rpm overnight. The starter culture was then diluted 1:100 into TB broth supplemented with 20 mM glucose and 5 ug/ml kanamycin. Cells was grown at 37°C and 250 rpm until the optical density at 600 nm (OD600) reached 1.0. The cells were induced by the addition of isopropyl  $\beta$ -D-1-thiogalactopyranoside (IPTG) (final concentration 0.5 mM) and were allowed to grow for another 3 hr at 37°. The cells were harvested by centrifugation at 9000  $\times$ g for 15 min and then the pellets were frozen at -20 °C.

For refolding and purification, the pellet was resuspended in 1/40 culture volume of ice-cold lysis buffer (20 mM Tris-HCl, 100 mM NaCl, pH 8.0) supplemented with 0.2 mM phenylmethylsulfonyl fluoride (PMSF) and 2  $\mu$ g/ml DNase I, then lysed using a cell disruptor. The cell lysate was centrifuged at 12,000  $\times$ g for 30 min at 4°C. The supernatant was discarded, and the pellet was washed using the wash buffer (20 mM Tris-HCl, 100 mM NaCl, 10 mM Ethylenediaminetetraacetic acid (EDTA), 1% Triton-X 100, pH 8.0) for three times and then washed using the lysis buffer to remove residual Triton-X100. The washed inclusion body (IB) was then dissolved in the dissolving buffer (8 M urea, 50 mM Tris-HCl, 2 mM Dithiothreitol (DTT), pH 8.0) (1ml dissolving buffer per 0.1g of IB). The mixture was incubated for 1 hour at room temperature before centrifuge at 18000 $\times$ g at room temperature for 30 min. The supernatant was then applied on a Hitrap Q FF column (GE Healthcare) and eluted using gradient elution (0 to 500 mM NaCl over 30 CV). Fractions containing the pure unfolded OmpG were pooled and concentrated using Amicon 10kD centrifugal device.



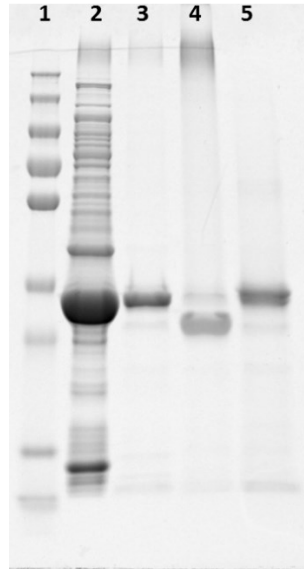


**Figure C- 4.** SDS-PAGE gel of eOmpG. Lane 1: molecular weight ladder; 2: dissolved inclusion body before FPLC purification; 3: purified unfolded sample; 4: refolded eOmpG; 5: heat-denatured refolded protein.

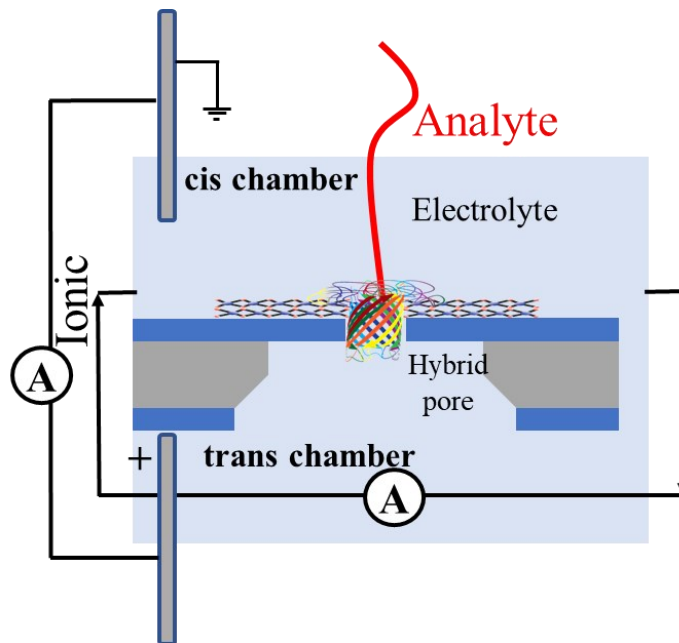


**Figure C- 5.** Schematic explaining the cis and trans sides of hybrid eOmpG-MoS<sub>2</sub> nanopore sensing set-up.

## **Appendix D**

### **Data acquisition and analysis:**

Single nucleotide and DNA sequencing data were acquired at a sampling rate of 200 kHz. No in-built filtering was used to recorder larger bandwidth and prevent data loss due to filtering. The data was resampled by a factor of 100 to reduce the rise time and accurately calculate the blockade and dwell time values for short-lived single nucleotide translocation events. After resampling the white gaussian noise is also transferred to the resampled trace to prevent aliasing and for accurate representation and prevention of artifacts. Then the raw data were filtered at a cut-off frequency of 20 kHz, using 8-pole low-pass Bessel filter of Clampfit software. This was done to confidently identify translocation events and separate them from non-translocation interactions and attenuated events. The translocation statistics of the selected events were then calculated from unfiltered and resampled data and reported in **Chapter 6**. Polynucleotide and THC translocations through hybrid nanopore were conducted at 20 kHz frequency. No resampling was required or done in this study. Translocation events were identified in the same way as before at a cut-off of 2kHz. The noise analysis in **Chapter 7** was carried out on raw data, high pass filtered at 1 Hz to remove low-frequency baseline fluctuations.